



HAL
open science

Electric and chemical manipulation of magnetic anisotropy of ultrathin ferromagnetic films

Nan Di

► **To cite this version:**

Nan Di. Electric and chemical manipulation of magnetic anisotropy of ultrathin ferromagnetic films. Physics [physics]. Ecole Polytechnique, 2015. English. NNT: . tel-01224224

HAL Id: tel-01224224

<https://pastel.hal.science/tel-01224224>

Submitted on 4 Nov 2015

HAL is a multi-disciplinary open access archive for the deposit and dissemination of scientific research documents, whether they are published or not. The documents may come from teaching and research institutions in France or abroad, or from public or private research centers.

L'archive ouverte pluridisciplinaire **HAL**, est destinée au dépôt et à la diffusion de documents scientifiques de niveau recherche, publiés ou non, émanant des établissements d'enseignement et de recherche français ou étrangers, des laboratoires publics ou privés.



Thèse présentée pour obtenir le grade de

DOCTEUR DE L'ÉCOLE POLYTECHNIQUE

Spécialité: Sciences des Matériaux

Par

Nan DI

<p>Electric and chemical manipulation of magnetic anisotropy of ultrathin ferromagnetic films</p>
--

Soutenue le 16 septembre 2015 devant les membres du jury :

Dr V. MAURICE	IRCP, Ecole National Supérieur de Chimie Paris	Rapporteur
Dr A. THIAVILLE	LPS, Université Paris-Sud	Rapporteur
Dr. J-E WEGROWE	LSI, Ecole Polytechnique	Examineur
Dr. F. OZANAM	PMC, Ecole Polytechnique	Examineur
Dr. P. ALLONGUE	PMC, Ecole Polytechnique	Co Directeur
Dr. F. MAROUN	PMC, Ecole Polytechnique	Directeur

Remerciements

A mes parents

谨献给我挚爱的父母



J'ai réalisé mon doctorat à l'Ecole Polytechnique, au sein du laboratoire de Physique de la Matière Condensée (PMC) dans l'équipe de l'électrochimie avec une allocation International de thèse 'Gaspard Monge' du 1^{er} octobre 2012 pour une durée de trois ans. Je tiens à remercier au travers de ces quelques lignes les différentes personnes qui ont participé au bon déroulement de ce projet.

En premier lieu je tiens à remercier les deux personnes qui ont dirigé ce travail : Fouad Maroun, mon directeur de thèse et Philippe Allongue, mon co-directeur de thèse. Je souhaite à exprimer ma reconnaissance pour leur encadrement minutieux de ce rapport, pour leurs visions scientifique qui ont rendu tant d'exploitation de résultat utile et pertinente et pour m'avoir aidé à finaliser ce travail dans les temps.

Ensuite je tiens à remercier les membres du jury qui m'ont fait l'honneur de juger ce travail avec mes deux rapporteurs Vincent Maurice et André Thiaville et mes deux examinateurs Jean-Eric Wegrowe et François Ozanam.

Je remercie sincèrement Isabelle Maurin pour m'avoir encouragée et m'avoir soutenue tout le temps jusqu'à la fin de la thèse, également Catherine Henry De Villeneuve, Anne Moraillon, Anne-Chantal Gouget, Michel Rosso, et tous les autres membres du PMC pour leurs sympathie. J'aimerais aussi remercier Robert Cortès pour les mesures par rayons X sur mes substrats. Je tiens à remercier aussi Alistair Rowe pour son souci des carrières des doctorants. Je pense aussi à Yves Lassailly pour ces cafés et ces thés.

Je remercie aussi professeur Geoffrey S.D.Beach au MIT pour m'avoir accueilli dans son équipe pour effectuer mon programme d'échange, où j'ai passée un temps formidable. J'ai bien pris le temps pour profiter des nouvelles technologies et aussi une richesse scientifique et culturelle.

Je souhaite faire des remerciements particuliers à l'ensemble des doctorants de PMC pour leur implication forte dans la vie du laboratoire au travers des séminaires thésards, pots de thèse, visites de laboratoires, etc... et avec qui j'ai pu nouer des liens d'amitié forts et durables. Je pense notamment à Lucie Devys, Daniel Alves Dalla Corte, N. Le Thang Long, Viacheslav Kubyskvi, Nicolas Desboeuf, Barbara Brudieu, Hongye Yuan, Tapajyoti Das gupta, Manon Lafouresse, Maria Castellano Sanz , Marine Brunet, Marco Piccardo, Timothy Aschl, Stefan Klaes , Duc VU-ANH , Petr Polovodov, Fabien Cadiz, Godefroy Lemenager, Boo-Min Koo, Minyeong Kang, Nikoletta Jegenyés, Maud Thiriet...dont la presence au

laboratoires les soirs de semaines ou les week ends nous ont amené à partager des moments qui me laisseront des souvenirs impérissables. J'espère grandement que nous saurons perpétuer ces relations privilégiées qui nous unissent au sein du laboratoire.

En fin, je remercie mes parents qui soutiennent toujours mes choix et m'encourageant toute ma vie.

CONTENTS

CHAPTER 1 INTRODUCTION	1
REFERENCES	4
CHAPTER 2 THEORETICAL BACKGROUND AND EXPERIMENTAL DETAILS: GROWTH AN MAGNETISM OF ELECTRODEPOSITED CO/AU(111) LAYERS.....	9
2.1. INTRODUCTION.....	9
2.2. MAGNETIC ANISOTROPY ENERGY OF ULTRATHIN FILMS	9
2.3. IN SITU MAGNETIC CHARACTERIZATIONS.....	14
2.3.1. <i>Principle of MOKE</i>	14
2.3.2. <i>Experimental set-up</i>	14
2.4. BASICS CONCEPTS OF ELECTROCHEMISTRY:	17
2.4.1. <i>Structure of the electrochemical interface</i>	17
2.4.2. <i>Principle of Electrodeposition</i>	17
2.5. ELECTRODEPOSITION OF Co/AU(111) LAYERS	20
2.5.1. <i>Preparation of the Au(111)/Si(111) substrate</i>	20
2.5.2. <i>Nucleation and growth of Co/Au(111) layers</i>	21
a) Electrochemical and optical measurements.....	21
b) STM observations	25
c) In-situ P-MOKE measurements.....	26
2.6. CONCLUSIONS	30
2.7. REFERENCES	30
CHAPTER 3 ELECTROCHEMICAL OXIDATION OF COBALT AND ITS INFLUENCE ON THE MAGNETIC PROPERTIES OF CO/AU (111) LAYERS.....	33
3.1. INTRODUCTION.....	33
3.2. CO ELECTROCHEMICAL OXIDATION REVISITED: RESULTS AND DISCUSSION	35
3.2.1. <i>Electrochemical response</i>	35
3.2.2. <i>Potential – phase diagram of Co</i>	37
3.3. TRANSFER OF CO/AU SAMPLES INTO ELECTROLYTES OF PH 12	39
3.4. MAE OF CO THIN FILMS UPON OH ADSORPTION (PEAK A ₁).....	45
3.4.1. <i>Results</i>	45
3.4.2. <i>Discussion</i>	51
a) Cobalt surface chemistry in peak A ₁	51
b) Oxide coverage dependence of the magnetic surface anisotropy.....	53
3.4.3. <i>Conclusion</i>	55

3.5.	MAE OF Co/AU(111) FILMS UPON Co(OH) ₂ FORMATION (PEAK A ₂).....	55
3.5.1.	<i>Electrochemistry: results and discussion</i>	55
3.5.2.	<i>Magnetic properties of Co layers in the range of peak (A₂): results and discussion</i>	62
3.6.	CONCLUSIONS	68
3.7.	REFERENCES	69

CHAPTER 4 INFLUENCE OF SURFACE CHEMISTRY ON THE MAE AND MEC OF CO/AU(111) ULTRATHIN FILMS 71

4.1.	INTRODUCTION.....	71
4.2.	EXPERIMENTAL METHODS	75
4.3.	RESULTS: IMPACT OF SURFACE CHEMISTRY ON MAE.....	75
4.4.	RESULTS: MEC EFFECTS OF CO COVERED WITH MOLECULAR LAYERS.....	84
4.4.1.	<i>Electrochemical characterizations</i>	84
4.4.2.	<i>MEC results</i>	86
	a) In-plane magnetization films ($t_{Co} > t^*$)	86
	b) Films of thickness close to t^*	89
	c) Films of thickness below t^* (i.e. out-of-plane magnetized)	90
4.5.	DISCUSSION.....	97
4.5.1.	<i>Determination of MEC coefficients</i>	97
	a) Films thicker than t^*	97
	b) Films of thickness close to t^*	99
4.5.2.	<i>Mechanisms of MEC</i>	100
4.5.3.	<i>Correlation MAE - structure of modified surfaces</i>	106
4.5.4.	<i>Correlation MEC coefficient - structure of modified surfaces</i>	106
4.6.	CONCLUSIONS	107
4.7.	REFERENCES	108

CHAPTER 5 INFLUENCE OF HYDROGEN ON THE MAGNETIC ANISOTROPY OF Pd/CO BILAYERS AND PdCO ALLOY LAYERS 113

5.1.	INTRODUCTION.....	113
5.2.	EXPERIMENTAL METHODS	114
5.3.	PREPARATION OF Pd/CO BILAYERS AND INFLUENCE OF H ADSORPTION/ABSORPTION ON THE Pd/CO BILAYERS' PROPERTIES.....	117
5.3.1.	<i>Pd/Co bilayer prepared through electrochemical deposition</i>	117
5.3.2.	<i>Pd/Co bilayers prepared through sputter deposition</i>	120
5.3.3.	<i>H₂ induced modification of magnetic anisotropy for Pd/Co bilayers</i>	121
5.4.	PREPARATION OF PdCO ALLOYS AND INFLUENCE OF H ADSORPTION/ABSORPTION ON	

THE PdCo ALLOYS' PROPERTIES.....	130
5.4.1. PdCo alloy prepared by electrochemical deposition.....	130
5.4.2. PdCo alloys prepared by sputter deposition	133
5.4.3. H-induced modification of the magnetic anisotropy of PdCo alloys	134
5.5. DISCUSSION.....	145
5.5.1. Growth of the Pd/Co bilayer and PdCo alloys.....	145
5.5.2. Magnetic properties of the Pd/Co bilayers	146
5.5.3. Magnetic properties of the PdCo alloy layers.....	148
5.5.4. Time response of the Pd/Co bilayers and PdCo alloy layers	149
5.6. CONCLUSION.....	150
5.7. REFERENCES	151
CHAPTER 6 CONCLUSIONS.....	153
APPENDIX: STUDY OF Pd DEPOSITION ON Au(111)/Si(111) AND H	
ADSORPTION/ABSORPTION IN THE Pd/AU SYSTEM.....	157
A.1. INTRODUCTION.....	157
A.2. EXPERIMENTAL METHODS	159
A.3. RESULTS AND DISCUSSION	159
A.4. CONCLUSIONS	166
A.5. REFERENCES	167

ABBREVIATIONS

AFM	Atomic force microscopy
Bpy	2,2'-dipyridine
CO	Carbon monoxide
DES	Diethyl disulfide
DFT	Density functional theory
DMS	Dimethyl disulfide
DL	Dielectric layer
DTPy	4,4'- dithiodipyridine
FM	Ferromagnetic
GMR	Giant magneto resistance
HDD	Hard disk drives
HER	Hydrogen evolution reaction
HOR	Hydrogen oxidation reaction
HREELS	High-resolution electron energy loss spectroscopy
LEED	Low energy electron diffraction
MAE	Magnetic anisotropy energy
MCA	Magnetocrystalline anisotropy
MEC	Magneto electric coupling
MOKE	Magneto optic Kerr effect
MRAM	Magnetic random accessory memories
MSE	Mercury/mercurous sulfate electrode
PMA	Perpendicular magnetic anisotropy
P-MOKE	Polar magneto optic Kerr effect
PMC	Laboratoire de physique de la matière condensée
PVD	Physical vapor deposition
SAM	Self-assembly monolayer
SCN	Thiocyanate
SFI	Sputtered films incorporated
SHE	Standard hydrogen electrode reference
SQUID	Superconducting quantum interference device
SRT	Spin reorientation transition
STM	Scanning tunneling microscope
STT	Spin transfer torque
TDS	Thermal desorption spectroscopy
TMR	Tunneling magneto resistance
UHV	Ultra-high vacuum
VSM	Vibrating sample magnetometer
XPS	X-ray photoelectron spectroscopy experiments
XRR	X-ray reflectometry

Chapter 1 Introduction

Ferromagnetic materials and permanent magnets are involved in many devices of our daily life (e.g. electrical motors, transformers, electromagnets, loudspeakers) [1]. Depending on their application, different magnetic properties are required. The magnetic moment per atom is one important property and the magnetic softness or hardness is the other key property. These physical properties can be tailored thanks to the chemical composition and microstructure of alloys. Magneto crystalline anisotropy (MCA), one important property which contributes to the hardness of a magnet, is for instance related to the symmetry of the crystal structure due to spin orbit coupling [1]. The shape of the material is also important as it contributes to define the direction of magnetization at zero external magnetic field.

The magnetic anisotropy energy (MAE), which defines the easy axis of magnetization, is an essential property in technological devices. Magnetic hard disk drives (HDD) must for instance retain the stored information over 10 years which imposes a large MAE [2]. Proper functioning of giant magneto resistance (GMR) or tunneling magneto resistance (TMR) devices (**Fig. 1.1**) requires that the magnetization vector of one ferromagnetic (FM) layer is “pinned”, i.e. remains in a well-defined direction, while the magnetization vector of the second FM must be easily switchable in order to obtain a parallel (low resistance) or an antiparallel (high resistance) configuration (**Fig. 1.1**). A. Fert and P. Grünberg received the Nobel Prize in Physics in 2007 for the discovery of GMR¹. The scheme in **Fig. 1.1** is oversimplified as it omits that an antiferromagnetic layer is usually implemented to pin the magnetization of the lower FM layer. Different thicknesses can also be used for the two FM layer to differentiate their coercive forces and allow magnetization reversal of one layer without affecting the other layer. GMR and TMR components are now the building block of spin electronics. They are used as magnetic sensors to read data, create magnetic random access memories (MRAM) or can be used to design logic devices when coupled with magnetic domain wall motion [3].

¹see : http://www.nobelprize.org/nobel_prizes/lists/year/index.html?year=2007&images=yes

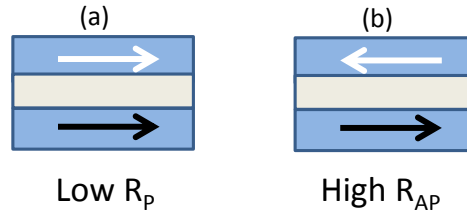


Fig. 1.1: Simplified representation of GMR or TMR junction. All layers have a thickness in the range of a few nm. The ferromagnetic layers (blue) are separated by a thin noble metal interlayer (GMR) or an insulating layer (TMR). The lower FM is “pinned”. The top one is switchable.

The very strong relationship between the magnetic properties of a bulk material with its electronic structure and crystal symmetry explains that reducing the physical dimensions of a magnetic material may promote very different magnetostatic properties. In fact, the atomic and/or chemical environment of surface atoms and the symmetry breaking at the surface are expected to induce new properties (moment, MAE). As will be developed in **Chapter 2**, the MAE of 2D ultrathin films can be written as $K_V + K_S/t$, where t is the film thickness. In this expression, K_V is a volume contribution and K_S a surface contribution. Without entering into the details, the second term is responsible for the perpendicular magnetization anisotropy (PMA) [4], nowadays a key property in spin electronics. However, in several surface science studies, the capping metal was substituted with chemisorbed species, which also influenced PMA.

As in microelectronics, there is a strong trend to downsizing components in spin electronics. This raises two major issues:

1) The so called superparamagnetic limit. Below a critical volume of material the blocking temperature is approaching room temperature and thermal agitation promotes spontaneous switching of the direction of magnetization.

2) Addressing the magnetization reversal in individual nanostructure: To really localize or address the magnetization reversal in one nanostructure at a time (and not surrounding ones) a mature technique is the injection of a spin polarized current to exert a Spin Transfer Torque (STT) [3,5]. This requires however huge current densities (10^6 to 10^7 A/cm²) which induces Joule heating.

Regarding point (2) the recent discovery that the application of an electric field modifies the MAE [6] has prompted numerous experimental [7,8] and theoretical works [9]. The idea is promoting the magnetization reversal in a given nanostructure while the

surrounding ones stay unaffected for a given external magnetic field. This phenomenon is also expected to help reducing the device power consumption.

The influence of electric field (E-field) on the MAE has been studied using various approaches. Most of the works deal with solid state structure as the one shown in **Fig. 1.2 (a)**. A dielectric layer is first deposited on the FM film to make a contact to apply the E-field. Effects remain generally very small because of the magnitude of the electric field is limited by the oxide thickness and dielectric properties. In addition, the presence of defects within the oxide induces an asymmetric response due to charge trapping. This phenomenon could be exploited to build magnetoelectric charge trap memory[8].

Historically, the first report about E-field effect on MAE [6] was obtained by immersing a ferromagnetic thin film in an electrolyte to exploit the very large electric field present at the metal surface. The simplified structure of the electrochemical interface is in fact shown in **Fig. 1.2c**. It shows that the negative charge on the metal surface is balanced by an excess of solvated cations on the solution side. Their closest approach distance from the surface being one solvent molecule diameter explains that electric fields in the range 1V/nm can be applied [10].

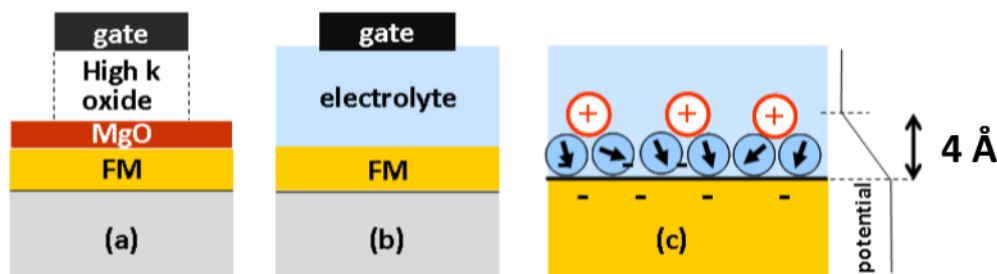


Figure 1.2: (a) Simplified solid state structure used to investigate the magneto-electric coupling (MEC). FM designates the ferromagnetic layer. In (b) the FM layer is grown in vacuum and then transferred in contact with an electrolyte. (c) Schematic representation of the electrochemical interface showing the electrochemical double layer (DL) where the negative charge on the metal is balanced by an excess of cations on the electrolyte side. The small charge separation (≈ 0.4 nm) leads to very large electric fields of ≥ 1 V/nm.

Point (1) above is essentially a material science issue to grow nanostructures with tailored MAE. Regarding this point, and because this is relevant to the present work, we want to emphasize that electrochemical deposition is one alternative technique to grow epitaxial films [11]. Thanks to the advent of in situ scanning tunneling microscopy (STM) [12] and the development of in situ X-ray techniques (at synchrotron radiation facilities) [13] it is in fact

possible to investigate in situ the mechanisms of nucleation and growth and to characterize the morphology and structure of layers grown by electrodeposition. The electrochemistry group at laboratory of condensed matter physics (PMC), Ecole Polytechnique investigated the electrodeposition of iron group metal (Ni, Co, Fe) [14,15,16,17,18] and Ni alloys (NiFe, NiPd, NiAu) [18,19]. Ex situ magnetic characterizations showed that a strong PMA is obtained with Au or Cu/Co/Au (111) bilayers [14,16]. In addition, the PMC electrochemistry group developed real time in situ magnetic characterizations to primarily investigate the magnetic state of layer while they are growing [15,20]. These works also demonstrated the strong influence of surface chemistry on MAE [17,18] and the facility offered by the set-up was exploited to investigate magneto electric coupling (MEC) at Co/Au(111) films in contact with an electrolyte [10,21].

This work is in the continuity of past work of the electrochemistry group at PMC. We exploit the double advantage of the electrochemical interface to grow high quality epitaxial magnetic films and investigate MEC as function of thickness and surface chemistry. As explained above, macroscopically uniform and very large electric fields ($>1\text{V/nm}$) may be easily obtained, allowing a quantitative study of the MEC effect. Moreover, this “soft” contact does not generate any structural defects in the magnetic film.

This manuscript is organized as follows. **Chapter 2** presents the basics about the magnetism of ultrathin films as well as the experimental set-up, based on magneto optical Kerr effect (MOKE), to characterize in situ the magnetic properties and MEC. This chapter briefly gives the elements necessary to understand the functioning of the electrochemical interface. It finally revisits the analysis of the spin reorientation transition (SRT) induced during the growth of Co/Au(111) films. In **Chapter 3**, we deal with the influence of Co/Au(111) electrochemical oxidation on MAE. Two oxidation states are considered. In **Chapter 4** we study the influence of chemisorbed molecules on MAE and MEC of Co/Au (111) layers. The work in **Chapter 5** was partly conducted in the group of Prof. G. Beach at MIT. It concerns the influence of H-adsorption and H-incorporation on the MAE of Pd/Co/Pt and CoPd/Pt layers. A general conclusion completes the manuscript.

References

- [1] S. Chikazumi, *Physics of magnetism*. (Wiley and Sons, New York, 1964).
- [2] M. K. Grobis, O. Hellwig, T. Hauet, E. Dobisz, and T. R. Albrecht, High-density bit patterned media: magnetic design and recording performance, *IEEE Transactions on magnetics* **47** (1), 6 (2011).
- [3] C. Chappert, A. Fert, and F. N. Van Dau, The emergence of spin electronics in data storage, *Nat Mater* **6** (11), 813 (2007).
- [4] M. T. Johnson, P. J. H. Bloemen, F. J. A. den Broeder, and J. J. de Vries, Magnetic anisotropy in metallic multilayers, *Reports on Progress in Physics* **59** (11), 1409 (1996); D. Sander, The magnetic anisotropy and spin reorientation of nanostructures and nanoscale films, *Journal of Physics: Condensed Matter* **16** (20), R603 (2004); K. Bennemann, Magnetic nanostructures, *Journal of Physics: Condensed Matter* **22** (24), 243201 (2010).
- [5] Arne Brataas, Andrew D. Kent, and Hideo Ohno, Current-induced torques in magnetic materials, *Nat Mater* **11** (5), 372 (2012); A. Manchon and S. Zhang, Theory of spin torque due to spin-orbit coupling, *Phys. Rev. B* **79** (9), 094422 (2009).
- [6] M. Weisheit, S. Fahler, A. Marty, Y. Souche, C. Poinignon, and D. Givord, Electric-field-induced modification of magnetism in thin-film ferromagnets, *Science* **315** (5810), 349 (2007).
- [7] F. Bonell, S. Murakami, Y. Shiota, T. Nozaki, T. Shinjo, and Y. Suzuki, Large change in perpendicular magnetic anisotropy induced by an electric field in FePd ultrathin films, *Appl. Phys. Lett.* **98** (23), 232510 (2011); F. Bonell, Y. T. Takahashi, D. D. Lam, S. Yoshida, Y. Shiota, S. Miwa, T. Nakamura, and Y. Suzuki, Reversible change in the oxidation state and magnetic circular dichroism of Fe driven by an electric field at the FeCo/MgO interface, *Appl. Phys. Lett.* **102** (15), 152401 (2013); Takayuki Nozaki, Yoichi Shiota, Shinji Miwa, Shinichi Murakami, Frederic Bonell, Shota Ishibashi, Hitoshi Kubota, Kay Yakushiji, Takeshi Saruya, Akio Fukushima, Shinji Yuasa, Teruya Shinjo, and Yoshishige Suzuki, Electric-field-induced ferromagnetic resonance excitation in an ultrathin ferromagnetic metal layer, *Nat Phys* **8** (6), 492 (2012); A. Bernand-Mantel, L. Herrera-Diez, L. Ranno, S. Pizzini, J. Vogel, D. Givord, S. Auffret, O. Boulle, I. M. Miron, and G. Gaudin, Electric-field control of domain wall nucleation and pinning in a metallic ferromagnet, *Appl. Phys. Lett.* **102** (12), 122406 (2013); L. Herrera Diez, A. Bernand-Mantel, O. Michele, L. Vila, P. Warin, A. Marty, L. Ranno, and D. Givord, Electric-field effect on coercivity distributions in FePt magneto-electric devices, *Appl. Phys. Lett.* **102** (1), 012409 (2013); U. Bauer, S. Emori, and G. S. D. Beach, Electric

field control of domain wall propagation in Pt/Co/GdOx films, *Appl. Phys. Lett.* **100** (19), 192408 (2012).

[8] U. Bauer, M. Przybylski, J. Kirschner, and G. S. D. Beach, Magnetolectric Charge Trap Memory, *Nano Letters* **12** (3), 1437 (2012).

[9] K. H. He and J. S. Chen, The thickness, electric field, and strain effects on the magnetic anisotropy of FeCo/MgO(001) thin films: A first principles study, *J. Appl. Phys.* **111** (7), 07C109 (2012); K. H. He and J. S. Chen, First principles study of magnetic anisotropy and magnetolectric effect of FePd/MgO(001) ultrathin films, *J. Appl. Phys.* **113** (17), 17C702 (2013); K. H. He, J. S. Chen, and Y. P. Feng, First principles study of the electric field effect on magnetization and magnetic anisotropy of FeCo/MgO(001) thin film, *Appl. Phys. Lett.* **99** (7), 072503 (2011); Tsujikawa Masahito and Oda Tatsuki, Finite Electric Field Effects in the Large Perpendicular Magnetic Anisotropy Surface Pt/Fe/Pt(001): A First-Principles Study, *Phys. Rev. Lett.* **102** (24), 247203 (2009); Kohji Nakamura, Riki Shimabukuro, Toru Akiyama, Tomonori Ito, and A. J. Freeman, Origin of electric-field-induced modification of magnetocrystalline anisotropy at Fe(001) surfaces: Mechanism of dipole formation from first principles, *Phys. Rev. B* **80** (17), 172402 (2009); Shugo Suzuki, Sho Yasuda, Kazuki Edakawa, and Saori Seki, First-Principles Study of Electric Field Effects on Magnetic Anisotropy in MgO/TM/Au (TM = Fe, Co) Systems, *Journal of the Physical Society of Japan* **82** (12), 124715 (2013); M. Tsujikawa and T. Oda, Finite Electric Field Effects in the Large Perpendicular Magnetic Anisotropy Surface Pt/Fe/Pt(001): A First-Principles Study, *Phys. Rev. Lett.* **102** (24) (2009); Sho Yasuda and Shugo Suzuki, First-Principles Study of Magnetic Properties of Co/Pt(111) Film in Electric Field, *Journal of the Physical Society of Japan* **81** (8), 085002 (2012).

[10] N. Tournier, A. Engelhardt, F. Maroun, and P. Allongue, Probing the electrochemical interface with in situ magnetic characterizations: A case study of Co/Au(111) layers, *Surf. Sci.* **631** (0), 88 (2015); N. Tournier, A. P. Engelhardt, F. Maroun, and P. Allongue, Influence of the surface chemistry on the electric-field control of the magnetization of ultrathin films, *Phys. Rev. B* **86** (10), 104434 (2012).

[11] P. Allongue and F. Maroun, Metal electrodeposition on single crystal metal surfaces mechanisms, structure and applications, *Current Opinion in Solid State and Materials Science* **10** (3-4), 173 (2006).

[12] A. A. Gewirth and B. K. Niece, Electrochemical applications of in situ scanning probe microscopy, *Chem. Rev.* **97** (4), 1129 (1997).

- [13] F. Golks, Y. Gründer, A. Drünkler, J. Roy, J. Stettner, J. Zegenhagen, and O. M. Magnussen, In Situ Surface X-Ray Diffraction Studies of the Influence of the PEG-Cl-Complex on Homoepitaxial Electrodeposition on Cu(001), *J. Electrochem. Soc.* **160** (12), D3165 (2013); F. Golks, K. Krug, Y. Grunder, J. Zegenhagen, J. Stettner, and O. M. Magnussen, High-Speed in situ Surface X-ray Diffraction Studies of the Electrochemical Dissolution of Au(001), *Journal of the American Chemical Society* **133** (11), 3772 (2011); Frederik Golks, Klaus Krug, Yvonne Gründer, Joÿrg Zegenhagen, Jochim Stettner, and Olaf M. Magnussen, High-Speed in situ Surface X-ray Diffraction Studies of the Electrochemical Dissolution of Au(001), *Journal of the American Chemical Society* **133** (11), 3772 (2012).
- [14] L. Cagnon, T. Devolder, R. Cortes, A. Morrone, J. E. Schmidt, C. Chappert, and P. Allongue, Enhanced interface perpendicular magnetic anisotropy in electrodeposited Co/Au(111) layers, *Phys. Rev. B* **63**, 104419 (2001).
- [15] L. Cagnon, A. Gundel, T. Devolder, A. Morrone, C. Chappert, J. E. Schmidt, and P. Allongue, Anion effect in Co/Au(111) electrodeposition: structure and magnetic behavior, *Appl. Surf. Sci.* **164**, 22 (2000); A. Gundel, L. Cagnon, C. Gomes, A. Morrone, J. Schmidt, and P. Allongue, In-situ magnetic measurements of electrodeposited ultrathin Co, Ni and Fe/Au(111) layers, *Physical Chemistry Chemical Physics* **3** (16), 3330 (2001).
- [16] P. Prod'homme, F. Maroun, R. Cortes, P. Allongue, J. Hamrle, J. Ferre, J. P. Jamet, and N. Vernier, Preparation, characterization and magneto-optical investigations of electrodeposited Co/Au films, *J. Magn. Magn. Mater.* **315** (1), 26 (2007).
- [17] P. Allongue and F. Maroun, in *Electrocrystallization and Nanotechnology*, edited by G. Staikov (Wiley - VCH, Weinheim, 2006), pp. 217 ; P. Allongue and Fouad Maroun, Electrodeposited magnetic layers in the ultrathin limit, *MR Bulletin* **35** (10), 761 (2010).
- [18] Philippe Allongue, Fouad Maroun, Hugo F. Jurca, Nicolas Tournier, Gregory Savidand, and Robert Cortes, Magnetism of electrodeposited ultrathin layers: Challenges and opportunities, *Surf. Sci.* **603** (10-12), 1831 (2009).
- [19] A. Damian, I. Braems, F. Maroun, and P. Allongue, Electrodeposition of NiPd monolayer on Au(111): An in situ scanning tunneling microscopy study, *Electrochim. Acta* **112** (0), 824 (2013); F. Lecadre, F. Maroun, I. Braems, F. Berthier, C. Goyhenex, and P. Allongue, AuNi alloy monolayer films electrodeposited on Au(111): An in situ STM study, *Surf. Sci.* **607** (0), 25 (2013).
- [20] A. Gundel, A. Morrone, J. E. Schmidt, L. Cagnon, and P. Allongue, Magnetic properties of electro deposited Fe/Au(111) layers: in situ AGFM measurements, *J. Magn. Magn. Mater.* **226**, 1616 (2001).

[21] N. Di, J. Kubal, Z. Zeng, J. Greeley, F. Maroun, and P. Allongue, Influence of controlled surface oxidation on the magnetic anisotropy of Co ultrathin films, *Applied Physics Letters* **106** (12), 122405 (2015).

Chapter 2 Theoretical background and experimental details: growth and magnetism of electrodeposited Co/Au(111) layers

2.1. Introduction

This chapter aims at giving the experimental details and data analysis procedure about what will be used in the subsequent chapters. The first section of this chapter recalls the equations describing the MAE of films and also recalls the principles of magneto optic Kerr effect (MOKE) before it describes the experimental set-up used for in situ magnetic characterizations. In a second part, this chapter gives a description of the electrochemical interface and the principles of electrochemical deposition. In a third part, a brief description of the preparation of Au(111)/Si(111) substrate and Co/Au(111) is given. In the final part we investigate the thickness dependence of MAE of Co/Au(111) layers. A deeper analysis of the data is performed with respect to past works [1-4].

2.2. Magnetic anisotropy energy of ultrathin films

The magnetization of a magnetic material will tend to align along an "easy axis", which is the most favorable energetically. Thus, the easy axis will be the result of the minimization of the total magnetic anisotropy energy. There are several sources of magnetic anisotropy energy [5]:

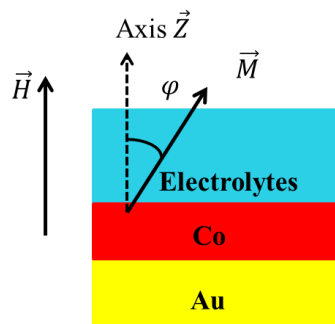


Fig. 2.1: Scheme defining the sample geometry and the angle φ between the magnetization easy axis and sample normal.

1) **Magnetocrystalline anisotropy energy:** this term arises mostly from spin-orbit coupling. It is basically the orbital motion of the electrons which couples with crystal electric field giving rise to the first order contribution to magnetocrystalline anisotropy. Therefore easy axis of magnetization is often along high symmetry axes of a crystal structure. In the case of hcp cobalt, the magnetocrystalline anisotropy favors the alignment of the magnetization along the c axis. The magnetocrystalline anisotropy energy per unit volume can be expressed as:

$$E_{mc}^v = K_{1mc}^v \sin^2 \phi + K_{2mc}^v \sin^4 \phi \quad (2.1)$$

where the angle ϕ is defined as the angle between the magnetization and the easy axis. In the case of hcp Co, the easy axis is along the c axis, i.e., the [0001] direction. $K_1^v \sim 5.6 \cdot 10^6 \text{ erg cm}^{-3}$ and $K_2^v \sim 1.6 \cdot 10^6 \text{ erg cm}^{-3}$ [1, 6] are bulk magnetocrystalline anisotropy constants of hcp Co(0001).

2) **Magnetoelastic anisotropy energy:** this is the energy related to the deformation of the lattice structure of the film. It may be written as:

$$E_{me} = \frac{3}{2} \lambda \sigma \cos^2 \phi \quad (2.2)$$

Where the angle ϕ is the angle between the magnetization and the strain, λ is the magnetostriction and σ is the mechanical stress [7]. In the case where $\lambda > 0$ and $\sigma > 0$ with exclusive in-plane contribution (in-plane expansion), then PMA is favored. In the case of coherent growth, i.e. when the deposited layer adopts the substrate lattice parameter [2], E_{me} can be expressed as

$$E_{me} = \frac{3}{2} \lambda E_A \eta \cos^2 \phi \quad (2.3)$$

where E_A is the Young module of the layer and η is the lattice mismatch. If above a critical thickness t_c , strain relaxation occurs within the layer, the expression of E_{me} becomes [2]:

$$E_{me} = \frac{3}{2} \lambda E_A \eta \cos^2 \phi t_c / t_{Co} \quad \text{for } t_{Co} > t_c, \quad (2.4)$$

3) **Dipolar anisotropy energy:** It originates from the total magnetic dipolar interaction, which depends on the shape of the sample. In the case of a thin film, its dependence over ϕ is

given by equation (2.5):

$$E_d = -2\pi M_s^2 \sin^2 \varphi \quad (2.5)$$

Where the M_s is the saturation magnetization of the bulk material, φ is the angle defined in **Fig.2.1**. In the case of cobalt, M_s is 1407emu/cm^3 at room temperature [3]. The dipolar energy favors in-plane magnetization.

4) **Zeeman energy**: It originates from the dipolar energy of a magnetized body in an external magnetic field H . It is given by:

$$E_Z = -\vec{H} \cdot \vec{M} = -HM_s \cos \varphi \quad (2.6)$$

where M_s is the saturation magnetization of the magnetized body.

5) **Interface anisotropy energy**: The interface anisotropy basically originates from the specific configuration of surface atoms with fewer neighbors. It is an important contribution for ultrathin film scaling with the inverse of the magnetic-film thickness. This anisotropy energy can be expressed as:

$$E_s = K_S \sin^2 \varphi / t_{Co} \quad (2.7)$$

If $K_s > 0$, PMA is favored. In the case of magnetic layers, there are two contributions to the interface anisotropy, K_s^{up} and K_s^{down} . In our case, $K_s^{down} = K_s^{Co-Au}$.

The total MAE E_T is therefore:

$$E_T = E_{mc} + E_{me} + E_d + E_Z + E_s \quad (2.8)$$

When $t_{Co} < t_c$, in the case of Co(0001) layers, and in the presence of strain in the film plane,

$$E_T = K_1^v \sin^2 \varphi + K_2^v \sin^4 \varphi - 2\pi M_s^2 \sin^2 \varphi - HM_s \cos \varphi + K_S \sin^2 \varphi / t_{Co} + \frac{3}{2} \lambda E_A \eta \sin^2 \varphi \quad (2.9)$$

The magnetoelastic anisotropy appears independent of the film thickness and can be regarded as volume anisotropy energy. It can be merged with the first term of the magnetocrystalline anisotropy by using $K_1 = K_1^v + \frac{3}{2} \lambda E_A \eta$

When $t_{Co} > t_c$

$$E_T = K_1^v \sin^2 \varphi + K_2^v \sin^4 \varphi - 2\pi M_s^2 \sin^2 \varphi - HM_s \cos \varphi + K_S \sin^2 \varphi / t_{Co} + \frac{3}{2} \lambda E_A \eta t_c / t_{Co} \quad (2.10)$$

The magnetoelastic anisotropy can be regarded as surface anisotropy energy, and it can be combined with the interface anisotropy.

Minimization of the total energy, leads to:

$$\sin \varphi [K_{eff} + 2K_2 \sin^2 \varphi + HM_s / 2 \cos \varphi] = 0 \quad (2.11)$$

$$K_{eff} = K_1 - 2\pi M_s^2 + K_S / t_{Co} \quad (2.12)$$

If the external field H is equal to zero and the effective anisotropy energy K_{eff} is positive, then the only solution to **Eq. 2.11** is $\sin \varphi = 0$. It implies that $\varphi = 0$, meaning the easy axis of the magnetization is perpendicular to the surface. Since $K_1 < 2\pi M_s^2$, when the layer thickens, K_{eff} becomes negative, and a solution $\varphi \neq 0$ exists. φ is given by $\sin^2 \varphi = \frac{-K_{eff}}{2K_2}$. In this case, the magnetization easy axis is tilted with respect to the surface normal and eventually become parallel to the surface plane when $|K_{eff}| > 2K_2$. This variation of direction of magnetization as a function of t_{Co} is a spin reorientation transition (SRT).

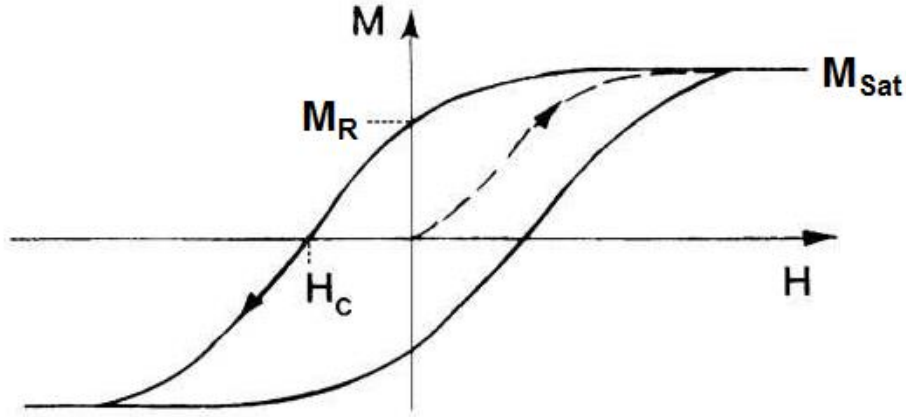


Fig.2.2: M - H curve (hysteresis loop) of a typical ferromagnetic material.

When $0^\circ < \varphi < 90^\circ$, φ can be determined from the M - H curve (see **Fig. 2.2**). The magnetization at $H = 0$ is denoted as the remnant magnetization M_R whereas M_{Sat} is the

saturation magnetization of the thin film. Depending on the used technique (MOKE, SQUID ...), the proportionality coefficient between M_{Sat} and M_S may be difficult to estimate (as in MOKE measurements).

Using equation (2.11), φ is given by:

$$\cos\varphi = M_R/M_{Sat} = [1 + (K_1 - 2\pi M_S^2 + K_s/t_{Co})/2K_2]^{1/2} \quad (2.13)$$

To characterize the SRT effect, we introduce an important parameter t^* . It is defined as the thickness where $\varphi = 45^\circ$. Thus

$$t^* = K_s / (2\pi M_S^2 - K_1 - K_2) \quad (2.14)$$

The determination of $\cos\varphi$ and K_{eff} depends on M_{Sat} , which is proportional to M_s and to the probed sample volume, i.e., the film thickness. However, M_s depends on the temperature T as follows [8]:

$$\frac{M_s(T)}{M_s(T_0)} = \left(1 - \frac{T}{T_c}\right)^\gamma \quad (2.15)$$

Where T_0 is the absolute zero, and T_c is the Curie temperature, and γ is the critical exponent. It has been shown that in the case of thin films, T_c depends on the film thickness [8].

M - H curve provides information of another important property of ferromagnetic materials --- coercivity, symbolized by H_c in **Fig. 2.2**. The coercivity, or the coercive field, is a measure of the ability of a ferromagnetic material to withstand an external magnetic field without becoming demagnetized. It is the intensity of the applied magnetic field required to reduce the magnetization of that material to zero after the magnetization of the sample has been reached to saturation.

Fig. 2.3 [8] illustrates the thickness-dependent T_c for different ferromagnetic films with different structures. N_0 is the critical thickness where the thickness-dependent law changes from linear to exponential.

Consequently, M_s depends indirectly on the film thickness. Thus, for low thickness, M_{Sat} is less than expected when considering a bulk value for T_c and is not proportional to the thickness.

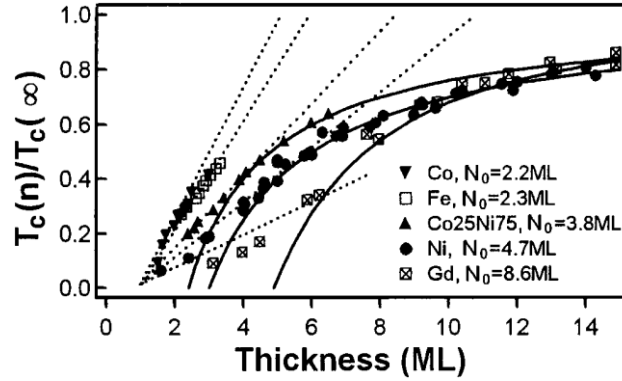


Fig. 2.3: Thickness-dependence of the Curie temperature for ultra-thin films. $T_c(n)$ is the Curie temperature of n -ML-thick thin films, $T_c(\infty)$ is the Curie temperature of bulk materials. N_0 is the thickness where the thickness-dependent law changes from linear to exponential. After Ref. [8]

2.3. In situ magnetic characterizations

2.3.1. Principle of magneto optical Kerr effects (MOKE)

Magneto Optical effects in magnetic materials arise due to the optical anisotropy of the materials depending on the magnetization orientation. The optical anisotropy alters the polarization state of light which is reflected on magnetic material surface [9-10].

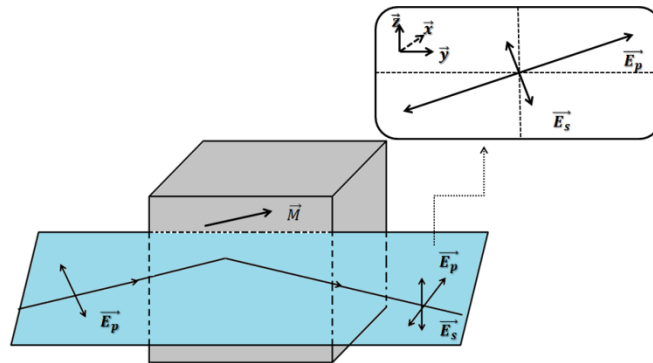


Fig. 2.4: Illustration of the light polarization change after reflection on a magnetic sample.

In the case of plane polarized incident light, the reflected light becomes elliptically polarized with its major axis rotated from the initial incident polarization plane (see Fig. 2.4).

The rotation angle of the major axis is known as the Kerr rotation. In the case of ultrathin films, the Kerr rotation angle is proportional to the film total magnetization.

2.3.2. Experimental set-up

The magnetic properties are measured in real time during electrodeposition using the home-built *in-situ* P-MOKE set-up (see Fig. 2.5). The sample is placed in an electrochemical flow cell (see Fig. 2.6). Light is reflected on the sample surface at normal incidence.

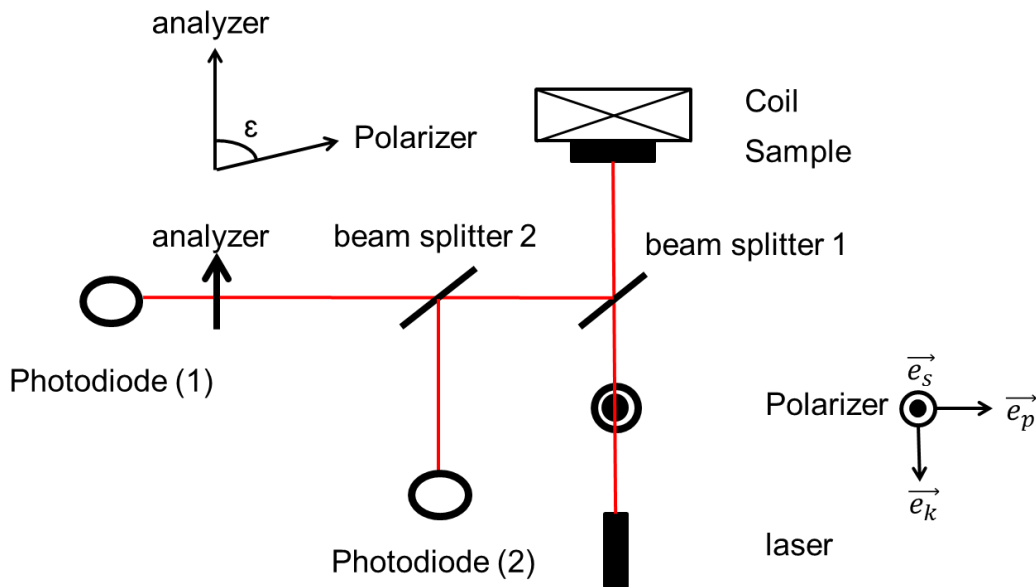


Fig. 2.5: scheme of the home-built *in-situ* P-MOKE set-up. See text for more explanation.

The incident laser beam (wavelength $\lambda = 633\text{nm}$) is polarized vertically. Upon reflection on the beam splitter 1, it is divided into two beams using the beam splitter 2. One beam is directly captured by photodiode (2) and the other passes through an analyzer and is acquired by photodiode (1). The current measured with Photodiode (2) I_2 is therefore proportional to the reflected light intensity, which is proportional to the incident light I_0 and the square of the module of the reflection coefficient $|r_{ss}|^2$. I_2 will be used in the MOKE experiment to monitor the Co thickness during deposition/dissolution and Co film stability during the electrolyte exchanges and molecular adsorption. The current measured with Photodiode (1) I_1 depends on the Kerr rotation θ and the sample reflectivity $|r_{ss}|^2$. I_1 and

I_2 are given by [4]:

$$I_1 \propto I_0 |r_{ss}|^2 [(1 + \cos 2\varepsilon) + 2\theta \sin 2\varepsilon] \quad (2.16)$$

$$I_2 \propto I_0 |r_{ss}|^2 \quad (2.17)$$

where ε is the angle between the analyzer and the polarizer. From the equations above, the value of the Kerr rotation θ is obtained by dividing I_1 by I_2 , which gives rise to the Kerr signal I . The MOKE signal is proportional to the magnetization projected on the surface normal.

$$I \propto (1 + \cos 2\varepsilon) + 2\theta \sin 2\varepsilon \quad (2.18)$$

The MOKE signal is given by the term $2\theta \sin 2\varepsilon$ which is maximum at $\varepsilon = 45^\circ$. However, the term $(1 + \cos 2\varepsilon)$ becomes dominant when $\varepsilon < 90^\circ$ since $\theta \sim 10^{-3}$ rad. A good compromise is to fix ε at a value yielding a signal slightly smaller than the saturation value of the I - V converter. Typically, we have a signal of $\sim 4V$ and the additional MOKE contribution of 1ML of Co is $\sim 10mV$. The measurements are performed with $\varepsilon = 83^\circ$. The diamagnetic signal due to the electrolyte is compensated by the software prior to deposition. The acquisition rate of the set-up is $2 M - H$ cycles per second.

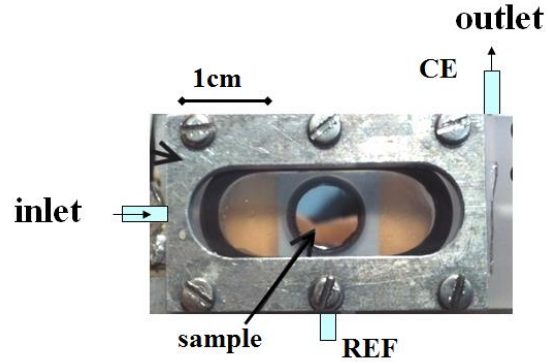


Fig. 2.6: Picture of the electrochemical flow cell adapted for in-situ P-MOKE measurement. The Au/Si sample is connected to a potentiostat. See text for more explanation.

The substrate is installed in a custom electrochemical flow cell that is adapted for the in-situ MOKE characterization. **Fig. 2.6** shows a picture of the cell. Its dimensions are: height 22mm, width 40mm. The electrolyte thickness is 5mm, which ensures an acceptable

diamagnetic signal of the electrolyte and an electrochemical behavior as in a standard cell. The volume of the cell is $\sim 1\text{mL}$. The flow of the solution is due to gravity force, and is pumped continuously to maintain the same electrolyte composition. Indeed, the Co magnetic properties are very sensitive to small pH changes and one side reaction at $\text{pH} \sim 4$ is hydrogen evolution reaction which reduces the H^+ concentration close to the electrode surface. The flux is about $1.0\text{mL}/\text{min}$. The Au/Si(111) sample is connected to a potentiostat via the back side of the Si substrate unless otherwise specified. A Pt wire of 0.5mm diameter is used as counter electrode. It is placed at the outlet of the cell. The reference electrode is Hg/Hg₂SO₄ (MSE). Measurements are performed under potentiostatic mode.

2.4. Basics concepts of electrochemistry:

2.4.1. Structure of the electrochemical interface

Fig. 2.7 displays the commonly accepted simplified description of the electrochemical interface structure. The surface charge of the metal (here < 0) is compensated by a reorganization of the charge distribution in the electrolyte, in the close vicinity of the electrode surface.

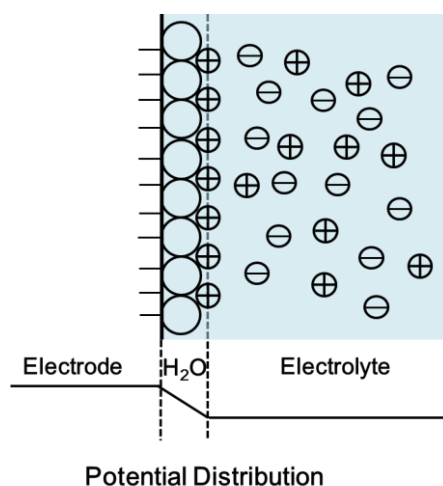


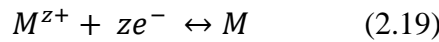
Fig. 2.7: Scheme of a simplified electrochemical interface structure and potential distribution.

The typical potential profile is linear between the electrode surface and the first cation

plane and then decays exponentially in the electrolyte. For typical electrolyte (0.1M K₂SO₄), the potential drop within the water monolayer is the dominant term and that in the electrolyte is negligible. In the following, we will consider that the whole potential drop takes place at the electrode/electrolyte interface and the system may be considered as a capacitor, of which the typical value is $C_{DL} \sim 10\mu\text{F}/\text{cm}^2$. This is valid only when the applied potential U is not close to the potential of zero charge. Under such condition, the capacity of ionic double layer structure does not depend significantly on the applied potential.

2.4.2. Principle of Electrodeposition

Electrodeposition corresponds to the reduction of M^{z+} ions at the electrode surface according to the reaction [11- 12]:



The dissolution is the inverse reaction.

The equilibrium potential of this reaction is defined by Nernst equation:

$$\begin{aligned} E(M^{z+}/M) &= E^0(M^{z+}/M) + \frac{RT}{zF} \ln\left(\frac{a_{M^{z+}}}{a_M}\right) - U_{Ref} \\ &= E^0(M^{z+}/M) + \frac{0.06}{z} \log\left(\frac{a_{M^{z+}}}{a_M}\right) - U_{Ref} \end{aligned} \quad (2.20)$$

Where:

- $E^0(M^{z+}/M)$ is the standard half-cell reduction potential with respect to SHE;
- R is the universal gas constant: $R = 8.31 \text{ J K}^{-1} \text{ mol}^{-1}$;
- T is the absolute temperature;
- a is the chemical activity for the relevant species;
- F is the Faraday constant, the number of coulombs per mole of electrons: $F = 9.65 \times 10^4 \text{ C mol}^{-1}$;
- z is the number of moles of electrons transferred in the cell reaction or half-reaction;
- U_{Ref} is the reference potential versus the standard hydrogen electrode reference (SHE). In this work, we used a saturated mercury/mercurous sulfate electrode (MSE) as reference of

potentials. $E(MSE) = E(SHE) + 0.64V$. In the following, all potentials will be quoted against MSE.

- a_M^{z+} and a_M are the activity of M^{z+} and the metal electrode M. At moderate concentration, a_M^{z+} is generally equal to $[M^{z+}]$ and $a_M = 1$.

For potentials close enough to the Nernst potential, the relationship between the current density i is given by the Butler-Volmer equation [13]:

$$i = i^+ + i^- = i_0 \left[\exp\left(\frac{(1-\alpha)zF}{RT}\eta\right) - \exp\left(\frac{-\alpha zF}{RT}\eta\right) \right] \quad (2.21)$$

where η is the overpotential, i.e., the difference between the applied potential and the Nernst potential.

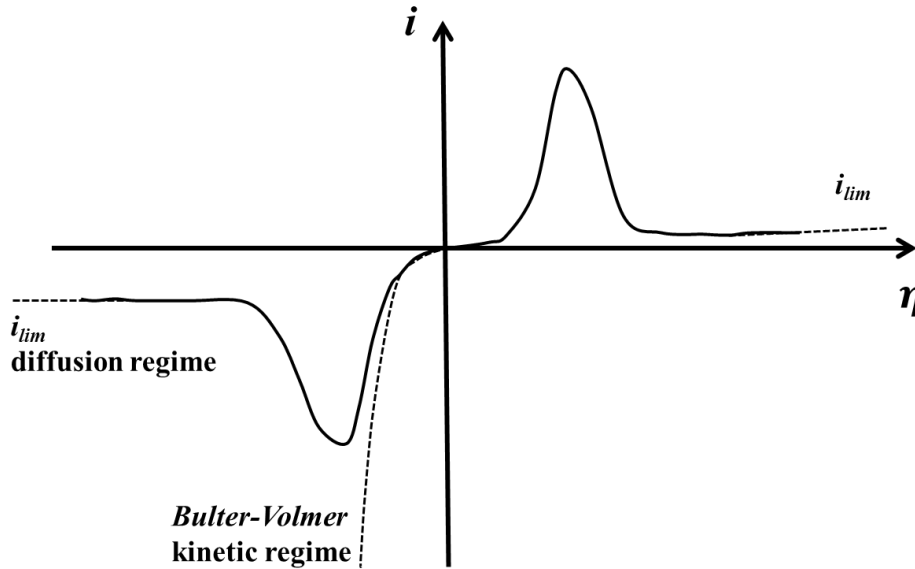


Fig. 2.8: current i – overpotential η curve for a deposition/dissolution reactions with kinetic and diffusion limitations. For $\eta \sim 0$, reaction kinetics dominate the deposition; for larger η , the deposition is limited by diffusion step.

The overall current density i is actually the sum of the partial current densities related to the anodic (metal dissolution) and cathodic (metal deposition) partial reactions (i^+ and i^- , respectively). The electrochemical charge transfer coefficient α is a measure of the symmetry of the activation barrier ($0 < \alpha < 1$). i_0 corresponds to the exchange current density and is related to reaction kinetics.

Figure 2.8 shows the typical dependence of the electrochemical current i on the

overpotential η . In the general case, however, the rate of electrochemical deposition is determined not only by the charge exchange kinetics but also by ion diffusion towards the electrode surface. In fact, increasing η depletes the electrolyte in M^{z+} in the vicinity of the electrode surface if their consumption rate is faster than their diffusion towards the electrode surface. In such a case, a concentration gradient of M^{z+} establishes and M^{z+} diffusion becomes the rate limiting step. In this case, the current density is given by the Fick's law [14]:

$$i_{lim} = zFD \frac{[M^{z+}]_{surf} - [M^{z+}]_{\infty}}{\delta} \quad (2.22)$$

where δ is the diffusion layer thickness, and D is the diffusion coefficient of M^{z+} in the electrolyte; $[M^{z+}]_{surf}$ and $[M^{z+}]_{\infty}$ are the ions concentration at the surface and in the electrolyte bulk.

On the atomic scale, once the metallic cation is discharged, the nucleation and growth process are similar to those in UHV. The formed adatoms which are irreversibly stabilized on the surface (redissolution back into the electrolyte is negligible) diffuse on the surface and aggregate with other adatoms into islands to form nuclei. These nuclei grow by incorporating other adatoms. For a given deposition current, the density of islands depends on the surface diffusion coefficient of the adatoms which may vary with η , via co-reactions, structural changes or changes in surface chemistry. For small magnitude of η , the metallic cation discharge step may become site selective and influence the nucleation and growth. For example, nucleation and growth at steps may be favored inducing in this case step flow growth and 2D morphology [15].

2.5. Electrodeposition of Co/Au(111) layers

2.5.1. Preparation of the Au(111)/Si(111) substrate

Co was grown on Au(111)/Si(111) substrate, of which the surface is atomically flatter on the nanoscale as compared to Au(111) single crystal, hence more adapted for optical measurements. The nucleation and growth of Au (111)/Si(111) buffer layers has been investigated previously [16-17]. In this part, we will give a brief description of their preparation.

The Si(111) samples were cleaved as squares ($1.2 \times 1.2 \text{ cm}^2$) from the 4 inch silicon (111) wafer (Siltronix, France), with one side polished and a miscut angle $\gamma = 0.2^\circ$ towards $\langle 11-2 \rangle$. Prior to Au deposition, the Si sample was cleaned in a hot solution of H_2SO_4 and H_2O_2 (2:1 by volume) carefully rinsed in ultrapure water. A H-terminated Si(111) surfaces was then obtained by anisotropic etching in oxygen-free 40% NH_4F for 10 min [16-17]. Oxygen-free NH_4F was prepared by adding $(\text{NH}_4)_2\text{SO}_3$ so as to reach a concentration of 0.05M. Microelectronic grade chemicals were used. Such a prepared surface present a well-defined topography with flat terraces $\sim 100\text{nm}$ wide and approximately parallel steps, as shown in **Fig. 2.9.a**. This contact mode AFM image (Molecular Imaging, Tempe, USA) was recorded under controlled N_2 atmosphere. The cantilever spring constant was 0.12N/m.

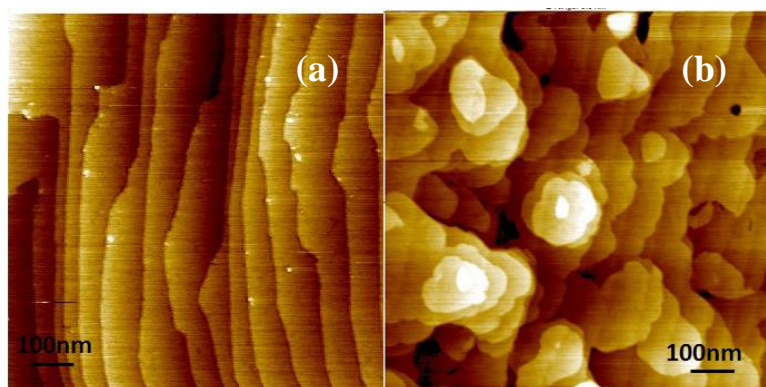


Fig. 2.9: AFM images showing the topography of (a) the H-Si(111) surface after anisotropic etching; and of (b) a 33 ML-thick Au(111) epitaxial buffer layer on H-Si(111). Both images are ($1 \times 1 \text{ }\mu\text{m}^2$).

For the deposition of Au(111) epitaxial layers on H-Si(111), an ohmic contact was formed by applying an InGa eutectic layer on the rear face of the Si sample before mounting it on a rotating electrode. The sample lateral edges were protected by an electrolytic scotch tape (Struers) to expose only the well-defined silicon surface to the solution. Gold was deposited at a rotation speed 1700 rpm during 150 sec. The composition of gold plating solution was 0.1 mM HAuCl_4 + 0.1M K_2SO_4 + 1mM KCl + 1mM H_2SO_4 (pH ~ 3.5). Deposition was performed at -2V vs MSE using a three-electrode electrochemical cell. The deposition rate was constant and equal to 0.22ML/s. A gold wire served as counter electrode. At the end of the deposition time, the sample was quickly removed from the solution, rinsed with ultrapure

water and dried with nitrogen. The AFM image (**Fig. 2.9.b**) demonstrates a continuous ultraflat Au(111) thin film on top of the substrate.

2.5.2. Nucleation and growth of Co/Au(111) layers

a) Electrochemical and optical measurements

Cobalt deposition was undertaken in a solution of pH ~ 3.5 - 4 mM CoSO₄ + 0.1M K₂SO₄ + 1mM KCl + 1mM H₂SO₄. **Fig. 2.10.a** presents a cyclic voltammogram of Au(111)/Si(111) substrate in the EC-flow cell. This kind of characterization helps identifying the reactions occurring at the electrode surface as a function of potential. In **Fig. 2.10.a**, the potential is swept from 0V to -1.5V vs MSE and backward. This voltammogram is consistent with past reports [4]. Several peaks are reproducibly identified. According to [4], peak (C₁) at $U \sim -1.05\text{V}$ corresponds to the hydrogen evolution reaction (HER) (see Eq.2.23.(a)). The other peak (C₂) at $U \sim -1.25\text{V}$ and peak (A) at $U \sim -0.84\text{V}$ are respectively corresponding to the reduction of Co (II) to Co and the Co dissolution reactions (see (Eq.2.23.(b) and (c))).

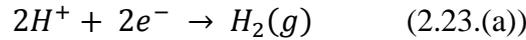


Fig. 2.10.b shows the corresponding variations of the sample relative reflectivity (determined from photodiode (2) signal) $\Delta R/R$ during the same potential scan. This plot clearly demonstrates that Co deposition starts around -1.23 V because there is a steep increase in $\Delta R/R$ at this potential. On the backward scan, $\Delta R/R$ is quasi constant between -1.3V and -1V and the sharp decrease coincides with the Co dissolution peak. The modelling of the optical properties of the multilayer assuming a stratified medium yields quantitatively similar increase of $\Delta R/R$ upon Co deposition. After a complete cycle of potential, $\Delta R/R$ returns to zero. Looking into more details, one further notices small but sizeable $\Delta R/R$ variations in absence of any Co deposition. In fact $\Delta R/R$ increases by ~ 1% during the negative going sweep of potential between 0V and -0.2V. This increase coincides with SO₄²⁻ desorption from the Au(111) surface and the formation of Au surface reconstruction [4].

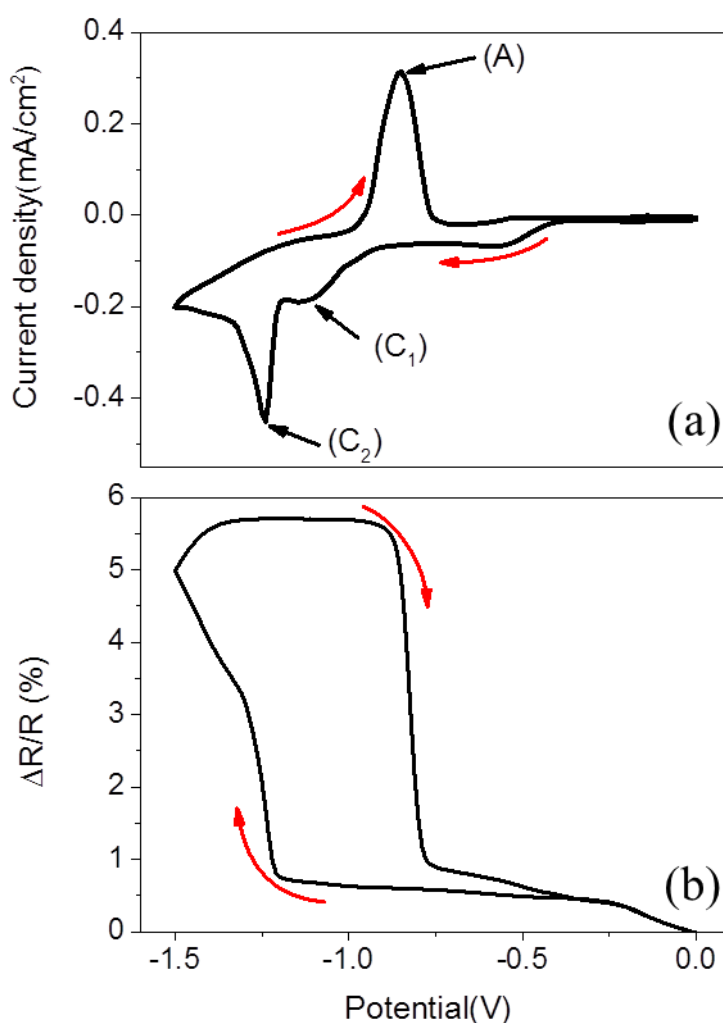


Fig. 2.10: (a) Voltammogram of Au(111)/Si(111) in pH ~ 3.5-4 1mM CoSO₄ + 1mM H₂SO₄ + 1mM KCl + 0.1M K₂SO₄. The sweep speed is 20mV/s. (b) Corresponding variations of the sample relative reflectivity $\Delta R/R$.

Cobalt deposition is performed at a constant potential by stepping the potential from 0 V to typically -1.3V or -1.4V to obtain a 2D growth (see section 2.5.2.b). **Fig. 2.11** presents a typical deposition procedure: the current (top panel) and $\Delta R/R$ (middle panel) transients corresponding to the potential program shown in the bottom panel. Deposition occurs between 0 and 35 s, the film is then stabilized at $U = -1.1$ V before a potential ramp is applied to dissolve the layer (see peak of current in the top panel at $t = 50$ s). The dissolution charge allows determining the layer thickness using Faraday's law as a function of deposition time. Whereas the deposition charge is dominated by HER current, the surface atomic density of as deposited Co(0001) is $1.85 \cdot 10^{15}$. As two electrons are exchanged during Co

dissolution/deposition, the charge for depositing 1ML of Co is $0.59\text{mC}/\text{cm}^2$. Consequently, the anodic charge Q_{an} while stripping off the Co thin film from -1.1V to 0V gives its thickness $t_{Co} = Q_{an}/0.59\text{ ML}$.

The variation of $\Delta R/R$ (**Fig. 2.11.(b)**) is used in a complementary way to determine t_{Co} in real-time. R_0 is the reference value of R , measured at -1.3V before Co deposition sets in.

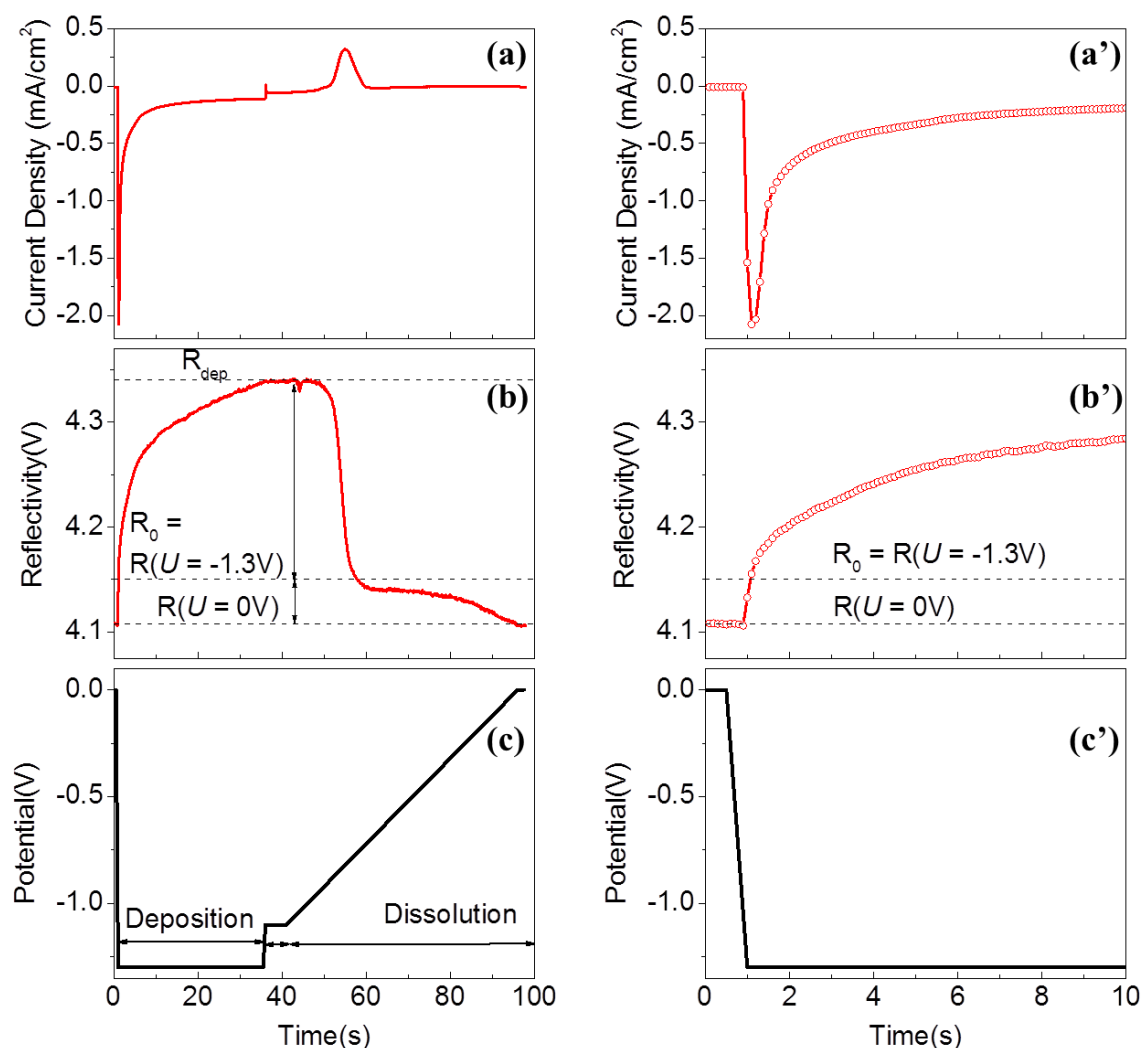


Fig. 2.11: Deposition of one Co(3.1ML)/Au(111) in $\text{pH} \sim 3.5 - 4$ $1\text{mM CoSO}_4 + 0.1\text{M K}_2\text{SO}_4 + 1\text{mM KCl} + 1\text{mM H}_2\text{SO}_4$ electrolyte at -1.3V during 35 sec . Stabilization of the thin film at -1.1V for 10sec . Dissolution of Co layers from -1.1V to 0V with $20\text{mV}/\text{s}$. (a) Variation of the electrochemical current density with time. The anodic peak yields the amount of deposited Co. (b) reflectivity variations. Three dash lines representing $R(U = 0\text{V})$, R_0 and R at the end of Co deposition respectively. (c) description of the potential sequence. (a') – (c'): zooms of images (a) – (c).

The correlation between $\Delta R/R_0$ and t_{Co} (see **Fig.2.12**) was established by depositing

and stripping Co films of different thickness. At the end of each deposition, $\Delta R/R_0$ is estimated and t_{Co} is obtained from the investigation of the anodic current peak yielding Q_{an} .

Fig. 2.12 evidences that $\Delta R/R_0$ is essentially linear with t_{Co} .

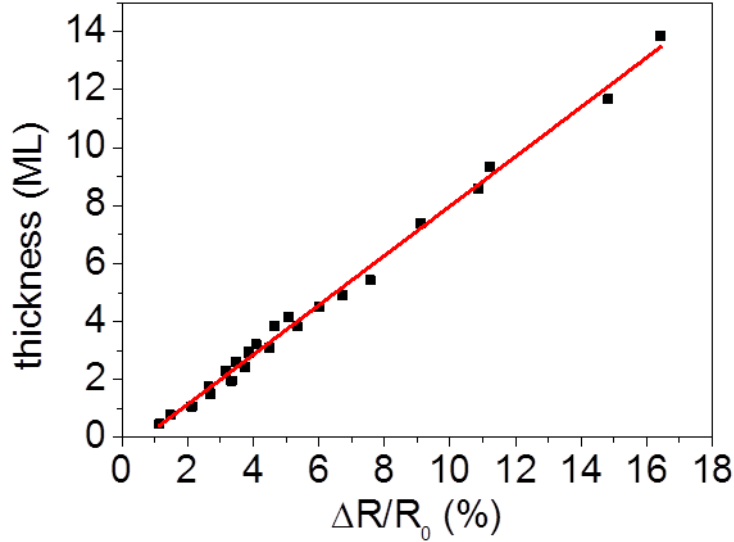


Fig.2.12: plot of the Co thickness t_{Co} as a function of $\Delta R/R_0$. Note the linear correlation.

Nonetheless for $t_{Co} < 2ML$, the data reveals a slightly different proportionality law. This is probably due to the fact that Co growth starts with the formation of 2ML-thick islands. Above 2ML, the surface is again homogenous and Co grows monolayer by monolayer. To estimate t_{Co} from $\Delta R/R_0$ during one deposition, different equations should apply according to t_{Co} :

$$t_{Co} = \begin{cases} \frac{(\Delta R/R_0)}{(\Delta R/R_0)_{2ML}} \cdot 2 & \Delta R/R_0 \leq (\Delta R/R_0)_{2ML} \\ \frac{(\Delta R/R_0) - (\Delta R/R_0)_{2ML}}{(\Delta R/R_0)_f - (\Delta R/R_0)_{2ML}} \cdot (t_{Co}^f - 2) + 2 & \Delta R/R_0 > (\Delta R/R_0)_{2ML} \end{cases} \quad (2.24)$$

Where $(\Delta R/R_0)_{2ML}$ is the reflectivity change for a 2-ML Co; $(\Delta R/R_0)_f$ and t_{Co}^f is the variation of the reflectivity and thickness once the deposition is complete. t_{Co}^f is determined by anodic charge Q_{an} . If Co dissolution is not undertaken, Q_{an} corresponds to the charge while stripping off one Co film deposited under the same conditions.

b) STM observations

The influence of the applied deposition potential on Co deposit morphology was studied in

details previously in the thesis of Grégory Savidand [4]. In this paragraph, we briefly recall that the Co nucleation step at -1.3V on Au(111) takes place through the formation of 2ML high nuclei which form preferentially at the Au steps (**Fig. 2.13**). These nuclei grow laterally until Au surface is completely covered. Further Co growth is layer by layer [1]. The Co films are (0001) oriented and are in-plane expanded. The in-plane strain is $\sim 3\%$ for 2ML and decays for thicker layers. The important conclusion is that Co layers thicker than 2ML are two dimensional and atomically flat.

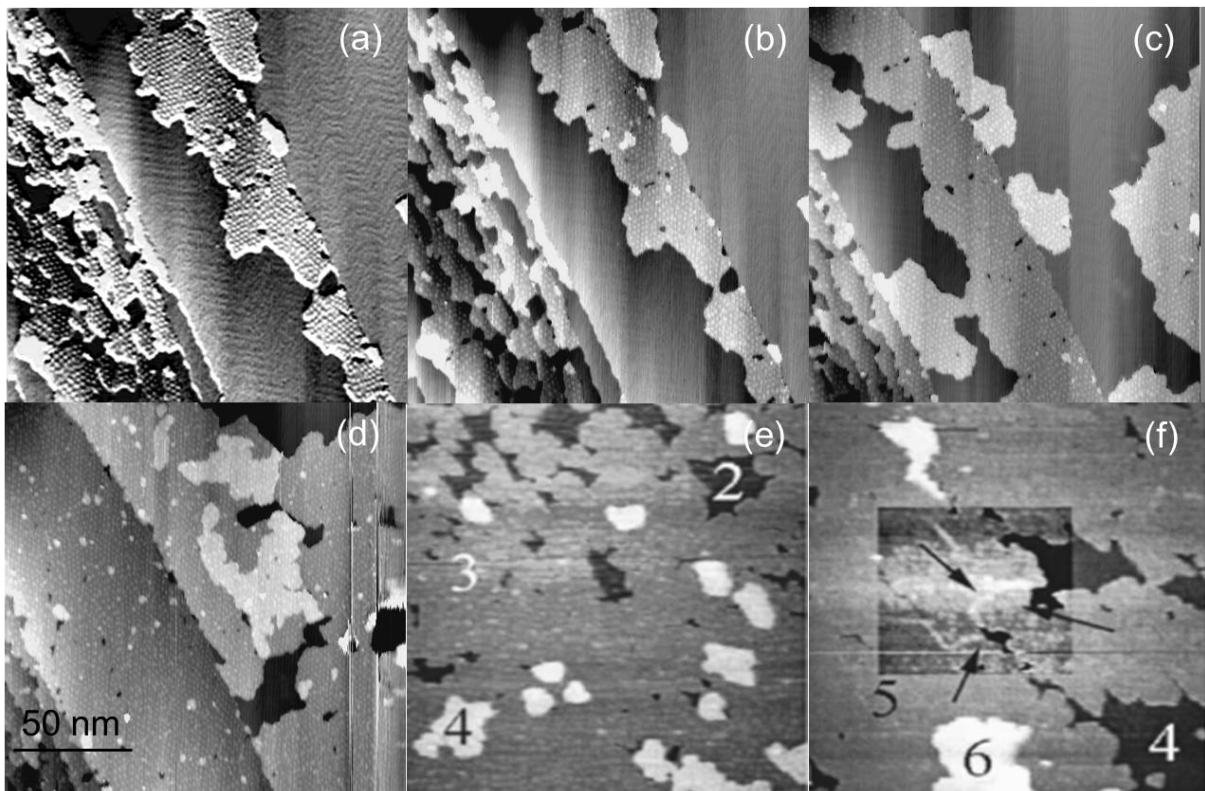


Fig. 2.13: In-situ STM images showing the morphology of Co/Au(111) layers deposited in a 1mM CoSO_4 solution in $0.1\text{M K}_2\text{SO}_4 + 1\text{mM KCl} + 1\text{mM H}_2\text{SO}_4$ with $\text{pH} \sim 3.5 - 4$. The deposition potential is -1.3V . The deposition time is (a) 1s; (b) 2s; (c) 4s; (d) 8s (2-ML Co with the coverage of Co biatomic islands as 1). (e) Image presenting a 3-ML Co. (f) Image presenting a 5-ML Co [1, 18, 19]. The contrast was enhanced in image (f) to show structure defects in the square.

c) In-situ P-MOKE measurements

Figure 2.14 displays a series of $M - H$ curves during Co deposition at -1.3V . The thickness t_{Co}

indicated in ML in each graph is determined from the variations of the reflectivity $\Delta R/R_0$.

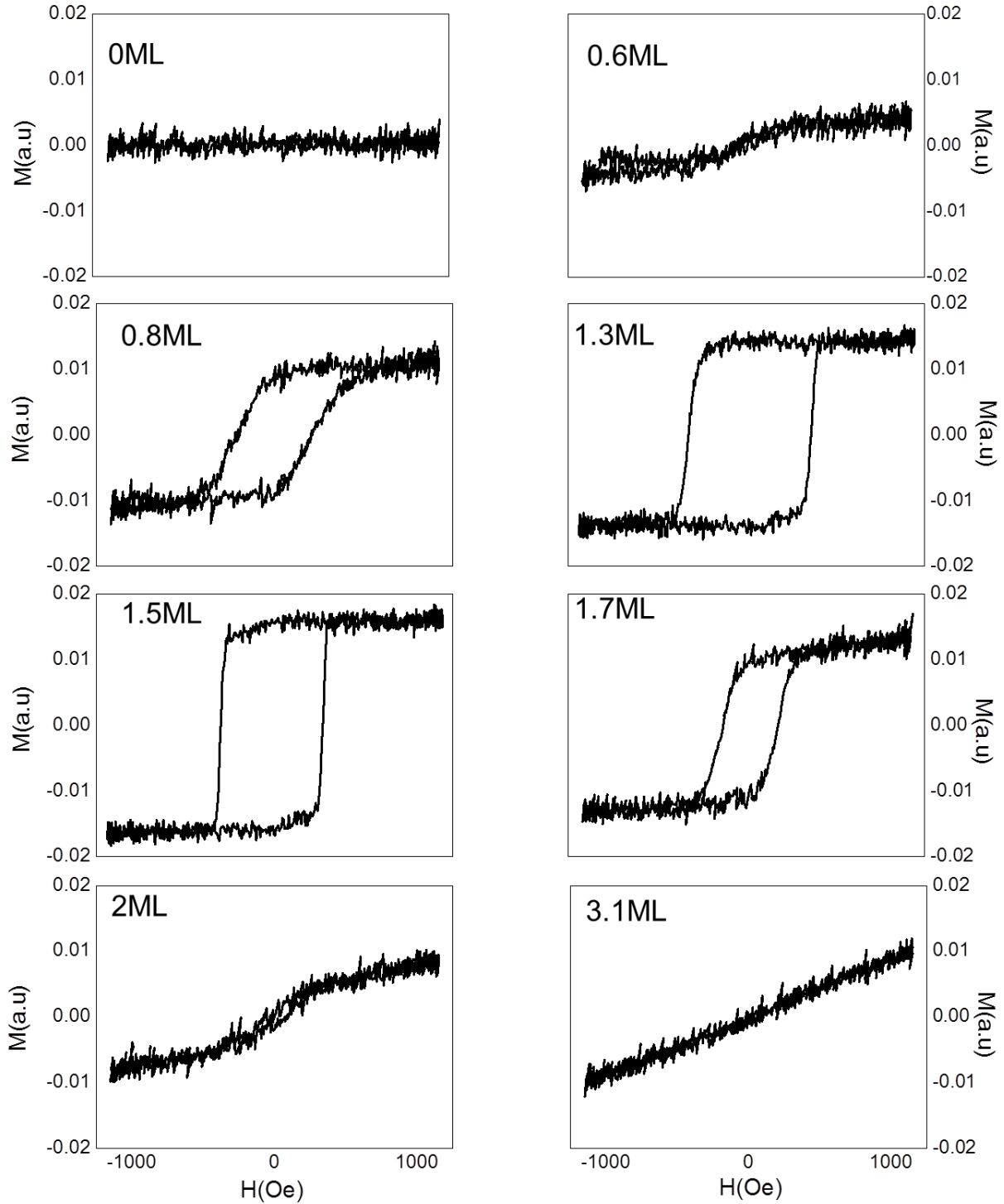


Fig. 2.14: selected M - H curves extracted from a complete series of plots recorded during the deposition at -1.3V of a Co/Au(111) film.

For $t_{Co} \leq 1.5\text{ML}$, the hysteresis loops are open and square with $H_c < 1000\text{Oe}$. This behavior means that the magnetization easy axis is perpendicular to the surface. One also

speaks of perpendicular magnetic anisotropy (PMA).

For $t_{Co} > 1.5\text{ML}$, the M - H curves gradually becomes linear and reversible with no remanence. Saturation cannot be achieved at 1KOe. This behavior indicates that the magnetization easy axis is now in-plane. Therefore, with increasing thickness there is a reorientation of the magnetization easy axis from out of plane to in plane direction. The phenomenon is often called spin reorientation transition (SRT). It is occurring around the critical thickness $t_{Co}^* \sim 1.5\text{ML}$, in agreement with past works [2-4]. Applying equation (2.14), the associated surface anisotropy K_s is $0.16 \text{ erg}\cdot\text{cm}^{-2}$. Given the Co-Au surface anisotropy $K_s^{Co-Au} \sim 0.50 \text{ erg}\cdot\text{cm}^{-2}$ [4] the hydrogenated surface anisotropy $K_s^{Co-H} \sim -0.34 \text{ erg}\cdot\text{cm}^{-2}$.

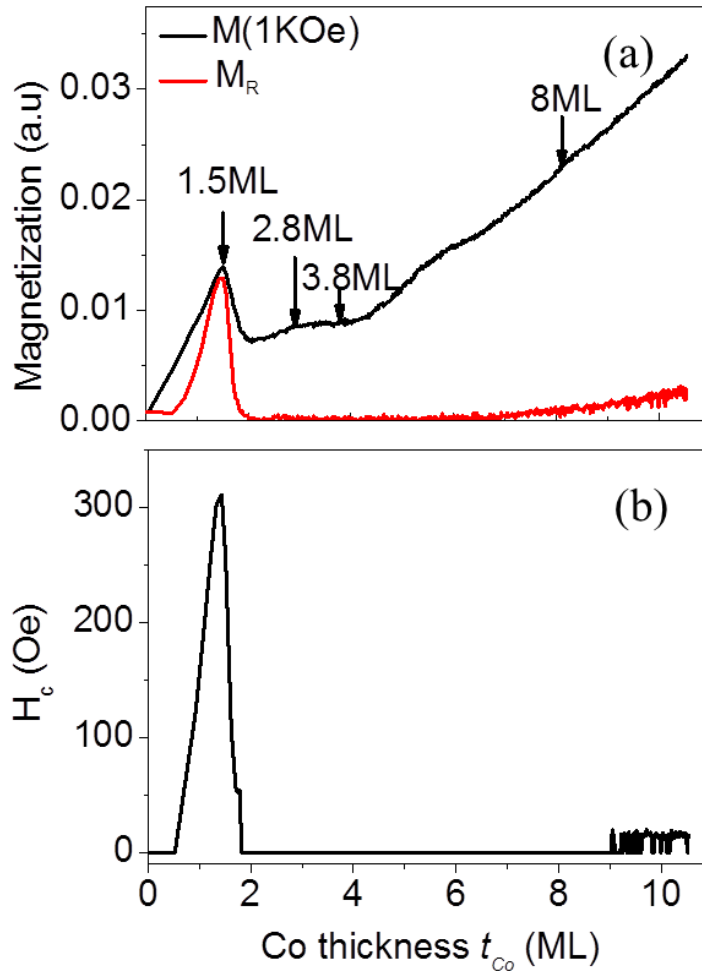


Fig. 2.15: Variations of $M(1\text{KOe})$ (black line (a)), M_R (red line (a)) and H_c (b) with Co thickness t_{Co} during deposition of one 10.5ML sample. The thickness is determined from the relative reflectivity $\Delta R/R_0$ in real time.

Figure 2.15 presents the variation of $M(1KOe)$ the magnetization at 1KOe, M_R the magnetization at 0Oe and H_c with t_{Co} during deposition of 10.5-ML Co. $M(1KOe)$ and M_R pass through a maximum around 1.5ML, which is related to the above mentioned spin reorientation transition (SRT). In correlation with the SRT, H_c goes also through a maximum (300 Oe) around 1.5 ML (**Fig. 2.15.b**). One may further notice that both H_c and M_R are null in the very initial stages of the growth. This behavior may be assigned to the fact that the Curie temperature T_c of the biatomic islands is close to room temperature in initial stages (see section I). According to **Fig. 2.15**, T_c must be increasing significantly around t_{Co}^* since full remnance is observed just prior to the SRT.

The increase of $M(1KOe)$ with t_{Co} above 2ML is consistent with past reports [2, 4]. This part of the transient bears interesting information. The minimization of the MAE gives:

$$K_{eff} = -(2K_2 \sin^2 \varphi + HM_s / 2 \cos \varphi) = K_1 - 2\pi M_s^2 + K_s / t_{Co} \quad (2.25)$$

$$K_{eff} \cdot t_{Co} = -(2K_2 \sin^2 \varphi + HM_s / 2 \cos \varphi) \cdot t_{Co} = (K_1 - 2\pi M_s^2) \cdot t_{Co} + K_s \quad (2.26)$$

At $H = 10000e$, $\cos \varphi$ is given by

$$\cos \varphi = \frac{M(1KOe)}{M_{Sat}} \quad (2.27)$$

where M_{Sat} is the MOKE signal at saturation.

Equation 2.26 indicates that a plot of $K_{eff} \cdot t_{Co}$ vs t_{Co} is a straight line of coefficient $K_1 - 2\pi M_s^2$. Its extrapolation to $t_{Co} = 0$ yields K_s , and another means to estimate it. For sufficiently thick layers it is reasonable to assume that T_c is well above RT and to consider the bulk anisotropy constants of hcp cobalt (0001), yielding a slope of $K_1 - 2\pi M_s^2 = -6.8 \cdot 10^6 \text{ erg} \cdot \text{cm}^{-3}$.

Experimentally, the only unknown is the angle φ between the easy axis and the surface normal, because the max magnetic field of our setup does not allow reaching M_{Sat} . Since M_{Sat} is proportional to t_{Co} for large values of t_{Co} , we can write:

$$M_{Sat} = \alpha * t_{Co} \quad (2.28)$$

where α is a coefficient, which depends on the sample. α is therefore determined for

each experiment in order to obtain the experimentally estimated $K_{eff} \cdot t_{Co}$ with a slope equal to $K_I - 2\pi M_s^2$ (**Fig. 2.16**). In the case of this experiment $\alpha = 0.026$ (red line). This value is significantly larger than the slope $\alpha = 0.01$ of $M(1K0e)$ vs t_{Co} for $t_{Co} < 1.5ML$. This is a clear indication that T_c of the Co film is rather low for $t_{Co} < 1.5ML$, which is consistent with other findings with many different systems (see Section 2.2).

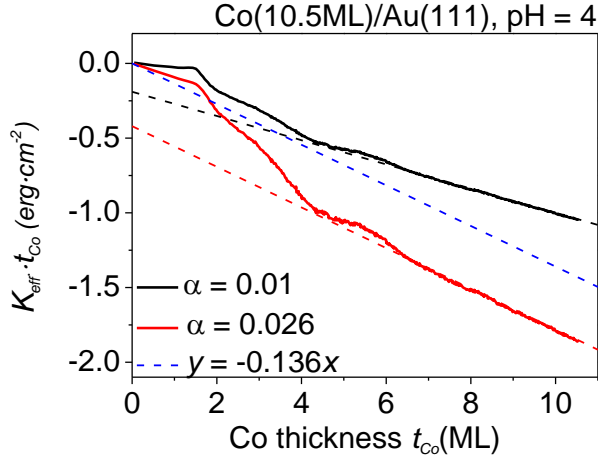


Fig. 2.16: Plot of $K_{eff} \cdot t_{Co}$ as a function of t_{Co} by using $\alpha = 0.01$ (black line) and $\alpha = 0.026$ (red line) for the same sample.

2.6. Conclusions

The experimental details for substrate preparation, Co growth and magnetic measurements are shown. We also show that the magnetization orientation is governed by the minimization of total anisotropy energy, which includes the magnetocrystalline, magnetoelastic, dipolar, interface anisotropy and Zeeman energies. We also demonstrate how it is possible to determine the Co thickness in real time using the sample reflectivity. We also present a method to determine M_{Sat} from $M(1K0e)$ by fitting the experimentally estimated $K_{eff} \cdot t_{Co}$ with a slope equal to $K_I - 2\pi M_s^2$.

2.7. References

[1] L. Cagnon, T. Devolder, R. Cortes, A. Morrone, J.E. Schmidt, C. Chappert, P. Allongue, Enhanced interface perpendicular magnetic anisotropy in electrodeposited Co/Au(111) layers, *Physical Review B*, 63 (2001).

[2] P. Allongue, F. Maroun, H.F. Jurca, N. Tournerie, G. Savidand, R. Cortes, *Magnetism of*

electrodeposited ultrathin layers: Challenges and opportunities, *Surface Science*, 603 (2009) 1831-1840.

[3] N. Tournier, A.P. Engelhardt, F. Maroun, P. Allongue, Influence of the surface chemistry on the electric-field control of the magnetization of ultrathin films, *Physical Review B*, 86 (2012).

[4] G. Savidand, Effets d'interfaces sur le retournement de l'aimantation de couches ultraminces électrodéposées Co/Au(111). Etude par MOKE et STM in situ. , in: *Physique*, Ecole Polytechnique, 2007.

[5] M.J. Donahue, D.G.D. Porter, Analysis of switching in uniformly magnetized bodies, *Ieee Transactions on Magnetics*, 38 (2002) 2468-2470.

[6] C. Chappert, P. Bruno, magnetic-anisotropy in metallic ultrathin films and related experiments on cobalt films, *Journal of Applied Physics*, 64 (1988) 5736-5741.

[7] M.T. Johnson, P.J.H. Bloemen, F.J.A. denBroeder, J.J. deVries, Magnetic anisotropy in metallic multilayers, *Reports on Progress in Physics*, 59 (1996) 1409-1458.

[8] C.M. Schneider, P. Bressler, P. Schuster, J. Kirschner, J.J. Demiguel, R. Miranda, Curie-temperature of ultrathin films of fcc cobalt epitaxially grown on atomically flat Cu(100) surfaces, *Physical Review Letters*, 64 (1990) 1059-1062.

[9] J.C. Suits, Faraday and Kerr effects in magnetic compounds, *IEEE Transactions on Magnetics*, MAG8 (1972) 95-105.

[10] M.J. Freiser, A survey of magneto optic effects, *IEEE Transactions on Magnetics*, MAG4 (1968) 152-161.

[11] M. Paunovic, M. Schlesinger, *Fundamentals of Electrochemical Deposition*, 2nd ed., John Wiley & Sons, Inc., Hoboken, New Jersey, 2006.

[12] J.O'M. Bockris, A.K.N. Reddy, *Modern Electrochemistry*, Plenum Press, New York, 1970.

[13] D.M. Kolb, Reconstruction phenomena at metal-electrolyte interfaces, *Prog. Surf. Sci.*, 51 (1996) 109-173.

- [14] P. Atkins, J.D. Paula, *Physical Chemistry* 8th ed., Oxford University Press, 2006.
- [15] P. Allongue, F. Maroun, Metal electrodeposition on single crystal metal surfaces mechanisms, structure and applications, *Curr. Opin. Solid State Mat. Sci.*, 10 (2006) 173-181.
- [16] M.L. Munford, R. Cortes, P. Allongue, The preparation of ideally ordered flat H-Si(111) surfaces, *Sensors and Materials*, 13 (2001) 259-269.
- [17] P. Prod'homme, F. Maroun, R. Cortes, P. Allongue, Electrochemical growth of ultraflat Au (111) epitaxial buffer layers on H-Si (111), *Applied Physics Letters*, 93 (2008).
- [18] A. Damien, In Situ STM Study of the growth and dissolution processes on bimetallic Pd/Au(111) Substrates and of Ultrathin Alloy Layers on Au(111), in: *Physique, Ecole Polytechnique*, 2009.
- [19] P. Allongue, F. Maroun, Electrodeposited magnetic layers in the ultrathin limit, *MRS Bulletin*, 35 (2010) 761-770.

Chapter 3 Electrochemical oxidation of cobalt and its influence on the magnetic properties of Co/Au (111) layers

3.1. Introduction

Achieving voltage control of magnetism was reported with solid state structure mainly. In such devices, the ultrathin ferromagnetic film is covered with a dielectric layer. A gate electrode (metallic contact) is then deposited to apply the electric field and modify the magnetic anisotropy energy (MAE) of the FM layer [1, 2]. Experimental data about the impact of electric field on MAE prompted many Density functional theory (DFT) calculations as in reference [3]. Results showed that the electric field changes the distance between the surface atomic plane of the ferromagnetic layer and the neighboring oxygen plane of the oxide layer associated with a change in the partial charge of the surface atoms of the magnetic layer. This partial charge transfer at the metal/oxide interface appears to be one possible origin of the change of the metal magnetic properties. In addition, recent investigations using X-ray absorption spectroscopy and magnetic circular dichroism [4] have shown that the oxidation state of the ferromagnetic metal atoms at the metal/oxide interface changes as a function of the applied electric field and is accompanied by changes of the magnetic signal. It is concluded that oxygen plays a very important role. Recent research is dedicated to control the oxidation of this insulating layer, inducing a magnetic anisotropy crossover from in plane to out of plane [5]. The aim of this chapter is investigating the influence of Co electrochemical oxidation on the MAE of epitaxial Co(0001)/Au/Si(111) ultrathin films.

Cobalt electrochemical oxidation was investigated in the past. The potential – pH diagram or Pourbaix diagram is shown in **Fig. 3.1**. Each line in this diagram corresponds to a reaction. The reaction may be chemical or electrochemical. A Pourbaix diagram provides a quick overview about the stability domain of a metal and it helps anticipating when oxidation leads to dissolution or oxide formation. In the case of cobalt, this diagram (**Fig. 3.1**) appears to be in very good agreement with electrochemical studies and surface characterizations. In particular it shows that Co may be dissolved at $\text{pH} < 6$, in agreement with **Chapter 2** since one could dissolve the Co films to determine their thickness. According to **Fig. 3.1**, growing a Co oxide layer requires the use of solution of $8 < \text{pH} < 13$. At $\text{pH} > 13$, dissolution is again expected.

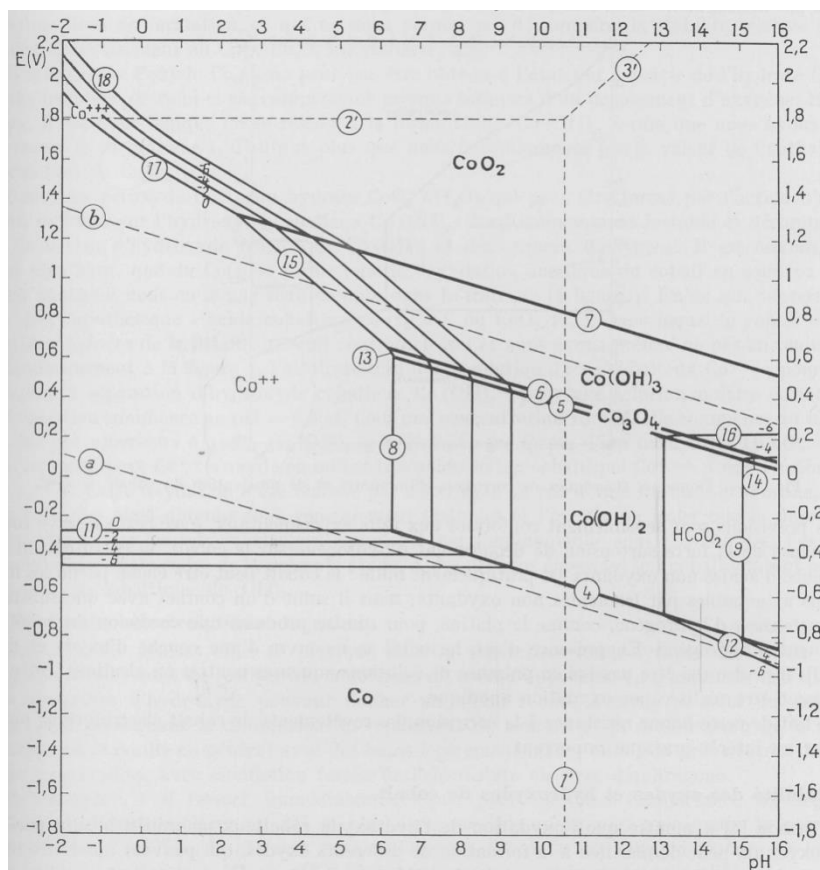


Fig. 3.1: Potential – pH diagram of Co [6]. The potential reference is SHE.

The passivation of cobalt (i.e. formation of an essentially insoluble oxide) has been studied in alkaline and slightly acidic solutions. Ellipsometry [7-10] showed that cobalt forms two kinds of passive layers. The first (primary passive layer) grows at low potentials and consists of CoO and Co(OH)₂; in the potential range of secondary passivity, a 3.7 nm thick outer layer of Co₃O₄ is formed on top of an inner CoO film. More recent studies with Co(0001) single crystal electrodes reported a new piece of information since these works showed the presence of a pre-oxidation peak (see **Fig. 3.3**, peak A₁). Such a feature is not predicted by the above Pourbaix diagram since Pourbaix diagrams treat bulk reactions only. **Fig. 3.2** presents *in situ* electrochemical scanning tunneling microscopy (STM) images of a Co(0001) electrode at cathodic potential (image a) and in the pre-oxidation state (image b). Image (a) is atomically resolved and it shows that the (0001) surface is (1 × 1). Under pre-oxidation conditions, image (b) reveals a new topography, with a hexagonal periodic corrugation closely corresponding to a (5 × 5) structure. This surface structure was interpreted as a Moiré structure resulting from the formation of a monolayer of CoO(111) or

β -Co(OH)₂(0001) on Co(0001) [10]. It was also shown that in an alkaline solution, such an oxidized Co(0001) surface can be reduced back to the metallic state [11].

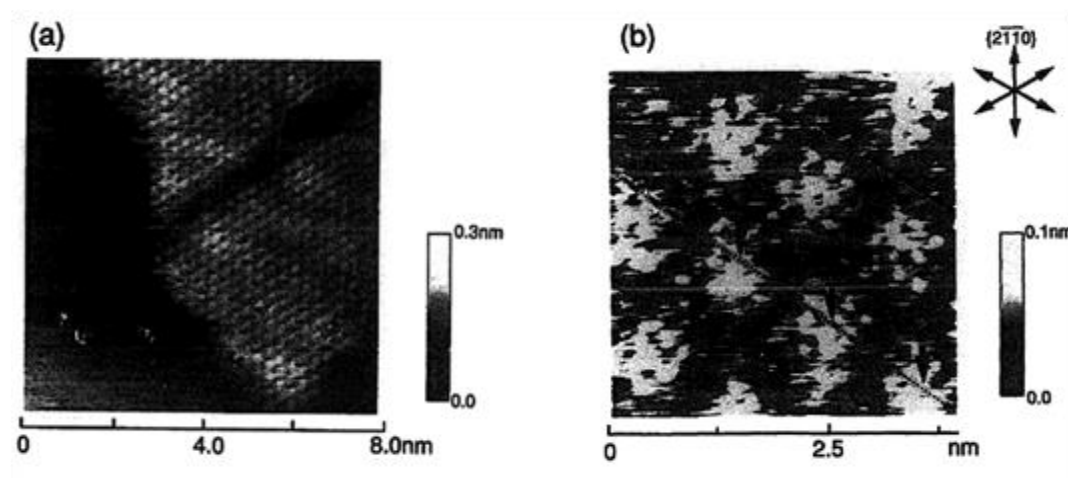


Fig. 3.2: Atomic resolution STM images of (a) Co(0001) obtained at -0.8V (vs SHE) (b) oxide layer in 0.05M Na₂SO₄ (pH =3) electrolyte [10].

This chapter is organized as follows. It starts with a first section which presents and discusses the Co electrochemical response over the entire range of potential and revisits the surface chemistry of this material in light of DFT calculations. The next section gives experimental details to achieve a controlled transfer of the Co/Au sample from the plating solution into the alkaline solution. In the last two sections we present and discuss MAE results in two different specific ranges of potential.

3.2. Co electrochemical oxidation revisited: results and discussion

3.2.1. Electrochemical response

Figure 3.3 presents the 1st cyclic voltammogram (i.e. variations of the electrochemical current with potential) of a Co(14ML)/Au(111)/Si(111) electrode in contact with the pH ~ 12 0.1M K₂SO₄ + 0.01M KOH electrolyte. The scan of potential starts from -1.45V towards positive values. Arrows in the figure indicate the direction of the potential sweep (10mV/s). The three anodic peaks, labeled A₁ to A₃, and the cathodic peaks, labeled C₃ and C₂ and C₁ are in very good agreement with those measured with of a Co(0001) single crystal electrode in a similar solution [10].

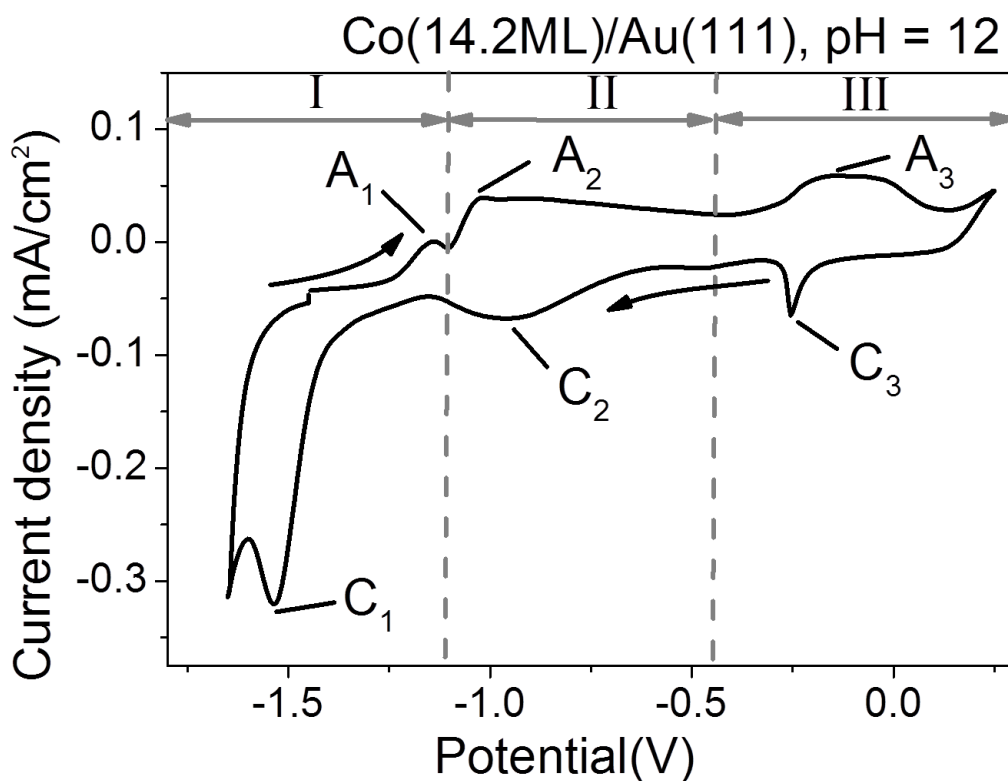


Fig. 3.3: variations of the electrochemical current density with potential (cyclic voltammogram) of a Co(14ML)/Au(111) sample in contact with the pH ~ 12 0.1M K₂SO₄ + 0.01M KOH electrolyte. The start potential is -1.45 V. Arrows indicate the scanning direction.

According to past electrochemical studies of polycrystalline Co electrodes, the anodic peaks A₂ and A₃ mark the transition between different Co oxidation states: CoO and Co(OH)₂ is formed for potential between peaks A₂ and A₃. At higher oxidation potential (more positive than peak A₃) a 3.7 nm thick outer layer of Co₃O₄ is formed on top of an inner CoO film [7 - 9]. As will be shown later on, oxidation in region II and III is accompanied with some Co dissolution. These regions of potential are consistent with the Pourbaix diagram. Upon reversal of the potential, from 0.25 V, the oxide is progressively reduced at peaks C₃ and C₂. The surface is fully reduced at potential negative of peak C₁.

As mentioned in the Introduction, we emphasize again that Peak A₁ in **Fig. 3.3** is only observable on Co(0001). It was never mentioned on polycrystalline. In this region of potential, in situ STM imaging revealed the formation of a hexagonal surface lattice with (5 × 5) symmetry corresponding closely to that of CoO(111) or Co(OH)₂(0001) (see **Fig. 3.2**) [10] which may be reduced electrochemically [11].

3.2.2. Potential – phase diagram of Co

Density functional theory (DFT) calculations were conducted in order to understand this structure. This work was conducted by J. Kubal and Z. Zeng under the supervision of Prof. J. Greeley at school of chemical engineering, Purdue University. The detailed calculations are given elsewhere [12]. The different structures of the Co(0001) surface considered in this work are:

(i) a H-terminated surface (coverage 0.25 to 1) as reduced state (**Fig. 3.4.a**);

(ii) a Co surface plane with Co bulk lattice parameters covered with a OH layer (coverage 0.25 to 1) (**Fig. 3.4.b**). They also considered surfaces with mixed (H + OH) layers with different H/OH coverage ratios.

(iii) a CoOH surface plane, which is a restructured OH-terminated surface with OH coverage 1 (with respect to the restructured Co top most plane). A (7×7)-CoOH with a lattice parameter expanded by 15%, a (6×6)-CoOH with a lattice parameter expanded by 20% and a (4×4)-CoOH with a lattice parameter expanded by 32% with respect to Co(0001) surface.

(iv) a Co(OH)₂ overlayer with different lattice parameters. A (5×5) with a lattice parameter expanded by 25%, a (4×4) with a lattice parameter expanded by 31%, a (8×8) with a lattice parameter expanded by 13% and a (6×6) with a lattice parameter expanded by 20% with respect to Co(0001) surface.

For the reduced state the (1×1)-H adlayer (H coverage of 1) was found to be the most stable (**Figure 3.4.a**). For the oxidized states, the (2×2)-OH adlayer (OH coverage of 0.25), the (6×6)-CoOH layer (CoOH coverage of 0.69) and the (5×5)-Co(OH)₂ layer (Co(OH)₂ coverage of 0.64) were found to be the most stable structures (**Figure 3.4.b, Figure 3.4.c and Figure 3.4.d** respectively).

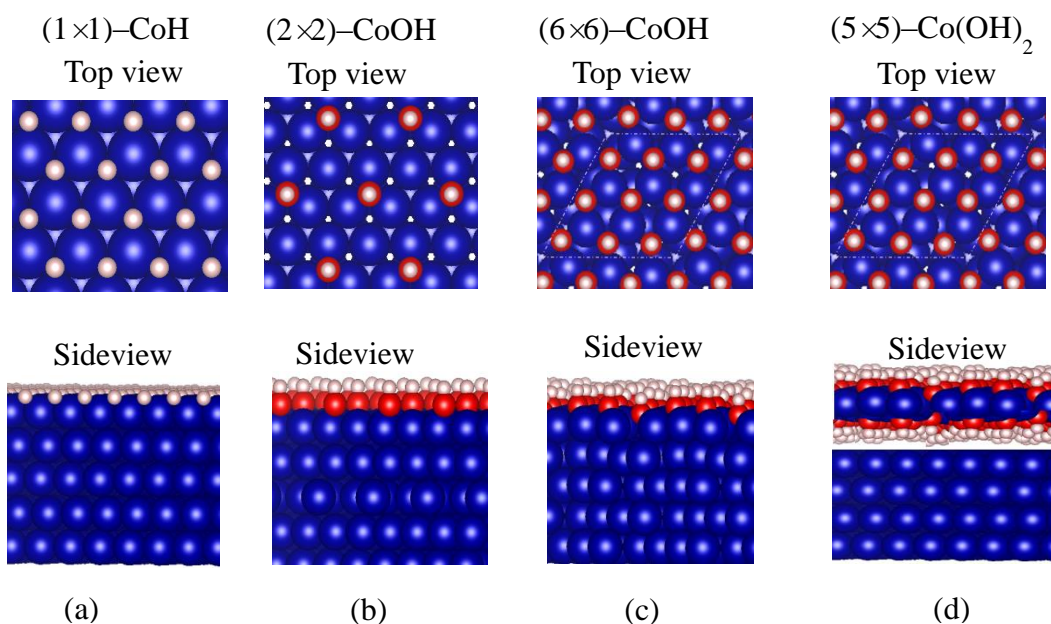


Fig. 3.4: Top views and side views of the four most stable structures: (a) (1×1) -CoH; (b) (2×2) -CoOH ; (c) (6×6) -CoOH; and (d) (5×5) -Co(OH)₂

Figure 3.5 presents the phase diagram versus applied potential, i.e. the Gibbs energy of each structure as a function of potential. The calculations show that the (1×1) -H on Co is the energetically most favourable structure for $U < -1.3$ V, i.e. in the potential range of peak (C₁) and that of the water decomposition reaction. For $U > -1.05$ V, the (5×5) -Co(OH)₂ structure is the most favourable one. In the potential range of peak (A₁), for -1.3 V $< U < -1.05$ V, the OH-termination is the energetically most stable surface chemistry. Its precise structure depends, however, on the interaction energy between the OH groups and the water molecules in the electrolyte (H-bonding). If the interaction energy of the OH group with water is set to zero (**Fig. 3.5.a**), the most stable structure is the Co surface with Co bulk lattice parameters covered by (2×2) -OH adlayer. On the other hand, setting this interaction energy to -0.2 eV per OH group (**Fig. 3.5.b**), the most stable structure is the (6×6) -CoOH.

To discriminate between the two diagrams, we may first compare the expected surface structure in peak A₁ with experimental *in situ* STM observations on Co(0001) in the potential range of peak A₁ [11]. The observed (5×5) moiré structure has a period of 12.5 Å (estimation using $a = 2.5$ Å for bulk Co(0001)). This moiré period was found also in ref. [10]. Since the DFT calculations yield no surface restructuring for a (2×2) -OH adlayer (**Fig. 3.5.b**), one may argue, that the actual potential – phase diagram must be that in **Fig. 3.5.b** where the (6×6) -CoOH structure forms in peak A₁. The in plane lattice $a = 3.03$ Å of this adlayer yields a

moiré of period 14.3 \AA which is compatible with the experimental value of 12.5 \AA mentioned above for the (5×5) adlayer.

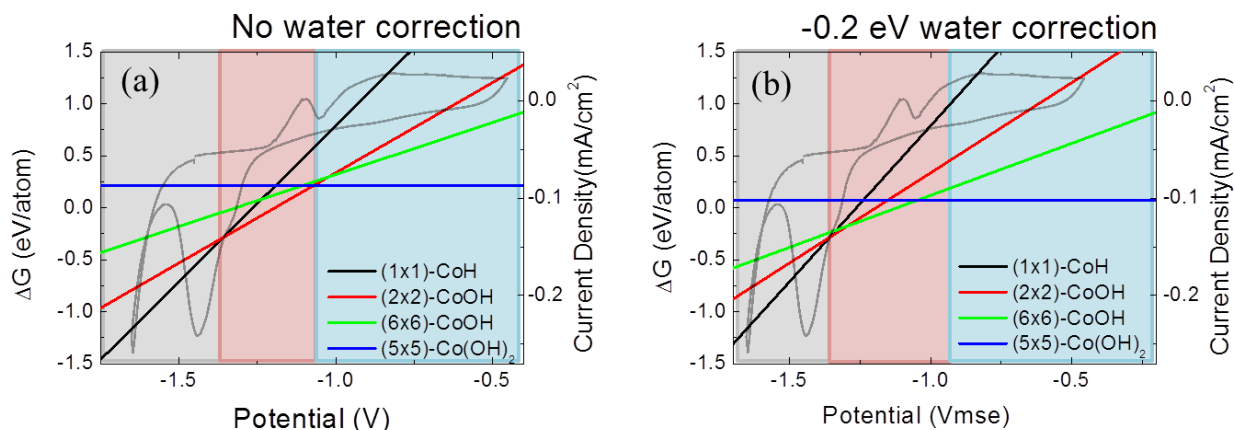


Fig. 3.5: Co phase diagram with no correction of water interaction (a) and with a correction of -0.2 eV water interaction per OH (b). The left y – axis indicates the Gibbs energy (eV) per Co atom for (1×1) -CoH (black line), (2×2) -CoOH (red line), (6×6) -CoOH (green line) and (5×5) -Co(OH)₂ (blue line). The light grey, red and blue region indicating the corresponding potential where CoH, CoOH and Co(OH)₂ are the most stable. The right y – axis presents the voltammogram of Co in pH = 12 electrolyte.

3.3. Transfer of Co/Au samples into electrolytes of pH 12

Since cobalt oxidation is performed in a supporting electrolyte of pH 12 ($0.1 \text{ M K}_2\text{SO}_4 + 0.01 \text{ M KOH}$), we needed to exchange electrolyte from the plating solution $1 \text{ mM CoSO}_4 + 0.1 \text{ M K}_2\text{SO}_4 + 1 \text{ mM KCl} + 1 \text{ mM H}_2\text{SO}_4$ (pH 3.5) to pH=12 solution. We paid strong attention to this procedure to avoid Co hydroxide formation on the surface and in solution during this exchange. Our aim is that the magnetic properties of the Co layer after transfer in pH=12 electrolyte are identical to those of the as-deposited Co layer.

The complete electrolyte transfer procedure is described in **Fig. 3.6**. The time scale is divided into three phases: **Phase I** is corresponding to cobalt deposition (dark grey background); In **phase II** (light gray background) the plating solution is exchanged with a Co^{2+} -free electrolyte of pH 3.5 to remove the Co^{2+} cations. This phase is necessary to avoid Co hydroxide formation when we inject the pH=12 solution. **Phase III** corresponds to the final exchange with the supporting electrolyte of pH=12. The potential program to the sample is shown in Panel (d). Throughout the sequence, we recorded the sample reflectivity $\Delta R/R$ (Panel a), the sample magnetization $M(1 \text{ kOe})$ (Panel b) and the ratio $M_R/M(1 \text{ kOe})$ (Panel c).

The variations of $\Delta R/R$, $M(1kOe)$ and $M_R/M(1kOe)$ during Co deposition at -1.3 V (**phase I**) have been commented and interpreted in details in **Chapter 2**. At the end of **phase I**, a 3.2-ML thick film Co/Au(111) was obtained in this experiment. It is stabilized at -1.1 V. In accordance with the results in **Chapter 2**, it is in plane magnetized ($M_R/M_{Sat} \sim 0$). The first solution exchange is then performed at -1.1V for 40s and then at -1.45V for 50s prior to the final exchange of electrolyte with the pH=12 electrotype. This proved to be indispensable to avoid uncontrolled surface oxidation (see **Fig. 3.1**).

It should be noticed that $\Delta R/R$ stays remarkably constant after deposition in **Fig. 3.6** (Panel a), which suggests perfect control of the film integrity during the whole procedure. We can safely state that the Co/Au(111) layer in contact with the solution of pH 12 is identical to the one just after deposition. Nevertheless, *systematic* variations of $M(1kOe)$ (see Panel b) are observed. The immediate decrease of $M(1kOe)$ when stabilizing the film at -1.1 V (Phase I) and its immediate increase while applying -1.45 V (Phase II) are consistent with magneto electric coupling. This point will be investigated in **Chapter 4**, where we will show that the MAE of as deposited Co/Au(111) layers *increases* when the potential is more negative. The decrease of $M(1kOe)$ upon injection of the alkaline pH electrolyte of pH 12 was unexpected since the applied potential is fixed at -1.45 V. It may not be due to changes of the Co film magnetic properties but to some modifications of the MOKE response of the solution. We therefore conducted complementary characterizations to understand the origin of this observation.

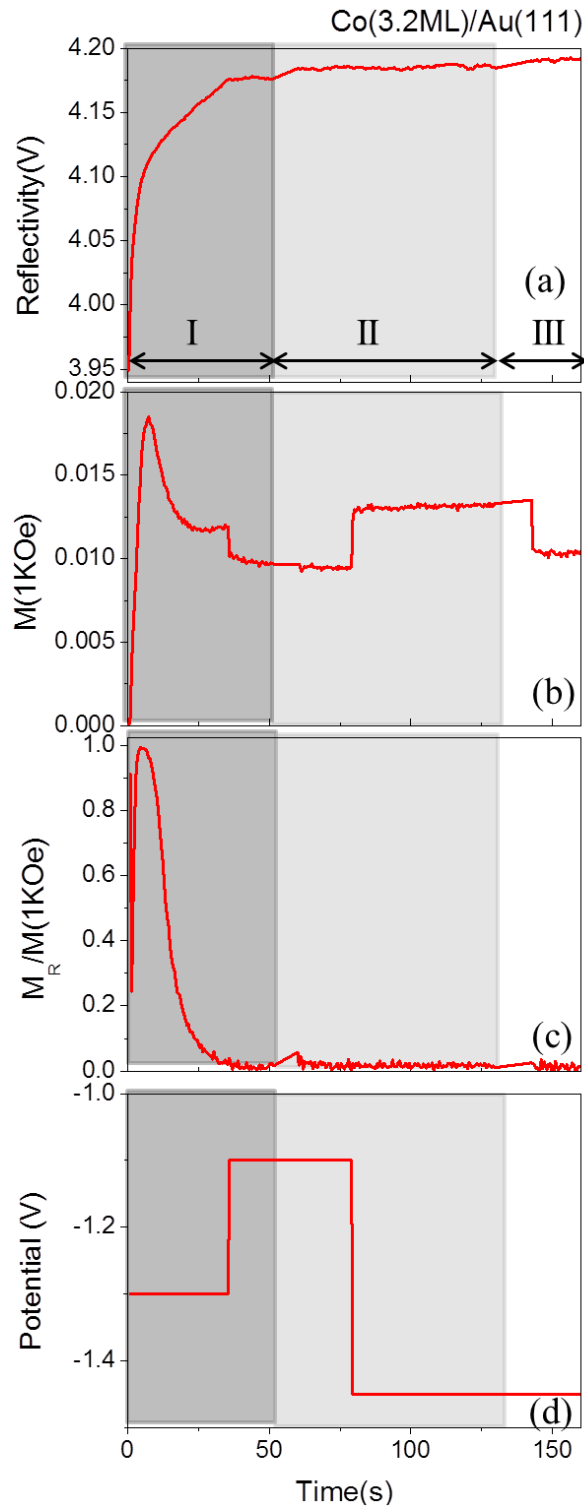


Fig. 3.6: (a) Reflectivity; (b) $M(1KOe)$; (c) $M_R/M(1KOe)$ during Co(3.2ML) deposition and stabilization in pH $\sim 3.5 - 4$ acid electrolyte (grey background) and transferring to pH = 12 alkaline electrolyte (light grey and white background). (d) describes the potential sequence.

Figure 3.7 shows the same experiment as in **Fig. 3.6** with a 1.6-ML film. As expected from **Chapter 2**, the film is out of plane magnetized since $M_R \sim M_{Sat}$ right after the deposition

(Phase I). A perfect stabilization of such a film is however more problematic during phase II. We assign this difficulty to the fact that a 1.6-ML Co/Au(111) layer consists of biatomic islands covering 80% of the gold surface (see **Chapter 2**). Therefore Co step sites are exposed to solution which favors slow dissolution/deposition at the equilibrium potential on the time scale of the solution exchange in phase II. In this experiment the slow increase of $\Delta R/R$ (Panel a) after the deposition indicates a slow growth, which explains that the magnetization easy axis rotates towards in plane direction ($M_R < M_{Sat}$ and decrease of H_c , in phase II). A stable state is however reached after 200s. Stepping the potential to -1.45 V ($t = 280$ s) increases the MAE (see increase of M_{Sat} , M_R and H_c) as observed above in **Fig. 3.6**. When the solution is exchanged from acid to alkaline electrolyte, a sudden decrease of these three parameters is consistent with a reduction of the surface anisotropy $K_S^{Co-Surf}$. Indeed, the modification of H_c can only be due to changes of the Co film MAE.

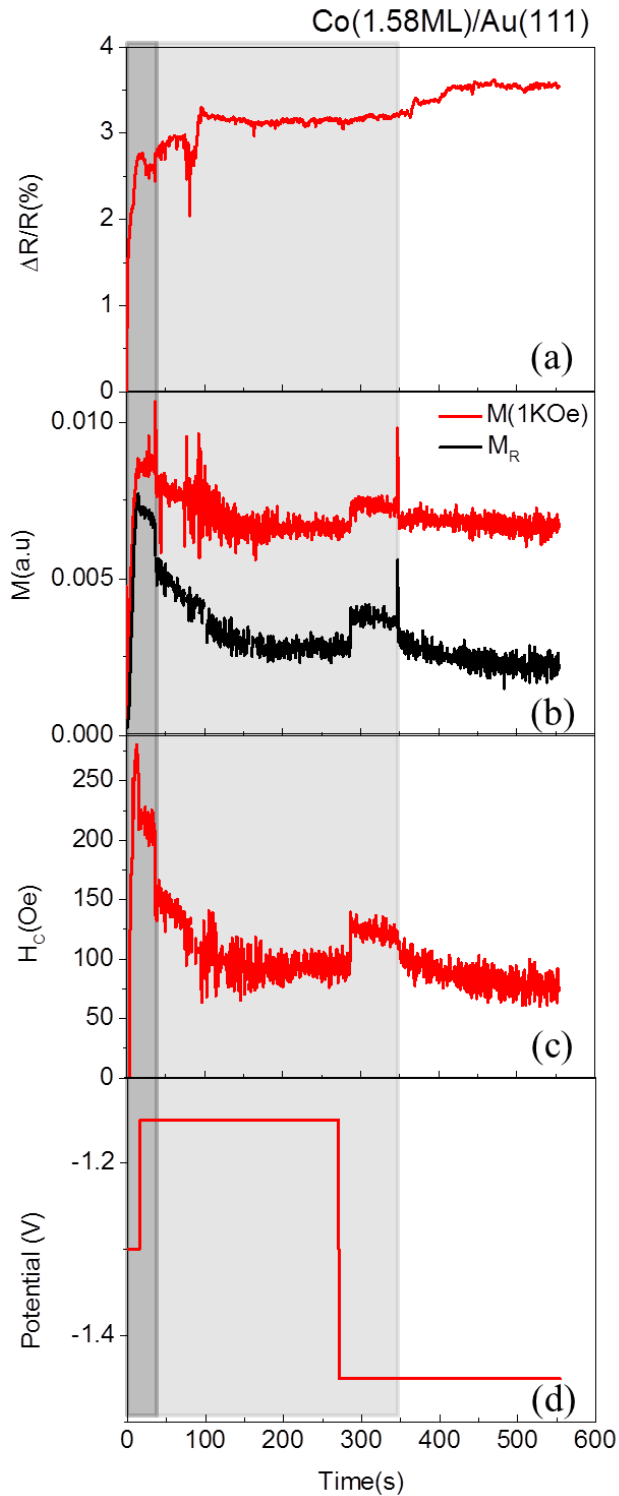


Fig. 3.7: (a) $\Delta R/R$; (b) $M(1KOe)$ and M_R ; (c) H_c during Co(1.58ML) deposition and stabilization in pH $\sim 3.5 - 4$ acid electrolyte (grey background) and transferring to pH = 12 alkaline electrolyte (light grey and white background). (d) describes the potential sequence.

To estimate the decrease of $K_S^{Co-Surf}$ upon solution exchange we have measured the relative variations of $M(1KOe)$ for Co with different thicknesses. **Fig.3.8** is a plot of

$\Delta M(1K0e)/M(1K0e)$ as a function of the Co thickness. These data were interpreted by assuming that the decay in $\Delta M(1K0e)/M(1K0e)$ is related to a reduction of the film anisotropy. We calculated ΔK_{eff} after having determined M_{Sat} for each of the samples using the method described in **Chapter 2**.

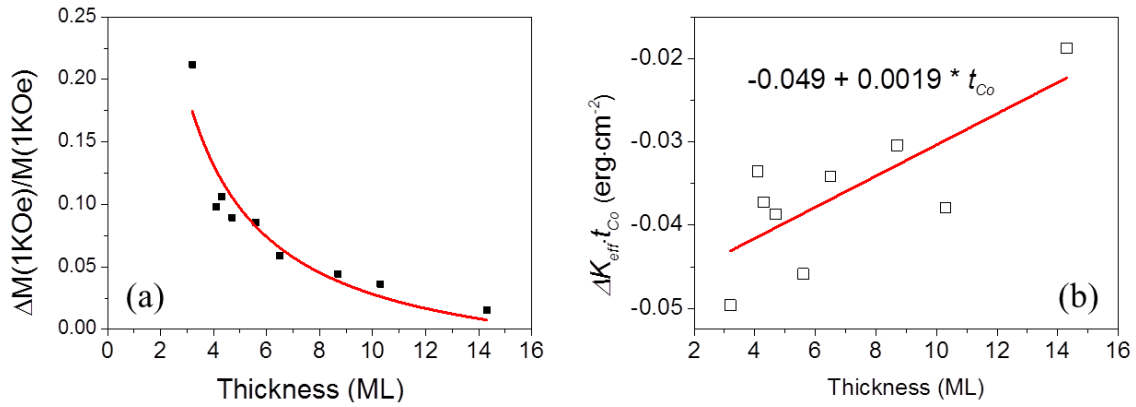


Fig. 3.8: (a) relative variations $\Delta M(1K0e)/M(1K0e)$ measured upon exchange of electrolyte of pH 3.5 by the electrolyte of pH 12; (b) variations $\Delta K_{eff} * t_{Co}$ as a function of the Co thickness.

Figure 3.8.b shows a plot of $\Delta K_{eff} * t_{Co}$ as a function of t_{Co} . The red straight line is a linear fit of data. Interestingly the slope $\Delta K_V = 0.0019/2 \cdot 10^{-8} = 2 \cdot 10^5$ erg/cm³. This value is about one order of magnitude smaller than bulk K_V ($\sim 5 \cdot 10^6$ erg/cm³) of the Co/Au(111) layer (see **Chapter 2**). Therefore, we can conclude from **Fig. 3.8.b** that the transfer of the sample from the solution of pH 3.5 into the solution of pH 12 induces a jump of surface anisotropy $\Delta K_S = -0.049$ erg/cm²; In other words $K_S^{Co-Surf}$ decreases by -0.049 erg/cm² in the alkaline solution. This difference does not seem to originate from a change of the surface chemistry because the Co surface remains H-terminated at -1.45 V in pH = 12 solution. The origin of this $K_S^{Co-Surf}$ decrease is not clear and deserves additional electrochemical characterizations, out of the scope of this work.

3.4. MAE of Co thin films upon OH adsorption (peak A₁)

In this section, we first focus on the changes in MAE of the H-terminated surface and of the Co surface in the potential range of peak A₁.

3.4.1. Results

Figure 3.9.a presents the variations of the electrochemical current as a function of U (voltammogram) for a 3.1 ML – thick Co/Au(111) film in contact with the electrolyte of pH = 12. The sweep starts from -1.45 V towards positive potential (see arrows). Except for the first one, the subsequent voltammograms are identical. The main features of interest in the voltammogram are the two peaks denoted (A₁) at $U = -1.16$ V and (C₁) at $U = -1.34$ V which correspond to the first Co oxidation/reduction step (the current increase at $U < -1.5$ V corresponds to water decomposition).

Figure 3.9.b presents the relative change of the sample reflectivity ($\Delta R/R$) with respect to that measured at -1.45 V during the same potential sweep. $\Delta R/R$ decreases by $\sim 1\%$ in the potential range of peak (A₁) and returns back to zero in the potential range of peak (C₁). $\Delta R/R$ remains constant at $U < -1.5$ V indicating that the Co surface chemistry remains unchanged during the water decomposition reaction. The same reversible $\Delta R/R$ variations are reproducible during several consecutive potential sweeps. The fact that $\Delta R/R$ returns to zero value after consecutive potential cycles demonstrates the absence of Co dissolution in this potential range. The variations of $\Delta R/R$ within peak A₁ are only related to the modification of the cobalt surface chemistry

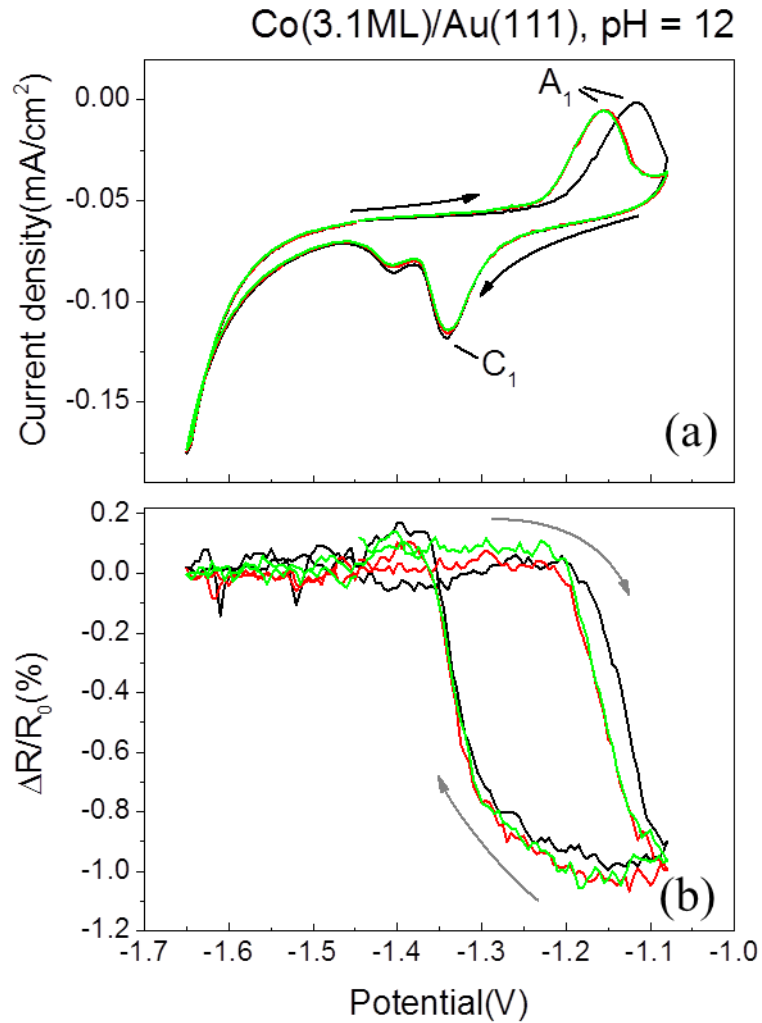


Fig. 3.9: (a) Electrochemical current density; (b) $\Delta R/R_0$ with respect to that at -1.45 V as a function of U for a 3.1 ML – thick Co/Au(111) film in contact with the electrolyte of pH = 12. The scan speed is 10mV/s.

Figure 3.10 shows again the voltammogram and gives in inset $M - H$ curves at selected potentials. The 3.1-ML film is in-plane magnetized (linear and reversible $M - H$) for $U < -1.25$ V and becomes perfectly out-of-plane magnetized (square $M - H$) at -1.08 V with a coercive field of 225 Oe. This behavior indicates a clear spin reorientation transition (SRT) in correlation with surface oxide formation. The reverse SRT is observed during the negative potential sweep since the film is again in-plane magnetized for $U < -1.45$ V.

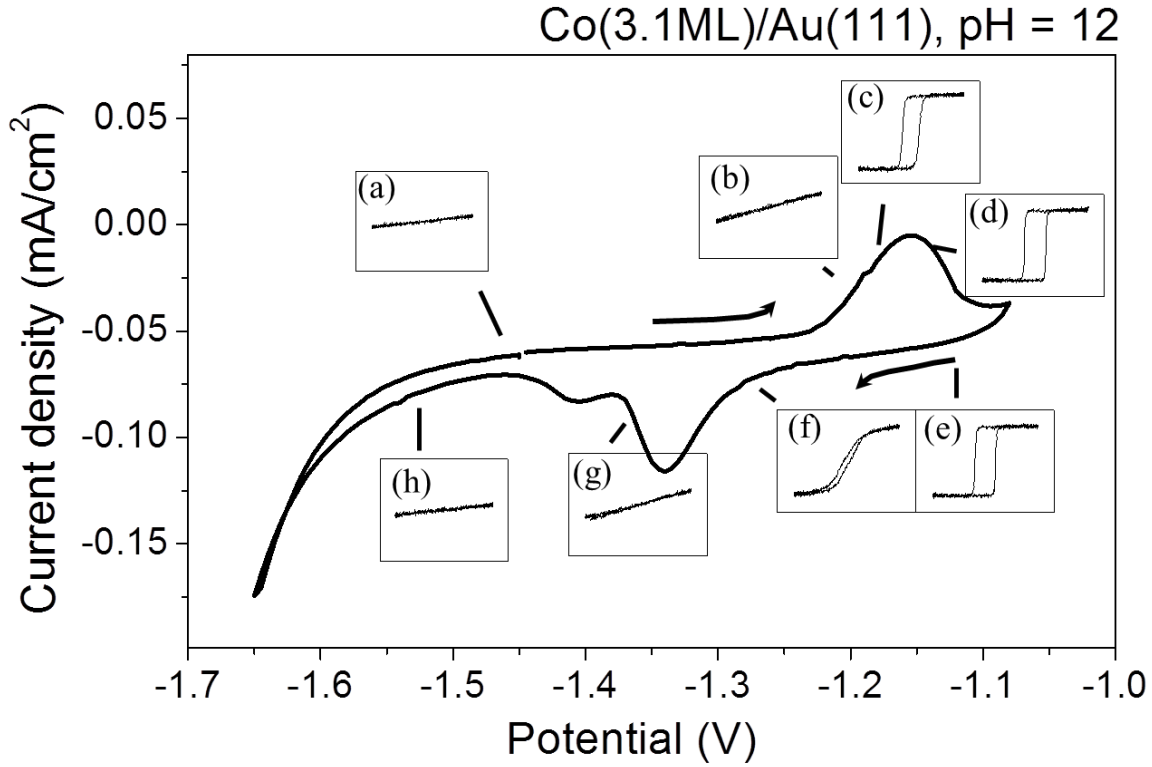


Fig.3.10: $M - H$ curves at selected potentials during the same potential scan as in Fig.3.9.

Figure 3.11 displays the variations of the $M_R/M(1KOe)$ (**Fig. 3.11.a**), H_c (**Fig. 3.11.b**) and the electrochemical current (**Fig. 3.11.c**) versus the applied potential during a potential scan for Co (2ML) (black line), Co (3.1ML) (red line), Co (4.1ML) (green line) and Co (5.3ML) (blue line) in contact with pH = 12 electrolytes. The position of peak A_1 (panel c) does not depend on the thickness when t_{Co} is thicker than 2ML. We have not investigated further why peak A_1 is systematically found at a potential 50 mV more negative than on the 2 ML sample. The magnetic data indicate a complete SRT from in plane to out of plane direction for Co (2ML) and Co (3.1ML)/Au(111), since $M_R/M(1KOe)$ reaches unity for these two samples in the range of peak A_1 . In the case of Co (4.1ML) and Co (5.3ML), the SRT is only partial, as the magnetization easy axis remains tilted. The behavior of H_c is similar to that of $M_R/M(1KOe)$ except that H_c continues to increase up to the most positive potential, indicating a continuous anisotropy increase.

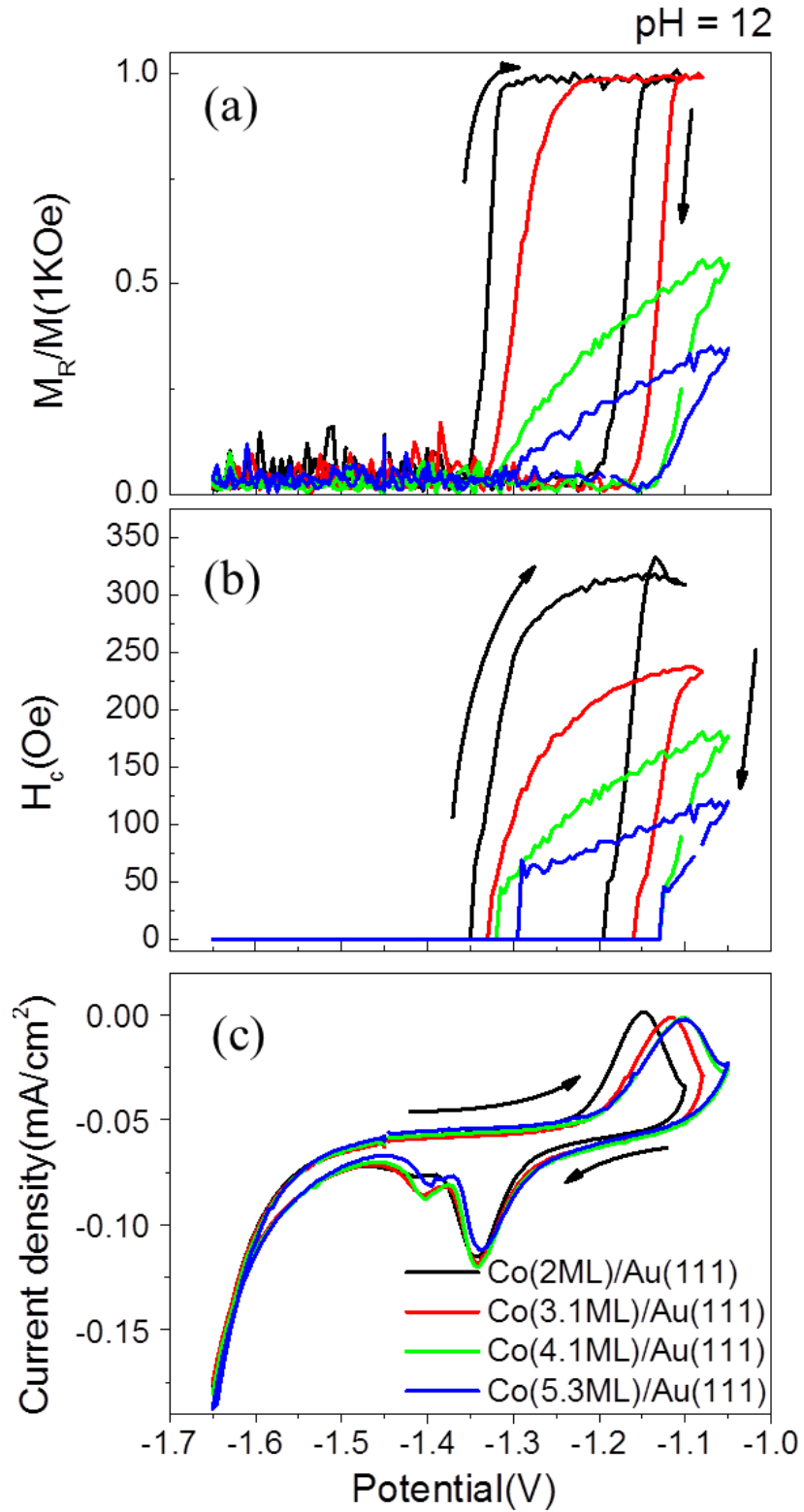


Fig. 3.11: (a) $M_R/M(1kOe)$; (b) H_c ; and (c) electrochemical current density during the first scans for 2.1-ML(black line), 3.1-ML(red line), 4.1-ML(green line) and 5.3-ML(blue line) Co. The scan speed is 10mV/s.

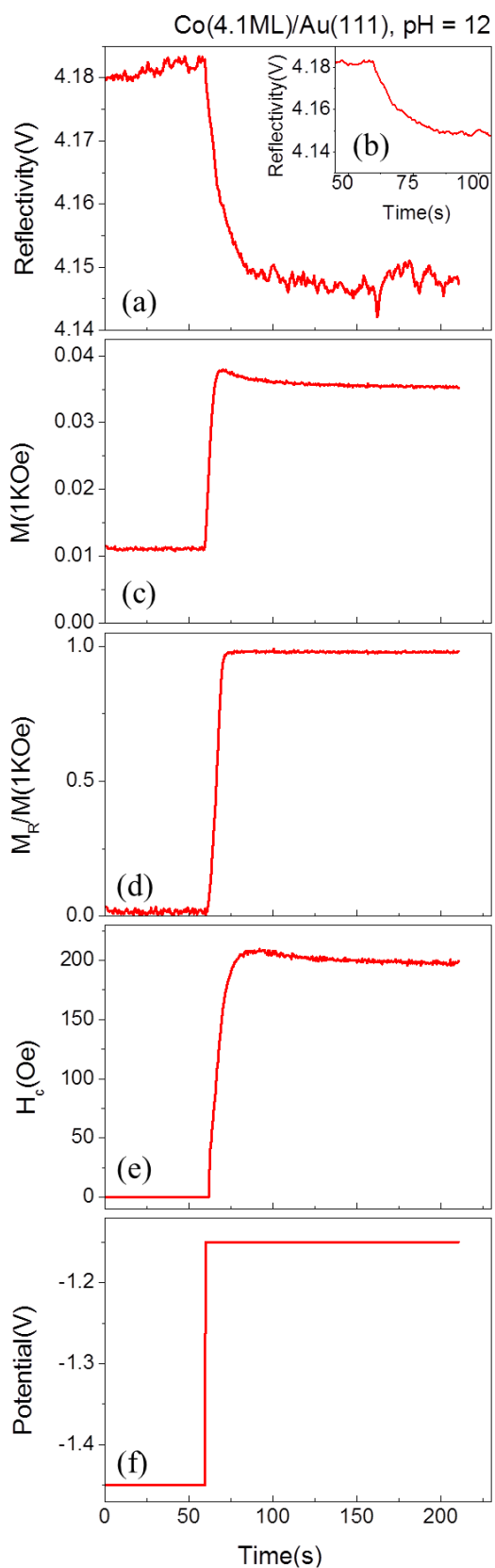


Fig. 3.12: (a) Reflectivity R ; (b) zoom of Reflectivity R between 55s and 100s; (c) $M(1KOe)$; (d) $M_R/M(1KOe)$; (e) H_c for a Co(4.1ML)/Au(111) in contact with pH = 12 electrolyte during one potential step experiment. (f) describes the potential sequence.

Potential steps experiments were carried out also for Co of various thickness. The applied potential was switched from -1.45V to -1.15V and was hereafter maintained under this potential control for 150sec. The purpose of this series of experiments is to determine the stability of the Co oxide layer in the range of peak (A_1).

Figure 3.12 depicts, for a Co(4.1ML)/Au(111) in contact with pH = 12 electrolytes, the impact of stepping the potential from -1.45V to -1.15V on the reflectivity (**Fig. 3.12.a**), $M(1Koe)$ (**Fig. 3.12.c**), $M_R/M(1Koe)$ (**Fig. 3.12.d**) and H_c (**Fig. 3.12.e**). **Fig. 3.12.f** illustrates the sequence of the potential steps. The inset **Fig. 3.12.b** is a zoom of the reflectivity from 55sec to 100sec. The magnetic properties reach saturation after typically ~10s after applying the potential step. They remain essentially unchanged for typically 140s at this potential indicating that the CoOH adlayer is rather stable for at least a few minutes.

Using these series of experiments, $M_R/M(1kOe)$ can be plotted versus Co thickness, as shown by **Fig. 3.13**. The solid curve and the dot curve presented on the figure indicate two different calculated curves (see **Chapter 2**). The first fitting gives the SRT thickness $t_{Co}^* \sim 4.25ML$, while as the second curve implies the $t_{Co}^* \sim 4.7ML$. Comparing to the critical thickness of H-covered surface ($t_{Co-H}^* \sim 1.75ML$), the formation of the -OH adlayer in the range of peak (A_1) enhances the perpendicular magnetic anisotropy (PMA).

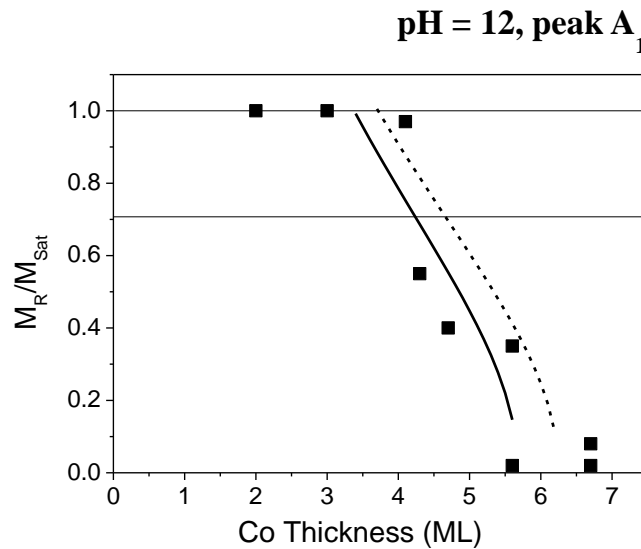
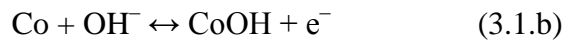
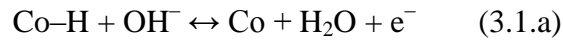


Fig. 3.13: M_R/M_{Sat} in the explored potential region in pH = 12 electrolyte as a function of Co thickness. The solid black line and dash black line represents two different fittings.

3.4.2. Discussion

a) Cobalt surface chemistry in peak A₁

In light of DFT calculations (section 3.2.2), we can write the following oxidation reaction taking place at the Co surface in the explored potential range:



This reaction scheme is different from the commonly admitted one yielding the formation of Co(OH)₂ layer and omitting the presence of the H layer [9, 12]. From this reaction and the calculated structures (**Fig. 3.4**), we may estimate the electric charge necessary for removing the H layer *and* forming the different Co hydroxide layers. The removal of the (1×1)-H adlayer necessitates 0.29 mC/cm² (considering an in-plane Co distance of $a = 2.5 \text{ \AA}$ and an atomic density of $1.85 \cdot 10^{15} \text{ cm}^{-2}$). The charge necessary for the formation of the (2×2)-OH adlayer equals 0.073 mC/cm², that of (6×6)-CoOH layer equals 0.2 mC/cm². Consequently, the *total* charge to remove the H adlayer *and* form the OH adlayer or the restructured (6×6)-CoOH layer is in the range 0.36–0.49 mC/cm². The total charge in the case of the formation of (5×5)-Co(OH)₂ layer equals 0.66 mC/cm².

The above charges may be compared with the experimentally measured anodic charge Q_{an} and cathodic charge Q_{cat} in **Fig. 3.9** measured under peaks A₁ and C₁. In order to integrate the charge, a baseline partly due to water decomposition should be at first extracted. We use the reflectivity as a criterion for the baseline choice. Indeed, the 1st order derivative of the reflectivity as a function of time dR/dt is well correlated with the voltammogram as shown in **Fig. 3.14.a**. Therefore, a good baseline correction should yield a nice overlap between the reflectivity and the voltammogram integral (**Fig. 3.14.b**). The absolute value of the integrated electric charge per unit electrode area of peak (A₁) Q_{an} is very close to that of peak (C₁) Q_{cat} and is equal to $Q_{an} = Q_{cat} = Q_0 = 0.4 \pm 0.02 \text{ mC/cm}^2$.

From the above estimate, we can exclude the formation of (5×5)-Co(OH)₂ layer because the required charge is significantly larger than measured. The value of Q_0 is consistent with the formation of a (2×2) OH adlayer or a (6×6)-CoOH layer. However, the second structure only is consistent with the periodic corrugation is observed in STM images [10, 11]. Therefore, the (6×6)-CoOH adlayer appears as the most plausible form of the Co oxide. This conclusion contrasts with previous works where the electric charge was assigned to the sole formation of the Co(OH)₂ layer [11].

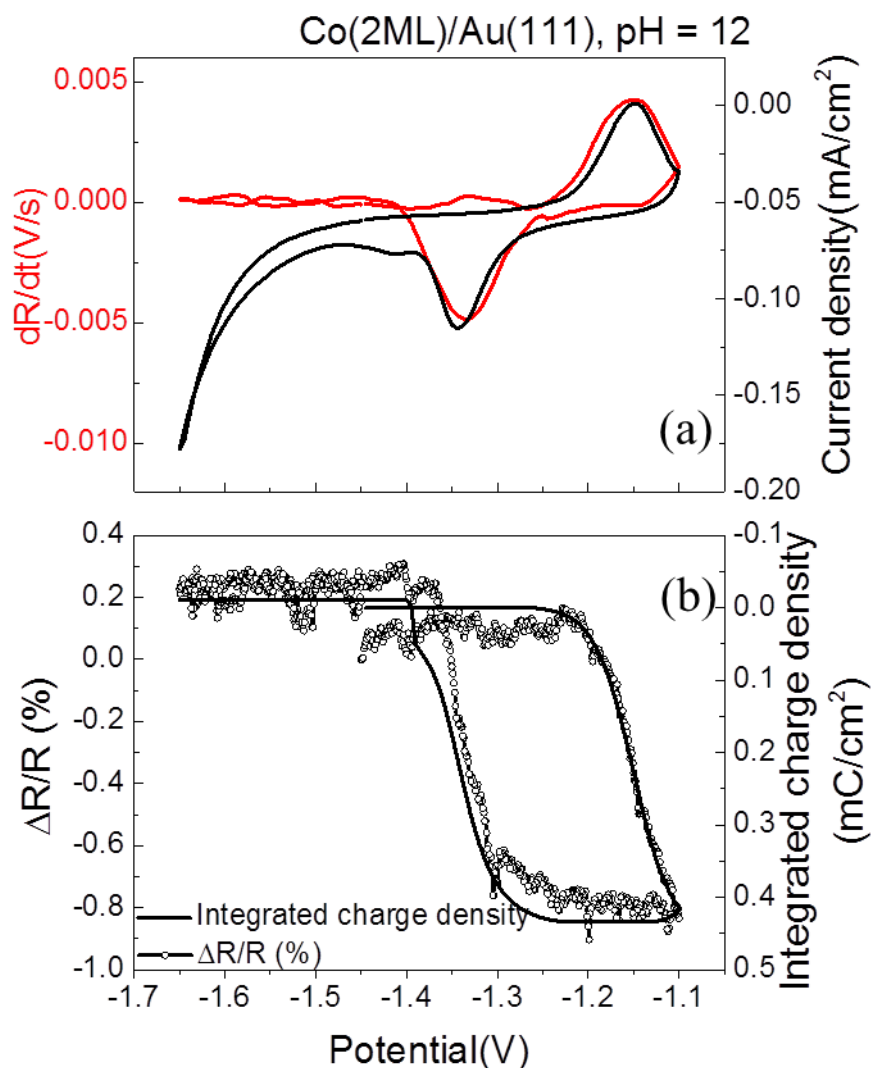


Fig. 3.14: (a) the 1st derivative of the reflectivity (red line, left y-axis) and the electrochemical current density for one Co(2.4ML)/Au(111) in contact with pH = 12 electrolyte; (b) the relative change of reflectivity with respect to that of -1.45V (line and open symbol, left y-axis) and the integrated charge density after baseline correction during the same potential sweeping.

As a consequence of the formation of the (6×6)-CoOH layer, which lattice parameter is much larger than that of the Co(0001) topmost Co atomic plane, surface roughening is anticipated upon electrochemical reduction of the surface. The reaction is indeed accompanied with a significant rearrangement of surface adatoms which is most probably at the origin of the small yet systematic difference between the first and subsequent voltammograms. The fact that Q_0 is independent of t_{Co} above 2 ML is consistent with a surface limited oxidation/reduction reaction in peaks (A₁) and (C₁). These observations are in very good agreement with those reported earlier on Co(0001) single crystals [11].

In **Fig. 3.14.b**, the integral of the electrochemical current (line and right y-axis) is plotted as a function of time as well as $\Delta R/R$ (open symbol and left y-axis) is plotted versus U . The good agreement between $\Delta R/R$ and the charge shows that these two measurements may be used in a complementary manner to estimate the potential dependence of relative oxide coverage, taking as reference the oxidation state of the surface at the positive limit of the voltammogram.

b) Oxide coverage dependence of the magnetic surface anisotropy

Figures 3.15.a-b display the variations of the magnetic properties as a function of the relative oxide coverage θ_{OH} , taking as a reference $\theta_{OH} = 1$ at $U = -1.08$ V. In the case of the 2 and 3 ML films, the remnant and the saturation magnetizations (respectively M_R and M_{Sat}) become equal above a critical coverage θ_{OH}^* , meaning that the sample is perfectly perpendicularly magnetized (see also $M - H$ plots in **Fig. 3.10**). One notices that the value of θ_{OH}^* is increasing with the Co thickness. In the case of 4.1 ML, a saturation of M_R and M_{Sat} is also reached at $\theta_{OH} \sim 0.8$. This film remains however essentially in plane magnetized since $M_R/M_{Sat} \leq 0.5$. In correspondence, the coercive field (H_c) increases and reaches a maximum around θ_{OH}^* . **Figure 3.15.a** evidences thus a complete SRT in-plane \rightarrow out-of-plane for the 2 ML and 3.1 ML thick films. The backward SRT (not shown) occurs upon oxide reduction. The reorientation of the magnetization easy axis upon oxidation is only partial if $t_{Co} \geq 4.1$ ML. The same changes of the Co magnetic properties as a function of θ_{OH} are reproducibly found upon subsequent oxidation/reduction cycles. It is worth noticing that M_R and $M(1KOe)$ slightly decrease as a function of θ_{OH} for $\theta_{OH} > \theta_{OH}^*$. This decrease is quasi-linear with θ_{OH} and is equivalent to $\sim 60\%$ of the magnetization of 1 ML of Co at $\theta_{OH} = 1$. It suggests the formation of a ferromagnetically dead layer upon surface oxidation. This dead layer would correspond to the entire (6 \times 6)-CoOH monolayer.

The above magnetic data, which are suggesting an oxide induced enhancement of the perpendicular magnetic anisotropy energy of the Co film, were analyzed using the model described in **Chapter 2**. The minimization of the magnetic anisotropy energy yields:

$$K_s = t_{Co} [2\pi M_s^2 - K_1 - 2K_2(1 - \cos^2\varphi) - HM_s/(2\cos\varphi)] \quad (3.2)$$

where $K_1 = 5.6 \cdot 10^6$ erg/cm³ and $K_2 = 1.5 \cdot 10^6$ erg/cm³ are the hcp Co magneto-crystalline anisotropy energies, K_s the interface anisotropy energy, $M_s = 1407$ emu/cm³ the Co magnetic moment, H is the applied magnetic field perpendicular to the surface, φ is the angle between

the magnetization and the surface normal, where $\cos \varphi = M_R/(\alpha^*M_S)$. The curves in **Fig. 3.15.a** yield directly $K_S \sim 0.46 \text{ erg/cm}^2$ at full oxide coverage. Since $K_S = K_S^{\text{Co-Au}} + K_S^{\text{Co-Ox}}$ and given the value of $K_S^{\text{Co-Au}} \sim +0.5 \text{ erg/cm}^2$ [13, 14], we obtain $K_S^{\text{Co-OH}} \sim 0 \text{ erg/cm}^2$ for $\theta_{OH} = 1$. This gives 0.3 erg/cm^2 increase with respect to the H covered Co surface (see **Chapter 2**). Equation 3.2 was used to determine K_S as a function of θ_{OH} , assuming that the volume anisotropy energy is not affected by the oxide formation (i.e., K_1 and K_2 are independent of the oxidation). We considered Co films that are sufficiently thick (7.8 ML) to remain in plane magnetized upon full surface oxidation. At negative bias, the thickness t_{Co} was taken equal to that of the initial Co film. Upon surface oxidation, we accounted for the progressive formation of the magnetic dead layer (t_{Co} is replaced by $t_{Co} - 0.6\theta_{OH}$ in Eq. 3.2). **Figure 3.15.c** shows, that K_S increases almost linearly with θ_{OH} , from $\sim 0.1 \text{ erg/cm}^2$ at $\theta_{OH} = 0$ and reaches a plateau $\sim 0.46 \text{ erg/cm}^2$ above θ_{OH}^* , which is consistent with the determination above at full oxide coverage. The overall increase in K_S is 0.36 erg/cm^2 when the Co surface changes from hydrogen- to full oxide- termination. Since $K_S = K_S^{\text{Co-Au}} + K_S^{\text{Co-OH}}$ and given the value of $K_S^{\text{Co-Au}} \sim +0.5 \text{ erg/cm}^2$, we obtain $K_S^{\text{Co-OH}} \sim 0 \text{ erg/cm}^2$ for $\theta_{OH} = 1$.

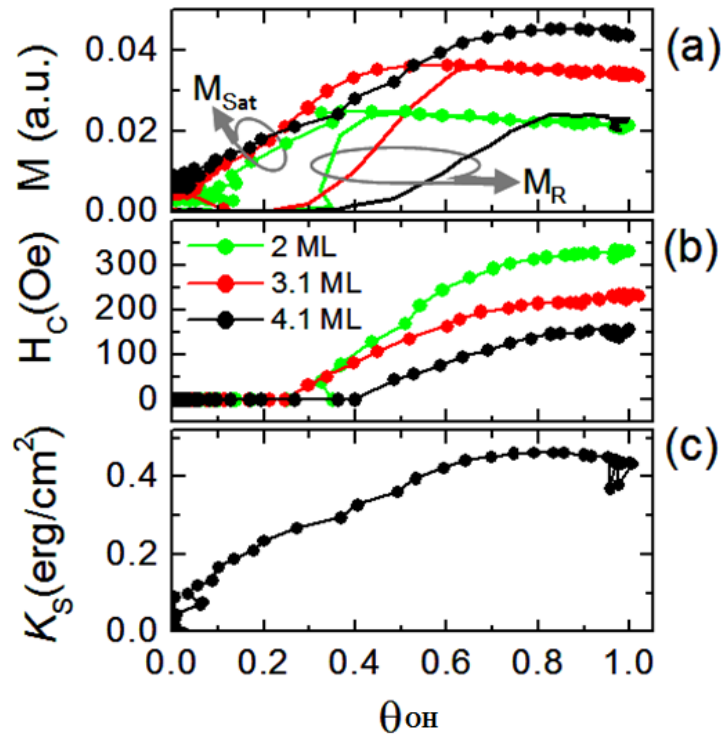


Fig. 3.15: Variations of (a) M_{sat} and M_R ; (b) H_c ; and (c) extrapolated K_S as a function of – OH coverage θ_{OH} for 2.1-ML (green line), 3.1-ML (red line) and 4.1-ML (black line) Co. The data in (c) correspond to a Co thickness of 7.8 ML.

3.4.3. Conclusion

To conclude this section, electrochemical characterizations and DFT calculations support the formation of a restructured (6×6)-CoOH layer at potentials corresponding to pre-oxide formation (i.e. in peak A_1 of **Fig. 3.3**). The process is reversible since one can reduce this adlayer by applying a sufficiently negative potential. The surface anisotropy energy K_S^{Co-OH} is ~ 0 erg/cm² at full OH-coverage, which is ~ 0.36 erg/cm² greater than on the H-terminated surface. As a result a reversible SRT may be observed with cobalt films thinner than 4 ML. The increase in K_S^{Co-OH} is almost proportional to OH coverage in initial stage of adlayer formation.

3.5. MAE of Co/Au(111) films upon Co(OH)₂ formation (peak A₂)

In this part, we investigate an extended potential range up to -0.45V and study the influence of further Co oxide growth on MAE.

3.5.1. Electrochemistry: results and discussion

Figure 3.16.a presents the variations of the voltammogram of a 5.3 ML – thick Co/Au(111) film in contact with the electrolyte of pH = 12 during three successive potential scans. The sweep starts at -1.45 V towards positive potential (see arrows). In addition to peak (A_1) corresponding to pre-oxidation at $U \sim -1.16$ V, further oxidation occurs until -0.45V, symbolized as peak (A_2). In this case, cathodic peak denoted as (C_2) shifts to $U \sim -1.5$ V. The current increase at $U < -1.56$ V corresponds to water decomposition. The cyclic voltammograms for the three successive scans differ from each other. It implies that redox reactions corresponding to the formation of Co(OH)₂ are not reversible. **Figure 3.16.b** presents the corresponding relative change of the sample reflectivity ($\Delta R/R$) with respect to that measured at -1.45 V (the 1st scan). It decreases with the oxidation reactions (peaks (A_1) and (A_2)) and re-increases within cathodic peak (C_2). $\Delta R/R$ reduces $\sim 8\%$ in the range of peak (A_2) until -0.45V as compared to $\sim 1\%$ in the range of peak (A_1). The reflectivity does not vary when the potential is swept back from -0.45V to -1.34V. It implies that no further oxide layer is formed.

The symbols shown in **Fig. 3.16.b** *i*, *f* and *s* represents the Co initial state before any redox reactions, the final state after one complete scan, and the state corresponding to saturated oxidation reaction at -0.45 V. The fact that $\Delta R/R$ measured at -1.45 V tends to decrease upon repeated potential cycles suggests that some Co was dissolved.

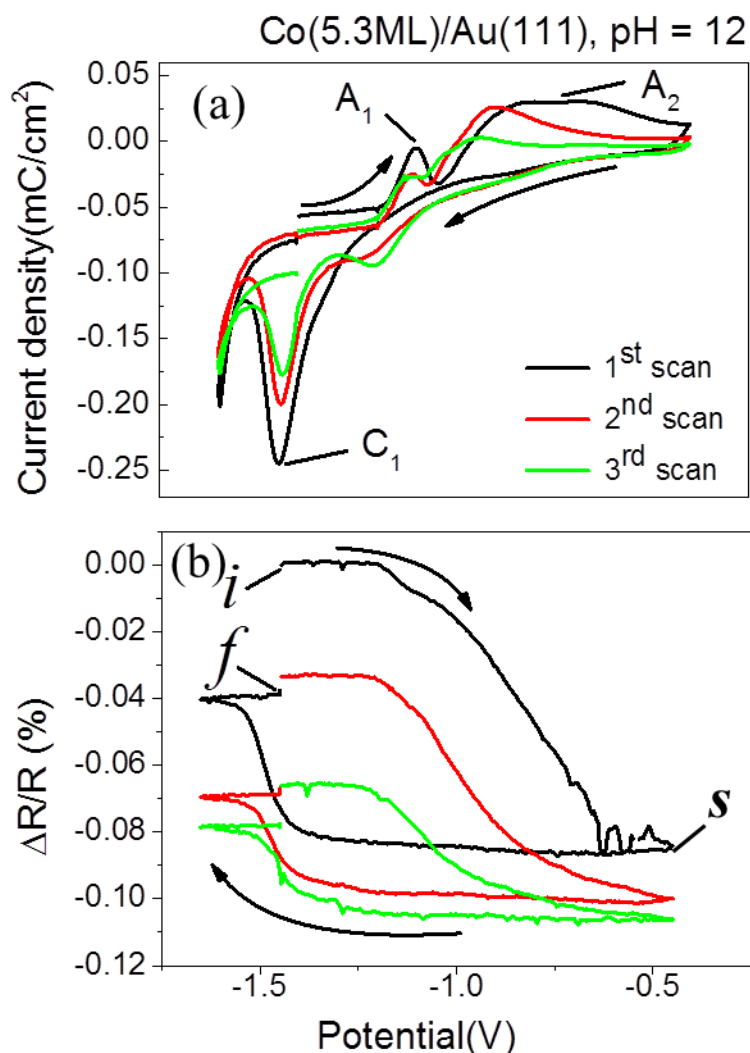


Fig. 3.16: (a) electrochemical current density; and (b) the relative change of reflectivity $\Delta R/R$ with respect to that at -1.45 V for a Co (5.3ML) layer in contact with $\text{pH} = 12$ electrolyte during three successive potential scans (1st scan : black line; 2nd scan: red line and 3rd scan: green line) between -1.65 V and -0.45 V. The symbols *i*, *s* and *f* indicate different states, which are described in the text.

The reactions that take place in this potential range can be written as:

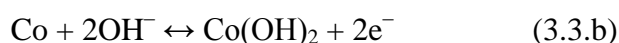


Figure 3.17 schematically illustrates the Co electrode structure during one scan from -1.65V to -0.45V. The initial state is a Co hydrogenated surface. The initial thickness t_{Co}^i is determined by the deposition time. When the potential is scanned from -1.25V to -0.45V, $Co(OH)_2$ is formed on top of the Co layer. t_{Co}^{ox} represents the *equivalent* thickness of Co metallic layers which are oxidized. $Co(OH)_2$ is slightly soluble at pH=12. Therefore, the $Co(OH)_2$ layer is partly dissolved. When the oxidation reaches its saturated state s , the quantity of Co atoms oxidized to $Co(OH)_2$ attains its maximum. At this state, the $Co(OH)_2$ layer lying on top have a thickness denoted as $t_{Co(OH)_2}$, and the thickness of remaining Co metallic layers is symbolized as t_{Co}^s . Afterwards, the reflectivity measurements indicate that no further oxidation reaction takes place. From -1.34V to -1.52V, the remaining $Co(OH)_2$ layers are reduced to Co. t_{Co}^r represents the thickness of Co obtained from the reduction of $Co(OH)_2$. Co of the final state f has a thickness of t_{Co}^f . The thickness of the dissolved Co is indicated by t_{Co}^{dis} .

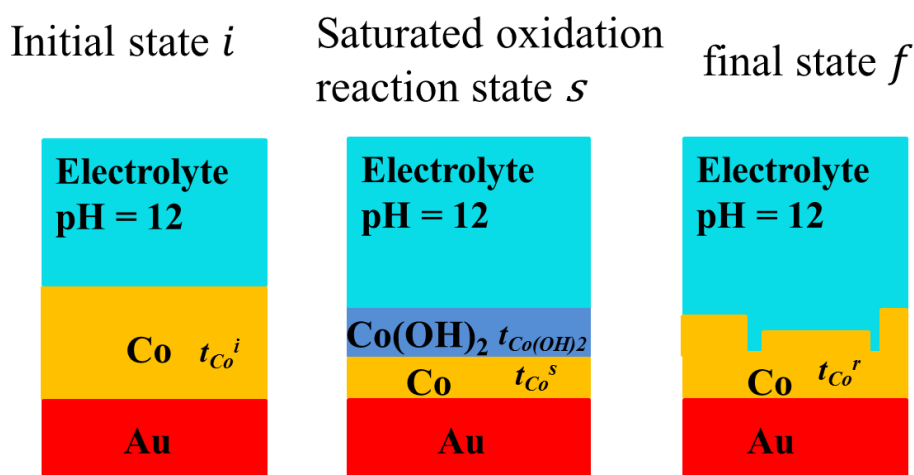


Fig. 3.17: Simplified scheme of the variations of chemical compositions corresponding to initial state i , oxide saturated state s and final state f .

As discussed above in the potential range of peak (A_1), the integration of the electrochemical current density as a function of time scan allow us to determine the variation of the charge density Q as a function of potential during the potential sweep. We use the same method as for the oxidation in the range of peak (A_1) to define the baseline. Again a good agreement is established between the 1st order derivative of reflectivity as a function of time dR/dt and the variation of the electrochemical current density (see **Fig. 3.18.a**). It validates the choice of the baseline in the range of peak (A_2). **Fig. 3.18.b** demonstrates that the integrated charge as a function of time is in consistent with $\Delta R/R$.

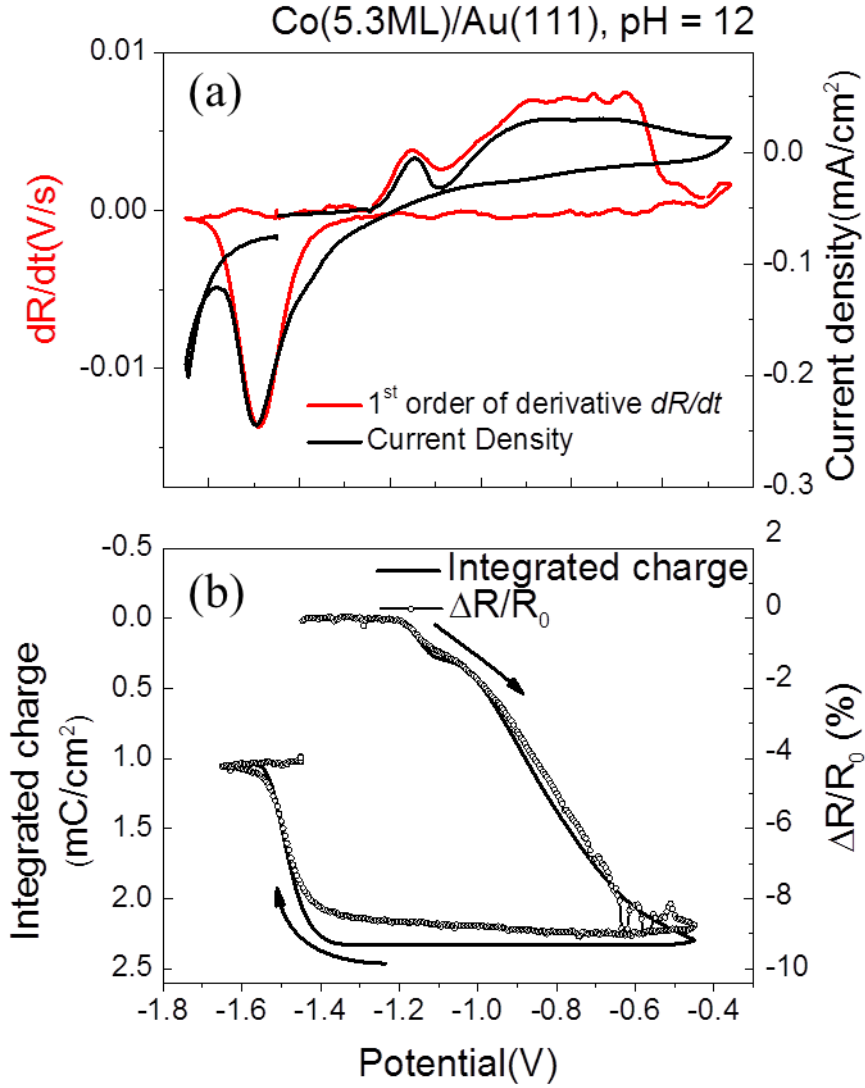


Fig. 3.18: (a) The 1st order derivative of the reflectivity as a function of time (red line, left y-axis) and electrochemical current density (black line, right y-axis); (b) the integrated charge as a function of time (black line, left y-axis) together with the changes of the relative reflectivity $\Delta R/R$ (black line and open symbols, right y-axis). The sample is a Co(5.3ML) layer during the 1st potential scan up to -0.45V in $\text{pH} = 12$ electrolyte.

The integrated anodic charge densities Q_{an} tells us in the state s when the oxidation reaction is saturated, the *average* thickness of metallic Co which is oxidized to $\text{Co}(\text{OH})_2$, denoted as $t_{\text{Co}}^{ox(s)}$ (in ML):

$$t_{\text{Co}}^{ox(s)} = \frac{Q_{an}}{0.59} \quad (3.4)$$

Since 0.59 mC/cm^2 are necessary to transform a Co monolayer into $\text{Co}(\text{OH})_2$, the integrated cathodic charge Q_{cat} (positive value) gives us the thickness of Co via reduction of

the $\text{Co}(\text{OH})_2$ layer which didn't undergo dissolution during the potential cycle. Thus, the thickness of the final state t_{Co}^f (ML) is then defined as:

$$t_{\text{Co}}^f = t_{\text{Co}}^i - \frac{Q_{\text{an}} - Q_{\text{cat}}}{0.59} \quad (3.5)$$

and the thickness of the dissolved Co $t_{\text{Co}}^{\text{dis}(1)}$ (ML) is:

$$t_{\text{Co}}^{\text{dis}(1)} = \frac{Q_{\text{an}} - Q_{\text{cat}}}{0.59} \quad (3.6)$$

The quantitative interpretation of $\Delta R/R$ during the potential sweep is rather complicated because one has to take into account the buildup of the Co oxide layer which optical properties are unknown. However, the DFT calculations predict that the most stable structure for $U < -1.3\text{V}$ is (1×1) Co-H structure. The surface chemistry is thus the same at the negative end of the potential cycle. Consequently, the reflectivity difference at the beginning and at the end of a potential cycle can be employed to determine the quantity of the dissolved Co. In **chapter 2**, the linear correlation between t_{Co} and $(R_{\text{dep}} - R_0)/R_0$ is presented. R_{dep} indicates the reflectivity in the end of Co deposition with a thickness as t_{Co} ; R_0 represents the original reflectivity before deposition. The determination of R_0 is given in **Chapter 2**. Thus, we can use this relation to determine t_{Co}^f and $t_{\text{Co}}^{\text{dis}(2)}$ using the reflectivity of the initial state i R_i and the final state f R_f .

$$t_{\text{Co}}^{\text{dis}(2)} = \frac{R_i - R_f}{R_{\text{dep}} - R_0} t_{\text{Co}}^i \quad (3.7)$$

Figure 3.19.a displays the integrated anodic charge density Q_{an} , cathodic charge density Q_{cat} , the charge density difference $\Delta Q = Q_{\text{an}} - Q_{\text{cat}}$, as a function of the number of the successive potential cycles in the case of a Co(8.5ML)/Au(111). Open round symbols (right axis) presents the relative reflectivity changes. Notice the good correlation between ΔQ and the relative reflectivity. **Fig. 3.19.b** presents the thickness of the $\text{Co}(\text{OH})_2$ layer using Q_{an} , the dissolved thickness $t_{\text{Co}}^{\text{dis}(1)}$ using ΔQ and that using the reflectivity $t_{\text{Co}}^{\text{dis}(2)}$. Again, $t_{\text{Co}}^{\text{dis}(1)}$ and $t_{\text{Co}}^{\text{dis}(2)}$ are very similar indicating that the determined thickness of dissolved Co during one potential cycle is reliable.

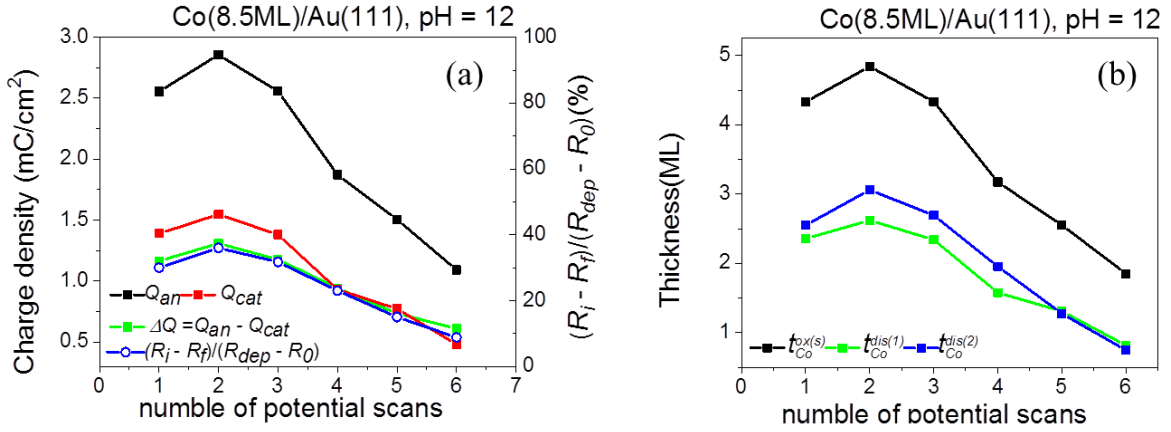


Fig. 3.19: (a) anodic charge density Q_{an} (black line and square, left y-axis), cathodic charge density Q_{cat} (red line and square, left y-axis), the difference between anodic and cathodic charge density ΔQ (green line and square, left y-axis), and $(R_i - R_f)/(R_{dep} - R_0)$ (blue line and open circle, right y-axis); and (b) the oxide layer thickness determined from Q_{an} (black line and square), the dissolved thickness determined by ΔQ (green line and square) and via the changing of reflectivity (blue line and square) for Co(8.5ML)/Au(111) in pH = 12 electrolyte during six successive potential scans between -1.65V and -0.45V.

During the first three potential scans, $t_{Co}^{ox(s)} \sim 4.3-4.7$ ML, $t_{Co}^{dis(1)} \sim t_{Co}^{dis(2)} \sim 2.5-3$ ML. Consequently, we learn that during each cycle, ~ 4.5 ML of Co are oxidized and ~ 2.5 ML of Co are dissolved. $t_{Co}^{ox(s)}$ and $t_{Co}^{dis(1)}$ remain quasi-constant during the first three cycles because the initial Co thickness (8.5 ML) is large enough to allow the oxidation of 4.5 ML after the dissolution of 2.5ML per cycle. For the following potential cycles, the Co thickness left is less than 4 ML explaining the drop of $t_{Co}^{ox(s)}$ and $t_{Co}^{dis(1)}$.

Due to the irreversibility during the potential scans in the range of peak (A_2), only results of the 1st scan are presented and discussed in the following. **Fig. 3.20.a** shows Q_{an} , Q_{cat} , and ΔQ during the 1st scan versus the initial Co thickness t_{Co}^i . Analogous to **Fig. 3.19**, **Fig. 3.20.b** illustrates the calculated corresponding $t_{Co}^{ox(s)}$, $t_{Co}^{dis(1)}$ and $t_{Co}^{dis(2)}$ as a function of the initial thickness t_{Co}^i . Q_{an} increases with t_{Co}^i until ~ 4.1 ML, then it becomes independent of the initial Co thickness. In **Fig. 3.20.b**, we observe a similar behavior for $t_{Co}^{ox(s)}$ with a saturation at ~ 4 ML. The dissolved thickness also saturates at around 2 ML irrespective to the initial Co thickness. These results are in good agreement with that of **Fig. 3.19**.

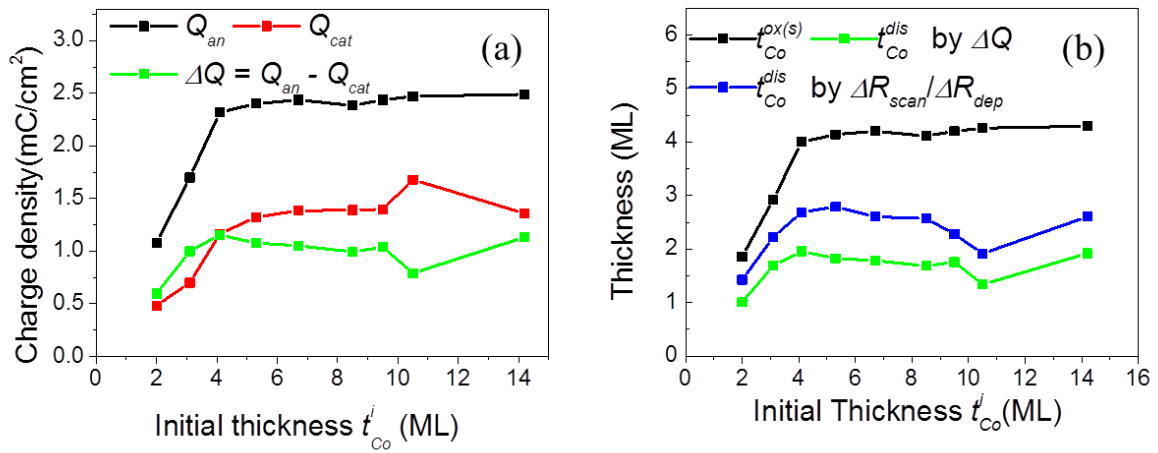


Fig. 3.20: (a) anodic Q_{an} (black line and square), cathodic Q_{cat} (red line and square) and difference ΔQ (green line and square) charge density as a function of the initial Co thickness during the 1st potential scans in pH = 12 electrolyte; (b) the associated oxidized $t_{Co}^{ox(s)}$ (black line and square); and dissolved Co thickness calculated by ΔQ (green line and square) and the changing of reflectivity (blue line and square).

Figure 3.21 sketches in details the variation of the Co thickness, the chemical composition and the surface chemistry during one potential scan.

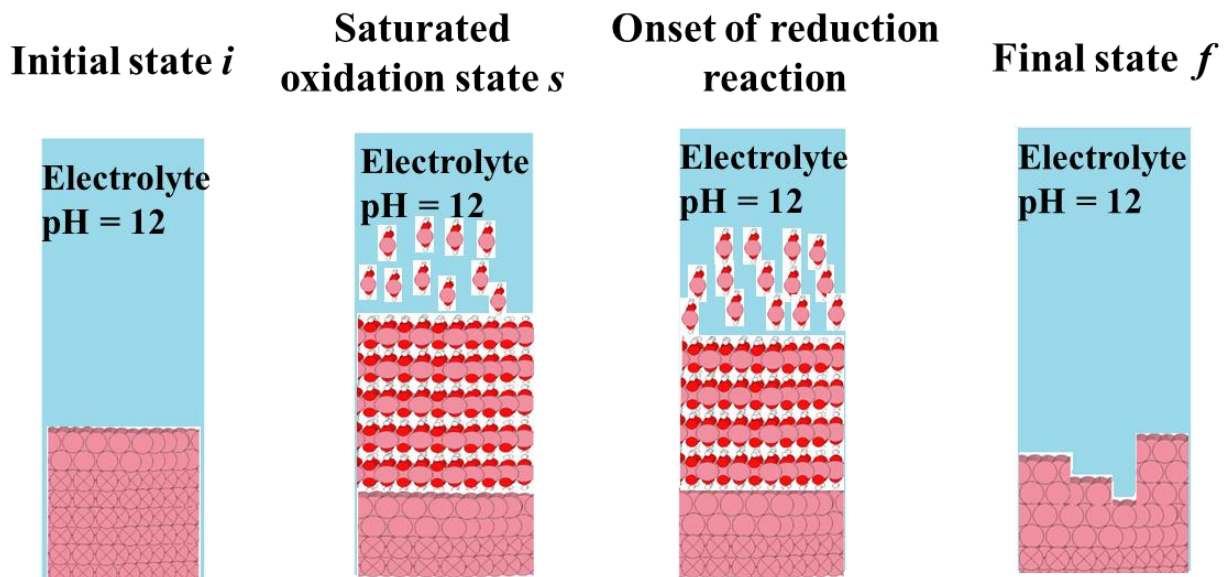


Fig. 3.21: Sketch of the changes of chemical composition and structure during one potential cycle in pH 12 electrolyte.

3.5.2. Magnetic properties of Co layers in the range of peak (A₂): results and discussion

Due to the irreversibility of reflectivity and dissolution of cobalt during the potential scans between -1.65V and -0.45V, only the results of magnetic properties regarding to the 1st sweeps are presented below and will be further discussed.

Figure 3.22 (inset) shows $M - H$ curves at selected potentials during the 1st potential scan between -1.65V and -0.45V in pH = 12 electrolyte. The 6.7 ML film is in-plane magnetized (linear and reversible $M - H$) for $U < -1.25$ V (**Fig. 3.22.a and b**). The formation of -OH adlayer in the range of peak (A₁) tilts the magnetization from in-plane to slightly out-of-plan orientation (**Fig. 3.22.c**). One monolayer of -OH on the surface is not sufficient to achieve perfectly perpendicular anisotropy, unlike the case of 3.1ML-Co presented in **Fig. 3.10**.

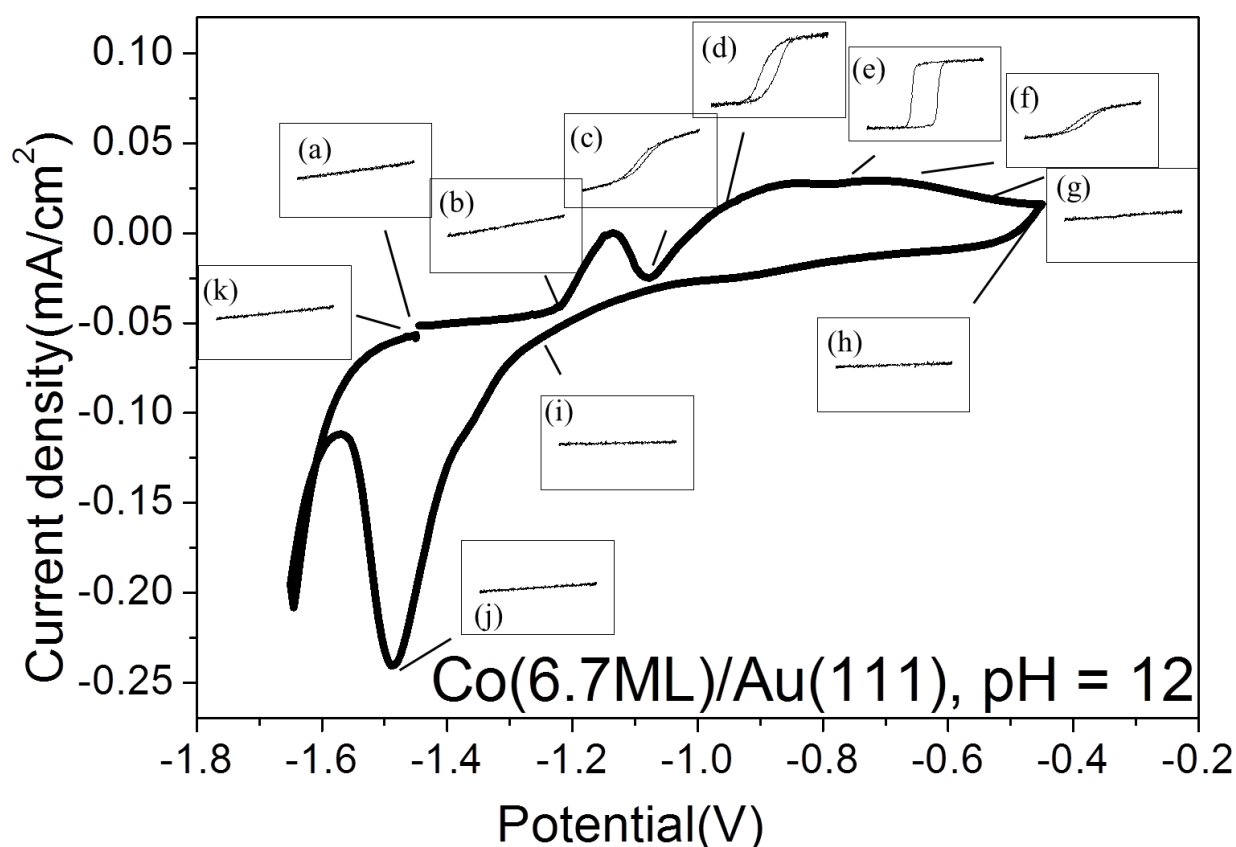


Fig. 3.22: $M-H$ curves at selected potentials for Co (6.7ML)/Au(111) during the 1st potential scan in pH = 12 electrolyte. The scan rate is 20mV/s.

The perpendicular anisotropy continues to increase with the formation of Co(OH)_2 oxide layer (**Fig.3.22.d**) until the potential sweeps to -0.8V . The anisotropy turns to be strictly perpendicular to the surface at -0.8V with a coercive field of 260 Oe (**Fig. 3.22.e**). Further oxidation, however, favors again the in-plane magnetization. The hysteresis loop becomes linear and reversible. The slope of the $M - H$ curve reduces when the potential scans to more positive region (**Fig. 3.22.f - h**). **Fig. 3.22.i** and **j** illustrate the $M - H$ curves at the onset and the peak of cathodic peak (C_2). The slope of $M - H$ curve at the final state (**Fig. 3.22.k**) is smaller than that of the initial state (**Fig. 3.22.a**).

Figure 3.23 displays the variations of $M(1\text{KOe})$ (**Fig. 3.23.a**), $M_R/M(1\text{KOe})$ (**Fig. 3.26.b**) and the electrochemical currents (**Fig. 3.26.c**) versus the applied potential during the 1st potential scan for Co(3.1ML) (black line), Co(5.3ML) (red line), Co(6.7ML) (green line) and Co(9.5ML) (blue line) in contact with $\text{pH} = 12$ electrolyte.

For Co layers thinner than 4ML, the magnetization is strictly perpendicular in the peak (A_1) range. At the beginning of peak (A_2), $M(1\text{kOe})$ or $M_R/M(1\text{kOe})$ are unaltered. In contrast, H_c increases (not shown), indicating a further increase of the PMA. For thicker films which remain in-plane magnetized in the peak (A_1) range, undergo large changes in the peak (A_2) range which are clearly visible on $M(1\text{kOe})$ or $M_R/M(1\text{kOe})$. For example, $M_R/M(1\text{KOe})$ reaches unity for Co up to 6.7 ML. For the Co(9.5ML)/Au(111) film this ratio is only 0.34. This enhancement of PMA is however only a transient phenomenon. Upon completion of the formation of Co(OH)_2 in plane magnetization is observed. The fact that Co oxide is dissolving complicates the interpretation of the magnetic behavior. It is worth noticing that the thicker the Co layer the more positive the potential where the PMA is maximum, in other words, the thicker the Co(OH)_2 layer necessary to enhance the PMA.

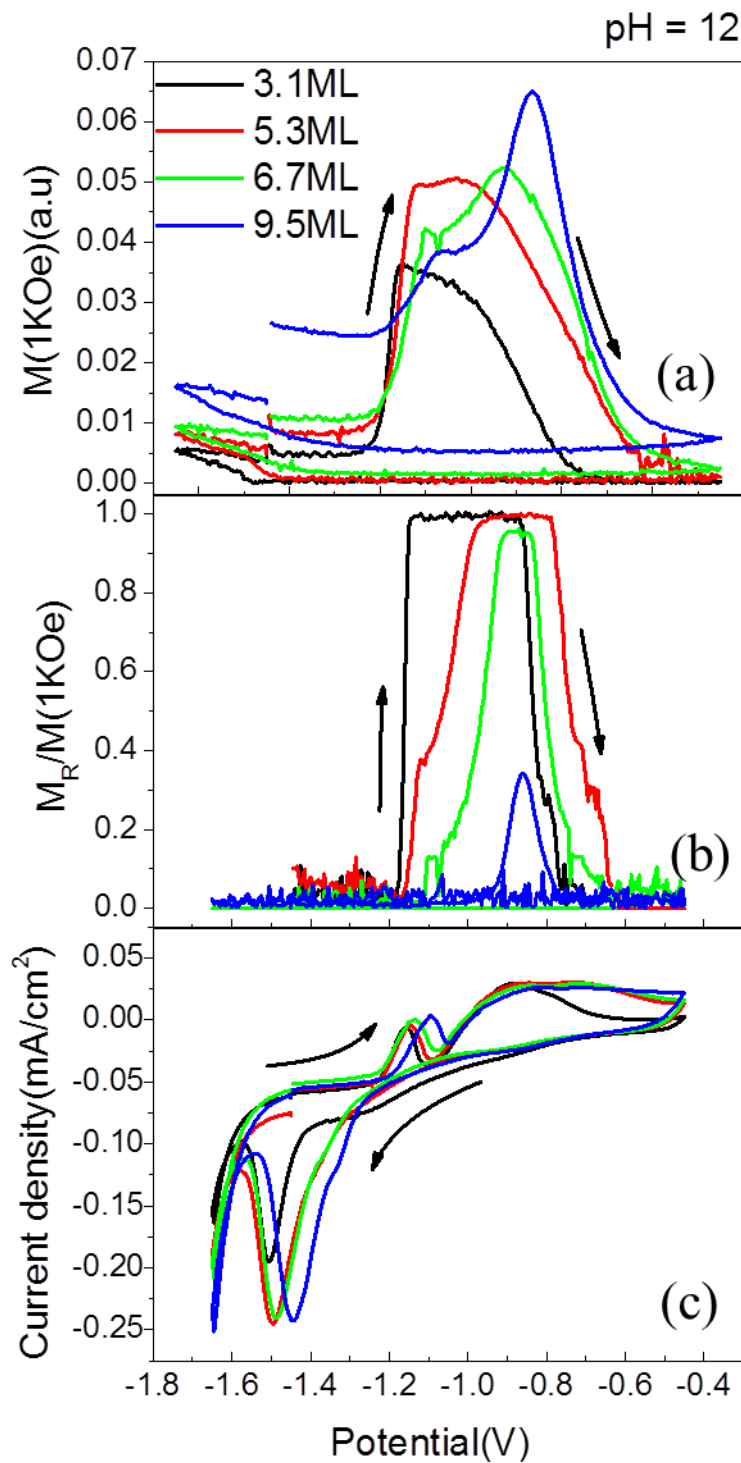


Fig. 3.23: (a) $M(1kOe)$; (b) $M_R/M(1kOe)$; and (c) the electrochemical current density during the first scans for 3.1-ML (black line), 5.3-ML (red line), 6.7-ML (green line) and 9.5-ML (blue line) Co layer. The scan rate is 10mV/s.

One may try to estimate the $Co(OH)_2$ thickness at maximum PMA. For this purpose, we will use the integrated charge density Q as a function of time which allows us to calculate the thickness of oxidized Co films t_{Co}^{ox} and the actual thickness of remaining Co metallic

layers underneath t_{Co}^a . **Fig. 3.24.a** presents M_R/M_{Sat} as a function of t_{Co}^{ox} during the 1st potential scans for Co of different initial thickness t_{Co}^i . The interesting observation is that oxidizing more than 2–2.5 ML of Co has a negative impact on the layer PMA for all film thicknesses.

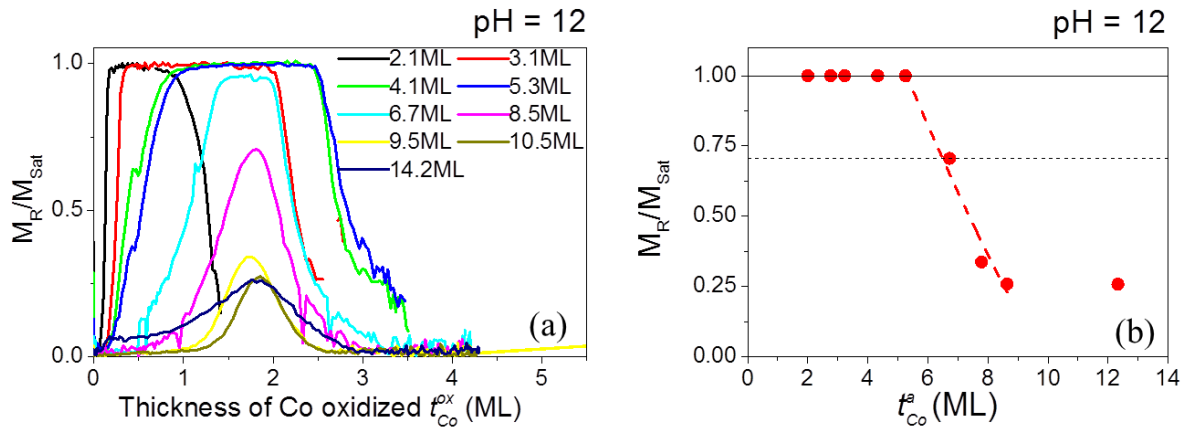


Fig. 3.24: M_R/M_{Sat} of the intermediate state as a function of thickness of (a) oxidized Co for Co of different initial thickness t_{Co}^i ; (b) of actual remaining Co thickness t_{Co}^a .

Furthermore, M_R/M_{Sat} as a function of the actual thickness of Co metallic layers t_{Co}^a for this intermediary state is illustrated in **Fig. 3.24.b**. It is important to clarify precisely how this plot is constructed: for each curve in **Fig. 3.24.a**, we determined the coordinates (x_{max} , y_{max}) of the point where M_R/M_{Sat} reaches its maximum starting from the origin; this point is reported in **Fig. 3.24.b** with the same ordinate y_{max} and with an abscise corresponding to the initial Co thickness minus x_{max} . **Fig. 3.24.b** resembles a typical M_R/M_{Sat} versus magnetic layer thickness with a critical thickness of 6.5 ML corresponding to the 8.5ML Co film covered by the equivalent of ~2 ML of Co oxidized into $Co(OH)_2$ (i.e., ~3 ML of $Co(OH)_2$). Since the critical thickness in the case of (6×6)-CoOH layer is ~4ML, one may understand the increase of the Co film PMA in peak (A_2) as due to the increase of the surface magnetic anisotropy energy K_S upon changing the surface chemistry from the (6×6)-CoOH to the (5×5)- $Co(OH)_2$. However, if we consider that the formation of the $Co(OH)_2$ layer is uniform on the Co the surface, ~1ML is enough to completely modify K_S . Instead, we observe that 3 ML of $Co(OH)_2$ are necessary to increase the PMA for Co films thicker than ~7ML and that **Fig. 3.24.b** is consistent with a typical thickness driven SRT. Thus, the increase of the PMA of the film may be partly due to the reduction of the Co film thickness due to the surface oxidation. Even though these explanations may appear satisfactory, it is not clear why the PMA drops upon

further oxidation in peak (A₂) instead of continuing to increase since the Co thickness continue decreasing. More investigations are necessary to unravel such apparent discrepancy.

Analogous to the analysis of K_S^{Co-OH} discussed above in the range of peak (A₁), $K_S^{CoOx(int)}$ ("int" for intermediate) can be calculated in the same way using $t_{Co}^{int(*)} \sim 7ML$. One obtains $K_S \sim 0.74 \text{ erg cm}^{-2}$. Given that $K_S^{Co-Au} \sim 0.5 \text{ erg cm}^{-2}$, $K_S^{CoOx(int)} \sim 0.24 \text{ erg cm}^{-2}$. In comparison, K_S^{Co-H} is $\sim -0.36 \text{ erg cm}^{-2}$ and K_S^{Co-OH} is $\sim 0 \text{ erg cm}^{-2}$. As described in **Chapter 2**, we can also determine K_S variations as a function of the Co surface chemistry using Co layers thicker than the critical thickness. The fitting of $K_{eff} * t_{Co}$ vs t_{Co} of 9.5ML-, 10.5ML-, and 14.2ML Co films yields K_S and α the proportionality coefficient between M_{Sat} and t_{Co} . We can estimate K_S for each surface chemistry state: the initial state i , the state when the $-OH$ coverage θ_{OH} equals to 1; the intermediary state in the range of peak (A₂) when the out-of-plane anisotropy is mostly enhanced; the state s with saturated oxidation reaction, and the final state f after one complete potential cycle. The thicknesses of remaining cobalt thin films are denoted respectively as t_{Co}^i ; t_{Co}^{-OH} , t_{Co}^{int} , t_{Co}^s and t_{Co}^f . The effective anisotropy coefficients are presented by K_{eff}^i ; K_{eff}^{-OH} , K_{eff}^{int} , K_{eff}^s and K_{eff}^f . The corresponding surface anisotropy coefficients are symbolized likely by K_s^i ; K_s^{-OH} , K_s^{int} , K_s^s and K_s^f . **Table 3.1** gives the calculated t_{Co}^a , K_{eff} and ΔK_{eff} of each state.

	9.5ML	10.5ML	14.2ML
α	0.025	0.027	0.02
$t_{Co}^{-OH}(ML)$	8.92	9.9	13.9
$t_{Co}^{int}(ML)$	7.84	8.64	12.33
$t_{Co}^s(ML)$	5.44	6.49	9.98
$t_{Co}^f(ML)$	7.85	9.14	12.24
$K_{eff}^i(erg \cdot cm^{-3})$	$-9.5 \cdot 10^6$	$-9.36 \cdot 10^6$	$-8.5 \cdot 10^6$
$K_{eff}^{-OH}(erg \cdot cm^{-3})$	$-7.15 \cdot 10^6$	$-7.5 \cdot 10^6$	$-6.9 \cdot 10^6$
$K_{eff}^{int}(erg \cdot cm^{-3})$	$-5.49 \cdot 10^6$	$-5.46 \cdot 10^6$	$-5.38 \cdot 10^6$
$K_{eff}^s(erg \cdot cm^{-3})$	$-16.5 \cdot 10^6$	$-16.4 \cdot 10^6$	$-13.3 \cdot 10^6$
$K_{eff}^f(erg \cdot cm^{-3})$	$-13 \cdot 10^6$	$-12.6 \cdot 10^6$	$-10.9 \cdot 10^6$
$\Delta K_{eff}^{-OH}(erg \cdot cm^{-3})$	$2.15 \cdot 10^6$	$1.86 \cdot 10^6$	$1.6 \cdot 10^6$
$\Delta K_{eff}^{int}(erg \cdot cm^{-3})$	$4.01 \cdot 10^6$	$3.9 \cdot 10^6$	$3.12 \cdot 10^6$
$\Delta K_{eff}^s(erg \cdot cm^{-3})$	$-7 \cdot 10^6$	$-7.04 \cdot 10^6$	$-4.8 \cdot 10^6$
$\Delta K_{eff}^f(erg \cdot cm^{-3})$	$-3.5 \cdot 10^6$	$-2.24 \cdot 10^6$	$-2.4 \cdot 10^6$

Table 3.1: t_{Co}^a , K_{eff} and ΔK_{eff} of each different state

Assuming that the volume anisotropy does not change, the variation of the effective anisotropy ΔK_{eff} is only due to the modification of the surface magnetic anisotropy. The variation of the surface magnetic anisotropy for each state is presented by **Table 3.2**. It is

interesting to notice that the obtained ΔK_S values of each state are very close for the different Co thicknesses. In addition, they are consistent with those obtained above using the critical thickness.

	9.5ML	10.5ML	14.2ML
$\Delta K_S^{-OH}(\text{erg} \cdot \text{cm}^{-2})$	0.45	0.40	0.454
$\Delta K_S^{int}(\text{erg} \cdot \text{cm}^{-2})$	0.72	0.78	0.73
$\Delta K_S^s(\text{erg} \cdot \text{cm}^{-2})$	-0.54	-0.73	-0.75
$\Delta K_S^f(\text{erg} \cdot \text{cm}^{-2})$	-0.46	-0.52	-0.52

Table 3.2: K_S of each state assuming that the anisotropy change is only due to the surface magnetic anisotropy.

3.6. Conclusions

In this chapter, we investigated the influence of the different Co surface oxidation states on the magnetic anisotropy energy of Co films electrodeposited on Au/Si(111). We presented a procedure to exchange the electrolyte from acidic to basic while keeping the Co layer and its surface unaltered. We studied the first oxidation step and compared our electrochemical and optical results with DFT calculations. We demonstrate that in this case, the Co surface is covered by (6×6)-CoOH layer. We show that this oxidation state is completely reversible upon bringing the potential in the oxide reduction range. Our magnetic measurements show that the CoOH layer increases the surface magnetic anisotropy by $\sim 0.4 \text{ erg/cm}^2$ with respect to that of the H-covered surface. We also investigated the second oxidation step and show, with the help of DFT and electrochemistry, that it yields to the formation of a (5×5)-Co(OH)₂ layer on top of Co. The reflectivity measurements clearly showed that this second step is accompanied by some dissolution. We could quantify this phenomenon and demonstrate that each potential cycle induces the oxidation of 4 ML of Co and the dissolution of 2 ML. Our

magnetic measurements showed an additional increase of the surface magnetic anisotropy energy up to $0.6\text{erg}/\text{cm}^2$ with respect to that of the H-covered Co surface.

3.7. References

- [1] Y. Shiota, T. Maruyama, T. Nozaki, T. Shinjo, M. Shiraishi, Y. Suzuki, Voltage-Assisted Magnetization Switching in Ultrathin Fe₈₀Co₂₀ Alloy Layers, *Applied Physics Express*, 2 (2009).
- [2] D. Chiba, S. Fukami, K. Shimamura, N. Ishiwata, K. Kobayashi, T. Ono, Electrical control of the ferromagnetic phase transition in cobalt at room temperature, *Nature Materials*, 10 (2011) 853-856.
- [3] Oleinik, II, E.Y. Tsymbal, D.G. Pettifor, Structural and electronic properties of Co/Al₂O₃/Co magnetic tunnel junction from first principles, *Physical Review B*, 62 (2000) 3952-3959.
- [4] A. Manchon, C. Ducruet, L. Lombard, S. Auffret, B. Rodmacq, B. Dieny, S. Pizzini, J. Vogel, V. Uhler, M. Hochstrasser, G. Panaccione, Analysis of oxygen induced anisotropy crossover in Pt/Co/MOx trilayers, *Journal of Applied Physics*, 104 (2008).
- [5] B. Rodmacq, S. Auffret, B. Dieny, S. Monso, P. Boyer, Crossovers from in-plane to perpendicular anisotropy in magnetic tunnel junctions as a function of the barrier degree of oxidation, *Journal of Applied Physics*, 93 (2003) 7513-7515.
- [6] M. Pourbaix, *Atlas of Electrochemical Equilibria in Aqueous Solutions*, Pergamon Press, Oxford, 1966.
- [7] K. Kudo, *An ellipsometric study of passivating films on cobalt in neutral borate solution, passivity of metals*, Electrochem. Soc. Inc., Princeton, New Jersey 1978.
- [8] K.E. Heusler, *Passivity and breakdown of passivity of nickel, cobalt, and chromium*, Electrochem. Soc. Inc., Princeton, New Jersey, 1978.
- [9] T. Ohtsuka, N. Sato, Anodic oxide film on cobalt in weakly alkaline solution, *Journal of Electroanalytical Chemistry and Interfacial Electrochemistry*, 147 (1983) 167-179.
- [10] S. Ando, T. Suzuki, K. Itaya, In situ electrochemical scanning tunneling microscopy of Co(0001) single crystal electrodes in acidic solution, *Journal of Electroanalytical Chemistry*, 431 (1997) 277-284.

- [11] A. Foelske, J. Kunze, H.H. Strehblow, Initial stages of hydroxide formation and its reduction on Co(0001) studied by in situ STM and XPS in 0.1 M NaOH, *Surface Science*, 554 (2004) 10-24.
- [12] N. Di, J. Kubal, Z. Zeng, J. Greeley, F. Maroun, P. Allongue, Influence of controlled surface oxidation on the magnetic anisotropy of Co ultrathin films, *Applied Physics Letters*, 106 (2015) 122405.
- [13] N. Tournier, A.P. Engelhardt, F. Maroun, P. Allongue, Influence of the surface chemistry on the electric-field control of the magnetization of ultrathin films, *Physical Review B*, 86 (2012).
- [14] L. Cagnon, T. Devolder, R. Cortes, A. Morrone, J.E. Schmidt, C. Chappert, P. Allongue, Enhanced interface perpendicular magnetic anisotropy in electrodeposited Co/Au(111) layers, *Physical Review B*, 63 (2001).

Chapter 4 Influence of surface chemistry on the MAE and MEC of Co/Au(111) ultrathin films

4.1. Introduction

As explained in **Chapter 1**, the atomic and chemical local environment of surface atoms of a ferromagnetic layer is expected to have an impact on the magnetic surface anisotropy. There are several experimental results, all obtained in the UHV, showing that the MAE of an ultrathin film may be varied upon molecular adsorption. In some instances, the MAE varies due to adsorption induced structural modifications (ex: H/Ni) [1]. Pure electronic effect can also lead to MAE variations (CO or rubrene on Co) [2-3].

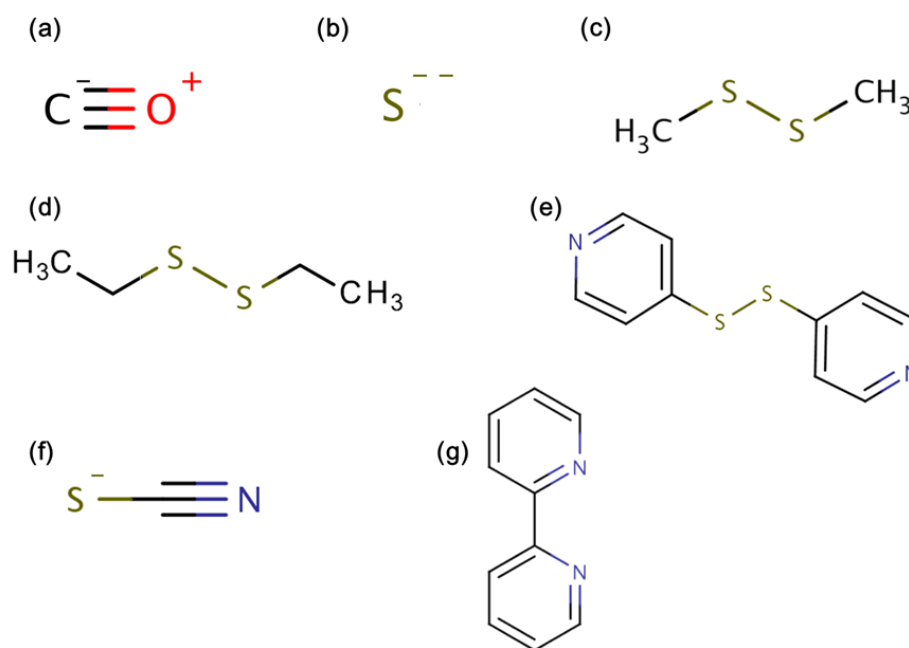


Fig. 4.1: Structure of the molecular precursor used in this work to modify the cobalt surface: a) carbon monoxide (CO); (b) sulfide (S²⁻); (c) dimethyl disulfide (DMS); (d) diethyl disulfide (DES); (e) 4,4'-dithiodipyridine (DTPy); (f) thiocyanate (SCN⁻); (g) 2,2'-bipyridine (Py-Py).

In this chapter, we consider the adsorption of molecules on Co/Au(111) layers from solution containing the precursors shown in **Fig. 4.1** which all contain a chemical function that is prone to interact with the cobalt surface. The resulting surface linkages Co-X linkages, with X = H, O, C, S and N are schematically presented in **Fig. 4.2**. Molecules containing a sulfide bridge split in two in contact with the metal surface. In the case of SPy, in analogy with Au [4], we infer that the Co-S bond energy is stronger than that of the Co-N bond. For the S-linkage, different kinds of adlayers are considered to vary the charge transfer Co-molecule and the molecule length.

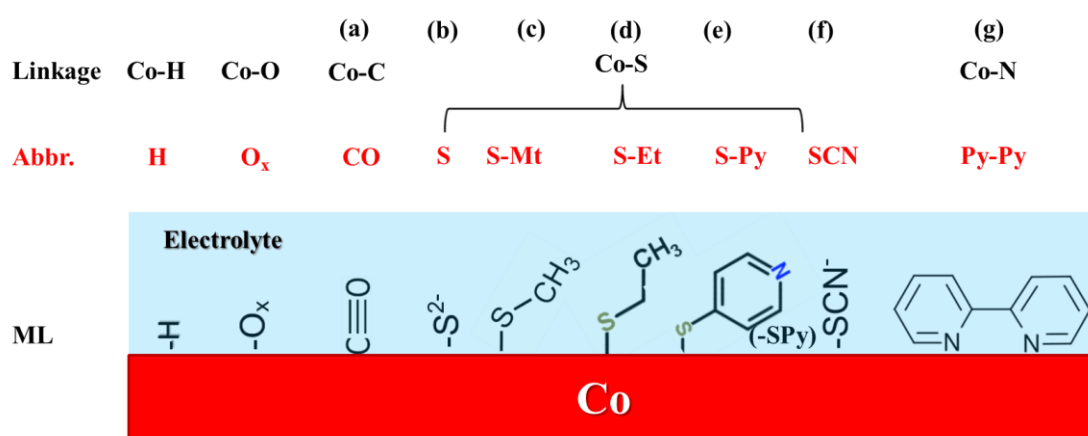


Fig. 4.2: Schematic structure of the cobalt surface termination after exposure to solution containing the precursors (a-g) presented in Fig.4.1. The abbreviation used in the text to design the different monolayers and the corresponding linkage Co-X, with X = H, O, C, S and N are given. Labels S-Mt, S-Et, S-Py and Py-Py stand for methyl, ethyl, pyridine thiol MLs and bipyridyl MLs. See text.

The above scheme of the interface is justified by past literature about the adsorption of molecules with similar chemical functions on metal surfaces. We give below a brief survey for each molecule with emphasis on Co surfaces. The influence of molecular adsorption on the magnetic properties of cobalt will be introduced in the discussion section.

The adsorption of carbon monoxide on transition metal surfaces has been extensively investigated, in relation with catalysis, on various noble metals and iron group metals [5, 6].

According to Blyholder [7] there is a donation of CO σ lone pair electrons to unoccupied metal surface orbitals and a back donation of metal electrons to CO unoccupied adsorbate π^* orbitals. It is generally concluded that CO is able to bond to the surface at low symmetry sites (on-top) as well as high symmetry sites (bridge, threefold, or fourfold) [8]. In the particular case of cobalt, the structure of chemisorbed CO monolayers on Co(0001) single crystal surfaces have been reported [9, 10]. LEED and surface potential data [10] show that the structure of the adlayer depends on temperature. Essentially a $(\sqrt{3}\times\sqrt{3})$ -CO structure with CO $R30^\circ$ adsorbed on top sites are found by XPS at room temperature. Lowering the sample temperature below 200 K, increases the CO coverage to 0.58 $((2\sqrt{3}\times 2\sqrt{3})$ -2CO $R30^\circ$ adlayer). In the electrolytic environment a dense CO adlayer forms (coverage ~ 0.6) at room temperature. Though no structural characterization was reported, a $(2\sqrt{3}\times 2\sqrt{3})$ -2CO adlayer structure is plausible on Co(0001) in contact with an electrolyte. The formation of such a CO-adlayer may be accompanied with the adsorption of alkali cations used for preparing the electrolyte.

Alkanethiols ($\text{CH}_3(\text{CH}_2)_n\text{SH}$) and dialkyl disulfides ($\text{CH}_3(\text{CH}_2)_n\text{S-S}(\text{CH}_2)_n\text{CH}_3$) on Au(111) surfaces have been the most widely studied systems due to the formation of stable and high ordering, self-assembled monolayers [11 - 13]. One advantage of disulfides is that they are not as susceptible to oxidation as thiols [13]. The results of high-resolution electron energy loss spectroscopy (HREELS), thermal desorption spectroscopy (TDS), and x-ray photoelectron spectroscopy experiments (XPS) concluded that S-S bond of dialkyl disulfides are cleaved at room temperature and the molecule is adsorbed as thiolate [14, 15]. HREELS and DFT calculations prove that the dimethyl disulfide is adsorbed on Au(111) as methylthiolate, and the sulfur atom is located at the off-centered bridge site towards the hollow sites, tilted from the surface normal by 53° [12]. Diethyl disulfide is adsorbed as ethylthiolate and located at the hollow sites [13]. Thiols adsorption has been also reported on other metals (Co, Ni and Fe) [16-21]. Hoertz *et al.* [20] showed that for the evaporated Ni and Co thin films prepared by electroreduction process, high surface coverage self-assembly

monolayers (SAMs) with low surface-oxide can be achieved with thiols. The extent of SAM formation on electroreduced films is comparable to what has been observed for SAMs/Au. For example, Chen *et al.* reported adsorption of methyl thiolate on the Co/Mo(110) surface [22]. Hence, it can be suggested that the dialkyl disulfide in acid electrolytes splits to form alkanethiol which eventually adsorbs on the surface with S atom.

In the case of Py-Py, surface enhanced Raman spectroscopy conducted by the group of Xie *et al.* [23] demonstrated that pyridine interacts strongly with Co surface at negative potentials (-1.5V vs MSE) and the signal starts decreasing at -1.72V vs MSE due to hydrogen evolution reaction. The group of Andrade *et al.* [24] shows that the adsorption of pyridine on Co is also potential dependent. The adsorption is stronger at -1.72V vs MSE than at -1.2V vs MSE (nearly no signal). However, the Co surface investigated by Xie *et al.* and Andrade *et al.* is very rough, whereas we have a flat 2D surface structure. Study about the adsorption of bipyridyl on Co is very limited. On the contrary, previous studies about the adsorption of bipyridyl and pyridine on Au have been carried out by a number of groups. They prove that desorption begins at negative potential ($\sim -1.2\text{V}$ vs MSE) [25]. In-situ STM studies [26] about Py-Py on gold surface in acid solution suggests an interaction via protonated (N-H)⁺ - group through electrostatic interaction.

The results of this chapter are reported in two parts. The first part deals with the dependence of MAE on surface chemistry, using the precursors in **Fig. 4.1**. We will also compare the data with those obtained in previous chapters 2 (H-terminated Co) and 3 (OH-terminated Co). In the second part, a systematic voltage dependent study is performed to investigate the MEC as a function of all of the surface chemistries. The last section of this chapter is a general discussion of the results.

4.2. Experimental methods

The Co/Au(111) layers are deposited and stabilized as previously described in **Chapter 2**. As will be described below, molecular adsorption was performed by exposing the as grown film to a solution containing the various precursors (see **Fig. 4.1**).

- For CO adsorption, we used an electrolyte of pH 3.5 saturated with CO (gas bubbling). The sample potential was -1.15V.

- The adsorption of S^{2-} and SCN^- was conducted using 1 mM Na_2S or $KSCN$ solution in 0.1M K_2SO_4 + 1mM KCl + 1mM H_2SO_4 pH ~ 4; Monolayers of thiol S-Mt, S-Et and S-Py were obtained in different solutions because of the poor solubility K_{SP} , of the precursor in water while they are quite soluble in ethanol. Therefore, 1 mM solution in mixed ethanol – water system (volume 7:3) was used.

- For Py-Py adsorption, a solution containing 1mM Py-Py + 0.1M K_2SO_4 + 1mM KCl and the pH was adjusted to ~ 4 – 4.5 with H_2SO_4 . At this pH, one of the two ring nitrogen atoms is protonated ($pK_{a1} = -0.20$, $pK_{a2} = 4.37$) [25]. This solution is circulated at -1.25V.

Electrolyte exchange from acidic to alkaline was performed at the sample's electrode potential of -1.35V.

4.3. Results: Impact of surface chemistry on MAE

The procedure to adsorb molecules on Co films is performed under potential control to control the interface structure and avoid any Co dissolution or oxidation. The procedure involves several exchanges of solutions after Co deposition so as to reach the situation where the modified Co film is in contact with a molecule-free supporting electrolyte.

Figure 4.3 describes the entire procedure in the case of the DTPy. From top to bottom, the different panels show the time dependence of $M(1000 Oe)$ (panel a), of the ratio $M_R/M(1000Oe)$ (panel b), of the coercive field H_c and of the relative reflectivity $\Delta R/R_0$. Panel (f) gives the potential applied to the sample. The time sequence is divided in several phases (I

to V in this instance).

- Phase I corresponds to the deposition of a 4.2 ML film. The evolution of the magnetic properties is in close agreement with those reported in Chapter 2.

- During Phase II the supporting electrolyte is injected into the flow cell to decrease the Co^{2+} concentration down to $\sim \mu\text{M}$ range. The DTPy solution of pH 4 is then injected to obtain a SPy terminated Co surface.

- Phase III is ended when the parameters $M(1000 \text{ Oe})$, $M_R/M(1000 \text{ Oe})$ and H_c have reached their saturation values.

- In phase IV, the supporting electrolyte is again injected to remove the excess of DTPy in solution. At the end the Co films is therefore covered by a SPy monolayer and is in contact with the supporting electrolyte of pH 3.5, allowing MEC measurements.

- To perform MEC measurements in alkaline solutions, the electrolyte was exchanged with the supporting electrolyte of pH 12 (Phase V). During phases II-IV, the potential is kept at -1.2 V and at -1.35 V prior to switch to Phase V. Phases IV and V correspond to suitable conditions to perform MEC measurements (see section 4.4).

As explained in the introduction, DTPy adsorbs on the Co surface by cleavage of the S-S bond which leads to a Co-SPy monolayer. After only 10 seconds of DTPy solution circulation, one observes that $M(1000 \text{ Oe})$ (panel a) increases and reaches a plateau. See also zoom in panels (f). At the same time the ratio $M_R/M(1000 \text{ Oe})$ (panels b,g) increases from zero to reach unity and the coercive field H_c also reaches a plateau value of $\sim 450\text{Oe}$ (panels c,g). It should be noted that $\Delta R/R_0$ stays constant with time from the end of the deposition (i.e. $t = 70\text{s}$) up to phase V. This is an experimental proof that the layer thickness stays constant.

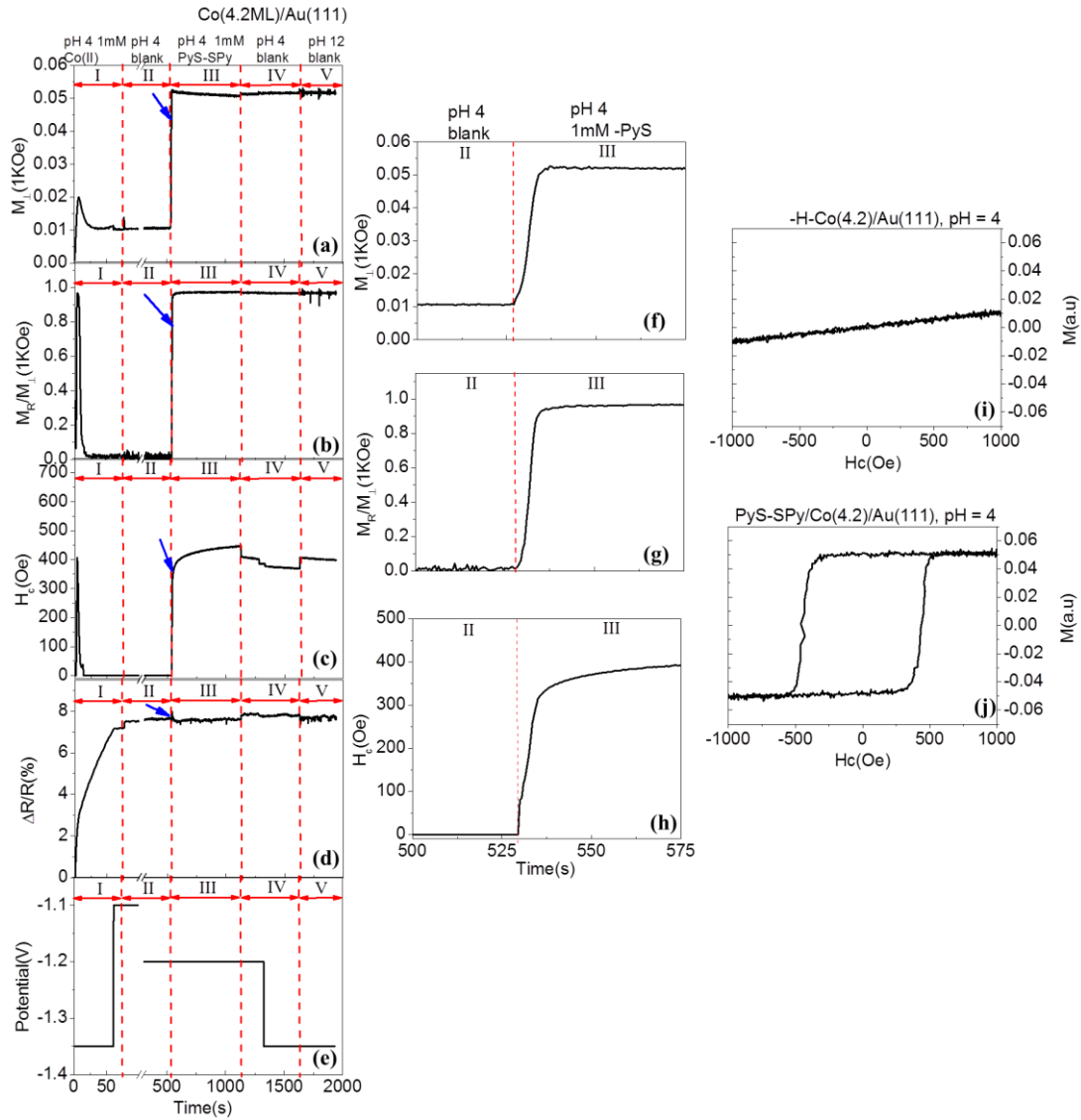


Fig.4.3: Influence of SPy adsorption on the magnetic properties of a 4.2-ML thick Co/Au(111) layer deposited in phase I. Panels (a) shows $M(1kOe)$; (b) $M_R/M(1kOe)$; (c) H_c ; (d) $\Delta R/R$. Phase II corresponds to the circulation of the supporting electrolyte to eliminate the Co^{2+} cations; Phase III corresponds to the adsorption of SPy in a solution of pH $\sim 3.5-4$; Phase IV and V correspond to the exchange of the solution with the supporting electrolyte of pH ~ 4 and pH ~ 12 respectively. (f), (g) and (h) are the zooms between region II and region III, as indicated by the blue arrows. (i) and (j) are the $M-H$ curves at the end of Phase II (H-covered surface) and Phase III (SPy covered surface).

Therefore all the modifications of the magnetic properties observed in **Fig. 4.3** must be assigned to the molecular adsorption. Obviously the magnetic state of the film must depend on the surface coverage. The behavior observed in **Fig. 4.3** corresponds in fact to a SRT from in plane (an as deposited 4.2 ML film is in plane magnetized, see Chapter 2) to out of plane as

the adsorbate coverage increases. Here we only focus on the final state of the system, when the adsorbate coverage is at its maximum. This coverage was not determined in this work. We can only assume that it is close to its maximum since we circulated the DTPy solution for a sufficient long period of time to reach plateau values for $M(1000\text{ Oe})$, M_R/M_{Sat} and H_c .

In the following, adsorption of $-\text{CO}$ and Py-Py will be briefly described.

In the case of $-\text{CO}$ on Co, **Fig.4.4** presents a typical behavior. After depositing 4.6-ML Co (end of region I), the hysteresis loop is linear (**Fig.4.4.(f)**). The circulation of CO saturated electrolyte (pH ~ 4) in the cell yields an increase of $M(1\text{KOe})$ from 0.017 to 0.051a.u, of $M_R/M(1\text{KOe})$ from 0 to ~ 1 , and of H_c from 0 to $\sim 200\text{Oe}$. These changes are gradual and take place on the scale of $\sim 100\text{s}$. The reflectivity remains constant, indicating that the Co layer is stable. At the end of region II, the $M-H$ curve (**Fig.4.4.(g)**) becomes strictly square.

Figure 4.4.(a')-(e') describes the reflectivity and magnetic properties for a $-\text{CO}$ dosed 4.8ML-Co upon transfer in an alkaline electrolyte after shifting the potential from -1.15V to -1.45V. The variation observed at 10s resulted from the potential step in region III is due to MEC, which will be discussed later. The associated changes of the reflectivity are measurable but very small ($< 0.2\%$). When the electrolyte is transferred to pH ~ 12 electrolyte at an electrode potential of -1.45V, the main changes are M_{Sat} increase by 5%, H_c increase by $\sim 25\%$, and $\Delta R/R$ increase by $\sim 0.4\%$. The changes observed at 110s upon switching the potential from -1.45V to -1.15V in region IV are also due to MEC.

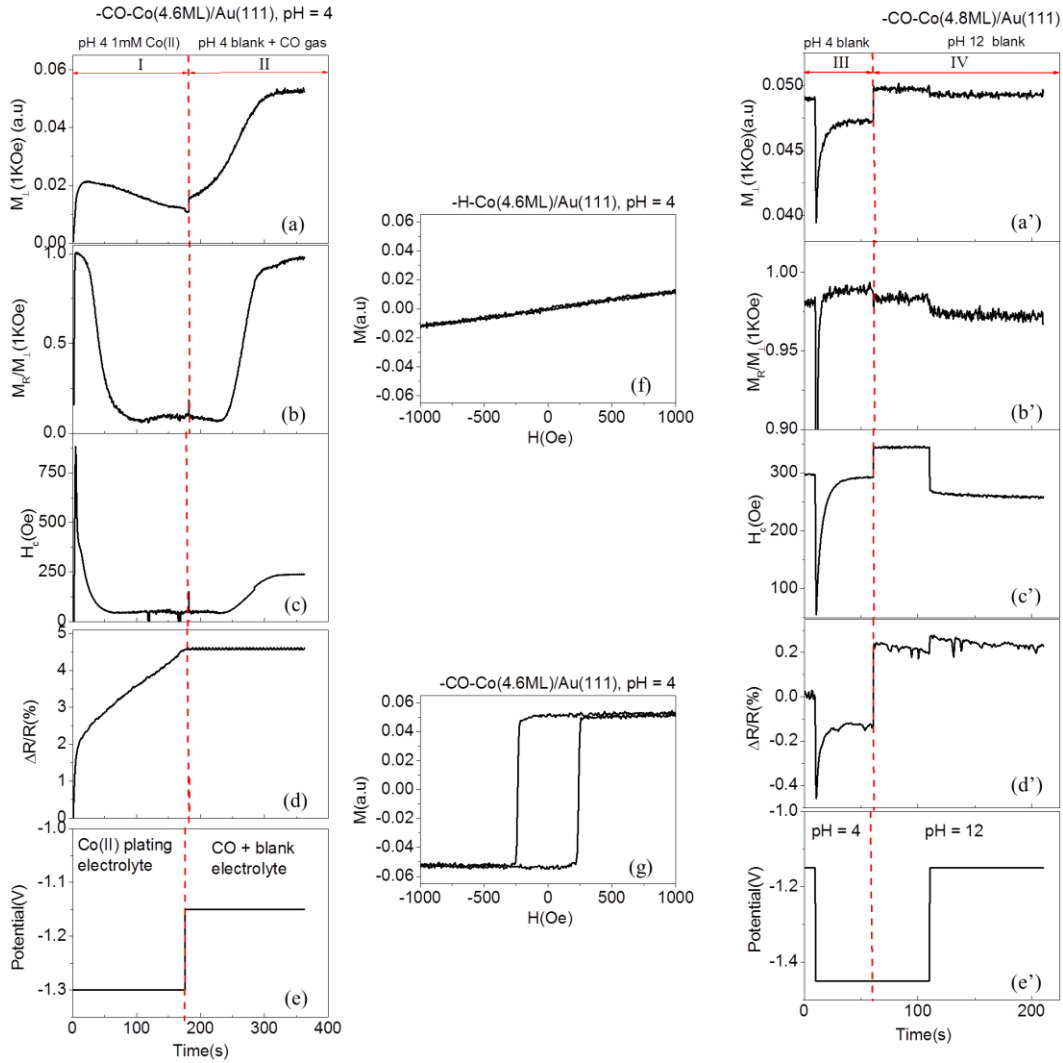


Fig. 4.4: (a) $M(1KOe)$; (b) $M_R/M(1KOe)$; (c) H_c ; (d) $\Delta R/R_0$ and (e) applied potentials during 4.6-ML Co deposition and $-CO$ adsorption. Region I indicates the Co deposition in a pH ~ 3.5 -4 1mM Co(II) plating electrolyte; region II corresponds to adsorption of $-CO$ in a pH ~ 3.5 – 4 blank electrolyte saturated with CO gas. (f) and (g) M - H curves at the end of region I and of region II respectively. (a') $M(1KOe)$; (b') $M_R/M(1KOe)$; (c') H_c ; (d') $\Delta R/R_0$ and (e') applied potentials for a $-CO$ dosed 4.8-ML Co in an acid (region III) and alkaline (region IV) blank electrolyte.

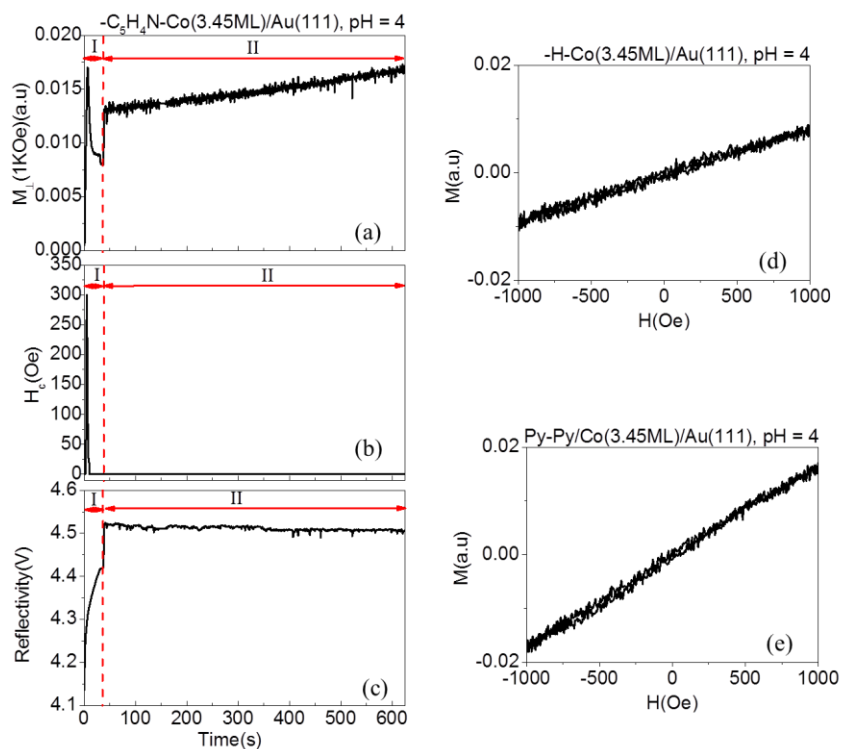


Fig. 4.5: (a) $M(1\text{KOe})$; (b) H_c ; (c) reflectivity during Co deposition and Py-Py adsorption. Region I indicates the Co deposition in a pH ~ 3.5-4 1mM Co(II) plating electrolyte; region II corresponds to adsorption of Py-Py in a pH ~ 3.5 – 4 1mM Py-Py containing electrolyte. (f) and (e) M - H curves at the end of region I and of region II respectively.

Figure 4.5 presents a typical behavior for the adsorption of bipyridyl. At the end of 3.45-ML Co deposition (region I), the thin film is in-plane magnetized. Region II describes the reflectivity and magnetic properties in an acidic 1mM Py-Py electrolyte. **Fig. 4.5.(d)** and **(e)** depicts the M - H curves corresponding to the end of region I and the end of region II after several hours of Py-Py electrolyte flow. In both cases, the M - H curve is linear but the slope is ~ 2 times larger at the end of region II. However, it is not clear whether this change is due to the MAE increase or to MOKE electrolyte signal drift after several hours of electrolyte circulation. Consequently, it is not possible to conclude whether Py-Py adsorbs on Co in these conditions, and if it is the case, whether it has an effect on the magnetic properties.

For each molecular precursor, the similar experiments described above (**Fig. 4.3-Fig. 4.5**) were repeated with Co layers of variable thicknesses to measure the magnetization plots M - H shown in **Fig. 4.6**. Films thicker than 2ML are only considered here (except for the as

prepared H-terminated film) because it is very difficult to perfectly stabilize Co film thinner than 2ML during the electrolyte transfer procedure. The data in **Figure 4.6** reveal that a SRT from out of plane to in plane occurs for all surface chemistries since square $M-H$ plots are measured below a critical thickness t^* and reversible plots are measured above t^* . This is the standard behavior in case of interface induced PMA. The interesting point in **Fig. 4.6** is the surface chemistry dependence of t^* . One may conclude that these variations are essentially related to the surface chemistry if one neglects the variations of K_S^{Co-Au} from sample to sample. From **Fig. 4.6**, we can conclude that K_S^{Co-MOL} increases in the order Co-H < Co-OH < Co-CO ~Co-S.

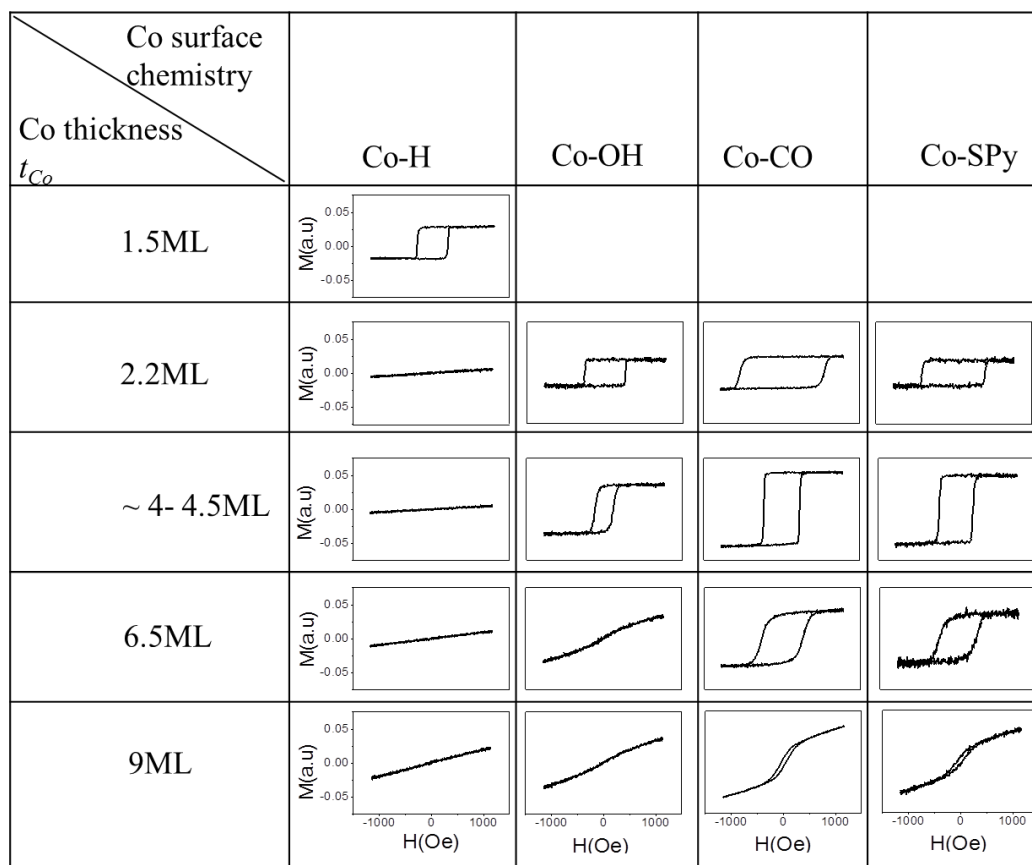


Fig. 4.6: $M-H$ curves for Co of different thickness covered by different molecular layers.

A quantitative determination of K_S^{Co-MOL} may be obtained by plotting the thickness dependence of M_R/M_{Sat} as a function of Co thickness for each surface chemistry. The experimental data (symbols) are plotted in **Fig. 4.7**. The solid curves in this figure are

calculated using Eq. 2.13, with the Co bulk values for K_1 , K_2 and the magnetic moment per atom (see chapter 2). The data for H and OH-terminated surfaces are taken from chapters 2 and 3. One sees that the data points for S^{2-} , SCH_3 overlap within the experimental error. This indicates that the major influence of the molecule layer on the Co film magnetic anisotropy is introduced by the molecule anchoring function. The values of t^* and K_S^{Co-MOL} are given in **Table 4.2**, which will be presented in the discussion section.

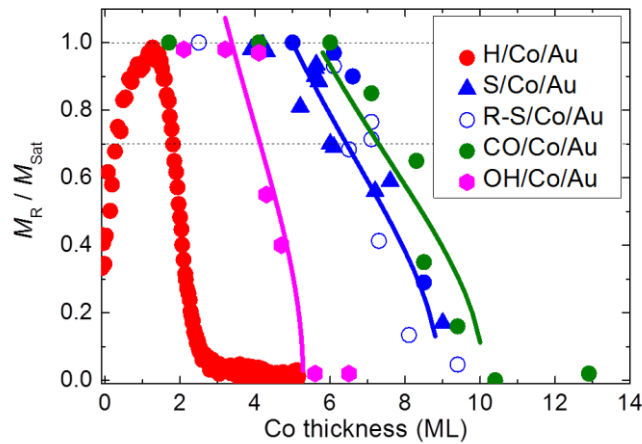


Fig.4.7: M_R/M_{Sat} as a function of t_{Co} for Co covered by different molecular layers. Symbols are experimental data. Solid lines are calculated (see text for explanation).

Figure 4.8 displays the coercive field H_c as a function of Co thickness t_{Co} for different molecular layers. The solid symbols correspond to a strictly perpendicularly magnetized film with $M_R/M_{Sat} = 1$. Hollow symbols correspond to films with tilted or in plane magnetization easy axis (i.e. $M_R/M_{Sat} < 1$). Solid lines are fits of the data for each surface linkage according to the law $C_1/t_{Co} + C_2$ law, where C_1 and C_2 are constants. The values of C_1 and C_2 depend on the molecular layer. They are reported in **Table 4.1.a** and **Table 4.1.b**.

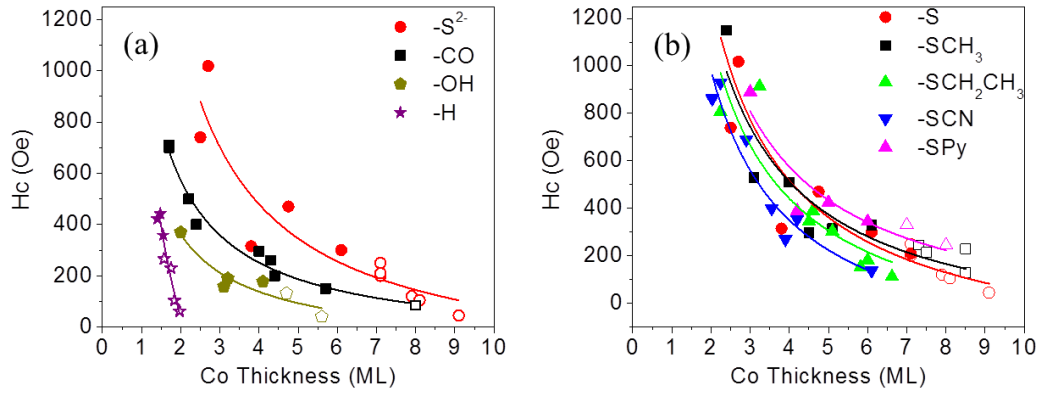


Fig. 4.8: (a) H_c as a function of t_{Co} for Co–X termination with X = S^{2-} , CO, OH and H as indicated in the figure. (b) H_c as a function of t_{Co} for S^{2-} , $-SCH_3$, $-SCH_2CH_3$, $-SCN$ and $-SPy$ linked Co

Linkage	H	OH	CO	S^{2-}
C_1 (Oe ML)	NA	891 ± 151	1285 ± 70	2673 ± 370
C_2 (Oe)	NA	-85 ± 47	-70 ± 26	-189 ± 82

Table 4.1.a: C_1 and C_2 values extracted from the fittings of H_c as a function of t_{Co} corresponding to Fig.4.8.(a).

Linkage	S^{2-}	SCH_3	SCH_2CH_3	SCH^-	SPy
C_1 (Oe ML)	2673 ± 370	2774 ± 375	2701 ± 584	2516 ± 278	2812 ± 127
C_2 (Oe)	-189 ± 82	-181 ± 85	-234 ± 147	-278 ± 102	-127 ± 113

Table 4.1.b: C_1 and C_2 values extracted from the fittings of H_c as a function of t_{Co} corresponding to Fig.4.8.(b).

From the above data and **Table 4.1**, we may conclude that the surface anisotropy energy increases in the order $H < OH < CO < S$. This behavior is very close to that of the anisotropy energy given by t^* , except for S. This suggests that the H_c value is not influenced by the morphology of the Au(111) substrate or by the structural imperfection of the Co films.

4.4. Results: MEC effects of Co covered with molecular layers

In this section we study magneto-electric coupling of Co/Au(111) films covered with various organic monolayers, obtained as described in **section 4.3**. Before dealing with MEC measurements, we present a brief electrochemical study in the supporting electrolytes used to conduct the MEC characterizations.

4.4.1. Electrochemical characterizations

We first characterize the electrochemical behavior of each system in supporting electrolytes of pH 3.5 and/or 12 to characterize the electrochemical reactions in the stability domain of the layers. We also characterize the influence of the molecules on the dissolution of cobalt since this may provide some indication about the molecule – Co interactions.

In the acidic electrolyte, the current peak measured in **Fig. 4.9.(a)** corresponds to the hydrogen evolution reaction by reduction of the protons ($H^+ + e^- \rightarrow \frac{1}{2} H_2$). It is observed at $\sim -1.35V$, $\sim -1.29V$ and $\sim -1.22V$ respectively for H, CO and S covered surfaces. Adsorption of –SR seems to inhibit the HER current density. Regarding the dissolution, surface modification (**Fig. 4.9.b**) affects the onset potential. It is around $-0.98V$ for –H and –S capped samples, whereas it is around $-0.66V$ for –CO covered films¹.

In pH = 12 electrolyte, as shown in **Chapter 3**, the voltammogram of the as-deposited Co layers presents oxidation/reduction peaks corresponding to the adsorption/desorption of the OH adlayer (**Fig. 4.10.a**). At the S- and CO- terminated Co surfaces no

¹ The peculiar shape of the i - V curve, which presents a plateau of current is assigned to a larger Schottky barrier n-Si(111)/Au diode in the case of this sample. This behavior was occasionally observed with some samples. The measured onset potential is not affected by this phenomenon since we obtain a sharp dissolution peak at the same position with other samples.

OH-adsorption/desorption peaks observed in the same potential range. For potentials > -1.15 V, passivation looks however very similar at the CO- and H-terminated surfaces, because the oxidation peak A_2 (chapter 3) overlap for these two samples.—Only the R-S-terminated sample present a different behavior with an oxidation peak shifted toward more positive potentials. Consequently, it can be concluded that in a pH ~ 4 electrolyte, Co-H and Co-S-R surface are stable for $U < -1$ V, Co-CO surface is stable for $U < -0.7$ V; in a pH ~ 12 electrolyte, Co-H surface is stable for $U < -1.35$ V, Co-CO and Co-S-R can protect the surface from oxidation for $U < -1.05$ V and Co-OH layer is stable between -1.15 V and -1.2 V. Hence, in the following study, the explored potential range is limited between -1.15 V and -1.5 V for Co-CO and Co-S-R surface in both of acid and alkaline electrolytes; -1.5 V $< U < -1.15$ V for H-covered surface in acid solution; and -1.2 V $< U < -1.15$ V for $-OH$ adsorbed in alkaline electrolyte.

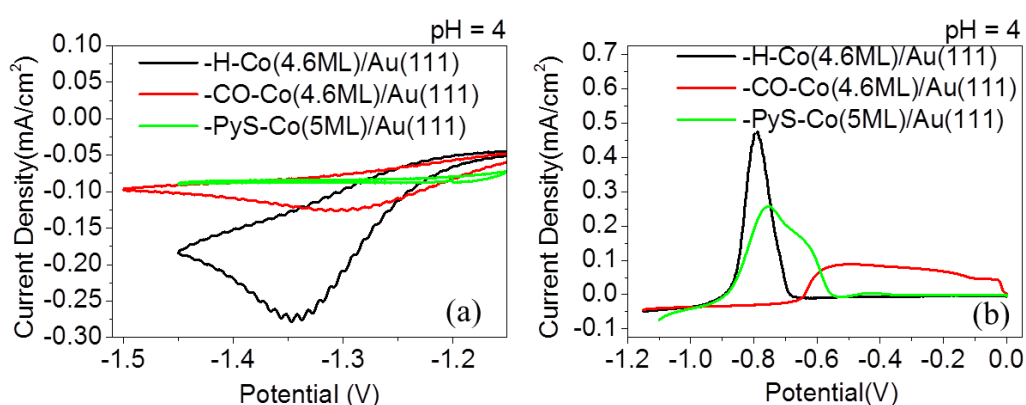


Fig. 4.9: (a) Variations of electrochemical current density versus potential for -1.5 V $< U < -1.15$ V of Co covered with $-H$ (black line), $-CO$ (red line) and $-SPy$ (green line) in pH ~ 4 blank electrolyte (b) Variation of electrochemical current density versus potential for -1.15 V $< U < 0$ V of Co covered with $-H$ (black line), $-CO$ (red line) and $-SPy$ (green line) in pH ~ 4 blank electrolyte. The scan rate is 10mV/s.

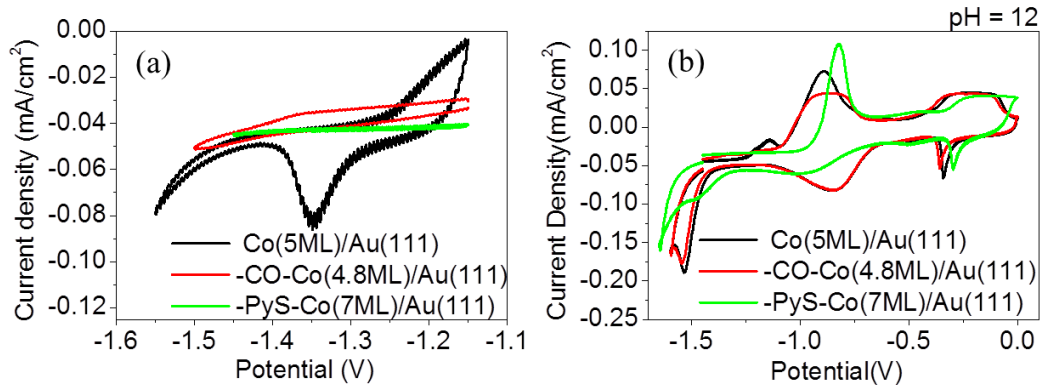


Fig. 4.10: (a) Variations of electrochemical current density versus potential for $-1.65V < U < 0V$ of Co surface (black line), covered with $-CO$ (red line) and $-SPy$ (green line) in $pH \sim 12$ blank electrolyte (b) Variation of electrochemical current density versus potential for $-1.55V < U < -1.15V$ of Co surface $-H$ (black line), covered with $-CO$ (red line) and $-SPy$ (green line) in $pH \sim 12$ blank electrolyte. The scan rate is $10mV/s$.

4.4.2. MEC results

Assuming that MEC is a pure surface effect, it may be anticipated that its manifestation will decay with increasing Co thickness. It is therefore desirable to consider very thin Co films. MEC measurements with out-of-plane magnetized film are presented at the end of this section. However, considering out-of-plane magnetized film is not adequate to make a quantitative determination of $K_S(U)$ with our set-up. To quantitatively characterize MEC, i.e. the potential dependence of PMA, it is preferable considering in-plane magnetized films or films of thickness very close to t^* . The theoretical description of this quantitative analysis is given in Section 4.5.1.

a) In-plane magnetization films ($t_{Co} > t^*$)

Data are only available for H- ($t^* \sim 2$ ML) and OH-terminated ($t^* \sim 4$ ML) cobalt films. **Figure 4.11.(a)** presents hysteresis loops for a 4.6-ML H-covered Co/Au(111) layers polarized at $-1.15V$ and $-1.5V$ in the acidic blank electrolyte. The $M-H$ curves are linear and reversible at both potentials, implying an in-plane magnetization. The slope of these $M-H$ plots yields the magnetic susceptibility $\chi = \Delta M / \Delta H$. It is larger by $\sim 16\%$ at -1.5 V than that at $-1.15V$. **Fig. 4.11.(b)** compares the variations of χ with the applied potential for 3.9-ML and 4.6-ML-thick

H-terminated Co/Au(111) films. In both cases, χ varies linearly and reversibly with the applied potential. The slope $\Delta\chi/\Delta U$ of the straight line is larger (in absolute value) for the thinner film, which is consistent with a surface effect.

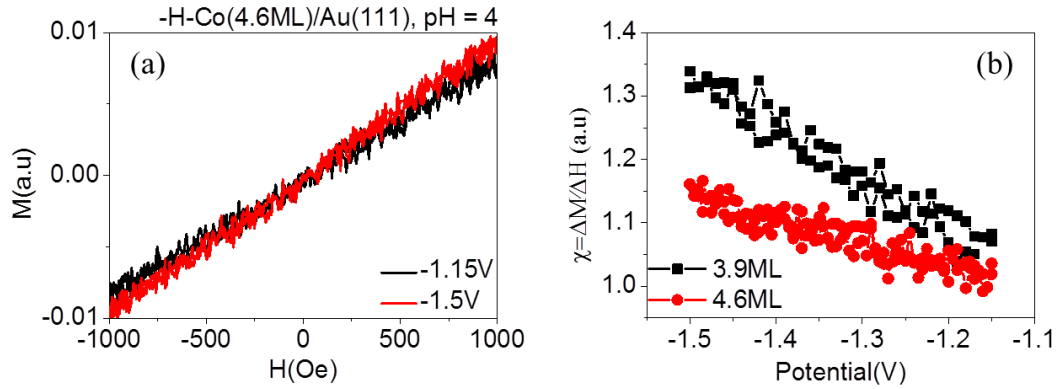


Fig. 4.11: (a) M - H curves for H-covered 4.6-ML Co/Au(111) at -1.15V and -1.5V in a pH ~ 4 blank electrolyte; (b) Variation of χ versus potential for H-covered 3.9-ML (black line) and 4.6-ML (red line) Co/Au(111) in a pH ~ 4 blank electrolyte during potential sweepings between -1.15V and -1.5V. The scan speed is 10mV/s.

Similar experiments have been performed for -OH terminated Co layers. **Fig.4.12.(a)** shows the hysteresis loops of a -OH covered 8.2-ML Co at -1.15V and -1.2V. The magnetic susceptibility $\chi = \Delta M / \Delta H$ increases by ~ 14% when the potential is 50mV more negative. In **Fig. 4.12.(b)**, the voltage-dependent variation of magnetic susceptibility χ is shown for 8.2-ML and 10.3-ML OH-covered Co/Au(111) for $-1.2V < U < -1.15V$. χ is linear and reversible with potential. $\Delta\chi/\Delta U$ is also thickness-dependent and is larger by a factor of 2 for Co(8.2ML) than for Co(10.3ML).

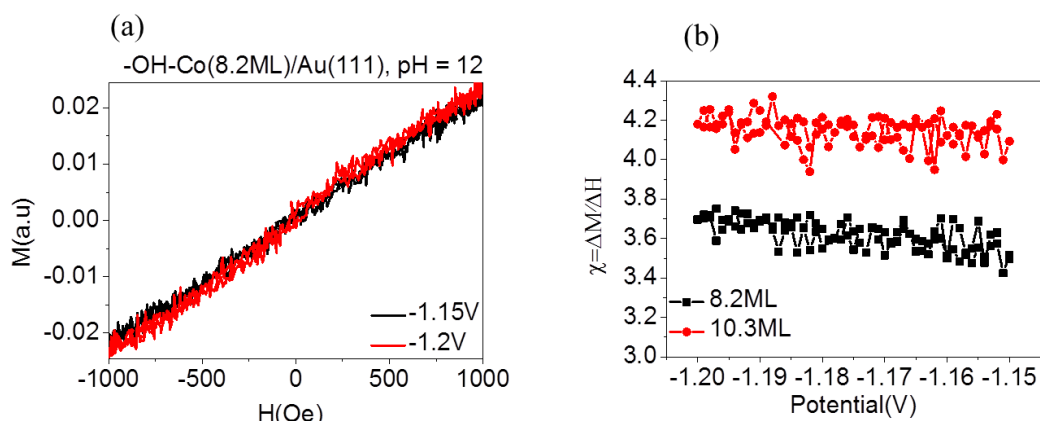


Fig. 4.12: (a) M - H curves for OH-covered 8.2-ML Co/Au(111) at -1.15V (black line) and -1.2V (red line) in a pH \sim 12 blank electrolyte; (b) Variation of χ versus potential for OH-covered 8.2-ML (black line) and 10.3-ML (red line) Co/Au(111) in a pH \sim 4 blank electrolyte during potential sweepings between -1.15V and -1.2V. The scan speed is 10mV/s.

As has been shown previously [27], $|(\Delta\chi/\chi)/\Delta U|$ is a good method to demonstrate whether MEC is a pure surface effect.

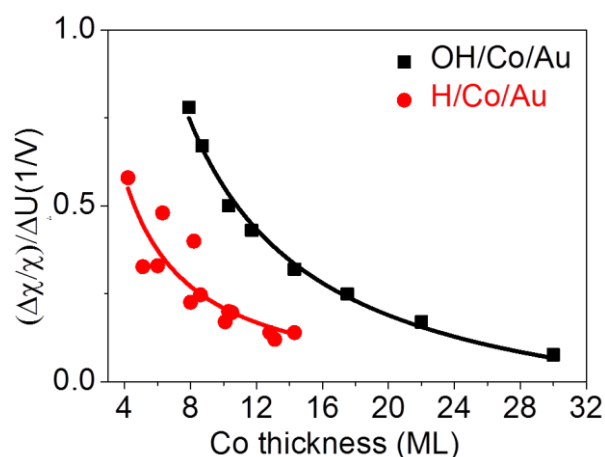


Fig. 4.13: Relative variations of the magnetic susceptibility as a function of applied potential $|(\Delta\chi/\chi)/\Delta U|$ (absolute value) versus Co thickness for $-H$ (red circles) and $-OH$ (black squares) covered surface. The red and black curves indicate the best fittings following the $C_1/t_{Co} + C_2$ law. The signs of $(\Delta\chi/\chi)/\Delta U$ in both cases are negative.

Figure 4.13 shows $|(\Delta\chi/\chi)/\Delta U|$ as a function of Co thickness t_{Co} for H- and OH-

terminated surfaces. The black and red curves present the best data fitting by using $C_1/t_{Co} + C_2$ law. The best fittings give:

- For Co-H interface, $C_1 = 2.46 \pm 0.41V^{-1}$, $C_2 = -0.036 \pm 0.05V^{-1}$;
- For Co-OH interface, $C_1 = 7.31 \pm 0.25V^{-1}$, $C_2 = -0.176 \pm 0.02V^{-1}$;

b) Films of thickness close to t^*

Figure 4.14 presents a set of MEC characterizations for OH (a, a'), CO (b, b') and SPy (c, c') covered Co films in contact with the supporting electrolyte of pH 12 and 3.5 respectively. The $M-H$ plots measured at two potentials are presented in the left column. The variation of M_R/M_{Sat} as a function of potential for Co covered with different molecular layers is shown in the right column. Linear and reversible variations are observed within the respective potentials limits.

- In the case of $-OH/Co(4.3ML)$, $M_R/M_{Sat} = 0.452$ with $\varphi = 63.1^\circ$ (Equation 2.13 in Chapter 2) at $-1.15V$; and $M_R/M_{Sat} = 0.553$ with $\varphi = 56.4^\circ$ at $-1.2V$. $\Delta(M_R/M_{Sat}) = 0.101$ from $-1.15V$ to $-1.2V$.
- In the case of $-CO/Co(7ML)$, $M_R/M_{Sat} = 0.836$ with $\varphi = 33.2^\circ$ at $-1.1V$; and $M_R/M_{Sat} = 0.876$ with $\varphi = 28.8^\circ$ at $-1.25V$. $\Delta(M_R/M_{Sat}) = 0.04$ from $-1.15V$ to $-1.25V$.
- In the case of $-S/Co(7ML)$, $M_R/M_{Sat} = 0.87$ with $\varphi = 29.6^\circ$ at $-1.2V$; and $M_R/M_{Sat} = 0.852$ with $\varphi = 31.5^\circ$ at $-1.45V$. $\Delta(M_R/M_{Sat}) = -0.018$ from $-1.2V$ to $-1.45V$

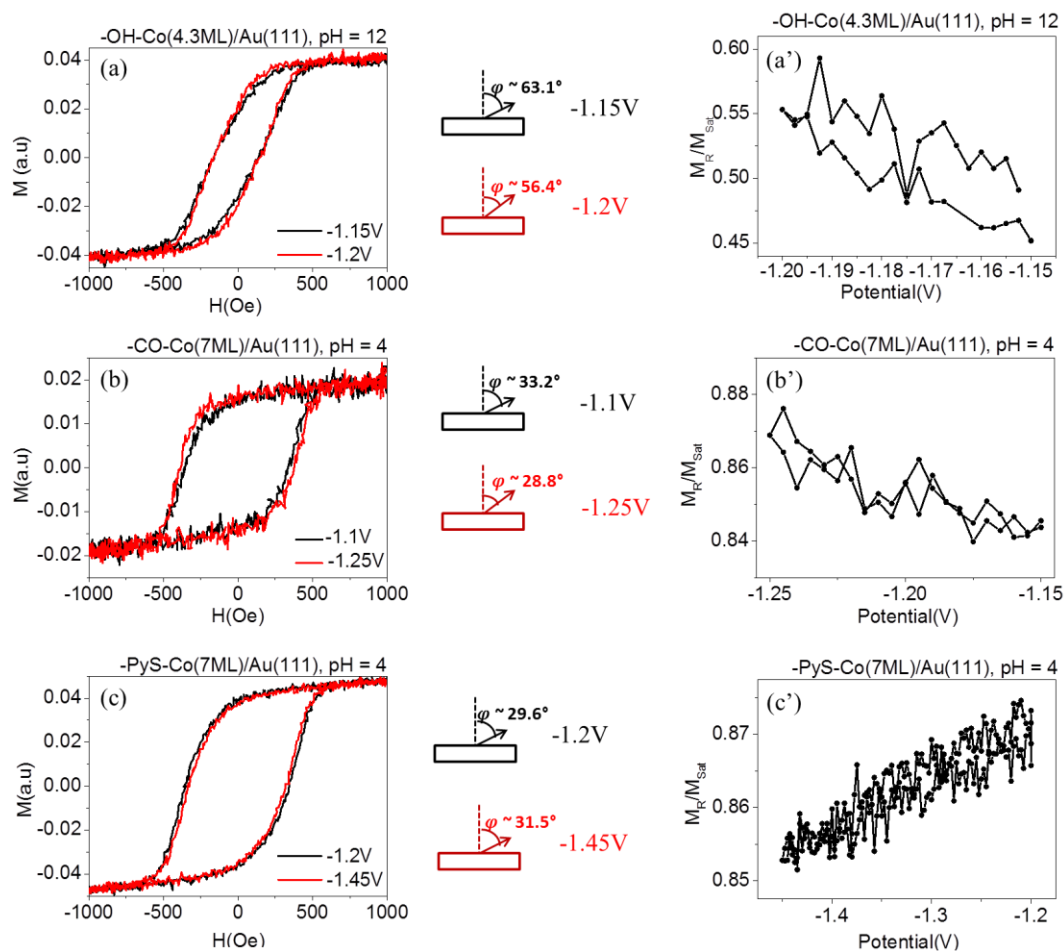


Fig. 4.14: (a) M - H curves of $-\text{OH}$ covered 4.3-ML Co at -1.15V (black line) and -1.2V (red line) in a $\text{pH} \sim 12$ blank electrolyte; (a') Variation of M_R/M_{Sat} of $-\text{OH}$ covered 4.3-ML Co versus potential between -1.15V and -1.2V in $\text{pH} \sim 12$ blank electrolyte; (b) M - H curves of $-\text{CO}$ covered 7-ML Co at -1.1V (black line) and -1.25V (red line) in a $\text{pH} \sim 4$ blank electrolyte; (b') Variation of M_R/M_{Sat} of $-\text{CO}$ covered 7-ML Co versus potential between -1.15V and -1.25V in a $\text{pH} \sim 4$ blank electrolyte; (c) M - H curves of $-\text{SPy}$ covered 7-ML Co at -1.2V (black line) and -1.45V (red line) in a $\text{pH} \sim 4$ blank electrolyte; (c') Variation of M_R/M_{Sat} of $-\text{SPy}$ covered 7-ML Co versus potential between -1.2V and -1.45V in a $\text{pH} \sim 4$ blank electrolyte.

c) Films of thickness below t^* (i.e. out-of-plane magnetized)

In principle MEC data with out-of-plane magnetized film cannot easily be correlated to surface anisotropy since the value of H_c is not an intrinsic parameter of the system. These measurements are nevertheless presented below because they bear interesting information about the film magnetic properties.

-H-terminated surface:

Figure 4.15 summarizes the MEC measurements conducted with a 1.48-ML-thick H-covered Co in an acidic blank electrolyte. The M - H curves recorded at -1.15V and -1.5V (a) evidence that the film is strictly perpendicular to the surface over the whole investigated potential range. **Fig. 4.15.b** shows that H_c increases by $\sim 5\%$ when the potential decreases from -1.15V to -1.5V while M_{Sat} and M_R/M_{Sat} remain constant. The other panels in **Fig. 4.15** display the voltage dependence of $\Delta M_R/M_R$ (panel c) and electrochemical current (panel d).

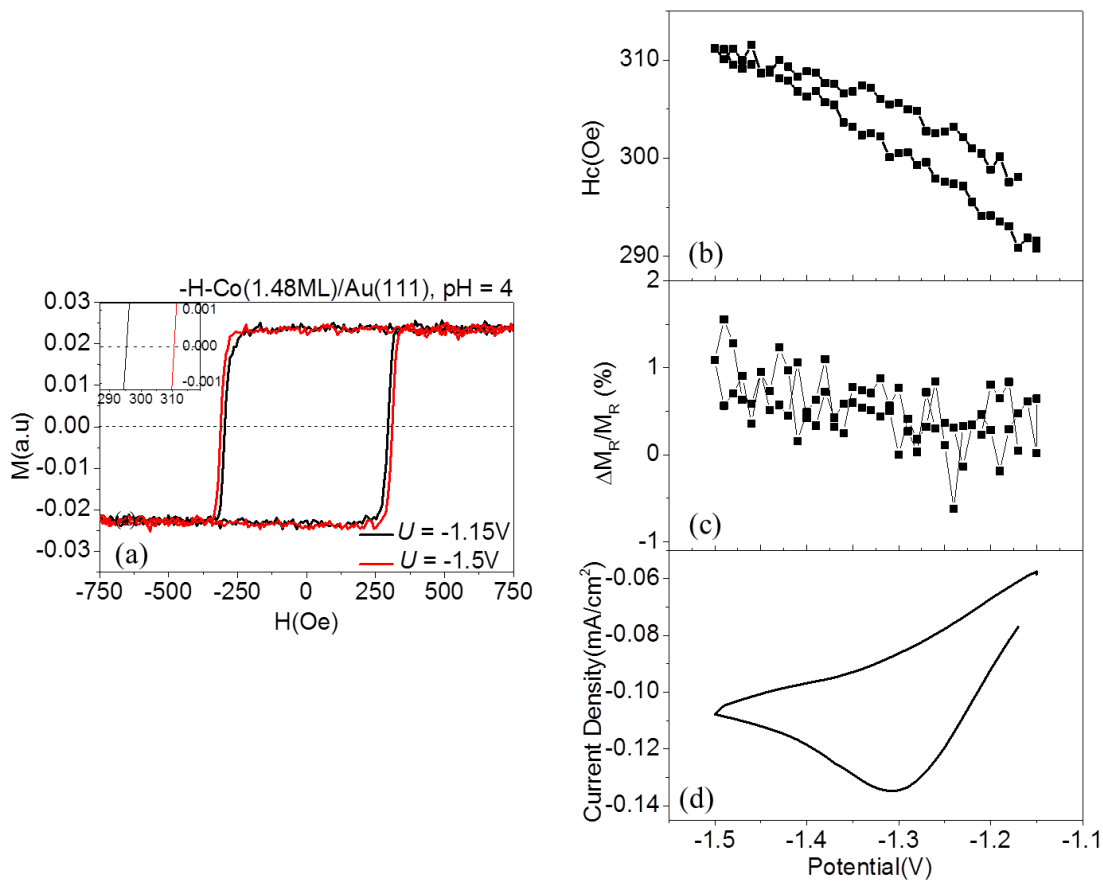


Fig. 4.15: (a) M - H curves of -H covered 1.48-ML Co at -1.15V (black line) and -1.5V (red line) in a pH ~ 4 blank electrolyte; (b) H_c as a function of potential between -1.15V and -1.5V; (c) M_R as a function of potential between -1.15V and -1.5V; (d) electrochemical current density as a function of potential between -1.15V and -1.5V of the same sample covered with -H during potential scans. The scan speed is 10mV/s.

The remarkable fact is the quasi linear and reversibility variations of H_c with applied

potential. Panel (c) confirms that the magnetic moment remains independent of the applied voltage (magnetic moment's variation less than 1%). The observed irreversibility is probably due to some experimental drift. The relative variation of H_c is $(\Delta H_c/H_c)/\Delta U \sim -18\%/V$.

- OH-terminated surface:

Figure 4.16 summarizes the MEC behavior for a 2.1-ML Co in a pH ~ 12 electrolyte. For a OH covered films the major difficulty is the narrow potential range (50 mV) where the OH coverage can be considered as constant (see Chapter 3).

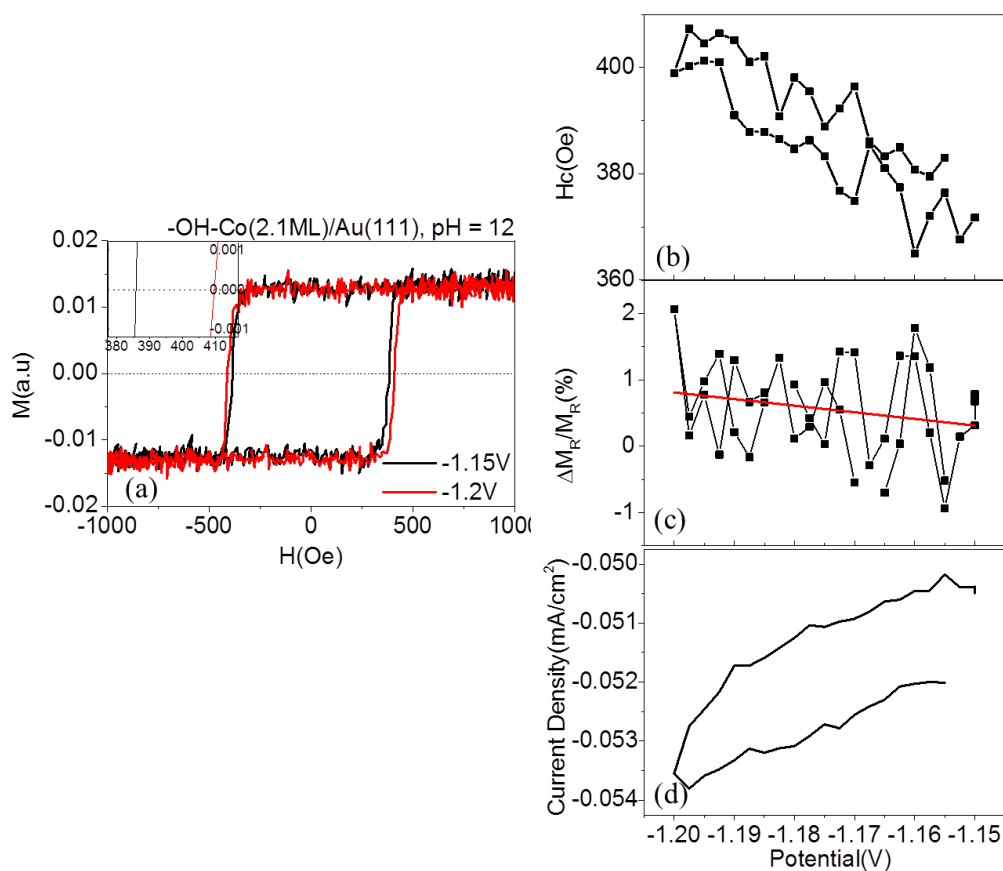


Fig. 4.16: (a) M - H curves of $-OH$ covered 2.1-ML Co at $-1.15V$ (black line) and $-1.2V$ (red line) in a pH ~ 12 blank electrolyte. The inset corresponds to the zoom of the two M - H curves between 380-410Oe. (b) H_c as a function of potential between $-1.15V$ and $-1.2V$; (c) M_R as a function of potential between $-1.15V$ and $-1.2V$; (d) electrochemical current density as a function of potential between $-1.15V$ and $-1.2V$ of the same sample covered with $-OH$ during potential scans. The scan speed is 5mV/s.

The hysteresis loops (panel a) recorded at -1.15V and -1.2V show significant variations of H_c (panel b) with a slight increase of $\Delta M_R/M_R$ by 1% (panel c). The relative variations of H_c is $(\Delta H_c/H_c)/\Delta U \sim -193\%/V$, which is about 10 times greater than for the H-terminated surface.

- CO-terminated surfaces:

The magnetic anisotropy of a 4.8-ML CO-dosed Co/Au(111) film is strictly perpendicular to the surface over the whole investigated potential range. **Fig. 4.17** compares the MEC behavior of CO-terminated Co film in the supporting electrolyte of pH 3.5 (left column) and 12 (right column). The hysteresis loops (panels a and a') show that the Co film is strictly out of plane magnetized and that H_c depends on the applied voltage. **Fig. 4.17** (b and b') display the potential dependence of H_c between -1.15V and -1.5V. Panels (c) and (c') show the variation of M_R . Arrows indicate the potential sweep direction. **Fig. 4.17** (d and d') show the electrochemical current density as a function of potential during the same sweep.

In the solution of pH 3.5, a close inspection of the data reveals two MEC regimes:

- For $-1.25V < U < \sim -1.15V$, H_c increases quasi-linearly and is independent on the variation of the electrochemical current, with $(\Delta H_c/H_c)/\Delta U \sim -40\%/V$.

- For $-1.5V < U < -1.25V$, H_c behavior is completely different. H_c becomes nearly proportional to the electrochemical current with a slope of $-476 \text{ Oe}/(\text{mA}\cdot\text{cm}^{-2})$. This behavior is also reversible with the potential sweeping. The remanence M_R changes in the same way as H_c . This behavior can be observed after removing dissolved CO from the solution, indicating that the CO coverage of the Co surface is not altered during the potential cycle. We also emphasize that this behavior is specific of the CO-terminated surface as it is not observed in the case of H-covered surface. This behavior is consistent with the work of Tournerie *et al.* [27].

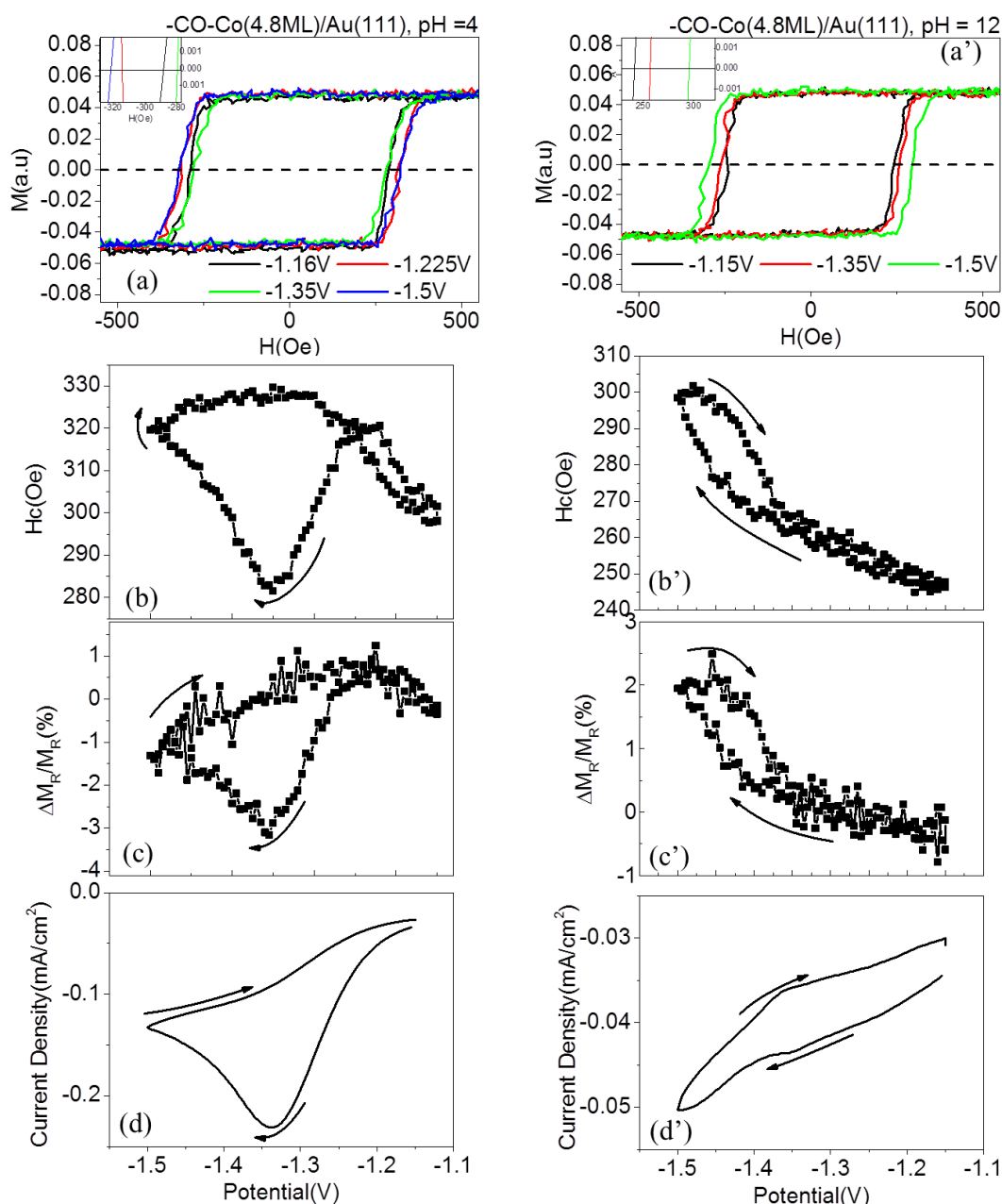


Fig. 4.17: (a)/(a') M - H curves of $-\text{CO}$ covered 4.8-ML Co in a pH~ 4 electrolyte at -1.15V (black line), -1.225V (red line), -1.35V (green line) and -1.5V (blue line)/in a pH ~ 12 blank electrolyte at -1.15V(black line), -1.35V(red line) and -1.5V (green line); (b)/(b') H_c ; (c)/(c') M_R ; (d)/(d') electrochemical current density as a function of potential between -1.15V and -1.5V of the same sample covered with $-\text{CO}$ during potential scans in pH ~ 4/pH ~12 blank electrolyte. The scan speed is 10mV/s. Arrows indicate the sweep directions.

To confirm that the correlation of H_c with HER current, we performed the same MEC measurements in the electrolyte of pH = 12 with the above 4.8-ML (after exchange of the

electrolyte). **Fig. 4.17.(b')** shows that H_c varies quasi linearly with the applied potential during one sweeping between -1.15V and -1.5V. Two slopes are however observed:

- For $-1.375V < U < -1.15V$, the relative variation is $(\Delta H_c/H_c)/\Delta U \sim -45\%/V$. This result is consistent with $(\Delta H_c/H_c)/\Delta U$ observed in the 1st regime in the acid electrolyte.

- For $-1.5V < U < -1.375V$, H_c presents a hysteresis with $(\Delta H_c/H_c)/\Delta U \sim -74\%/V$. M_R behaves in the same way with potential as H_c . H_c versus potential has a negative slope.

- SPy terminated surface:

The MEC measurements with this surface was conducted in the two electrolytes of pH 3.5 (left column in **Fig. 4.18**) and 12 (right column in **Fig. 4.18**). The Co thickness is 4.2 ML in this experiment. The $M-H$ curves (**Fig. 4.18.(a)** and **(a')**) confirm that the layer is out-of-plane magnetized in the two electrolytes. The variation of H_c (panels b and b') are very similar in both electrolytes with quasi-linear variations and a quasi-reversible potential dependence. It is remarkable to notice that the slope of the variation has changed compared to all other surface terminations. The average relative variation is $(\Delta H_c/H_c)/\Delta U \sim +14\%/V$ in the acid solution and $(\Delta H_c/H_c)/\Delta U \sim +16\%/V$ in the alkaline solution. The results suggest that the surface chemistry is the same for the two electrolytes.

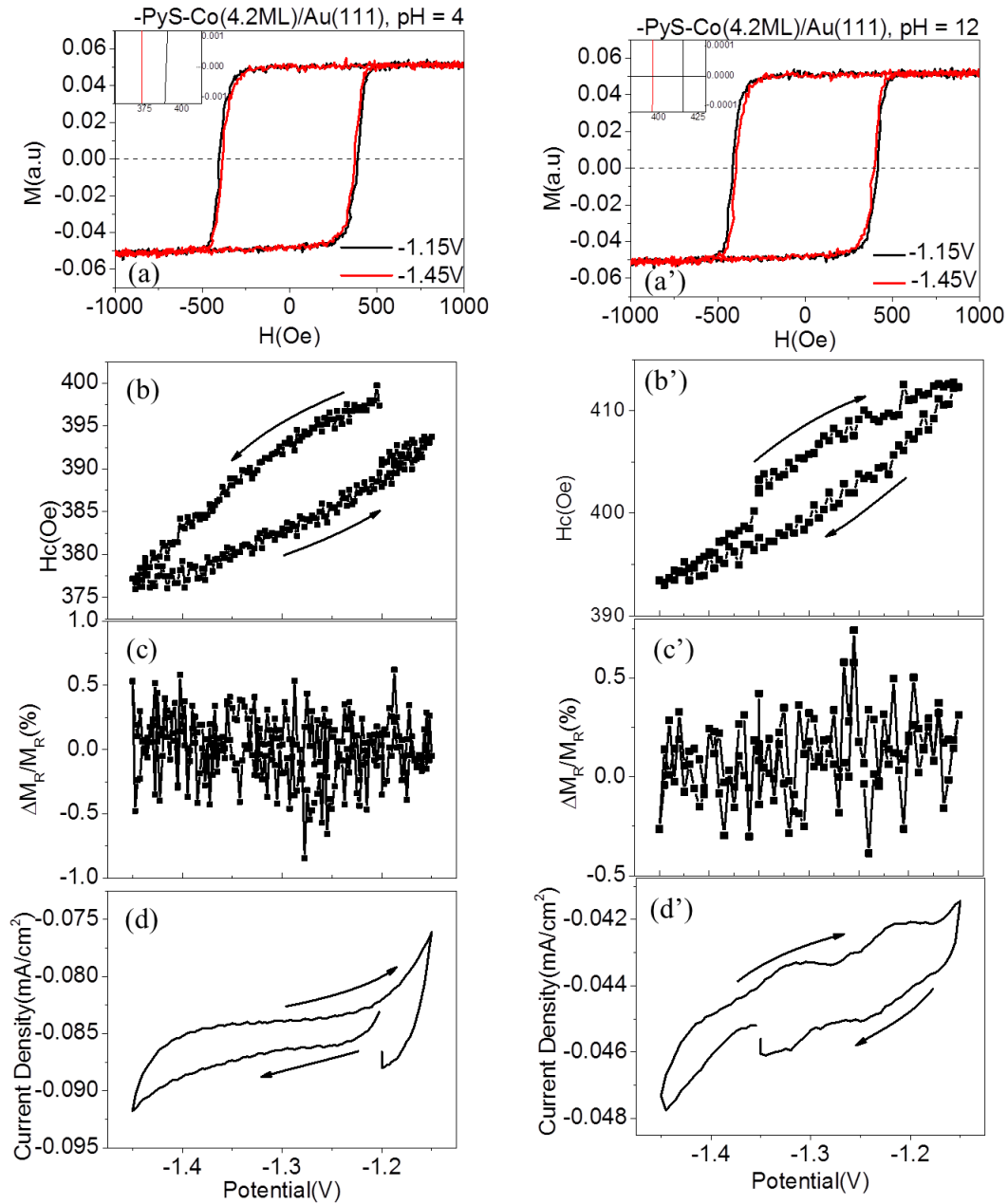


Fig. 4.18: (a)/(a') M - H curves of -SPy covered 4.2-ML Co at -1.2V (black line), and -1.45V (red line) in a pH~ 4/pH ~ 12 blank electrolyte; (b)/(b') H_c ; (c)/(c') M_R ; (d)/(d') electrochemical current density as a function of potential between -1.2V and -1.45V of the same sample covered with -SPy during potential scans in pH ~ 4/pH ~12 blank electrolyte. The scan speed is 10mV/s.

Figure 4.19 presents $(\Delta H_c/H_c)/\Delta U$ as a function of Co thickness t_{Co} for different interface chemistry. In the case of -CO, $(\Delta H_c/H_c)/\Delta U$ is extracted from the region where the variation is linear and reversible. For different -S molecules, $(\Delta H_c/H_c)/\Delta U$ is nearly the same, confirming that MEC effect is mainly due to the first atom linked with the surface, the

influence of second groups being negligible. $(\Delta H_c/H_c)/\Delta U$ is thickness-independent for –OH, –CO, –S linked surface. In the case of the –OH covered 4.3-ML Co, $(\Delta H_c/H_c)/\Delta U$ is slightly smaller than that of 2~4-ML Co. This is due to the fact that 4.3ML is very close to the t_{Co-OH}^* , and the hysteresis loop is not strictly perpendicular with a $M_R/M_{Sat} \sim 0.88$ instead of 1. The sign of $(\Delta H_c/H_c)/\Delta U$ and the absolute value depend on the surface chemistry: the sign is positive only for –S linked surface, and negative for –CO, -H and –OH covered surface. The absolute value of $(\Delta H_c/H_c)/\Delta U$ increases in the following order: -S<-H<-CO<-OH.

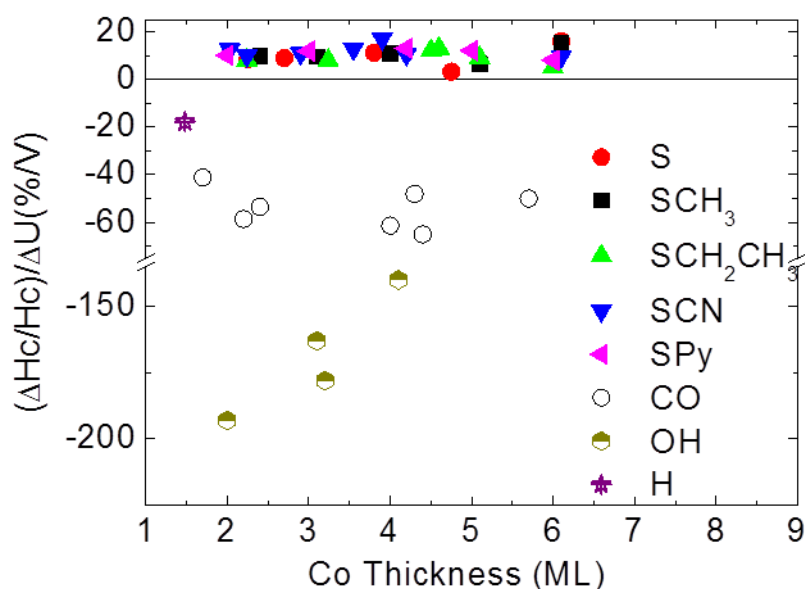


Fig. 4.19: Relative variation of H_c versus applied potential as a function of Co thickness for Co thin films covered with different molecular layers.

4.5. Discussion

4.5.1. Determination of MEC coefficients

a) Films thicker than t^*

In the case of in-plane magnetized film the MEC coefficient $\Delta K_S/\Delta U$ can be determined from the dependence of $\Delta\chi/\Delta U$ on the Co thickness (**Fig. 4.13**). Tournerie *et al.* [27] established the analytical expression of $\Delta\chi/\Delta U$ from the standard model developed in **Chapter 2** to describe

the MAE of an ultrathin magnetic layer. Equations (2.21) and (2.22) in **Chapter 2** describe the case of a film with an in-plane magnetization easy axis:

$$K_1 - 2\pi M_S^2 + K_s/t_{Co} + 2K_2(\sin \varphi)^2 + HM_S/(2 \cos \varphi) = 0 \quad (4.1)$$

$$\cos \varphi (H) = M(H)/M_{Sat} = M(H)/(\alpha M_S) \quad (4.2)$$

where α is proportionality constant.

For Co films much thicker than t_{Co}^* and an applied field H much smaller with respect to Co saturation field (10^4 Oe), the angle between magnetization with the surface normal φ is very close to $\pi/2$; i.e. $\sin \varphi$ is very close to 1. Replacing $\cos \varphi$ in equation (4.1) with equation (4.2), we have:

$$\chi = \frac{M(H)}{H} = \frac{\alpha M_{Sat}^2}{2(2\pi M_S^2 - 2K_2 - K_1 - K_s/t_{Co})} \quad (4.3)$$

$$K_v = 2\pi M_S^2 - 2K_2 - K_1 \sim 3.6 \cdot 10^6 \text{ erg} \cdot \text{cm}^{-2} \quad (4.4)$$

Assuming all the variables depend on applied potential U

$$\frac{\Delta \chi}{\Delta U} = \frac{\frac{\Delta}{2(K_v - K_s/t_{Co})} \frac{\alpha M_{Sat}^2}{\Delta U}}{\Delta U} = \frac{2\alpha M_{Sat} \frac{\Delta M_{Sat}}{\Delta U}}{2(K_v - K_s/t_{Co})} - \frac{\alpha M_{Sat}^2}{2(K_v - K_s/t_{Co})^2} \left(\frac{\Delta K_v}{\Delta U} - \frac{\Delta K_s/t_{Co}}{\Delta U} \right) \quad (4.5)$$

$$\begin{aligned} \frac{1}{\chi} \frac{\Delta \chi}{\Delta U} &= \frac{2}{M_{Sat}} \frac{\Delta M_{Sat}}{\Delta U} - \frac{1}{(K_v - K_s/t_{Co})} \left(\frac{\Delta K_v}{\Delta U} - \frac{\Delta K_s/t_{Co}}{\Delta U} \right) \\ &= \frac{2}{M_{Sat}} \frac{\Delta M_{Sat}}{\Delta U} - \frac{1}{K_v} \frac{1}{\left(1 - \frac{K_s/t_{Co}}{K_v}\right)} \frac{\Delta K_v}{\Delta U} + \frac{1}{K_v} \frac{1}{\left(1 - \frac{K_s/t_{Co}}{K_v}\right)} \frac{\Delta K_s/t_{Co}}{\Delta U} \end{aligned} \quad (4.6)$$

When the Co film is much thicker than t^* (i.e. thicker than 4ML for H-terminated layer and thicker than ~ 10 ML for OH-terminated films) one may consider $K_s/t_{Co} \ll K_v$. Consequently, χ can be written as in the first order of $(K_s/t_{Co})/K_v$ through the Maclaurin series:

$$\begin{aligned} \frac{1}{\chi} \frac{\Delta \chi}{\Delta U} &= \frac{2}{M_{Sat}} \frac{\Delta M_{Sat}}{\Delta U} - \frac{1}{K_v} \frac{\Delta K_v}{\Delta U} \left(1 + \frac{K_s/t_{Co}}{K_v} + O\left(\left(\frac{K_s/t_{Co}}{K_v}\right)^2\right) \right) \\ &+ \frac{1}{K_v} \frac{\Delta K_s/t_{Co}}{\Delta U} \left(1 + \frac{K_s/t_{Co}}{K_v} + O\left(\left(\frac{K_s/t_{Co}}{K_v}\right)^2\right) \right) \end{aligned} \quad (4.7)$$

From equation (4.7), the dominant term decaying with the thickness t_{Co} is $\frac{1}{K_v} \frac{\Delta K_s/t_{Co}}{\Delta U}$.

As a result, the $\Delta K_s/\Delta U$ can be estimated from the data fitting $C_1/t_{Co} + C_2$ law with:

$$C_1 = (\Delta K_s/\Delta U)(1/K_v) \quad (4.8)$$

The best fittings in **Fig.4.13** give:

- For Co-H interface, $C_1 = 2.46 \pm 0.41V^{-1}$, $C_2 = -0.036 \pm 0.05V^{-1}$;

This yields $\Delta K_s^{Co-H}/\Delta U = -0.177 \text{ erg}\cdot\text{cm}^{-2}\cdot\text{V}^{-1}$. The order of the magnitude is consistent with the result reported before [27]. The value of C_2 is within the error bar and may be considered negligibly small with respect to the values of $(1/\chi)(\Delta\chi/\Delta U)$, demonstrating that the dominant change in equation (4.7) upon varying the potential is that of K_s and that the MEC is a pure surface effect.

- For Co-OH interface, $C_1 = 7.31 \pm 0.25V^{-1}$, $C_2 = -0.176 \pm 0.02V^{-1}$;

Thus, $\Delta K_s^{Co-OH}/\Delta U = -0.526 \text{ erg}\cdot\text{cm}^{-2}\cdot\text{V}^{-1}$. In this case, C_2 is significantly larger than the error bar. It may stem from $\frac{1}{M_{Sat}} \frac{\Delta M_{Sat}}{\Delta U}$ or from $-\frac{1}{K_v} \frac{\Delta K_v}{\Delta U}$. Indeed, **Fig. 4.16.(c)** indicates that M_{Sat} varies with U , with $\frac{1}{M_{Sat}} \frac{\Delta M_{Sat}}{\Delta U} \sim -0.1$, which is in an agreement with C_2 . The origin of this changing of M_{Sat} with potential is still unclear.

b) Films of thickness close to t^*

In the case of Co having a spontaneous out-of-plane anisotropy with $0 < M_R/M_{Sat} < 1$, equation (4.1) also allows us to relate $\Delta K_s/\Delta U$ with $\Delta(M_R/M_{Sat})/\Delta U$. Replace $(\sin \varphi)^2$ by $1 - (M_R/M_{Sat})^2$ and $H = 0 \text{ Oe}$, we get:

$$\begin{aligned} K_1 - 2\pi M_s^2 + K_s/t_{Co} + 2K_2 - 2K_2(M_R/M_{Sat})^2 \\ = K_s/t_{Co} - 2K_2(M_R/M_{Sat})^2 - K_v = 0 \end{aligned} \quad (4.9)$$

As the MEC effect is a pure surface effect, the volume's anisotropy K_2 , K_v does not vary with the applied potential. For two different potentials U_1 and U_2 , we have:

$$K_s(U_1)/t_{Co} - 2K_2(M_R/M_{Sat})^2(U_1) - K_v = 0 \quad (4.10)$$

$$K_s(U_2)/t_{Co} - 2K_2(M_R/M_{Sat})^2(U_2) - K_v = 0 \quad (4.11)$$

Where $K_s(U_1)$, and $K_s(U_2)$ are the corresponding magnetic anisotropy coefficients at U_1 and U_2 respectively; and $(M_R/M_{Sat})^2(U_1)$, $(M_R/M_{Sat})^2(U_2)$ are the ratio of remanence to saturation at U_1 and U_2 respectively.

By subtracting equation (4.10) from equation (4.9), we have:

$$K_s(U_2)/t_{Co} - K_s(U_1)/t_{Co} = 2K_2[(M_R/M_{Sat})^2(U_2) - (M_R/M_{Sat})^2(U_1)] \quad (4.12)$$

i.e.:

$$\Delta K_s/t_{Co} = 2K_2\Delta[(M_R/M_{Sat})^2] \quad (4.13)$$

Consequently, $\Delta K_s/\Delta U$ can be expressed by:

$$\frac{\Delta K_s}{\Delta U} = 2K_2 t_{Co} \frac{\Delta(M_R/M_{Sat})^2}{\Delta U} \quad (4.14)$$

From the results presented in **Fig. 4.14**, we have:

- In the case of $-\text{OH}/\text{Co}(4.3\text{ML})$, $\Delta K_s^{\text{Co-OH}}/\Delta U$ is $-0.558 \text{ erg}\cdot\text{cm}^{-2}\cdot\text{V}^{-1}$. This is in good agreement with $\Delta K_s^{\text{Co-OH}}/\Delta U = -0.526 \text{ erg}\cdot\text{cm}^{-2}\cdot\text{V}^{-1}$ calculated using $(1/\chi)(\Delta\chi/\Delta U)$. Hence, analysis of $\Delta K_s/\Delta U$ through $\Delta(M_R/M_{Sat})/\Delta U$ is a reliable alternative method.
- In the case of $-\text{CO}/\text{Co}(7\text{ML})$, $\Delta K_s^{\text{Co-CO}}/\Delta U$ is $-0.204 \text{ erg}\cdot\text{cm}^{-2}\cdot\text{V}^{-1}$.
- In the case of $-\text{S}/\text{Co}(7\text{ML})$, $\Delta K_s^{\text{Co-S}}/\Delta U$ is $+0.07 \text{ erg}\cdot\text{cm}^{-2}\cdot\text{V}^{-1}$.

4.5.2. Mechanisms of MEC

Table 4.2 summarizes the K_s values and MEC coefficients found in this work. The table primarily evidences that the H monolayer reduces the overall PMA of a Co/Au(111) film ($K_s^{\text{Co-H}} < 0$) and that OH adsorption has nearly no impact with respect to a bare surface. The value of $K_s^{\text{Co-MOL}}$ is found larger upon CO and S adsorption. The value of $K_s^{\text{Co-CO}}$ is consistent with past determination [27]. These data are therefore demonstrating that the surface anisotropy energy is depending on the adsorbate. Regarding MEC data, one notices the very

good agreement between the different methods of determination developed in paragraphs (a) and (b).

Linkage	Bare surface (UHV)	H	OH	CO	S
t^* (ML)	4-5	1.7	4	7.5	6.5
K_s (erg·cm ⁻²)	0	-0.36	-0.05	0.25	0.15
$\Delta K_s/\Delta U$ ^{a)} (erg·cm ⁻² ·V ⁻¹)	NA	NA	-0.558	-0.204	+0.07
$\Delta K_s/\Delta U$ ^{b)} (erg·cm ⁻² ·V ⁻¹)	NA	-0.177	-0.526	NA	NA
$(\Delta H_c/H_c)/\Delta U$ (%/V)	NA	-45	-175	-60	+15

a) Determination using Co films of thickness close to t^* (see 4.5.1 section b)

b) Determination using Co films of thickness $> t^*$ (see 4.5.1 section a)

Table 4.2 the calculated t^* , K_s ; $\Delta K_s/\Delta U$ and $(\Delta H_c/H_c)/\Delta U$ of Co covered with different molecular overlayer.

It is worth noting that even though $(\Delta H_c/H_c)/\Delta U$ cannot be used to quantitatively determine $\Delta K_s^{Co-S}/\Delta U$, when different surface chemistry are compared, the two parameters follow the same law of variation with the applied potential and they also vary approximately with similar ratio (the deviation is within 30%). Namely, H_c varies linearly when K_s varies linearly and H_c is nearly proportional to HER current when K_s varies with HER (**Fig. 4.17**).

Linkage	Bare surface (UHV)	H	OH/O	CO	S
Most stable adsorption sites	NA	fcc / hcp	hcp / fcc	fcc / hcp	fcc / hcp
Relative change of the distance between topmost the first 2 Co planes $\Delta d_{12}/d_{12}$	-1.7%	+4% [30]	+0.8% [31]	-1%	-3% [32]
d (ads-Co) (Å)	NA	~1.86 [8]	1.9 [33]	1.9 [34]	2.17 [35]
$\Delta\Phi$ (eV)	0	~ 0 [36]	+ 1 ($\theta_{OH} = 0.25$) [37]	+ 1.2 [38]	0.2 ($\theta=0.33$) [35]
Charge on Co atom σ (e/atom) ($\theta_{Co-ads} \sim 0.5$)		<0.1 [36] 0.29 [29]	0.77 [29] 0.36 [37]	+0.28 [37]	~+0.2 [32]
Binding energy E_{ads} (eV/atom)	NA	-2.87 [30] -2.72 [39] ($\theta = 1$)	-3.45 [39] -2.7 ($\theta= 0.5$) [31] -2.2($\theta=0.25$) [31] -3.78 [37]	-1.66 [39] -1.11 [40] -1.36 [31]	-2.92 [32] ($\theta=0.33$)
Magnetic moment of surface atoms (μ_B)	1.7	0.9 [41]	0.4 – 1.4 [40]	1.4 NN [40] 1.7 NNN [40] 0.87 (Top)	1.7 [32]

Table 4.3: Structure and electronic data derived from DFT calculation of Co-molecules monolayers.

A pure electric field effect may be inferred when K_S varies linearly and reversibly with the applied voltage as is the case for H-, OH- and S- covered surfaces over the entire potential range (see **Fig. 4.11**; **Fig. 4.12** and **Fig. 4.18**); This is also the case for CO-modified surfaces when no HER takes place (see **Fig. 4.17**).

In fact, according to the structure of the electrochemical contact metal/electrolyte (see **Chapter 2, Fig. 2.7**), the electric field $E = U/d$, where d is the distance between the Co surface plane and the first plane of compensating charges in solution. This expression holds true for potential far enough from the point of zero charge (pzc) of the surface (close to pzc the capacity of ionic double-layer structure would strongly depend on the applied potential). The pzc of cobalt was estimated to be -0.9 to -1.1 V_{MSE} (i.e. close to the dissolution onset potential of H-terminated Co, see **Fig. 4.9**) [28]. Given the values of $\Delta\Phi$ (metal work function change upon molecule adsorption) in **Table 4.3**, the pzc of S- and CO-terminated surfaces is more positive than -0.9 V. Therefore all MEC measurements reported here are performed in a potential range sufficiently more negative than the pzc. Hence a linear dependence of χ with potential U implies a pure electric field effect as long as the surface chemistry remains *unchanged*. This behavior is also in very good agreement with the fact that the reported MEC is a pure surface effect (**Fig. 4.8**) since the E-field is very efficiently screened at metal surfaces, within the first atomic plane.

In presence of HER, MEC has different origin since $K_S^{Co-CO-HER}$ is proportional to the current density. Tournier *et al.* attributed this behavior to the adsorption of atomic hydrogen at the vacancy sites of the CO-terminated Co film. [27] In fact, it is well-known that the hydrogen evolution reaction (HER) involves this intermediate species. At the CO-terminated surface, the HER is taking place for $U < -1.25$ V (in **Fig. 4.17.d**). In this region of potential, one may consider to first order that the surface anisotropy energy $K_S^{Co-CO-HER}$ is the sum of two contributions K_S^{Co-H} and K_S^{Co-CO} , the weight of each contribution is related to the corresponding adsorbate surface coverage, because the magnetic domains are much larger

than the molecular domains (in other words, one may consider the surface with a uniform surface chemistry CO + H). The potential dependence of $K_S^{Co-CO-HER}$ is assigned to the potential dependence of H_{ads} coverage since the CO coverage is *constant* and equal to ~ 0.6 . Within this scheme, the observed SRT upon HER is consistent with the fact that $K_S^{Co-H} \sim -0.34$ erg/cm² and $K_S^{Co-CO} = 0.05$ erg/cm², because $K_S^{Co-CO-HER}$ may become smaller than K_S^{Co-CO} . The fact that HER has no influence on MEC at the as deposited layers (**Fig. 4.11**) is consistent with a H_{ads} coverage that is independent of the applied potential. This finding is in agreement with DFT calculations [29].

4.5.3. Correlation MAE - structure of modified surfaces

The remaining of the discussion is an attempt to identify trends between the K_S , MEC coefficient with *calculated* structural and electronic properties of the cobalt surfaces (see **Table 4.2** and **Table 4.3**). Unfortunately these DFT calculations never give the anisotropy energy because this is very challenging. MAE is in fact a small energy (\sim meV/atom) compared to all other energies (binding, adsorption energies) which are in the range \sim eV range.

As explained in **Chapter 2**, K_S is sensitive to magnetoelastic contribution. The increase of K_S may be related to the variations of the distance between the two topmost Co atomic plans (d_{12}). Following the formulation of Gutjahr-Löser *et al.*, we can write, $K_{ME} = B_2 \times \Delta d_{12}$. In this expression $B_2 = -2.9 \cdot 10^8$ erg/cm³ is the magnetoelastic coefficient along the Co(0001) direction in the hcp representation [42]. For a compression of the topmost plane only, K_{ME} will therefore contribute to K_S^{Co-MOL} the magnetic anisotropy energy of the Co/electrolyte interface. A vertical compression leads to an increase of K_S^{Co-MOL} since B_2 is negative.

Figure 4.20 shows plot E_{ads} (panel a), σ (panel b) and K_{ME} (panel c) as a function of K_S^{Co-MOL} . Panel (a) suggests that K_S^{Co-MOL} is not correlated with the adsorption energy. K_S^{Co-MOL} does not seem to be correlated with the charge transfer at the Co – molecule linkage. There is surprisingly a reasonable correlation between K_S and K_{ME} .

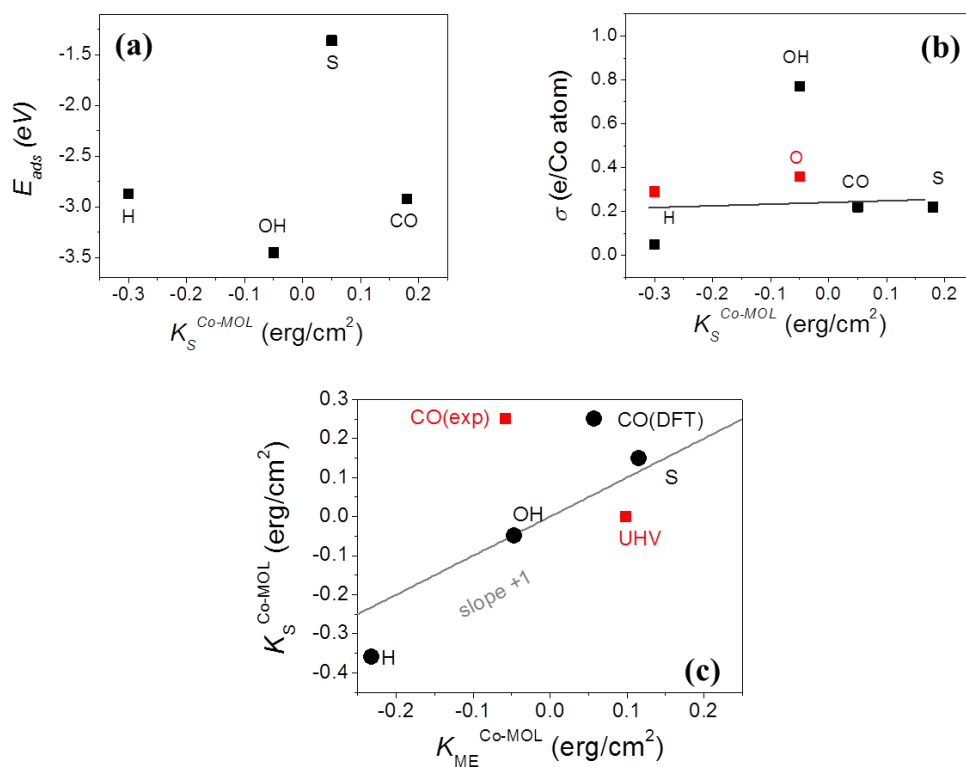


Fig. 4.20: Plots of E_{ads} , σ (see Table 4.3) and K_{ME} (see Table 4.4) as a function of experimental value of K_S^{Co-MOL} (see Table 4.2).

Experimentally we measure ΔK_S^{Co-MOL} upon adsorption of a molecular layer on the H-terminated surface. **Table 4.4** compare K_S^{Co-MOL} ($K_S^{Co-MOL} = \Delta K_S^{Co-MOL} + K_S^{Co-H}$, where $K_S^{Co-H} = -0.34$ erg/cm²) with K_{ME} . In the case of H and CO adsorption K_{ME} is clearly different from K_S^{Co-MOL} which means that surface electronic effects associated with the hybridization of Co surface atoms with H or CO adsorbates contribute also to the PMA increase. In the case of OH- and S-terminated Co surface, the good agreement suggests that surface relaxation is the dominant factor.

Linkage	H	OH/O	CO	S
K_S^{Co-MOL} ($\text{erg}\cdot\text{cm}^{-2}$)	-0.34	-0.05	0.15	0.25
K_{ME} ($\text{erg}\cdot\text{cm}^{-2}$)	-0.232	-0.0464	0.058	0.116
$\Delta d_{12}/d_{12}$	0	0.032	0.05 ^{a)}	0.07

a) Value consistent with in situ XRD data (F. Reikowski *et al.* to be published)

Table 4.4: Comparison between the experimental value of K_S^{Co-MOL} and gain in magneto elastic contribution K_{ME} associated with the relative compression of the distance $\Delta d_{12}/d_{12}$ with respect to H-covered Co. See text.

4.5.4. Correlation MEC coefficient - structure of modified surfaces

Assuming that potential induced surface relaxation is negligible, MEC may be related to a voltage induced modification of the charge transfer at the Co-Molecule interface.

Fig. 4.21 presents the charge transfer σ as a function of $\Delta K_S^{Co-MOL}/\Delta U$. We do not observe a clear correlation. $\Delta K_S^{Co-MOL}/\Delta U$ is probably correlated with the Co – molecule bond polarizability. Unfortunately such information is difficult to find in the literature.

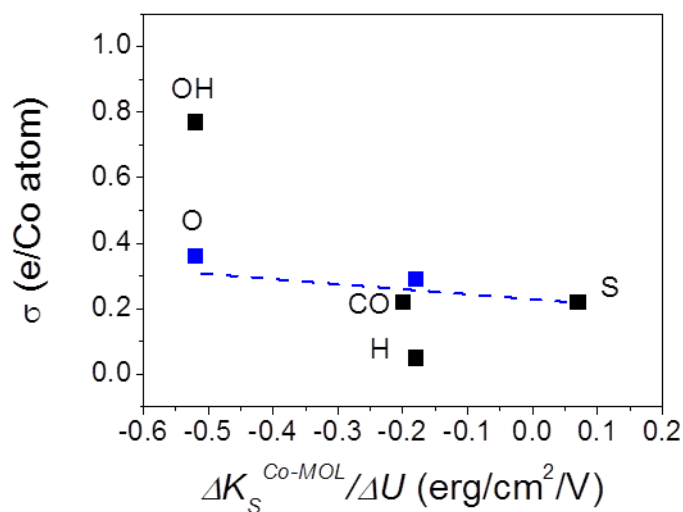


Fig. 4.21: Plot of σ (see Table 4.3) as a function of experimental value of $\Delta K_S^{Co-MOL}/\Delta U$ (see Table 4.2).

4.6. Conclusions

In this chapter, we demonstrated that the magnetic anisotropy energy (MAE) may be modified through the surface chemistry of the Co/Au(111) layer. Taking the bare cobalt as reference we found that the K_S value is essentially related to the linkage Co-X, with X = H, OH, C, S. K_S increases with the linkage in the following order: -H<-OH<-S ~ -C. It seems difficult to correlate the K_S value with the charge transfer between the Co atoms and the attached molecule. On the other hand, K_S appears correlated with the Co vertical strain induced by the molecular layer.

Regarding MEC, we have identified different mechanisms. A pure electric field effect may be inferred when K_S varies linearly and reversibly with the applied voltage. This is the case for H-, OH- and S- covered surfaces over the entire potential range. This is also the case for CO-modified surfaces when no HER takes place. It is further interesting to notice that the sign and amplitude of the E-field effect depends on the organic monolayer. $\Delta K_S/\Delta U$ increases in the order: -S<-H<-CO<-OH. We couldn't establish a clear correlation between the MEC

effect and a simple system parameter. DFT calculations are probably necessary to a better understanding of our experimental results.

4.7. References

- [1] R. Vollmer, T. Gutjahr-Loser, J. Kirschner, S. van Dijken, B. Poelsema, Spin-reorientation transition in Ni films on Cu(001): The influence of H₂ adsorption, *Physical Review B*, 60 (1999) 6277-6280.
- [2] D. Matsumura, T. Yokoyama, K. Amemiya, S. Kitagawa, T. Ohta, CO induced spin reorientation transition of Co/Pd(111) studied by XMCD and XPS, *Physica Scripta*, T115 (2005) 583-585.
- [3] X.M. Zhang, S. Mizukami, T. Kubota, Q.L. Ma, H. Naganuma, M. Oogane, Y. Ando, T. Miyazaki, Large change of perpendicular magnetic anisotropy in Cobalt ultrathin film induced by varying capping layers, *Journal of Applied Physics*, 111 (2012) 07B320.
- [4] B. Koslowski, A. Tschetschetkin, N. Maurer, P. Ziemann, J. Kucera, A. Gross, 4,4'-Dithiodipyridine on Au(111): A Combined STM, STS, and DFT Study, *J. Phys. Chem. C*, 117 (2013) 20060-20067.
- [5] B. Hammer, Y. Morikawa, J.K. Norskov, CO chemisorption at metal surfaces and overlayers, *Physical Review Letters*, 76 (1996) 2141-2144.
- [6] M. Gajdos, A. Eichler, J. Hafner, CO adsorption on close-packed transition and noble metal surfaces: trends from ab initio calculations, *J. Phys.-Condes. Matter*, 16 (2004) 1141-1164.
- [7] G. Blyholder, Molecular orbital view of chemisorbed carbon monoxide, *Journal of Physical Chemistry*, 68 (1964) 2772-2777.
- [8] J.L. Whitten, H. Yang, Theory of chemisorption and reactions on metal surfaces, *Surface Science Reports*, 24 (1996) 59-124.
- [9] M.E. Bridge, C.M. Comrie, R.M. Lambert, Chemisorption studies on cobalt single-crystal surfaces.1. carbon-monoxide on CO(0001), *Surface Science*, 67 (1977) 393-404.
- [10] H. Papp, The chemisorption of carbon-monoxide on a Co(0001) single-crystal surface –

studied by LEED, UPS, EELS, AES and work function measurements, *Surface Science*, 129 (1983) 205-218.

[11] T. Hayashi, Y. Morikawa, H. Nozoye, Adsorption state of dimethyl disulfide on Au(111): Evidence for adsorption as thiolate at the bridge site, *The Journal of Chemical Physics*, 114 (2001) 7615-7621.

[12] T. Hayashi, A. Fricke, K. Katsura, C. Kodama, H. Nozoye, Adsorption state of diethyldisulfide on Au(111) studied with a combined system of HREELS and STM, *Surface Science*, 427-428 (1999) 393-397.

[13] J.C. Love, L.A. Estroff, J.K. Kriebel, R.G. Nuzzo, G.M. Whitesides, Self-assembled monolayers of thiolates on metals as a form of nanotechnology, *Chem. Rev.*, 105 (2005) 1103-1169.

[14] R.G. Nuzzo, B.R. Zegarski, L.H. Dubois, Fundamental-studies of the chemisorption of organosulfur compounds on Au(111)-implications for molecular self-assembly on gold surfaces, *J. Am. Chem. Soc.*, 109 (1987) 733-740.

[15] T. Ishida, S. Yamamoto, W. Mizutani, M. Motomatsu, H. Tokumoto, H. Hokari, H. Azehara, M. Fujihira, Evidence for cleavage of disulfides in the self-assembled monolayer on Au(111), *Langmuir*, 13 (1997) 3261-3265.

[16] C. Vericat, M.E. Vela, G. Corthey, E. Pensa, E. Cortes, M.H. Fonticelli, F. Ibanez, G.E. Benitez, P. Carro, R.C. Salvarezza, Self-assembled monolayers of thiolates on metals: a review article on sulfur-metal chemistry and surface structures, *RSC Adv.*, 4 (2014) 27730-27754.

[17] M. Volmeruebing, M. Stratmann, A surface analytical and an electrochemical study of iron surfaces modified by thiols, *Appl. Surf. Sci.*, 55 (1992) 19-35.

[18] Longchun Cheng, Steven L. Bernasek, Andrew B. Bocarsly, and T. A. Ramanarayanan, Adsorption and decomposition of 1-alkanethiols on the Fe(100) surface, *Chemistry of Materials* 7 (10), 1807 (1995).

[19] James E. Sadler, Doug S. Szumski, Agnieszka Kierzkowska, Samantha R. Catarelli, Kevin Stella, Richard J. Nichols, Mariano H. Fonticelli, Guillermo Benitez, Barbara Blum, Roberto

C. Salvarezza, and Walther Schwarzacher, Surface functionalization of electro-deposited nickel, *Phys. Chem. Chem. Phys.* 13 (40), 17987 (2011).

[20] Paul G. Hoertz, Jeremy R. Niskala, Peng Dai, Hayden T. Black, and Wei You, Comprehensive Investigation of Self-Assembled Monolayer Formation on Ferromagnetic Thin Film Surfaces, *Journal of the American Chemical Society* 130 (30), 9763 (2008).

[21] Sébastien Devillers, Alexandre Hennart, Joseph Delhalle, and Zineb Mekhalif, 1-Dodecanethiol self-assembled monolayers on cobalt, *Langmuir* 27 (24), 14849 (2011).

[22] D.A. Chen, C.M. Friend, H. Xu, Reactions of methanethiol on cobalt-covered Mo(110), *Langmuir*, 12 (1996) 1528-1534.

[23] Y. Xie, D.Y. Wu, G.K. Liu, Z.F. Huang, B. Ren, J.W. Yan, Z.L. Yang, Z.Q. Tian, Adsorption and photon-driven charge transfer of pyridine on a cobalt electrode analyzed by surface enhanced Raman spectroscopy and relevant theories, *Journal of Electroanalytical Chemistry*, 554 (2003) 417-425.

[24] G.F.S. Andrade, M.L.A. Temperini, Identification of species formed after pyridine adsorption on iron, cobalt, nickel and silver electrodes by SERS and theoretical calculations, *J. Raman Spectrosc.*, 40 (2009) 1989-1995.

[25] P. Zelenay, L.M. Ricejackson, A. Wieckowski, Adsorption of pyridine on polycrystalline gold electrode studied by radioactive-labeling method, *Langmuir*, 6 (1990) 974-979.

[26] T. Dretschkow, D. Lampner, T. Wandlowski, Structural transitions in 2,2'-bipyridine adlayers on Au(111)—an in-situ STM study¹, *Journal of Electroanalytical Chemistry*, 458 (1998) 121-138.

[27] N. Tournerie, A.P. Engelhardt, F. Maroun, P. Allongue, Influence of the surface chemistry on the electric-field control of the magnetization of ultrathin films, *Physical Review B*, 86 (2012) 104434.

[28] A. Hamelin, T. Vitanov, E. Sevastyanov, and A. Popov, The electrochemical double layer on sp metal single crystals. The current status of data, *J. Electroanal. Chem.* 145, 225 (1983).

- [29] N. Di, J. Kubal, Z. Zeng, J. Greeley, F. Maroun, P. Allongue, Influence of controlled surface oxidation on the magnetic anisotropy of Co ultrathin films, *Applied Physics Letters*, 106 (2015).
- [30] D. J. Klinke Ii and L. J. Broadbelt, A theoretical study of hydrogen chemisorption on Ni(111) and Co(0001) surfaces, *Surf. Sci.* **429** (1–3), 169 (1999).
- [31] S. H. Ma, Z. Y. Jiao, T. X. Wang, and X. Q. Dai, First-principles studies of oxygen chemisorption on Co(0001), *Surf. Sci.* 619 (0), 90 (2014).
- [32] L. G. Wang, E. Y. Tsymbal, and S. S. Jaswal, First-principles study of adsorption of methanethiol on Co(0001), *Phys. Rev. B* **70** (7), 075410 (2004); L. G. Wang, E. Y. Tsymbal, and S. S. Jaswal, Structural and magnetic properties of clean and methylthiolate-adsorbed Co(0001) surfaces: a first-principles study, *Journal of Magnetism and Magnetic Materials* 286 (0), 119 (2005).
- [33] A. Foelske, J. Kunze, H.H. Strehblow, Initial stages of hydroxide formation and its reduction on Co(0001) studied by in situ STM and XPS in 0.1 M NaOH, *Surface Science*, 554 (2004) 10-24.
- [34] Š. Pick, H. Dreysse, Calculation of gas adsorption effect on magnetism of Co(0 0 0 1), *Surface Science*, 474 (2001) 64-70.
- [35] S.H. Ma, Z.Y. Jiao, Z.X. Yang, Coverage effects on the adsorption of sulfur on Co(0001): A DFT study, *Surface Science*, 604 (2010) 817-823.
- [36] K. Christmann, Interaction of hydrogen with solid surfaces, *Surf. Sci. Rep.* **9** (1-3),1 (1988).
- [37] D.S.D. Gunn, S.J. Jenkins, Adsorbate modification of the structural, electronic, and magnetic properties of ferromagnetic fcc {110} surfaces, *Physical Review B*, 83 (2011) 115403.
- [38] J. Lahtinen, J. Vaari, and K. Kauraala, Adsorption and structure dependent desorption of CO on Co(0001), *Surf. Sci.* **418** (3), 502 (1998).
- [39] X.-Q. Gong, R. Raval, P. Hu, CO dissociation and O removal on Co(0 0 0 1): a density functional theory study, *Surface Science*, 562 (2004) 247-256.

- [40] S. Pick, Density-functional study of the CO adsorption on ferromagnetic Co(0001) and Co(111) surfaces, *Surf. Sci.* **601** (23), 5571 (2007).
- [41] Stepán Pick and Hugues Dreyssé Tight-binding study of ammonia and hydrogen adsorption on magnetic cobalt systems, *Surf. Sci.* **460** (1-3), 153 (2000).
- [42] Gutjahr-Loser, T., et al. (2000). Magnetoelastic coupling in Co thin films on W(001). *Journal of Magnetism and Magnetic Materials* 220(1): L1-L7.

Chapter 5 Influence of hydrogen on the magnetic anisotropy of Pd/Co bilayers and PdCo alloy layers

5.1. Introduction

Hydrogen loading in metallic multilayers opens interesting possibilities to change the structural, electronic, magnetic and optical properties of these systems. Previous studies report some examples of an interesting effect of hydrogen on the properties of the layers [1, 2].

The palladium-hydrogen-system has been a largely investigated topic in the past, due to the high storage capacity of palladium, and its ability to release the gas easily at room temperature [3-5]. Hydrogen adsorption and/or absorption mechanism [4, 6] has since long been of great interest. The induced variations of the structure [5] are well studied. It has been since long known that there are two phases in the Pd-H₂ system [4]. The α -phase has lattice constants close to Pd metal. It is characterized by a rather low concentration of hydrogen on interstitial sites. At room temperature the H: Pd ratio for this phase is 0.03. As more hydrogen dissolves in the metal, the lattice constant increases up to 3.5% where the β -phase appears [7, 8]. The H: Pd ratio of the β -phase is approximately 0.6 at room temperature. Both the α - and the β -phase have the same metal lattice structure and consist of octahedrally coordinated hydrogen atoms.

H absorption into Pd induces mechanical stress [3, 9] and changes of the optical properties [3, 10]. In the case of a thin Pd film deposited on a rigid substrate, the limited in-plane lattice expansion due to the substrate leads to compressive mechanical stress [3]. Stafford *et al.* [9] claimed a compressive surface stress about -2GPa with a maximum atomic H/Pd loading of 0.63, corresponding to the formation of β -phase. The studies of Leervad Pedersen *et al.* [3] about H₂ absorption in thin Pd-films deposited on glass demonstrates a changing of the electrical resistivity and optical absorption coefficient, which scales with the increasing hydrogen content in the metal lattice. For examples, they found that the Pd transmittance increases upon H absorption.

Many studies have been devoted to the combination of Pd layers with other functional thin films, especially with magnetic materials [11, 12]. The use of hydrogen to modify the

electronic structure in magnetic thin films and heterostructures has opened new routes to tailor the magnetic properties [13].

This chapter is dedicated to the study of the influence of H adsorption and absorption on the magnetic properties of Pd/Co bilayers and PdCo alloy layers. Two methods for preparing such layers will be described: electrodeposition and sputtering. The electrochemical properties of Pd layers on Au/Si(111) are detailed in the Appendix.

5.2. Experimental methods

Pd–Co bilayers or alloys were prepared using two different methods: electrochemical deposition and sputter deposition.

For electrochemical deposition, Pd-Co layers were grown on the Au(111)/Si(111) substrate in the P-MOKE electrochemical cell. In the case of Pd/Co bilayers, the conventional pH ~ 3.5-4 1mM CoSO₄ + 0.1M K₂SO₄ + 1mM KCl + 1mM H₂SO₄ was employed to grow 2D Co thin films. Following the deposition of Co, Pd was grown in 1mM K₂PdCl₄ + 0.1M K₂SO₄ + 1mM KCl + 1mM H₂SO₄ pH ~ 3.5-4 electrolyte. In the case of PdCo alloys, a pH ~ 3.5 -4 1.5mM K₂PdCl₄+ 1mM CoSO₄ + 0.1M K₂SO₄ + 1mM KCl + 1mM H₂SO₄ was used. After Co and Pd deposition, Co²⁺ and PdCl₄²⁻ were removed from the cell by circulating pH ~ 3.5-4 0.1M K₂SO₄ + 1mM KCl + 1mM H₂SO₄ electrolyte. H adsorption and absorption were performed in the latter electrolyte.

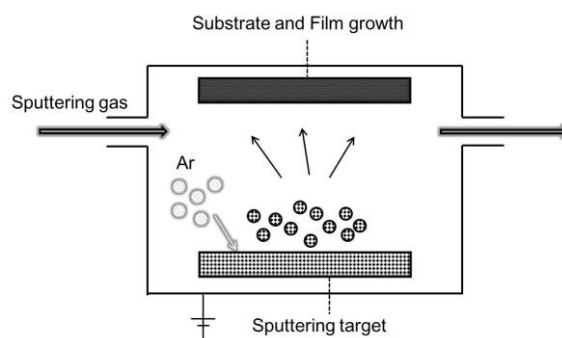


Fig.5.1: Mechanism of the sputter deposition.

For sputter deposition, the investigated samples were prepared during my three-month exchange program in the Department of Materials Science and Engineering, MIT. Sputter deposition (see Fig.5.1) is a physical vapor deposition (PVD) method of thin film deposition

by sputtering. This involves ejecting material from a "target" that is a source onto a "substrate" such as a silicon wafer. Sputtered atoms ejected from the target have a wide energy distribution, typically up to tens of eV (100,000 K). The sputtered ions (typically only a small fraction of the ejected particles are ionized — on the order of 1%) can ballistically fly from the target in straight lines and impact energetically on the substrates or vacuum chamber (causing resputtering).

Thin films studied in this chapter were deposited using a home-built high-vacuum magnetron sputtering setup, a modified Sputtered Films Incorporated (SFI) system (see **Fig.5.2** [14]) A turbomolecular pump attains a background pressure of $\sim 10^{-6}$ Torr. An improved background pressure of $\sim 8\text{-}20 \cdot 10^{-8}$ Torr is achieved by using two liquid nitrogen cold traps. The sputtering gas is ultrahigh purity Ar (99.999%), and a sputtering pressure of 2.0 mTorr or 3.0 mTorr is maintained by balancing the pumping speed through a mechanical baffle and the flow rate of Ar is fixed at $30.0 \text{ cm}^3/\text{min}$.

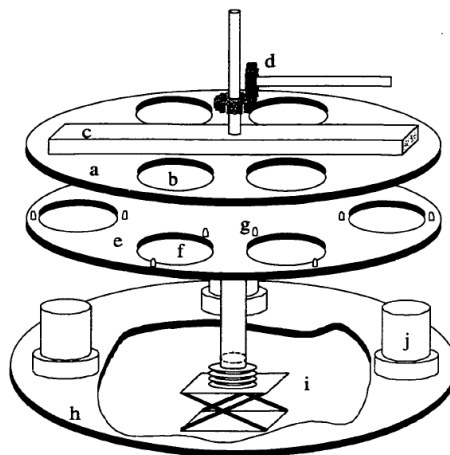


Fig. 5.2: Interior of the high-vacuum magnetron sputterer: (a) substrate table, (b) hole for mounting a substrate holder, (c) liquid nitrogen reservoir, (d) table rotation assembly, (e) mask table, (f) hole for mounting a mask, (g) pins to align the mask and substrate table, (h) chamber door, (i) cutaway showing the jack and bellows below the chamber door, (j) chimney and a sputtering gun assembly. Adapted from [14].

This sputtering system is equipped with four sputtering guns (**Fig. 5.2.(j)**). All metals are sputtered using DC power supplies. Ferromagnetic metals (and some nonmagnetic metals) are sputtered from two-piece donut-shaped targets in SFI guns with especially strong built-in magnetic fields. Metals such as Ta and Cu are sputtered from a 2" planar U.S. sputtering gun, whereas precious metals such as Pd and Au are sputtered from a 1" planar U.S. sputtering gun.

Each sputtering gun is directed upwards and covered with a cylindrical chimney to limit the angular dispersion of the sputtered material. A pneumatically actuated shutter at the top of each chimney is opened and closed for deposition with controlled timing. Substrates used here are commercially purchased 380 μ m-Si (001) with a 50-nm thick overlayer of thermally grown oxides. They are mounted on the substrate table (**Fig. 5.2.(a)**), face down towards the sputtering guns. Deposition can be done with the substrate table either stationary above a particular gun or rotating with ~ 7 revolutions per minute. The rotating mode allows for more precise control of thickness of ultrathin films studied in this chapter. The sputtering system is also equipped with a second disk called the “mask changer” (**Fig. 5.2.(e)**), to block off selected substrates during rotating depositions, so that thin films of different thicknesses or compositions can be deposited in one pump-down.

The sputtering rate typically scales with the sputtering current (or sputtering power in the case of RF sputtering). The deposition rate of a material is calibrated by measuring the thickness of a “calibration film” and dividing by the sputtering time for this film. In some cases, the film thickness is measured with X-ray reflectometry (XRR) using a Bruker D8 HRXRD system.

In our work, all the depositions were achieved with the substrate table rotating of ~ 7 revolutions per min. For all the Pd-Co samples studied in this chapter, 3nm Ta was grown firstly on SiO_x(50nm) covered Si wafer using a current $I = 0.05$ A. 4nm Pt was deposited on top of Ta afterwards with $I = 0.05$ A, $P = 22$ W and $V = 437$ V. Pd/Co bilayers and PdCo alloys are then sputtered above. Before each deposition, the Co target is pre-sputtered for 2min to remove the oxidized surface layer. The experimental conditions for Pd are $I_{Pd} = 0.05$ A, $P_{Pd} = 18$ W and $V_{Pd} = 355 - 360$ V. For Pd/Co bilayers, Co was sputtered on top of Pt with $I_{Co} = 0.4$ A, $P_{Co} = 125$ W and $V_{Co} = 338$ V under 3.0mTorr for various durations to have different thickness (0.8nm, 1.05nm, 1.2nm and 1.35nm; the velocity of Co sputter deposition is 1.08nm/min). Pd was then grown for 1min. The thickness of Pd is around 1.9nm. For PdCo alloys, both the shutters of gun 1 with Pd target and gun 2 with Co target underneath are open to deposit Pd and Co together on the substrates. And the Co sputtered conditions are $I_{Co} = 0.3$ A; 0.4A and 0.5A, $P_{Co} = 125$ W and $V_{Co} = 335 - 340$ V. The three Co sputtering currents allowed to change the ratio of Pd to Co in the PdCo alloys. Different co-sputtering durations (1min and 2min) are also performed to obtain alloys with different thickness. The pressure in the sputtering chamber was maintained at 3.5mTorr. No further treatment was done before doing in-situ P-MOKE measurement.

5.3. Preparation of Pd/Co bilayers and influence of H adsorption/absorption on the Pd/Co bilayers' properties

In this part, results about preparation of Pd/Co bilayers by electrodeposition and sputter deposition will be given. Next the magnetic properties as a function of H adsorption and absorption will be studied.

5.3.1. Pd/Co bilayer prepared through electrochemical deposition

The difficulties in electrodepositing Pd-Co system lie in the different potential regions to deposit and dissolve Pd and Co. The previous studies show that Co deposition onset is $\sim -1.3\text{V}$. In this potential region HER occurs, inhibiting the growth of more than 1ML of Pd (see Appendix).

Inspired from the pulse procedure to deposit layer-by-layer 2D Pt layer [15], the following procedure is conceived and presented by **Fig. 5.3**: 4.2-ML Co layer was grown at -1.3V with an in-plane magnetic anisotropy (see **Fig. 5.3 (a)**, the $M-H$ curve is linear and reversible). Next 1ML-Pd is deposited on top of the Co at -1.1V for 600s. The changing of $M(1\text{KOe})$ and M_R demonstrates that with 1-ML Pd on top, Co goes through a spin reorientation transition (SRT), where the magnetization turns from in-plane to perpendicular (**Fig. 5.3 (b)**). Then the applied potential is scanned several times back and forth between -0.9V to -0.8V with 10mV/s separated by a potential plateau during 150s in order to grow several more monolayers of Pd without dissolving the as-deposited Co layers underneath. At the end, the potential is brought to -0.75V for 150s (the respective hysteresis loop is illustrated by **Fig. 5.3 (c) - (f)**).

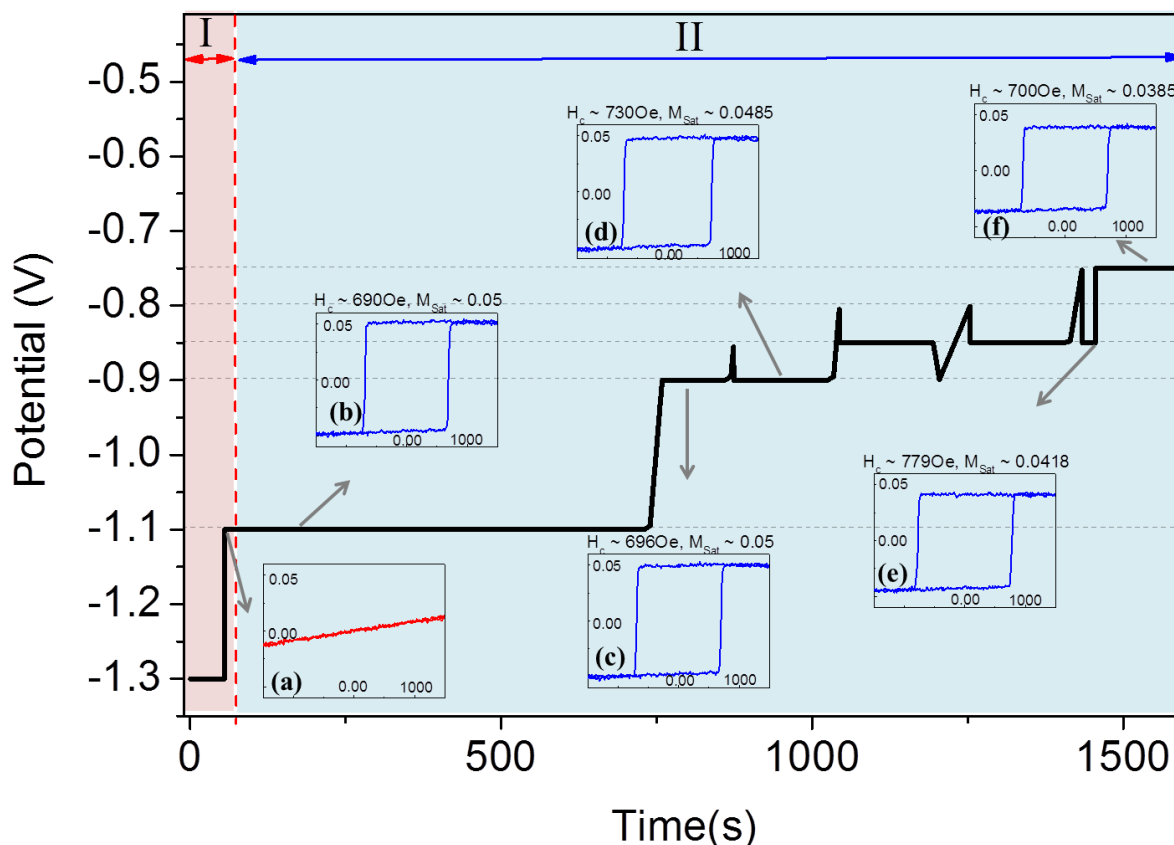


Fig. 5.3: an electrochemical approach to deposit the Pd/Co bilayer --- region I of the light red background corresponding to the deposition of 4.2-ML Co at -1.3V during 50s and stabilization at -1.1V for 15s in pH ~ 3.5-4 1mM Co(II) plating electrolyte; region II of the light blue background illustrating in pH ~ 3.5-4 1mM Pd(II) plating solution at -1.1V during 600s, then at -0.9V for 100s. The Pd is then deposited with potential scans between -0.9V and -0.8V with 10mV/s, separated by potential steps for 150s. At the end, the Pd is further deposited at -0.75V during 100s. A set of M - H curves during the Co and Pd deposition are extracted from the in-situ P-MOKE measurement.

During the whole deposition procedure, M - H curves and reflectivity signal (**Fig. 5.4**) are acquired. The variations of reflectivity during ~ 1-ML Pd deposition at -1.1V are not straightforward to rationalize. The increase may be attributed to the growing of Pd on the bare Co surface, and the decrease of the reflectivity hereafter may be due to the modification of the Pd optical properties due to H ad/absorption.

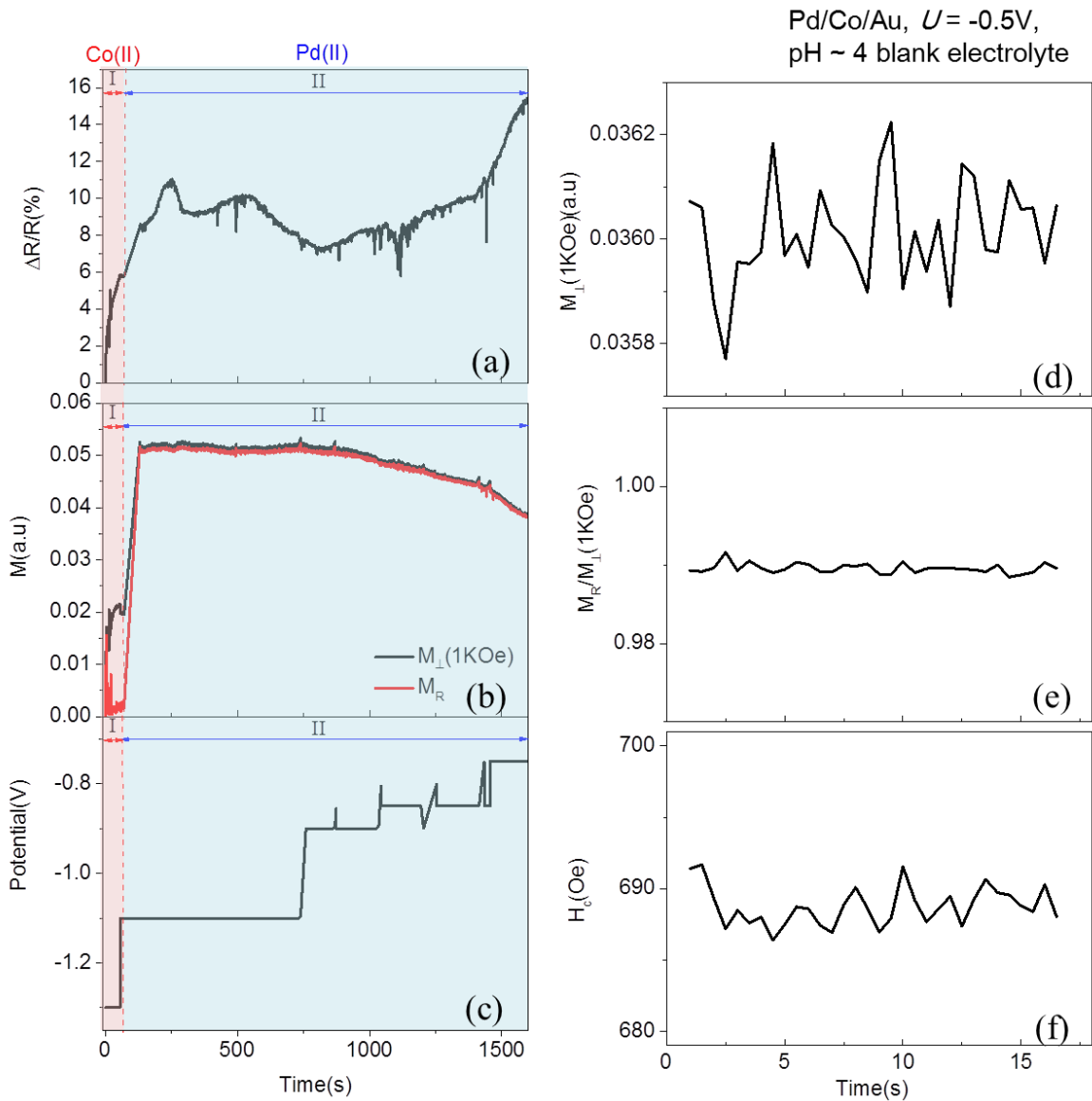


Fig. 5.4: (a) – (c) the relative reflectivity $\Delta R/R$; the magnetization at 1kOe $M(1kOe)$ and remanence M_R as a function of time; potential sequences during the deposition of Pd on top of 4.2-ML Co. The experimental conditions are described above for Fig. 5.3. (d) – (f) perpendicular magnetization $M(1kOe)$; $M_R/M(1kOe)$ and coercivity H_c of the deposited Pd/Co bilayer in a pH ~ 4 blank electrolyte at -0.5V.

During the potential sweep-and-step deposition procedure, $M(1kOe)$ continues to decrease; and the reflectivity increases all the time, indicating the thickening of the Pd layer. The decrease of $M(1kOe)$ is thus attributed to the light absorption by the Pd overlayer [16]. After circulating pH ~ 4 blank electrolyte, the protection of the Co layer by the Pd overlayer is tested by bringing the potential at -0.5V. We observed no changes at this potential (Fig. 5.4 (d)-(f)). The grown Pd/Co bilayer has a spontaneous perpendicular magnetization with $H_c \sim 690Oe$.

5.3.2. Pd/Co bilayers prepared through sputter deposition

The deposition procedure of sputtered Pd/Co bilayers is explained in section 5.2. The morphology of the deposited Pd-Co bilayer is measured by the ex-situ AFM. Pd/Co bilayer is schematized in **Fig. 5.5**. $0.5\mu\text{m} * 0.5\mu\text{m}$ and $1\mu\text{m} * 1\mu\text{m}$ AFM images are presented for Pd(1.9nm)/Co(1.35nm) bilayers. The height profiles along the white line presented in each AFM image are also displayed. The AFM images indicate that the film adopts a granular morphology with a grain size of 10-30nm.

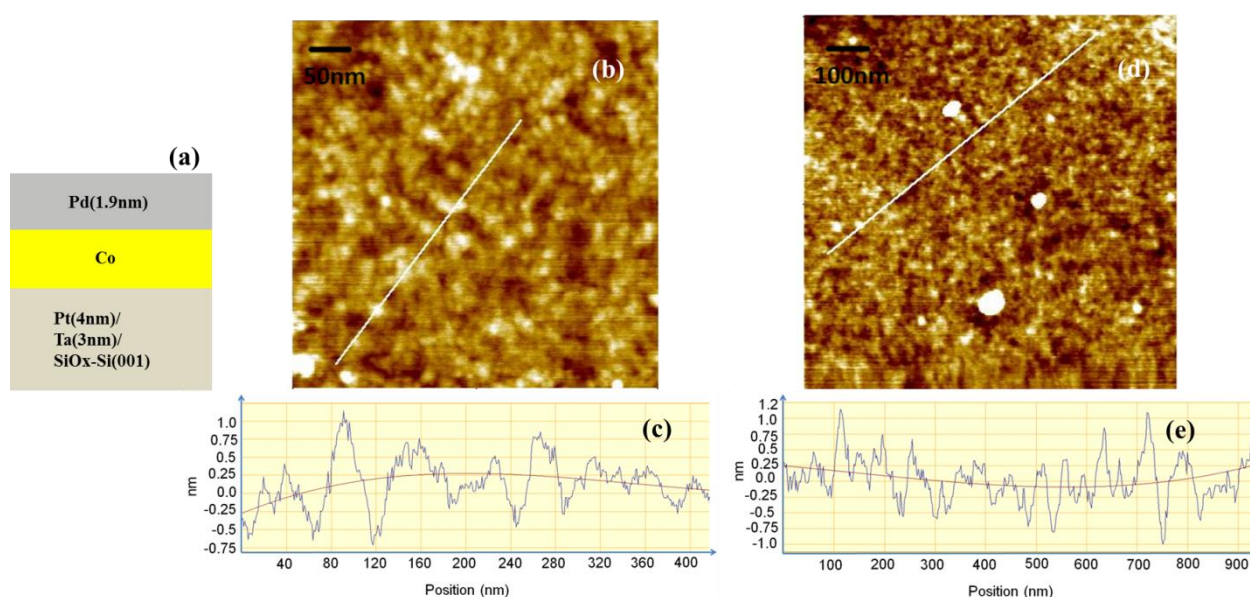


Fig. 5.5: (a) scheme of Pd/Co bilayer structure; (b) $0.5\mu\text{m} * 0.5\mu\text{m}$ AFM image of Pd(1.9nm)/Co(1.35nm) bilayer; (c) height profile along the white line of image (b); (d) $1\mu\text{m} * 1\mu\text{m}$ AFM image of Pd(1.9nm)/Co(1.35nm) bilayer; (e) height profile along the white line of image (d).

The magnetic properties of the sputtered bilayers in the $\text{pH} \sim 3.5 - 4$ $0.1\text{M K}_2\text{SO}_4 + 1\text{mM KCl} + 1\text{mM H}_2\text{SO}_4$ electrolyte at open circuit potential ($\text{OCP} \sim -0.3\text{V}$) are shown in **Fig. 5.6**. All of the Pd/Co bilayers present a spontaneous perpendicular magnetic anisotropy. The coercivity is nearly the same for all the bilayers $\sim 150\text{Oe}$, and the magnetization increases with the Co thickness. The shape of the hysteresis loops are all strictly square, except for Pd(1.9nm)/Co(1.35nm), for which the $M-H$ curve presents a domain pinning effect (see the blue circles in **Fig. 5.6**).

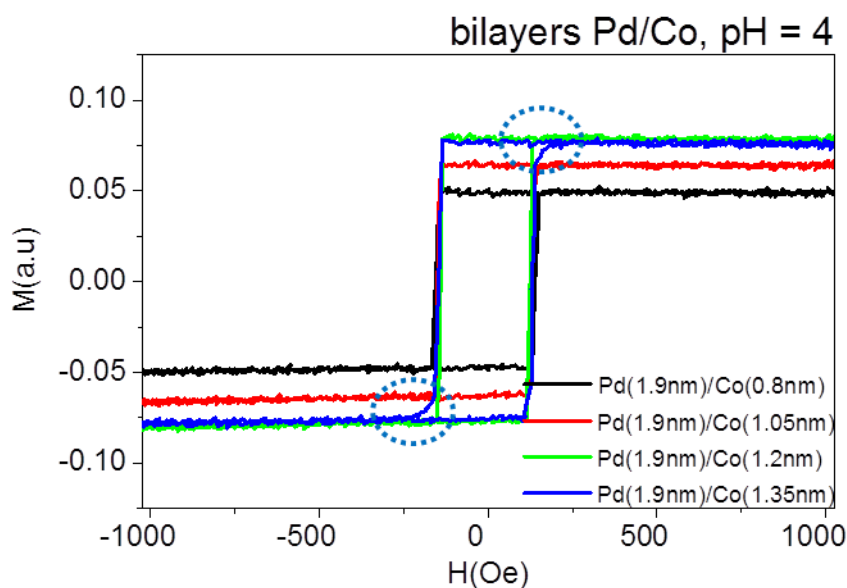


Fig. 5.6: The M - H curves of sputtered Pd(1.9nm)/Co bilayers in an acidic blank electrolyte at open circuit potential. The Co thickness is 0.8nm, (black line); 1.05nm, (red line); 1.2nm, (green line); and 1.35nm, (blue line).

5.3.3. H₂ induced modification of magnetic anisotropy for Pd/Co bilayers

This part is devoted to investigate the H-induced modification of the magnetic properties of Pd/Co bilayer films.

Figure 5.7 presents a voltammogram (sweep rate 10mV/s) of the electrodeposited Pd/Co bilayer in an acidic blank electrolyte during one potential scan between -0.5V and -1.25V. Similarly to what have been observed on Pd/Au (see Appendix), two cathodic peaks at $U \sim -0.63$ V and ~ -0.95 V are presented in **Fig. 5.7**. We also observe one anodic peak at $U \sim -0.61$ V and another relatively small one at $U \sim -0.57$ V. These cathodic and anodic peaks correspond to H adsorption/absorption, and H₂ formation and oxidation. The latter process is accompanied by H absorption into Pd and H removal from Pd.

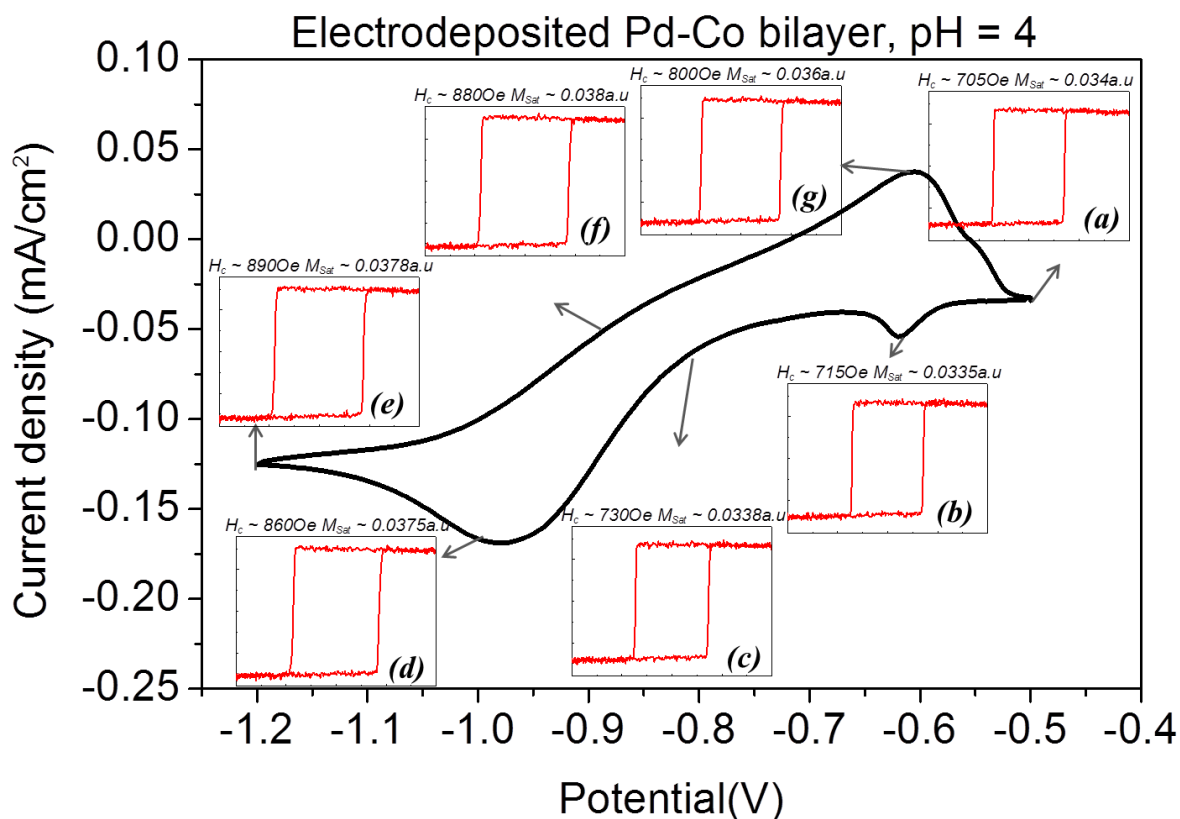


Fig. 5.7: The electrochemical current density versus potential of the electrodeposited Pd/Co (~4ML)/Au bilayer in a pH ~ 4 blank electrolyte during potential scan between -0.5V and -1.25V. The sweep starts at -0.5V and the scan rate is 10mV/s. (a)-(g): the extracted M - H curves along with the potential scan at -0.5V, -0.65V, -0.8V, -0.95V, -1.2V, -0.85, and -0.6V respectively.

Along with the voltammogram, M - H curves are shown in **Fig. 5.7**. The electrodeposited Pd/Co bilayer is perpendicularly magnetized over the whole investigated potential range. H_c increases slightly from 7050e to 7150e (**Fig. 5.7 (b)**) with adsorption of H_{ads} , and M_{Sat} stays nearly the same. With the onset of HER at -0.8V (**Fig. 5.7 (c)**), H_c goes up to 7300e and M_{Sat} remains nearly unchanged. In the potential range where HER takes places (**Fig.5.7 (d) –(e)**), H_c continues to increase until ~ 8900e ($\Delta H_c/H_c \sim 26\%$) and M_{Sat} increases from 0.034a.u to 0.038a.u (~ 11%). These changes are reversible with the potential.

For the sputtered Pd/Co bilayers, results of two samples are presented below: Pd(1.9nm)/Co(0.8nm)/Pt(4nm)/Ta(3nm)/SiO_x(50nm)/Si, and Pd(1.9nm)/Co(1.35nm)/Pt(4nm)/Ta(3nm)/SiO_x(50nm)/Si. The M - H curve of the second sample slightly changed upon potential control in the electrolyte (**Fig. 5.6** and **Fig. 5.9**). Both samples are perpendicularly

magnetized.

The voltammograms of these two samples are very similar. Two major peaks are observed: a cathodic one at $\sim -0.95\text{V}$ and an anodic one at $\sim -0.7\text{V}$. The peaks corresponding to H adsorption and desorption are not clearly visible.

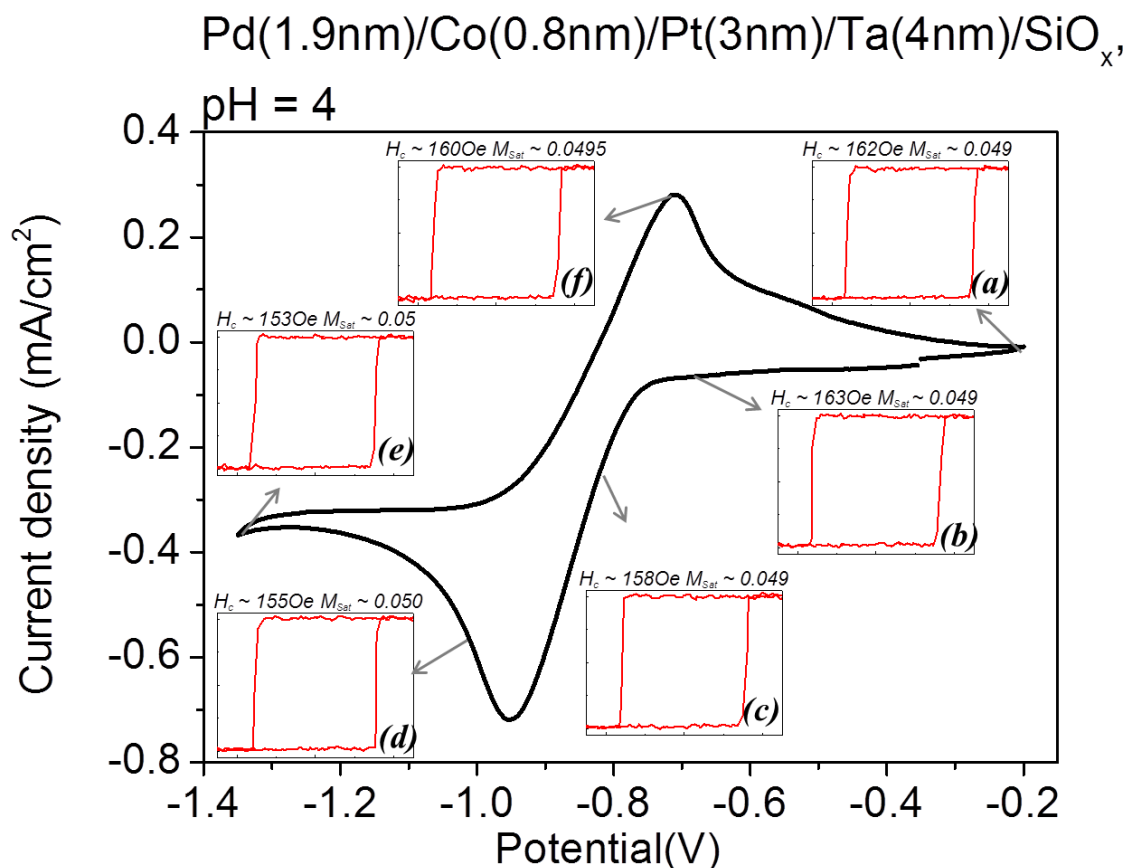


Fig. 5.8: The electrochemical current density versus potential of the sputtered Pd(1.9nm)/Co(0.8nm) bilayer in a pH ~ 4 blank electrolyte during potential scan between -0.2V and -1.35V . The sweeping starts from -0.35V (OCP) and goes forward to -1.35V . The scan rate is $10\text{mV}/\text{s}$. (a)-(f): the extracted M - H curves along with the potential scan at -0.2V , -0.65V (cathodic peak), -0.8V , -1V , -1.35V , and -0.6V (anodic peak) respectively.

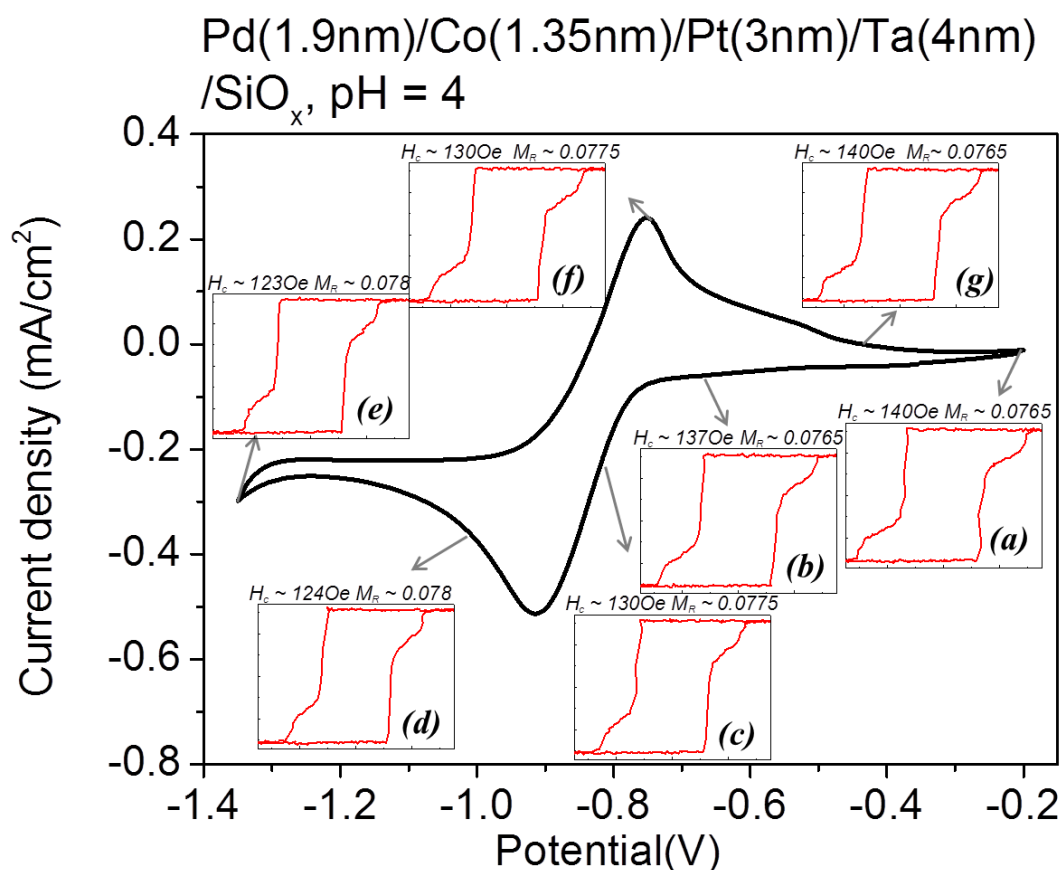


Fig. 5.9: The electrochemical current density versus potential of the sputtered Pd(1.9nm)/Co(1.35nm) bilayer in a pH \sim 4 blank electrolyte during potential scan between -0.2V and -1.35V. The sweeping starts from -0.35V (OCP) and goes forward to -1.35V. The scan rate is 10mV/s. (a)-(f): the extracted M - H curves along with the potential scan at -0.2V, -0.65V (cathodic peak), -0.8V, -1V, -1.35V, and -0.75V (anodic peak) respectively.

The magnetic behaviors of these two sputtered Pd/Co bilayers are similar. The two systems are perpendicularly magnetized over the whole investigated potential region and the general shape of the M - H curves remains the same. The only observed variations are those of H_c and M_R . For $U > \sim -0.75$ V before the onset of HER (**Fig. 5.8 (a) – (b)**), H_c and M_{Sat} does not alter. With the onset of HER (**Fig. 5.8 (c)**), H_c begins to reduce. At -0.8V, for Pd(1.9nm)/Co(0.8nm), H_c drops from 162Oe to 158Oe (\sim 2.5%); and for Pd(1.9nm)/Co(1.35nm), H_c decreases from 140Oe to 130Oe (\sim 7%). For $U < \sim -0.95$ V (**Fig. 5.8 (d)-(e)**), in the case of Pd(1.9nm)/Co(0.8nm), H_c varies to 153Oe (5.6%); and in the case of Pd(1.9nm)/Co(1.35nm), H_c becomes 123Oe (12%). M_{Sat} increases slightly with H₂ loading, about \sim 2% for both samples.

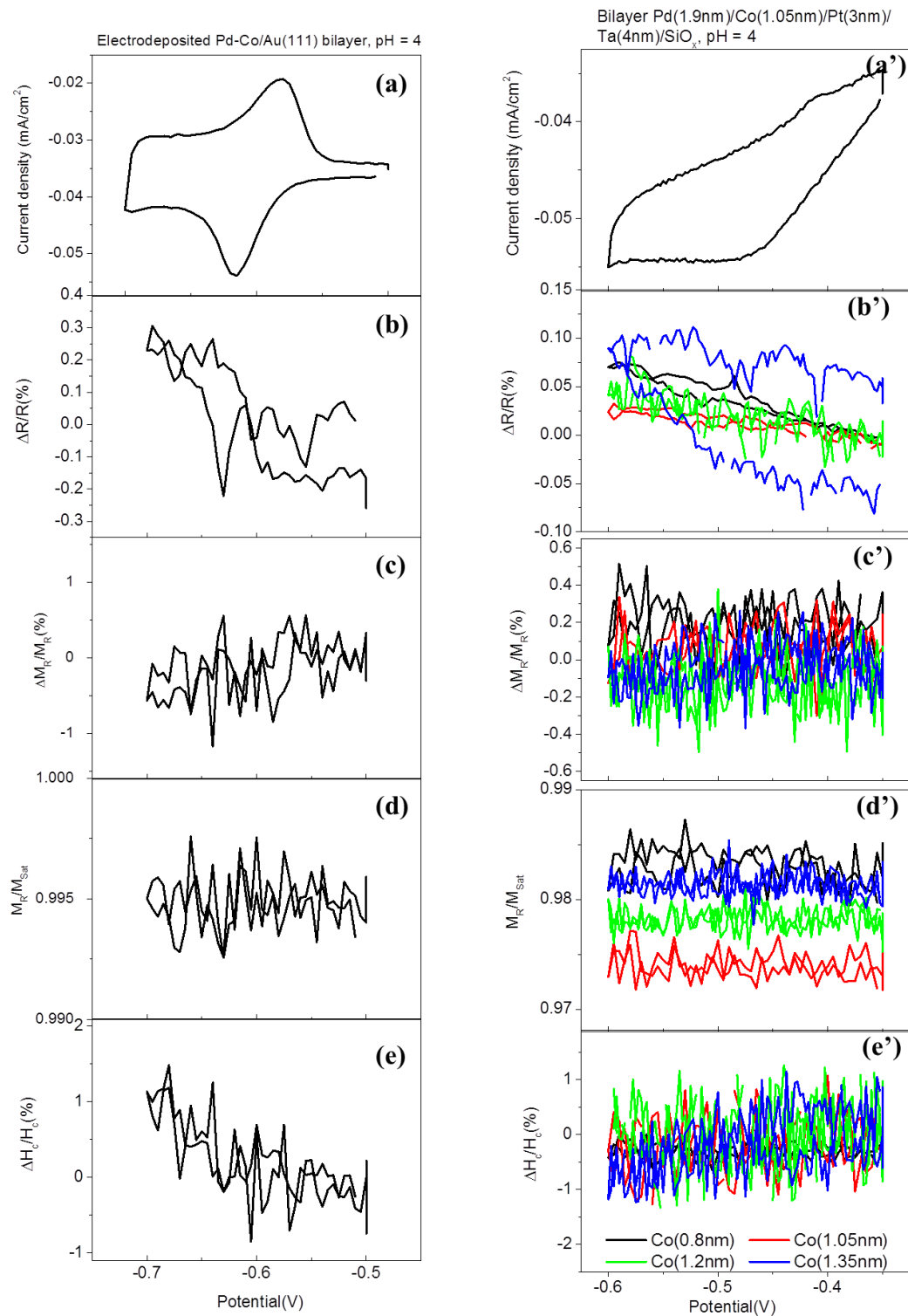


Fig. 5.10: (a) – (e) Electrochemical current density; $\Delta R/R$; $\Delta M_R/M_R$; M_R/M_{Sat} ; $\Delta H_c/H_c$ versus potential of the electrodeposited Pd/Co(0.84nm)/Au(111)/Si(111) in a pH ~ 4 blank electrolyte during the potential scan between -0.5V and -0.7V. The scan rate is 10mV/s. (a')-(e') Electrochemical current density; $\Delta R/R$; $\Delta M_R/M_R$; M_R/M_{Sat} ; $\Delta H_c/H_c$ versus potential of the sputtered Pd/Co sputtered bilayers in a pH ~ 4 blank electrolyte during the potential scan between -0.35V and -0.6V. The scan speed is 10mV/s. The Co thickness is indicated in (e').

A detailed analysis of the M - H curves as a function of potential is shown in **Fig. 5.10** and **Fig. 5.11**.

Fig. 5.10 (a) – (e) presents the voltammogram, $\Delta R/R$, $\Delta M_R/M_R$, M_R/M_{Sat} and $\Delta H_c/H_c$ for the electrodeposited Pd/Co(4.2ML, ~ 0.84 nm) between -0.5V and -0.7V. The variation of the electrochemical current density clearly indicates one cathodic peak at ~ -0.61 V and one anodic peak at ~ -0.58 V corresponding to the adsorption and desorption of H_{ads} . The relative reflectivity slightly increases by 0.3% upon H adsorption; and H_c goes up by $\sim 1\%$. All the other parameters remain unchanged. $\Delta R/R$ and $\Delta H_c/H_c$ are reversible in the explored potential range.

Fig. 5.10 (a')-(e') displays the results for the four sputtered Pd(1.9nm)/Co(0.8nm, 1.05nm, 1.2nm and 1.35nm) during potential scans between -0.35V and -0.6V. As we mentioned earlier, no clear peaks due to H adsorption/desorption are observed. $\Delta R/R$ presents a linear increase by 0.1% with potential. The magnetic properties remain unchanged over the investigated potential range.

For the electrodeposited Pd/Co(~ 0.84 nm) bilayer, **Fig. 5.11 (a) – (e)** presents the voltammogram, $\Delta R/R$, $\Delta M_R/M_R$, M_R/M_{Sat} and $\Delta H_c/H_c$ as a function of potential in a larger potential range. Arrows in the figure indicate the sweep direction. During the potential scan, M_R/M_{Sat} remains constant. $\Delta R/R$ decreases by 4.2% in HER potential range, similarly to what have been observed for Pd/Au (see Appendix). $\Delta R/R$ change is accompanied by $\Delta H_c/H_c$ and $\Delta M_R/M_R$ increase by $\sim 26\%$ and $\sim 12.5\%$ respectively. These changes are reversible upon sweeping back the potential.

For the four sputtered Pd(1.9nm)/ Co(0.8nm, 1.05nm, 1.2nm and 1.35nm) bilayers in a pH ~ 4 blank electrolyte between -0.2V/-0.35V and -1.35V, **Fig. 5.11 (a') – (e')** presents the same parameters as a function of potential. As compared to electrodeposited Pd/Co bilayers, the behaviors of $\Delta R/R$ and $\Delta M_R/M_R$ are similar but smaller by a factor 5 to 10, depending on the samples. The hysteresis between back and forth sweeps is also smaller than that of electrodeposited bilayers. The case of $\Delta H_c/H_c$ is very different since we observe a decrease by 4-9% for sputtered bilayers contrasting with the increase by 26% for the electrodeposited bilayer. The variations of $\Delta R/R$, $\Delta H_c/H_c$ and $\Delta M_R/M_R$ are reversible.

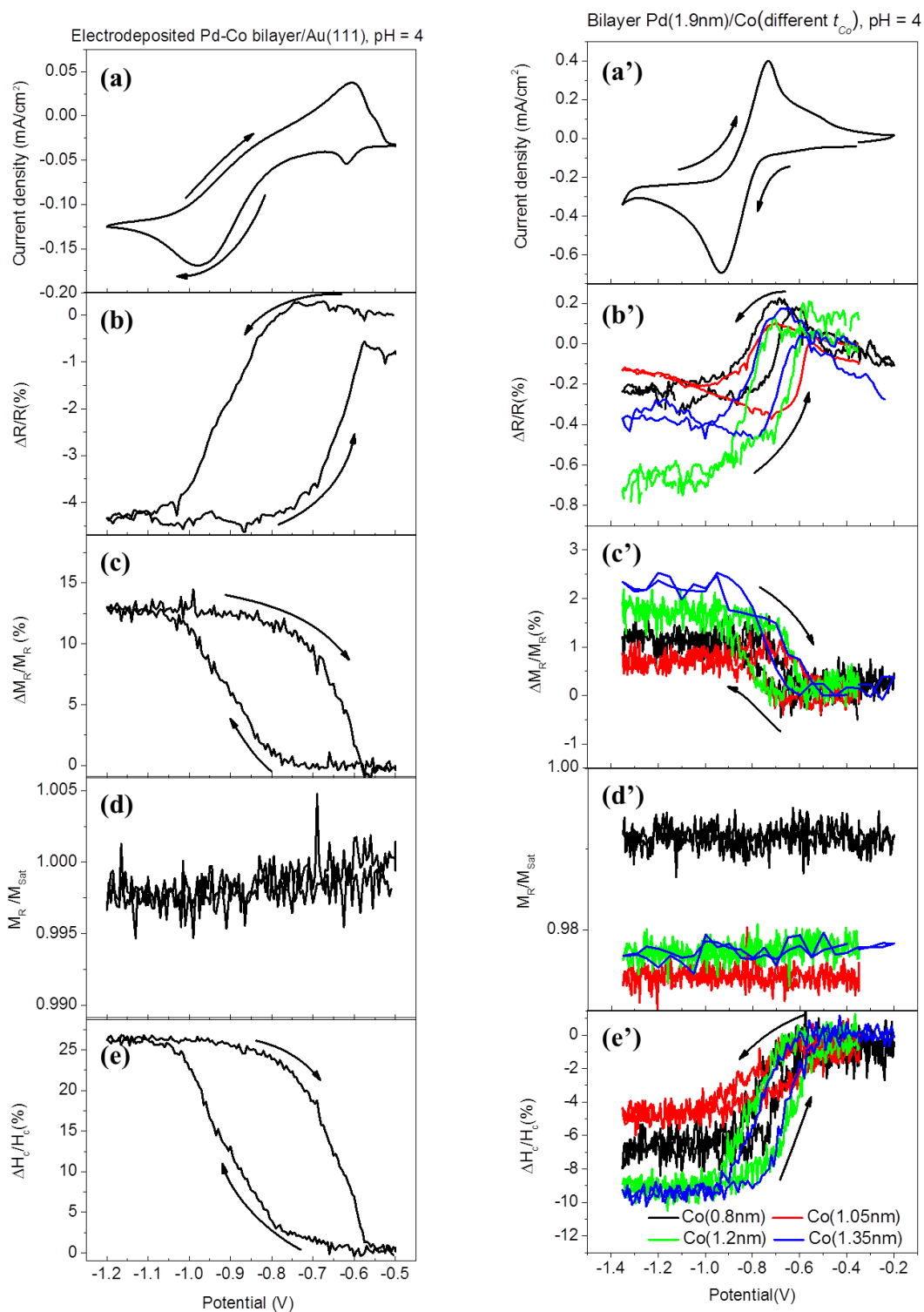


Fig. 5.11: (a) – (e) Electrochemical current density; $\Delta R/R$; $\Delta M_R/M_R$; M_R/M_{Sat} ; $\Delta H_c/H_c$ versus potential of the electrodeposited Pd/Co(0.84nm)/Au(111)/Si(111) during the potential scan between -0.5V and -1.2V. (a')-(e') Electrochemical current density; $\Delta R/R$; $\Delta M_R/M_R$; M_R/M_{Sat} ; $\Delta H_c/H_c$ versus potential of the sputtered Pd/Co bilayers during the potential scans between -0.2V and -1.35V. The scan starts from -0.35V. The scan rate is 10mV/s. The Co thickness is indicated in (e').

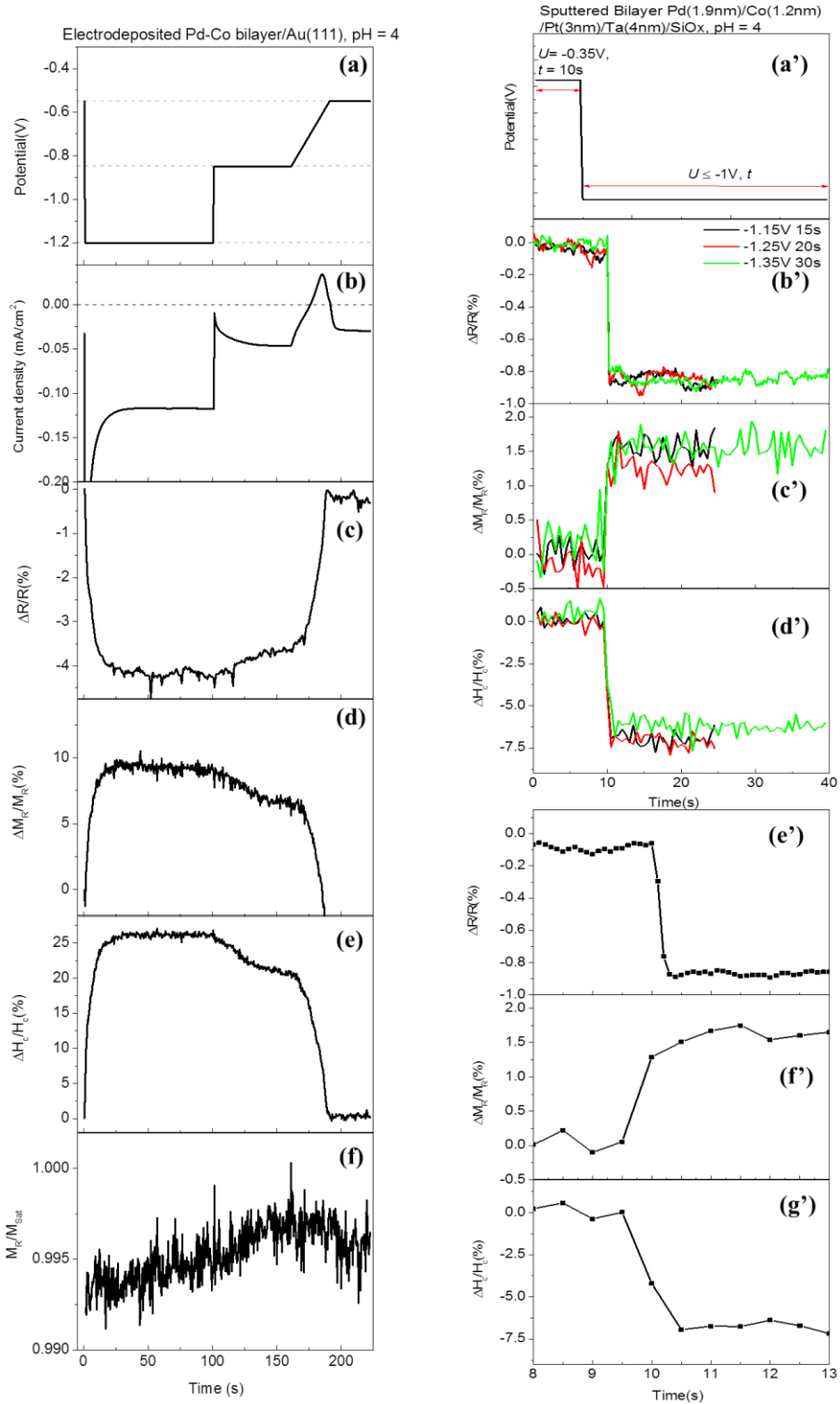


Fig. 5.12: (a) –(e): the electrochemical current density; $\Delta R/R$; $\Delta M_R/M_R$; $\Delta H_c/H_c$; and M_R/M_{Sat} of the electrodeposited Pd-Co bilayer/Au(111)/Si(111) during a potential-step experiment. The potential sequence is described in (a): the potential is switched from -0.55V to -1.2V for 100s and then stepped to -0.85V for 60s. In the following a potential ramp from -0.85V to -0.55V with 10mV/s is performed. (a'): potential sequences for the sputter Pd(1.9nm)/Co(1.2nm) bilayer: the potential is switched from -0.35V to -1.15V for 15s; (b')-(d'): $\Delta R/R$; $\Delta M_R/M_R$; and $\Delta H_c/H_c$; (e')-(g'): zoomings of (b')-(d').

Potential steps were performed for the two types of Pd/Co bilayers to study the time response of the magnetic properties (**Fig. 5.12**). For the electrodeposited Pd/Co(0.84nm), stepping the applied potential from -0.55V to -1.2V results in a transient current which stabilizes within 25s. $\Delta R/R$ drops by 4.25%. H_c and M_R increases by 26% and 10% respectively. The changes are consistent with those during the potential scans (see **Fig. 5.11**). The time constant of these changes is typically 5-10s. In order to determine electrochemically the amount of H absorbed into the Pd layer, one has to minimize the oxidation current of H_2 formed by HER at -1.2V. For this purpose, the applied potential is changed to -0.85V, where no HER occurs to let the concentration of H_2 in the vicinity of the sample to decrease. At this potential, small amount of absorbed H_2 is oxidized as seen in the small changes of $\Delta R/R$, $\Delta H_c/H_c$ and $\Delta M_R/M_R$. The potential is then ramped from -0.85V to -0.55V. $\Delta R/R$, $\Delta H_c/H_c$ and $\Delta M_R/M_R$ recover their value. The integrated anodic charge Q_{an} is $\sim 1.30\text{mC/cm}^2$. We can estimate the Pd thickness using the equation (A.2) and (A.3) described in Appendix. We obtain t_{Pd} is around $\sim 8.5\text{ML}$: i.e, $\sim 1.7\text{nm}$.

For the sputtered Pd(1.9nm)/Co(1.2nm) bilayer, stepping the potential negatively to $U \leq -1.1\text{V}$ yields a step behavior similar to the electrodeposited bilayer (**Fig. 5.12 (a')-(d')**). However, the change time constant is 0.2-0.5s, one order of magnitude smaller than for the electrodeposited bilayer (**Fig. 5.12 (e')-(g')**). These modifications do not depend on the potential step as long as U is in the HER range. This indicates that the variation of the magnetic anisotropy due to H absorption is rather fast for sputtered bilayer. This difference might be due to grain type morphology of these films.

5.4. Preparation of PdCo alloys and influence of H adsorption/absorption on the PdCo alloys' properties

In the first part, we present the preparation of PdCo alloys by co-electrodeposition and co-sputter deposition. Then the magnetic properties of PdCo alloys are examined as a function of H adsorption and absorption.

5.4.1. PdCo alloy prepared by electrochemical deposition

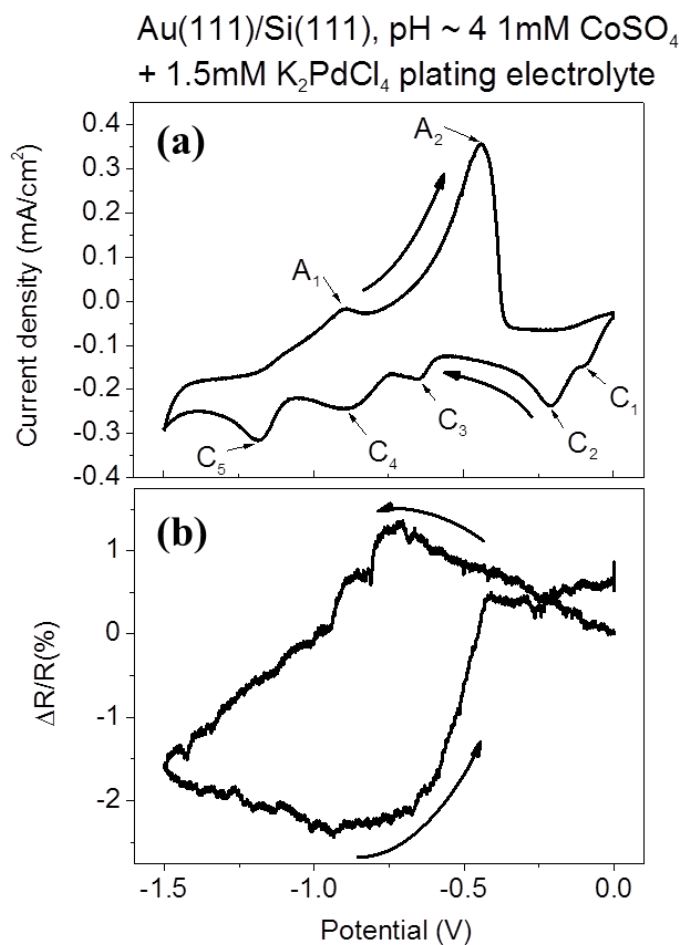


Fig. 5.13: (a) electrochemical current density as a function of applied potential of Au(111)/Si(111) in contact with a pH ~ 3.5-4 1.5mM K₂PdCl₄+ 1mM CoSO₄ + 0.1M K₂SO₄ + 1mM KCl + 1mM H₂SO₄ electrolyte during one potential scan between 0V and -1.5V. The scan rate is 10mV/s. (b) the corresponding reflectivity recorded in real time versus applied potential.

The co-deposition of Pd and Co took place in a pH ~ 3.5 – 4 1.5mM K₂PdCl₄+ 1mM

$\text{CoSO}_4 + 0.1\text{M K}_2\text{SO}_4 + 1\text{mM KCl} + 1\text{mM H}_2\text{SO}_4$ electrolyte. The Au(111)/Si(111) substrate is in contact with the plating electrolyte at 0V, more negative than the Pd deposition onset (see results of Pd/Au deposition in Appendix). **Fig. 5.13** presents the voltammogram and the sample reflectivity between 0V and -1.5V. We observe five cathodic peaks denoted as $C_1 - C_5$ and two anodic peaks symbolized as A_1 and A_2 . Peaks $C_1 - C_5$ appears at -0.09V, -0.2V, -0.65V, -0.88V and -1.19V. The two anodic peaks A_1 and A_2 show up at -0.9V and -0.45V. According to the study of electrodeposition of Pd on Au(111) [17], the Pd deposition onset is at least $\sim 100\text{mV}$ more positive than 0V. In the potential range of peaks C_1 and C_2 , $\Delta R/R$ increases monotonically, indicating continuous Pd deposition. Peaks C_1 and C_2 may thus be related to Pd deposition. From the study of Pd/Au(111) presented in Appendix, peaks C_3 and C_4 are attributed to hydrogen adsorption and HER reaction respectively. The results in Appendix have shown that HER reaction is accompanied by H absorption into Pd which decreases $\Delta R/R$. **Fig. 5.13 (b)** also shows $\Delta R/R$ decreases in the C_4 peak potential range. Peak C_5 is probably due to the deposition of Co, the potential of which is shifted by $\sim +0.09\text{V}$ as compared to the Co growth on Au(111)/Si(111) substrate ($\sim -1.28\text{V}$). This shift is probably due to the simultaneous deposition of Pd. Such deposition process has been reported previously as anomalous codeposition [18]. Peak C_5 is not accompanied by a $\Delta R/R$ increase as expected from Co deposition on Au/Si(111) and from simple optical modelling of the optical properties of the multilayer system. Such a behavior is probably due to H absorption in the PdCo alloy and its induced $\Delta R/R$ decrease. The anodic peak $A_1 \sim -0.9\text{V}$ corresponds probably to the dissolution of Co. Its potential is also shifted by $\sim +0.1\text{V}$ as compared to Co/Au(111)/Si(111) ($\sim -1\text{V}$). The other anodic peak $A_2 \sim -0.45\text{V}$ stems from the hydrogen oxidation reaction (HOR). Peak A_2 is accompanied by an increase of $\Delta R/R$ to slightly above its original value.

The potential sequences used for electrodepositing the PdCo alloys are schematized in **Fig. 5.14**. Since it is not possible to follow the PdCo alloy growth using $\Delta R/R$, we performed similar measurements looking into the magnetic properties. Two potential sweeps between 0V and -1.5V are performed at first. Next the applied potential is held at -1.3V for 25s and then switched to -1.1V for 5s. The solution is then exchanged to pH 4 Co(II) and Pd(II) free electrolyte at -1.1V for $\sim 300\text{s}$. Afterwards, the potential is maintained at -0.3V for 50s. Region I, II and III is in the Pd(II) and Co(II) plating electrolytes (light red background); whereas region IV and V is in the Pd(II) and Co(II) free electrolyte (light blue background).

A set of extracted $M-H$ curves from the in-situ P-MOKE measurements are presented as well in **Fig. 5.14**. At the end of the first negative sweep, we observe a double step $M-H$

curves with a square shape, indicating a PMA. However, our magnetic field range is too small in this first sequence to saturate the sample magnetization. At the end of the first negative and positive sweep (end of region I), the $M-H$ curve is square with a large H_c value ($\sim 1600\text{Oe}$). This indicates that PdCo alloy layer was deposited and it is protected by a Pd layer, which avoids Co dissolution even at 0V. However, we have no indication on the distribution of the Pd and Co atoms within the alloy.

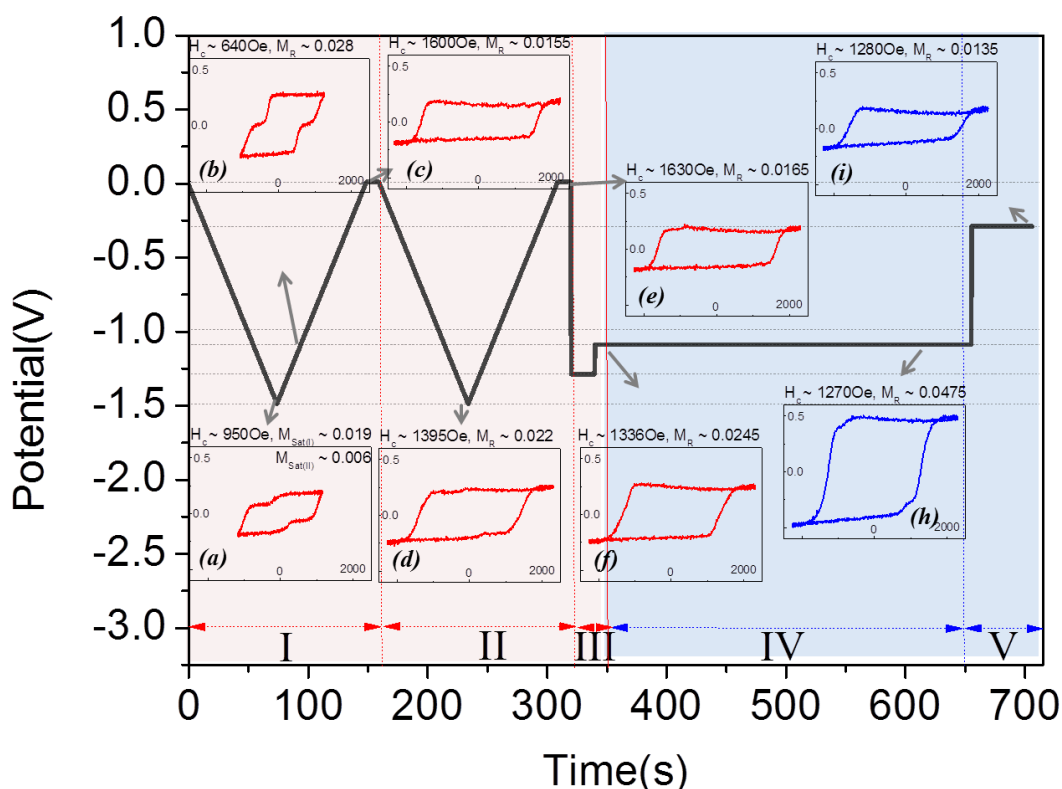


Fig. 5.14: experimental procedure to electrodeposit the PdCo alloy layers --- region I-III with the light red background describing the Au(111)/Si(111) in contact with pH $\sim 3.5-4$ 1.5mM K_2PdCl_4 + 1mM CoSO_4 + 0.1M K_2SO_4 + 1mM KCl + 1mM H_2SO_4 during two successive potential scans (region I and II) between 0V and -1.5V. The scan rate is 10mV/s. And then the sample is under potential control of -1.3V for 25s and at -1.1V during 5s. Region IV and V corresponding to electrolyte exchange to pH $\sim 3.5-4$ blank electrolyte at -1.1V during 300s and then at -0.3V for 50s. A set of $M-H$ curves during this procedure are extracted from the P-MOKE measurements.

At the end of the second potential sweep (region II), the hysteresis loop is very similar to that at the end of the first sweep, even though we have clear indication that Co is deposited. This behavior suggests that deposited Co is dissolved on the positive sweep. Consequently, Pd

deposition rate seems to significantly decrease and the Pd layer is not growing anymore as a protection layer for the additional Co. The changes of $M-H$ in region IV and V are most probably related to H absorption in the alloy and will be detailed later in this Chapter. It is worth noticing the stability of the alloy up to potentials close to 0V.

5.4.2. PdCo alloys prepared by sputter deposition

The deposition procedure of sputtered PdCo alloys is detailed in section 5.2. The morphology of the sputtered PdCo alloys is measured by the ex-situ AFM. **Fig. 5.15 (b) and (d)** present $0.5\mu\text{m} * 0.5\mu\text{m}$ and $1\mu\text{m} * 1\mu\text{m}$ AFM images of Pd(0.05A)-Co(0.5A) 1min alloys. The height profiles along the white line presented in each AFM image are also displayed (**Fig. 5.15 (c) and (e)**). The AFM images indicate that the film morphology does not present large flat terraces but rather a granular aspect. However, the surface roughness is rather low ($\sim 1\text{nm}$).

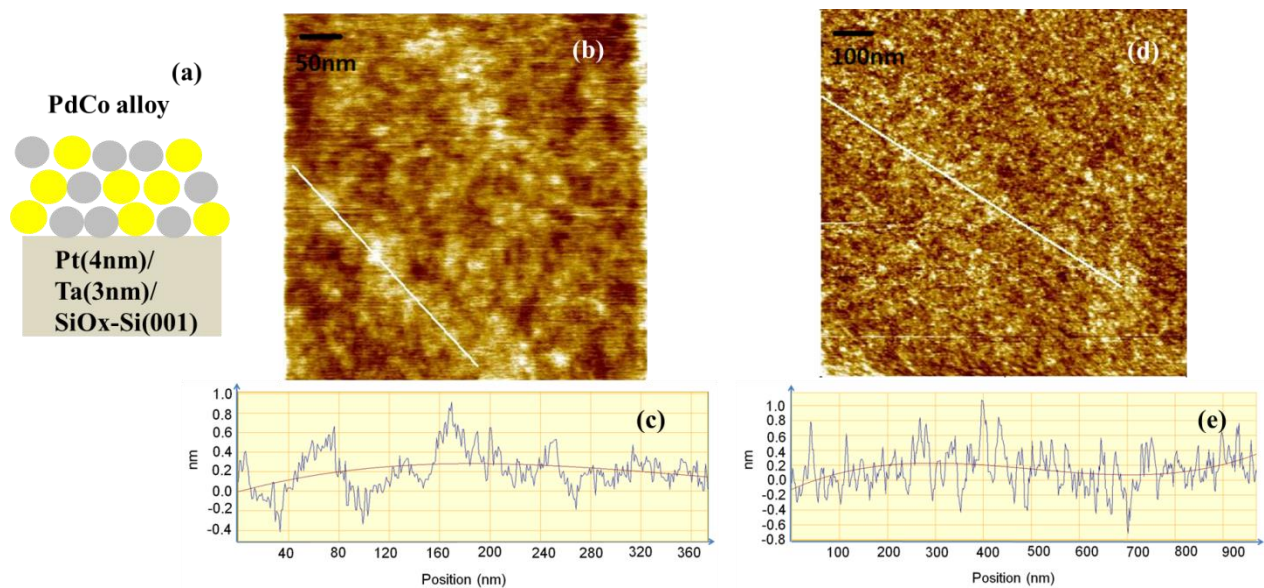


Fig. 5.15: (a) scheme of PdCo alloy structure; (b) $0.5\mu\text{m} * 0.5\mu\text{m}$ AFM image of Pd(0.05A)-Co(0.5A) alloy; (c) height profile along the white line of image (b); (d) $1\mu\text{m} * 1\mu\text{m}$ AFM image of the same PdCo alloy; (e) height profile along the white line of image (d).

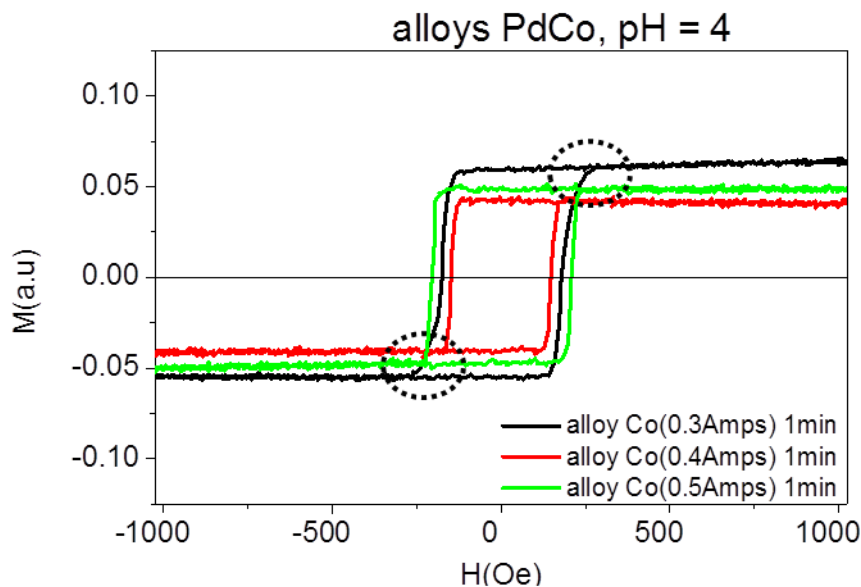


Fig. 5.16: The M - H curves of sputtered PdCo alloys in an acidic blank electrolyte at open circuit potential. The current for Pd deposition is $I_{Pd} \sim 0.05A$. The current for Co deposition I_{Co} is 0.3A (black line), 0.4A (red line) and 0.5A (green line).

The M - H curves of the sputtered alloys in the $pH \sim 3.5 - 4$ blank electrolyte at open circuit potential (OCP) are shown in **Fig. 5.16**. All of the PdCo alloys present a perpendicular magnetic anisotropy. The coercivity varies from 150Oe to 250Oe. The shapes of M - H curves are all strictly square, except for Pd(0.05A)-Co(0.5A), which presents a domain pinning effect (see the black circles in **Fig. 5.16**).

5.4.3. H-induced modification of the magnetic anisotropy of PdCo alloys

As in the case of Pd/Co bilayers, H induced variation of magnetic anisotropy is also investigated for the electrodeposited and sputtered PdCo alloys. All of the samples are immersed in an acidic blank electrolyte ($pH \sim 3.5-4$) under potential controls.

For the electrodeposited PdCo alloy, the voltammogram (**Fig. 5.17**) shows two cathodic peaks at $U \sim -0.62V$ and at $U \sim -0.94V$, indicating hydrogen adsorption and HER respectively. We also observe one anodic peak at $U \sim -0.41V$ corresponding to the hydrogen oxidation reaction (HOR).

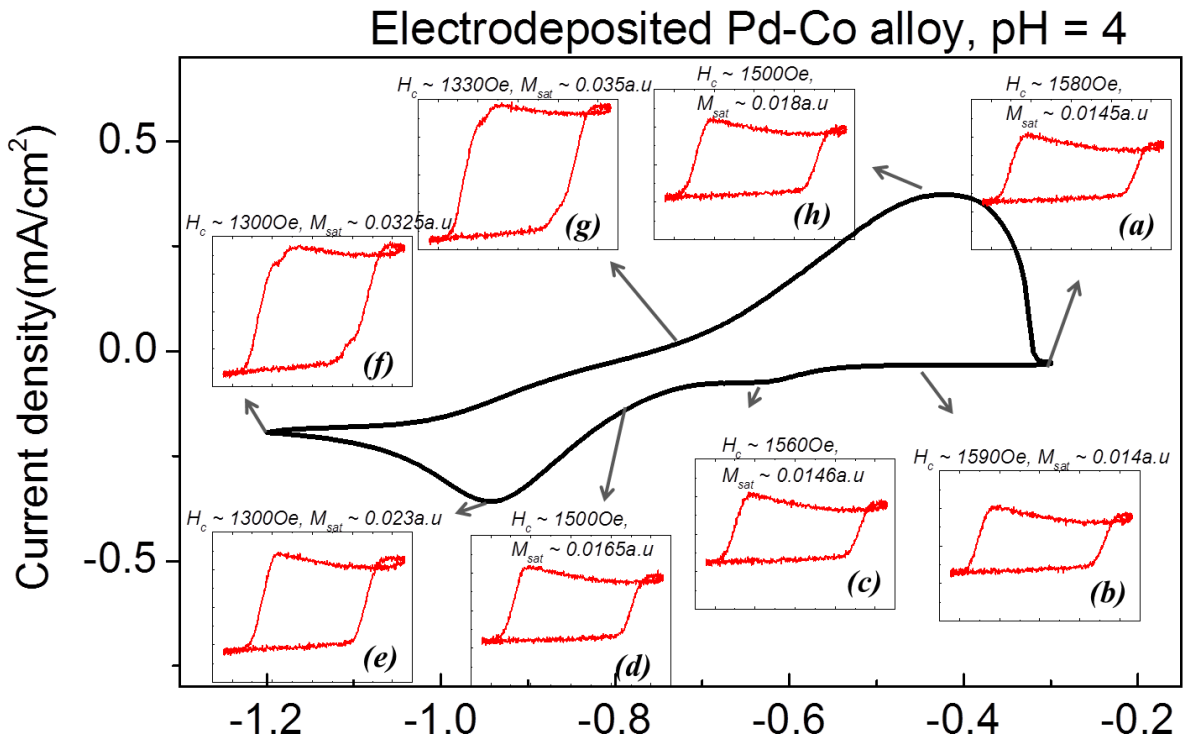


Fig. 5.17: The electrochemical current density versus potential of the electrodeposited PdCo alloy/Au(111)/Si(111) in a pH \sim 4 blank electrolyte during potential scan between -0.3V and -1.2V. The sweep direction is from -0.3V to -1.2V and the scan rate is 10mV/s. (a)-(g): the extracted M - H curves along with the potential scan at -0.3V, -0.45V, -0.65V, -0.8V, -0.95V, -1.2V, -0.7V (anodic), and -0.4V (anodic) respectively.

Along with the voltammogram, a set of M - H curves are presented in **Fig. 5.17**. The electrodeposited PdCo alloy is perpendicularly magnetized over the whole investigated potential range. The slight curvature of the M - H curves is due to a problem with the baseline correction. H_c decreases by 1.2% with adsorption of H_{ads} (**Fig. 5.18 (c)**), whereas M_{Sat} stays nearly unchanged. With the onset of HER at -0.8V (**Fig. 5.18 (d)**), H_c drops to 1500Oe ($\Delta H_c/H_c \sim -5.7\%$) and M_{Sat} increases by $\sim 10\%$. In the potential range where HER takes places (**Fig. 5.18 (e)-(f)**), H_c continues to decrease down to ~ 1300 Oe ($\Delta H_c/H_c \sim -18.2\%$). It is worth noting that unlike H_c which stays the same for $U < -0.95$ V, M_{Sat} continues to increase until $U \sim -1.2$ V on the negative sweep (**Fig. 5.18 (e)-(g)**), where $M_{Sat} \sim 0.035$ a.u. ($\Delta M_{Sat}/M_{Sat} \sim 150\%$) on the positive sweep until the hydrogen oxidation reaction takes place (**Fig. 5.18 (h)**). The M - H curve recovers its initial characteristics after sweeping the potential through the anodic

peak at -0.41V. These changes are thus reversible as a function of potential.

For the sputtered PdCo alloys, results of two samples are presented below: one is Pd(0.05A)-Co(0.5A) 1min, of which the hysteresis loop is strictly perpendicular and presenting no different domain pinning energy; the other is Pd(0.05A)-Co(0.3A) 1min.

The voltammograms of these two samples are very similar: two conventional cathodic peaks arise at $U \sim -0.6V$ and $U \sim -0.97V$, resulting from the adsorption of hydrogen H_{ads} and HER where the absorption of hydrogen takes place; and two anodic peaks at $U \sim -0.72V$ and $\sim -0.54V$, reflecting the oxidation of the hydrogen and the desorption of H_{ads} as well. Besides these four peaks, another cathodic peak at $\sim -0.10V$ also shows up in the voltammogram, the origin of this peak is not clear but may be related to the reduction of surface oxide.

A set of the $M-H$ curves during the potential scans for these two samples are shown as well in the **Fig. 5.18** and **Fig. 5.19**. In the case of the Pd (0.05A)-Co (0.5A) alloy, the $M-H$ curves are all strictly square, inferring a PMA during the whole potential scan. Coercivity starts to decrease from 300Oe (**Fig. 5.18 (a)**) to 215Oe (**Fig. 5.18 (b)**) ($\Delta H_c/H_c \sim -28.3\%$) with the adsorption of H at $\sim -0.6V$. The onset of HER continues to reduce H_c (**Fig. 5.18 (c)**) down to $\sim 190Oe$ (**Fig. 5.18 (d)** and **Fig. 5.18 (e)**) ($\Delta H_c/H_c \sim -36.7\%$). The coercivity goes up with hydrogen oxidation (**Fig. 5.19 (f)**), approaching to its original value. The absolute value of $\Delta H_c/H_c$ ($\sim 36.7\%$) is larger than that of the electrodeposited PdCo alloy ($\sim 18.2\%$). M_{Sat} remains almost unchanged. This is in contrast with the case of the electrodeposited PdCo alloys, where M_{Sat} increases remarkably by $\sim 150\%$.

Alloy Pd(0.05A)-Co(0.5A) 1min/Pt(3nm)
/Ta(4nm)/SiO_x, pH = 4

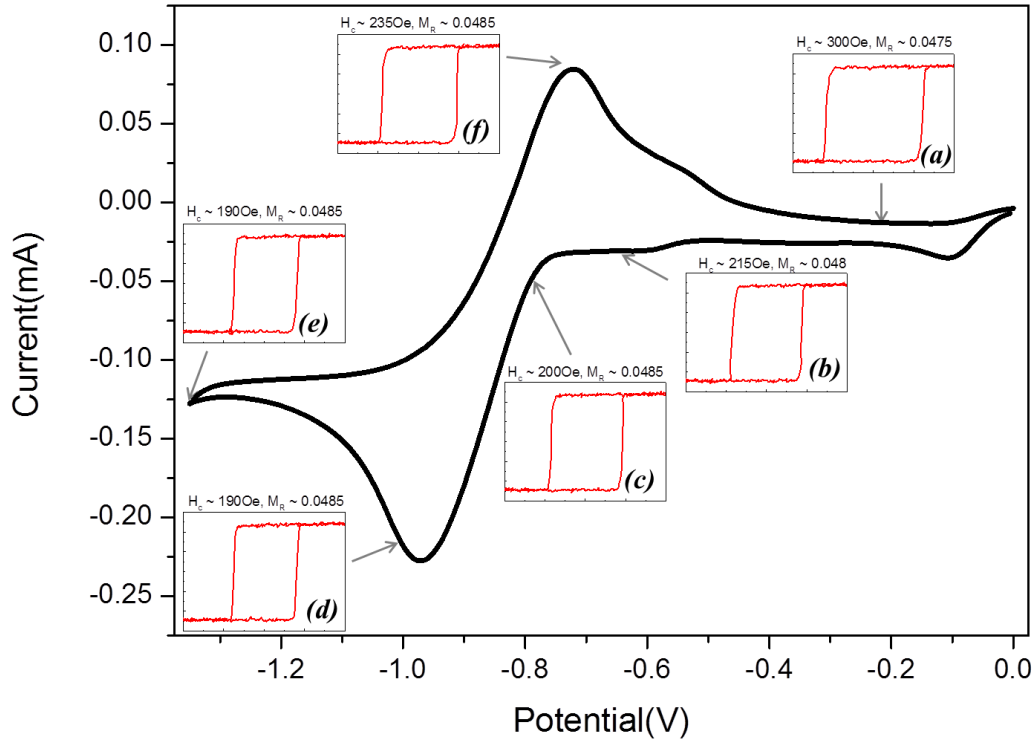


Fig. 5.18: The electrochemical current density versus potential of the sputtered Pd(0.05A) - Co(0.5A) 1min alloy in a pH ~ 4 blank electrolyte during potential scan between -0.2V and -1.35V. The sweeping starts from 0 (OCP) and goes forward to -1.35V. The scan rate is 10mV/s. (a)-(f): the extracted M - H curves along with the potential scan at -0.2V, -0.65V (cathodic peak), -0.8V, -1V, -1.35V, and -0.75V (anodic peak) respectively.

In the case of the Pd (0.05A)-Co (0.3A) alloy, the most eye-catching difference is that not only the coercivity is modified, but the magnetization can be tilted by HER. As for the 1st sample, the adsorption of H_{ads} decreases the coercivity from 250Oe (**Fig. 5.19 (a)**) to 230Oe (**Fig. 5.19 (b)**). In the HER potential range, the magnetization tilts away from the surface normal with a very small coercivity $H_c \sim 45$ Oe and $M_R/M_{Sat} \sim 0.13$ (**Fig. 5.19 (d)** and **(e)**). The magnetization orientation turns back to the surface normal with the hydrogen oxidation (**Fig. 5.19 (f)**) and we recover the initial M - H curve after the desorption of hydrogen (**Fig. 5.19 (g)**).

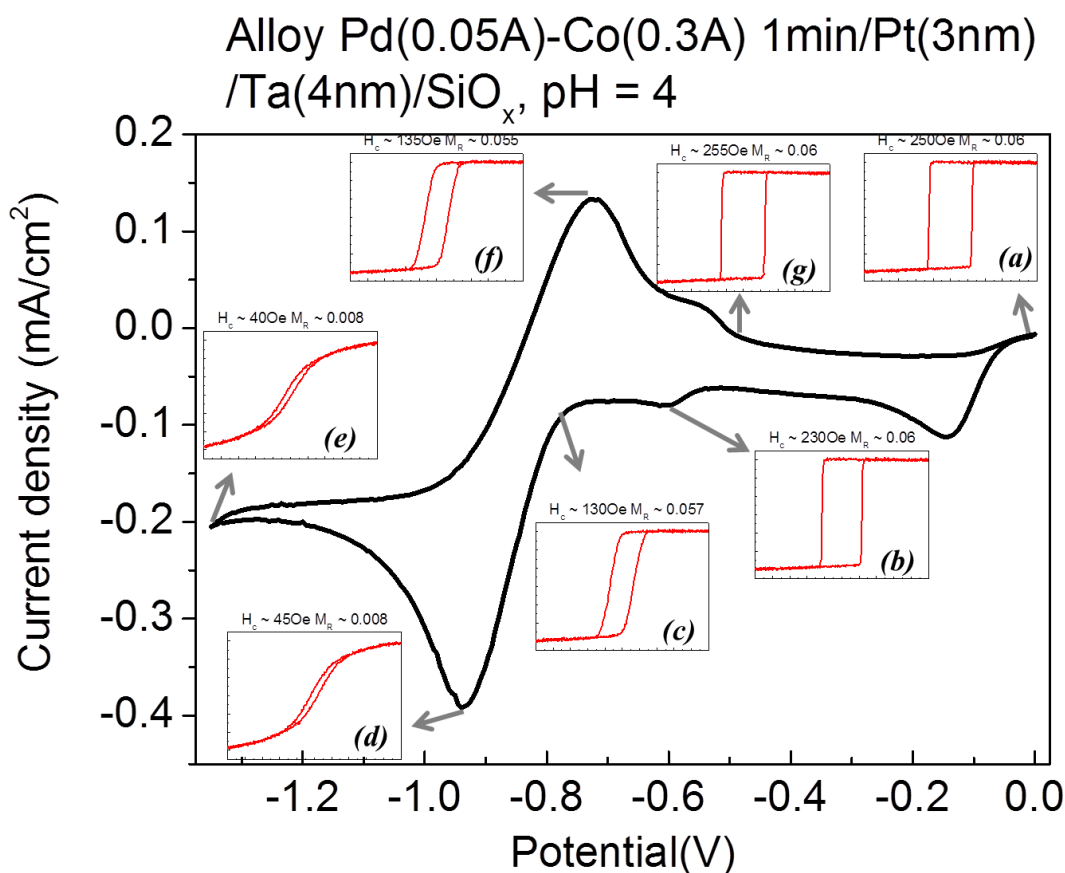


Fig. 5.19: The electrochemical current density versus potential of the sputtered Pd(0.05A) - Co(0.5A) 1min alloy in a pH ~ 4 blank electrolyte during potential scan between -0.2V and -1.35V. The sweep starts from 0V (OCP) and goes forward to -1.35V. The scan rate is 10mV/s. (a)-(f): the extracted M - H curves along with the potential scan at -0.2V, -0.65V (cathodic peak), -0.8V, -1V, -1.35V, -0.75V (anodic peak) and -0.5V (anodic peak) respectively.

The detailed analysis of $\Delta R/R$ and the M - H curves along with the voltammogram are presented in **Fig. 5.20** in the H adsorption range for the electrodeposited and sputtered PdCo alloys. **Fig. 5.20 (a) – (e)** shows that for the electrodeposited PdCo alloy, $\Delta R/R$ increases by ~ 0.2% upon H adsorption in the range -0.5V/-0.7V. The observed drop at $U < -0.63$ V is probably related to the onset of H absorption (see **Fig. 5.21**). The $\Delta R/R$ increase is accompanied by the increase of $\Delta M_R/M_R$ by ~ 7% and a decrease of $\Delta H_c/H_c$ by ~2%. These changes are completely reversible.

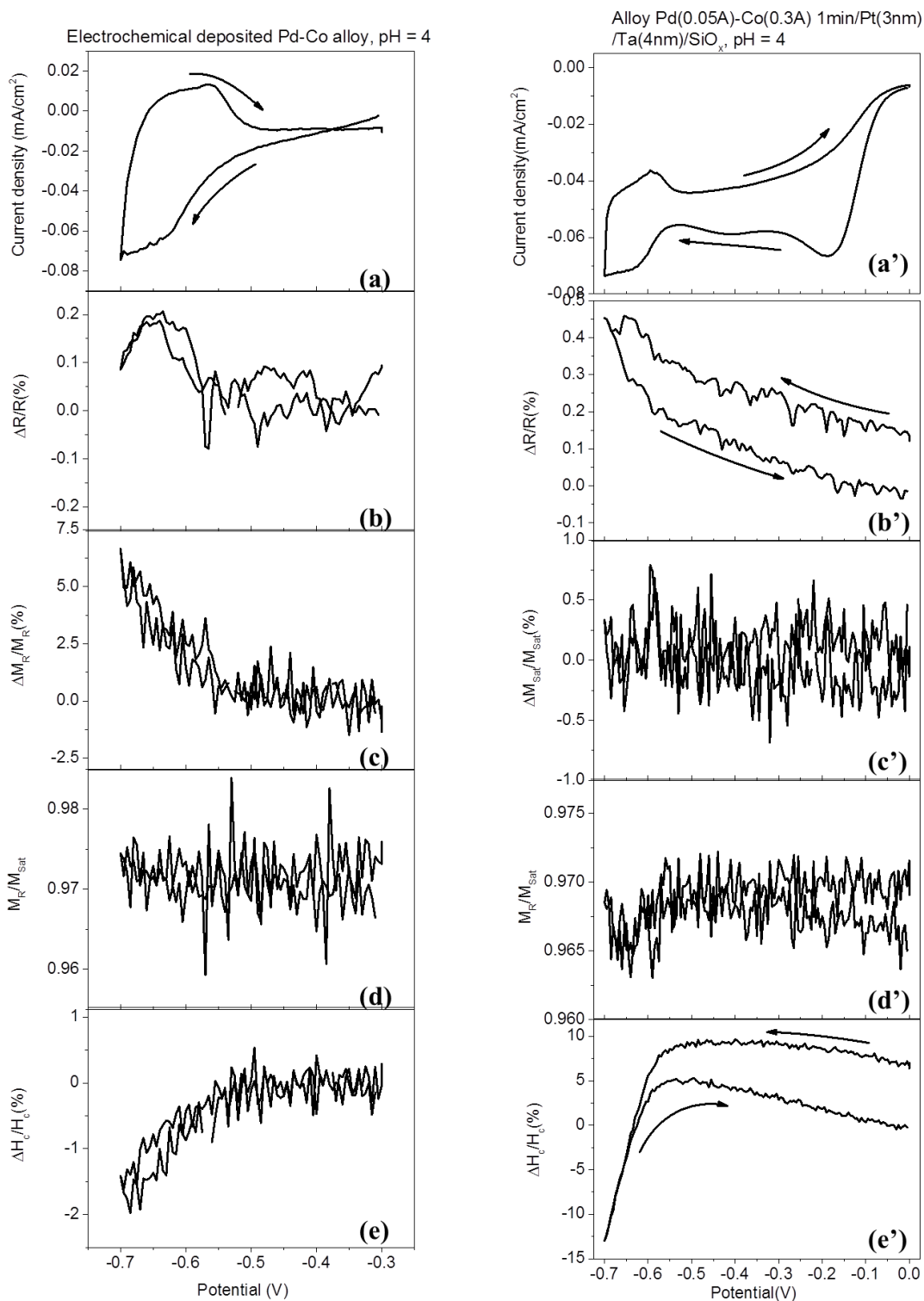


Fig. 5.20: (a) – (e) Electrochemical current density; $\Delta R/R$; $\Delta M_R/M_R$; M_R/M_{Sat} ; $\Delta H_c/H_c$ versus potential of the electrodeposited PdCo alloy/Au(111)/Si(111) in a pH ~ 4 blank electrolyte during the potential scan between -0.3V and -0.7V. The scan rate is 10mV/s. (a')-(e') Electrochemical current density; $\Delta R/R$; $\Delta M_R/M_R$; M_R/M_{Sat} ; $\Delta H_c/H_c$ versus potential of the sputtered Pd(0.05A) – Co(0.3A) 1min alloy in a pH ~ 4 blank electrolyte during the potential scan between 0V and -0.7V. The scan rate is 10mV/s.

For the sputtered Pd(0.05A)-Co(0.3A) alloy, **Fig. 5.20 (a') – (e')** also shows that $\Delta R/R$ increases by $\sim 0.4\%$ upon H adsorption. On the other hand, the only measurable changes in the $M-H$ curves are a drop of H_c by $\sim 13\%$. It is not clear whether this drop is exclusively related to H adsorption or the onset of H absorption. The quasi-linear potential dependence of $\Delta H_c/H_c$ between 0V and -0.5V is most probably related to MEC described in **Chapter 4**. The observed variations are only partly reversible, probably because of the extended sweep range at positive potential.

Figure 5.21 presents the dependence of $\Delta R/R$ and the $M-H$ curve analysis in the HER potential range for electrodeposited and sputtered alloys. For the electrodeposited PdCo alloys, **Fig. 5.21 (a)-(d)** clearly show a large reversible decrease of $\Delta R/R$ associated with HER and HOR. This behavior is similar to that of Pd/Co bilayers. This drop is concomitant with a large increase of M_R ($\sim 100\%$) and a significant drop of H_c ($\sim 18\%$). H_c changes stop at -1V whereas M_R and R continue to change until -1.2V and even on the backward sweep to -1V. All of these parameters recover their value upon HOR. The large hysteresis between forth and back sweeps is essentially related to large separation between HER and HOR peaks ($\sim 0.5V$). These changes associated with HER for the sputtered PdCo alloys are clearly different (**Fig. 5.21 (a')-(f')**). First, the $\Delta R/R$ drop due to HER is one order of magnitude smaller. In addition, $\Delta R/R$ variations reach a plateau before the negative sweep end. $\Delta R/R$ changes are essentially the same for the three sputtered alloys.

For the Pd(0.05A)-Co(0.4A) and Pd(0.05A)-Co(0.3A) alloys which are perpendicularly magnetized over the whole investigated potential range, the prominent changes are found for H_c which drops by $\sim 35\%$. In the case of the Pd(0.05A)-Co (0.3A) alloy, HER induces not only a H_c drop but also a drop of M_R , and $M_R/M(1KOe)$, indicating that the magnetization direction departs from the surface normal and becomes almost in-plane ($M_R/M(1KOe) \sim 0.1$) at -1V. These modifications are reversible upon sweeping the potential in HOR range. The hysteresis between the back and forth sweeps is rather small ($\sim 0.1V$) and is smaller than that between HER and HOR peaks ($\sim 0.2V$).

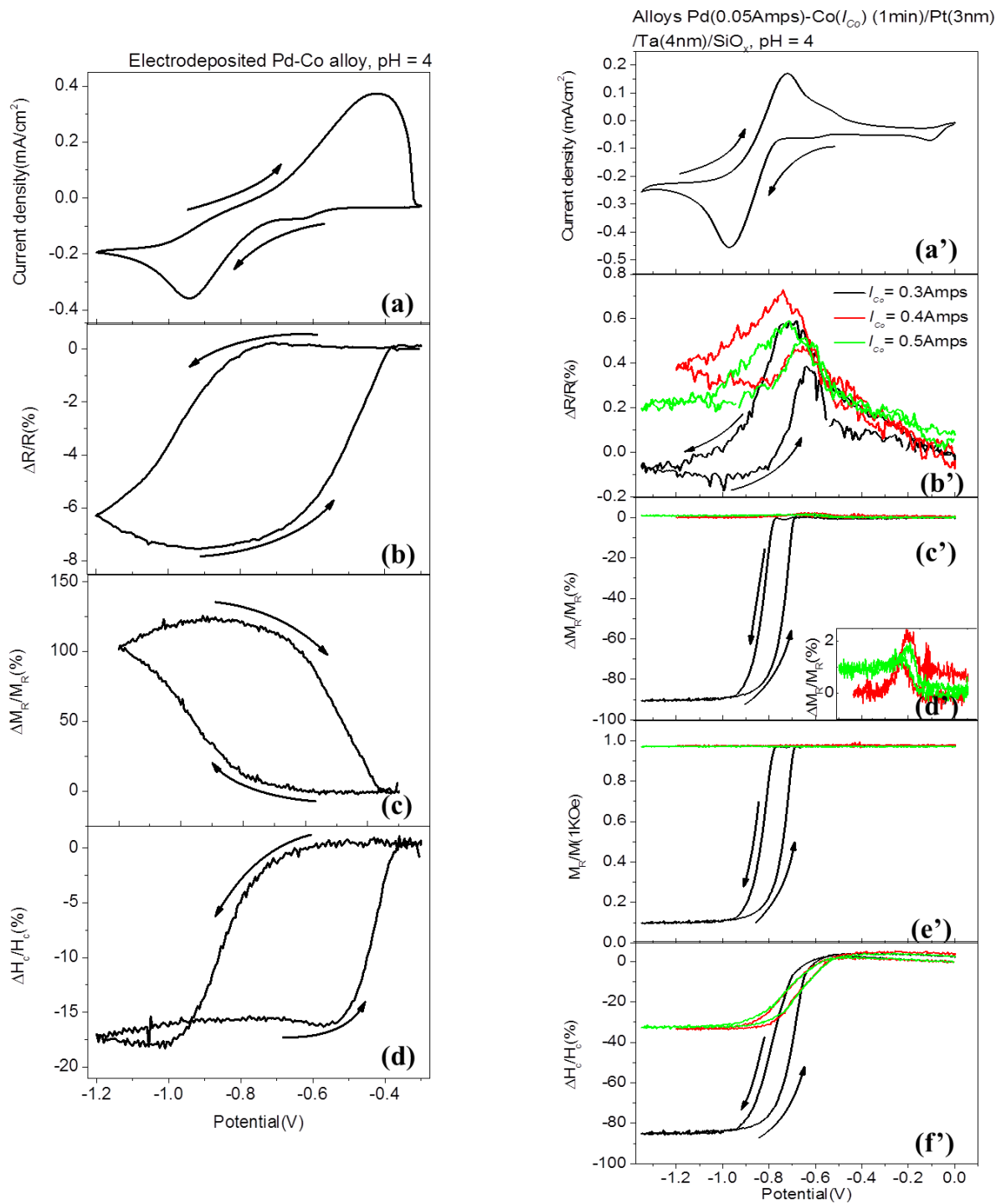


Fig. 5.21: (a) – (d) Electrochemical current density; $\Delta R/R$; $\Delta M_R/M_R$; $\Delta H_c/H_c$ versus potential of the electrodeposited PdCo alloy/Au(111)/Si(111) during the potential scan between -0.3V and -1.2V. The scan rate is 10mV/s. (a')-(f') Electrochemical current density; $\Delta R/R$; $\Delta M_R/M_R$; M_R/M_{Sat} ; $\Delta H_c/H_c$ versus potential of the sputtered PdCo alloys during the potential scan between 0V and -0.7V. The different curves correspond to different Co sputtering deposition currents. The inset (d') is the zoom of (c'). The scan rate is 10mV/s.

In order to examine the time response of the system, potential-step experiments are performed for the electrodeposited and sputtered PdCo alloys (**Figs. 5.22** and **5.23**). For the electrodeposited PdCo alloy, **Fig. 5.22.(a)-(e)** clearly show two distinct behaviors: (i) a rather progressive one with a time constant of at least 10s for $\Delta R/R$ and $\Delta M_R/M_R$; (ii) a fast one with a time constant of ~ 1 s for $\Delta H_c/H_c$. The variations of $\Delta R/R$ and $\Delta M_R/M_R$ as a function of time are very similar and almost overlap as shown in **Fig. 5.22.(e)** for three potential steps. It is interesting to note the time dependence of $\Delta R/R$, $\Delta M_R/M_R$ and $\Delta H_c/H_c$ whenever the potential stepped to -1V or more negative. For the latter, the saturation behavior is almost reached at -0.9V. The same values of reflectivity R , coercivity H_c and remanence M_R at -0.35V are found after each successive potential steps experiment. This demonstrates the very good reversibility of the system. The values at saturation of the different parameters are consistent with those obtained in **Fig. 5.21**. In addition, it is worth noting that $\Delta R/R$ and $\Delta M_R/M_R$ do not reach saturation at the end of 50-second pulse.

For the sputtered Pd(0.05A)-Co(0.3A), $\Delta R/R$ and $\Delta H_c/H_c$ have similar time response with a characteristic time of less than 1s (see **Fig. 5.23 (a)-(c)**). The variations of $M_R/M(1KOe)$ are somewhat slower with a characteristic time of ~ 7.5 s (**Fig. 5.23 (d)**). The variations of these parameters as a function of the step potential are in agreement with the data obtained in **Fig. 5.21**, and are reasonably reproducible upon applying several consecutive potential pulses (**Fig. 5.23 (a')-(d')**).

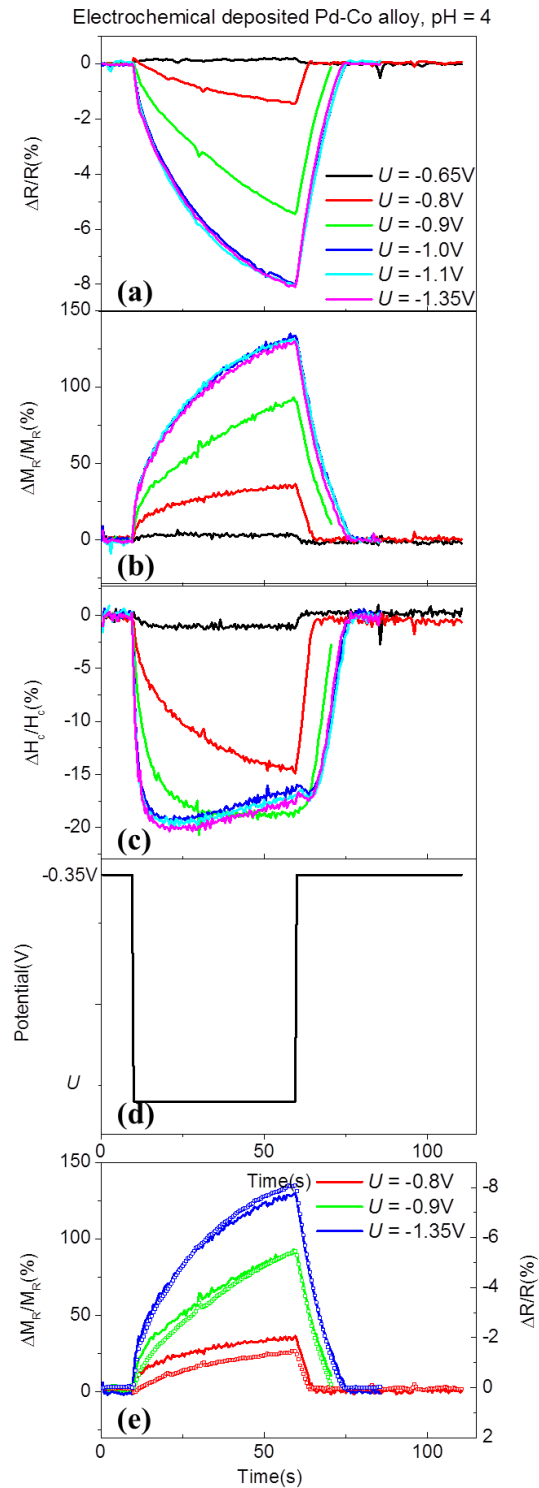


Fig. 5.22: (a) –(c): $\Delta R/R$; $\Delta H_c/H_c$; $\Delta M_R/M_R$ of the electrodeposited PdCo alloy/Au(111)/Si(111) in contact with a pH \sim 3.5-4 blank electrolyte during a series of potential steps experiments. The potential sequence is described in Fig.5.22.(d) : the potential is switched from -0.35V to U for 50s and then applied again at -0.35V for 60s, where U is -0.65V (black line), -0.8V (red line), -0.9V (green line), -1.0V (blue line), -1.1V (cyan line) and -1.35V (magenta line). (e): $\Delta M_R/M_R$ (left y-axis, line) and $\Delta R/R$ (right y-axis, open circles) during the potential – step experiments.

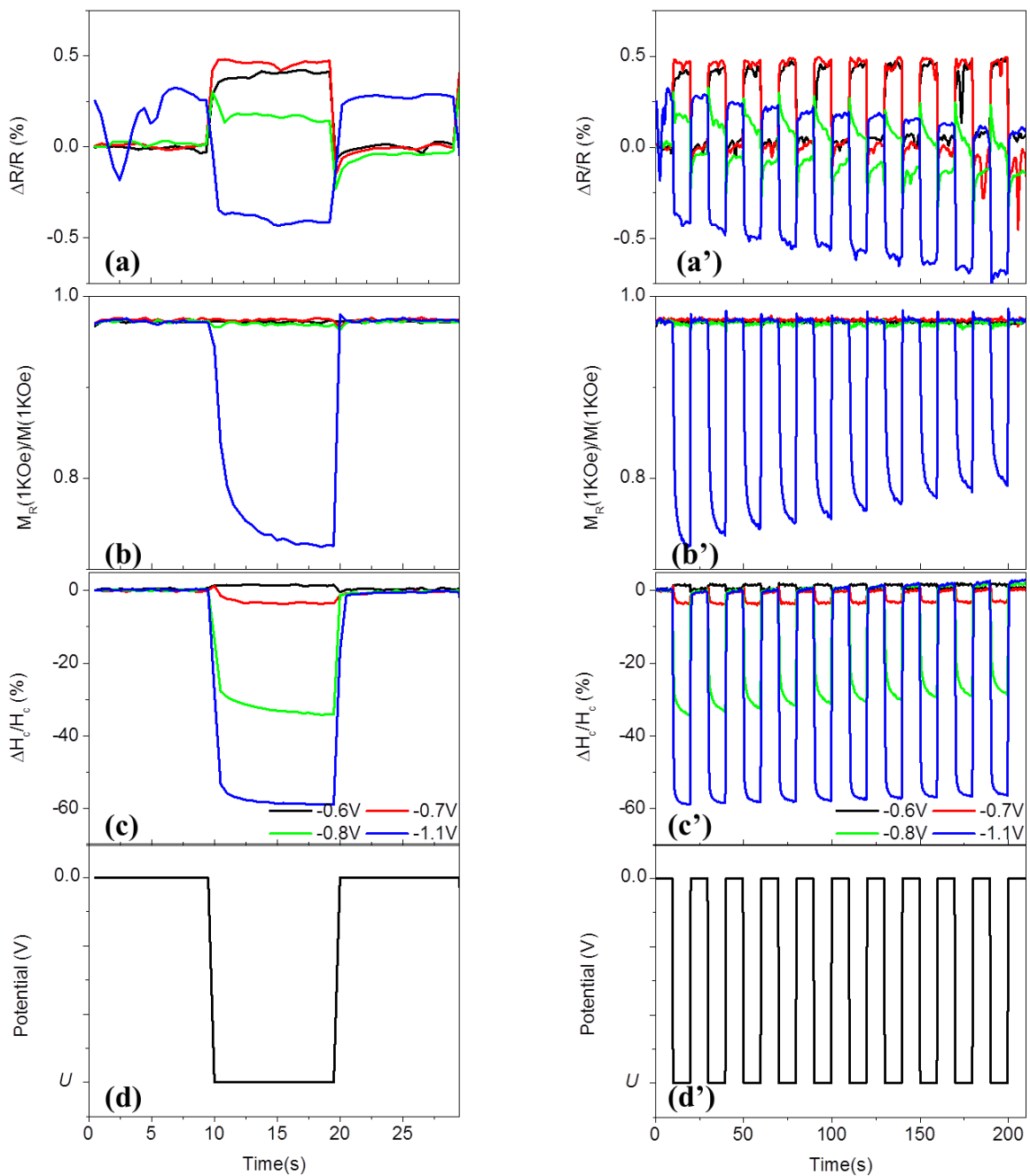


Fig. 5.23: (a)-(c) $\Delta R/R$; $M_R/M(1kOe)$ and $\Delta H_c/H_c$, of the sputtered Pd(0.05A) – Co(0.3A) alloy in contact with a pH \sim 3.5 – 4 blank electrolyte electrolyte, during the first potential sequence of a ten-time repetitive potential - step experiments. The first potential sequence are described in (d): the potential is applied at 0V for 10s; then switched under the potential control of U for another 10s, where U is -0.6V (black line), -0.7V (red line), -0.8V (green line) and -1.1V (blue line). This sequence is repeated 10 times. (a')- (d'): $\Delta R/R$; $M_R/M(1kOe)$; $\Delta H_c/H_c$; U during the ten-time repetitive potential-step experiments.

5.5. Discussion

5.5.1. Growth of the Pd/Co bilayer and PdCo alloys

As explained earlier, the main difficulty for the electrochemical growth of Pd/Co bilayers and PdCo alloys is to determine the growth mode and rate of the Pd at potentials where the Co does not undergo dissolution ($U < -1.1$ V). The results of Pd growth on Au shown in the Appendix clearly indicate that Pd growth on Au(111) at -1.1 V does not depend on the deposition time and is limited to ~ 1.5 ML, whereas ~ 10 ML may be deposited in 100s at -0.7 V. Such Pd growth process on Au is probably similar on Co. In addition, the reflectivity signal cannot be used to monitor Pd deposition at -1.1 V because of the large decrease of the sample reflectivity induced by H absorption into Pd or PdCo alloys. The change in the optical properties of Pd as a function of the amount of absorbed H is well-documented and all reported works show an increase of the Pd transmittance or a decrease of the Pd reflectivity upon H absorption [3, 5, 21]. The $M-H$ curves allow gaining insight into the growth of the first few MLs in the presence of Co, the Co magnetic anisotropy being sensitive to the Co interface. Our results clearly show (**Fig. 5.7**) that in the case of sequential Pd/Co growth (bilayer films), a Pd layer covers entirely the Co layer at -1.1 V preventing it from dissolution at more positive potentials. This suggests a rather bi-dimensional growth. However, the Pd thickness could not be determined. In the case of PdCo alloy layers (**Fig. 5.14**), the $M-H$ curves also clearly indicate the formation of the alloy covered by a Pd layer during the first potential sweep but no indication of any further alloy growth during the second sweep. In addition, we have no indication on the structure of the alloy, and whether it is a solid solution or composed of separated Co and Pd islands. Previous STM studies of PdCo codeposition showed that the formation of PdCo alloys competes with the formation of Co biatomic islands [19]. We thus suspect that the PdCo alloys in the present work are composed of Co and Pd islands, but we have no indication on their size.

In the case of sputtered films, the sharpness of the interfaces (Pd/Co and Co/Pt for the bilayer, PdCo/Pt for the alloy) may be questionable because of the kinetic energy of the deposited atoms. Thus, some intermixing at these interfaces is expected which may influence the film magnetic properties. This is furthermore supported by preliminary X-Ray reflectivity measurements (not shown) which suggest that the transition layer between Pt and Co, Pt and PdCo, and Co and Pd is 2–3 ML thick. Such intermixing is rather limited in the case of the

electrodeposited layers because the thermal energy of the deposited adatoms is much smaller. We also investigated the Co and the PdCo structure of the sputtered films by X-Ray diffraction. However, the presence of rather broad peaks of the substrate (Ta and Pt) and the absence of pure Co or Pd peaks prevented us from concluding on the Co and PdCo alloy crystallographic orientation. Finally, the AFM images indicate a granular structure with a typical size range of 10–30 nm. This granular morphology contrasts with that expected for the electrodeposited layers since the substrate is atomically flat and the growth of Co and Pd is bi-dimensional on Au(111) (see **Chapter 2** and Appendix and reference therein).

5.5.2. Magnetic properties of the Pd/Co bilayers

In the case of Pd/Co bilayers, we didn't observe any significant influence of H adsorption on Pd/Co on the magnetization of Co. Such a behavior is not surprising since the Pd capping layers are several monolayers thick and adsorbed H is expected to affect the electronic structure of the Pd topmost layer. To explore such effects a 1–2 ML thick Pd layer is a prerequisite, which is one of the perspectives of this work.

H absorption in the Pd layer has a strong influence on M_R and H_c (**Fig. 5.11**). The effect of H_{abs} on M_R in MOKE measurements has been reported for Pd capped Co layers and has been attributed to the modification of the refractive index of the Pd which becomes more transparent in the presence of H_{abs} , increasing thus the MOKE signal [3, 12]. Measurements on $(\text{Pd/Co})_n$ multilayers using non optical methods (SQUID, VSM), also showed modifications of the film magnetization upon H absorption [2, 20]. However, the magnetization in these films has in-plane and out-of-plane components and the magnetization change along one direction is accompanied by an opposite change in the other direction, indicating a magnetic anisotropy change rather a magnetization amplitude change. In our case, the drop of M_R as a function of potential is very well correlated with the drop of R indicating that the origin of M_R variations is not due to the modification of the Co magnetization but to that of the Pd transmittance. Additionally, even though we obtain an order of magnitude difference between the variations of M_R and R for the electrodeposited and those for the sputtered bilayers, the ratio $(\Delta M_R/M_R)/(\Delta R/R)$ is ~ 3 for both types of bilayers.

We modeled the optical properties of our samples using the simple matrix formalism adapted for stratified media and determined R variation upon changing the Pd layer into a β Pd–H phase. Different values of the refractive index of the β Pd–H phase may be found in the

literature. We considered those that reproduce reasonable well the experimental findings in published works using Pd films thicker than 10 nm deposited on glass or ITO. We thus chose the following refractive indexes $n_{\text{PdH}} = 1.8 + 3.2 i$ and $n_{\text{Pd}} = 1.9 + 4.2 i$ [21]. The simulation results present a drop of R upon H absorption by typically 5–8% for both types of samples, a value which is consistent with that obtained with the electrodeposited bilayers. The much lower $\Delta R/R$ value measured on the sputtered samples may be due to the presence of intermixing between Co and Pd and/or the granular morphology of these films which makes unreasonable their modeling as a stratified medium.

The variations of H_c may be considered as due to the variation of the magnetic anisotropy energy, as has been shown for electrodeposited samples in **Chapter 4**. Indeed, an increase of PMA has been shown upon H absorption into Pd for a Pd/Co/Pd layer [22], even though in this reference these variations were not reversible upon H removal, a behavior associated with the modification of the film structure. A rather reversible change of H_c of 17% has been shown by Lin *et al.* for a Pd/Co/Pd layers deposited in UHV upon H absorption [16]. In our case, the amplitude of $\Delta H_c/H_c$ is larger ($\sim 26\%$) for the electrodeposited bilayers. On the other hand, it is smaller by a factor of ~ 3 for the sputtered samples. However, the most important difference is the $\Delta H_c/H_c$ sign which is positive for the electrodeposited samples and negative for the sputtered ones. A H_c drop is also observed for the PdCo alloys which suggests that the Pd and Co intermixing in the sputtered bilayers is significant and that the resulting film structure is close to an alloyed phase. If one assumes that the magnetic domain nucleation and propagation is similar to CO-covered Co/Au layers with the same thickness studied in **Chapter 4**, a $\Delta H_c/H_c$ value of $+26\%$ would correspond to a K_S increase of $\sim 0.1 \text{ erg/cm}^{-2}$. If this anisotropy increase is due exclusively to the Co magneto-elastic anisotropy, we can determine the strain in the Co layer using the relation: $K_{ME} = (B_1 + 2B_3) \times \varepsilon_1 + B_2 \times \varepsilon_3$ where ε_1 is the strain along one in-plane axis and ε_3 the strain along the surface normal. The B_i are the magneto-elastic coefficients with $B_1 = -0.8 \cdot 10^8 \text{ erg/cm}^3$, $B_2 = -2.9 \cdot 10^8 \text{ erg/cm}^3$ and $B_3 = 2.8 \cdot 10^8 \text{ erg/cm}^3$ [23]. In an elastic deformation, ε_1 and ε_3 are related by the elastic constants c_{13} and c_{33} by: $\varepsilon_3 = -2(c_{13}/c_{33})\varepsilon_1$ [24]. For hcp Co, $c_{13} = 1.0 \cdot 10^{11} \text{ Pa}$ and $c_{33} = 3.6 \cdot 10^{11} \text{ Pa}$ [25]. Consequently, we can write: $K_{ME} = 6.4 \cdot 10^8 \varepsilon_1$. The measured interface magnetic anisotropy increase corresponds thus to $\varepsilon_1 \sim 0.8\%$. This value is smaller but reasonably close to the values of 2–3% found for the β Pd-H phase [2, 12]. Therefore, the observed increase of PMA may be entirely due to the strain in the Co layer induced by the formation of the β Pd-H phase.

5.5.3. Magnetic properties of the PdCo alloy layers

PdCo alloys crystallize in the fcc phase in a large range of composition. As has been experimentally shown by Fujiwara *et al.* [26], the (111) axis is the easy magnetization axis and the magneto–crystalline anisotropy energy constant depends on the Co content and at room temperature, it is in the range $5\text{--}7 \cdot 10^5 \text{ erg/cm}^3$ for a Co content between 30% and 50% [26]. In our case, the composition of the sputtered alloys is in the range 30–40%, corresponding to Co sputtering currents of 0.3A and 0.5A respectively. The total anisotropy energy may be thus estimated assuming a negligible magneto–elastic anisotropy energy and a Pd/Co interface anisotropy of 0.63 erg/cm^2 [27]. We obtain for our 3nm films a value of $3.6 \cdot 10^6 \text{ erg/cm}^3$ for the 30% alloy and $2.9 \cdot 10^6 \text{ erg/cm}^3$ for the 40% alloy. In both cases the anisotropy energy is significantly positive indicating a PMA in agreement with our observations. In the case of electrodeposited alloys, the composition and the structure of the alloy layer are unknown. It is thus difficult to derive similar estimations.

Regarding the reflectivity change upon H absorption (**Fig. 5.21**), we obtain a similar drop of $\Delta R/R$ as the case of bilayers with a similar difference between electrodeposited and sputtered alloys. The similarity with what we have observed for the bilayers suggests that the difference in the reflectivity behavior originates from the alloy morphology. H absorption seems also efficient for these layers, which is consistent with the fact that these alloys are Pd rich. $\Delta M_R/M_R$ curve is also very similar to that of $\Delta R/R$ as long as the magnetization remains perpendicular to the sample surface.

On the other hand, the variations of H_c indicate a PMA drop upon H absorption for both types of layers (**Fig. 5.21**). In addition, the sputtered alloy with 30% of Co undergoes a quasi-total SRT upon H absorption. Consequently, the magnetic anisotropy drop induced by H absorption is of the order of $3.6 \cdot 10^6 \text{ erg/cm}^3$. We can compare this energy to the magneto–elastic one as we did for the bilayers. An isotropic expansion of the alloy film won't induce a favored magnetization direction. We will thus assume that the dominant lattice expansion is along the surface normal. This is justified by the fact that the in–plane expansion is at least partially hindered by the substrate. This approximation may be valid for the electrodeposited 2D films but is rather crude for sputtered films because of their granular morphology. However, our simplification is justified since we are interested in order of magnitudes. Consequently, $K_{ME} = B_2 \cdot \varepsilon_3$, where ε_3 is the strain along the surface normal (111) direction,

and $B_2 = -3 c_{44} * \lambda_{111}$, c_{44} being the elastic stiffness coefficient and λ_{111} the magneto–striction constant along the surface normal of the PdCo alloy [25]. For a Co content in the range 30–40%, λ_{111} amounts $\sim -2.5 \cdot 10^{-4}$ [26]. We approximated the value of c_{44} for the PdCo alloy by $4.1 \cdot 10^{11}$ erg/cm³, the average value of that of fcc Co ($1.3 \cdot 10^{11}$ erg/cm³) [25] and that of Pd ($7 \cdot 10^{11}$ erg/cm³) [28]. In these conditions, $B_2 = +3.1 \cdot 10^8$ erg/cm³. Consequently, a vertical expansion of the alloy film will induce a PMA increase, which is the opposite behavior of what we observe experimentally. The reason of this discrepancy is not clear. One other possibility explaining the PMA drop is the modification of the film magneto–crystalline anisotropy due to the presence of H in the alloy. However, we couldn't find similar behavior in the literature. It is thus difficult to provide an unambiguous conclusion.

5.5.4. Time response of the Pd/Co bilayers and PdCo alloy layers

It is interesting to compare the system response time constant upon H absorption. In the case of sputtered layers (**Figs. 5.12** and **5.23**), the modification of R and H_c are systematically within the time resolution of our setup (0.5s). Since the diffusion coefficient of H into Pd is $D = 3.2 \cdot 10^{-7}$ cm²/s [29], the typical time constant for H diffusion in our few nm thick layers is a fraction of μ s. Thus the measured time constant is most probably limited by our setup time resolution.

In the case of electrodeposited layers, the time constant of H_c variation is also close to 1s. However, the time constant of R variation strongly defers and may be larger than 10s for the electrodeposited alloys (**Fig. 5.22**). The continuous R drop well after the saturation of H_c is accompanied by M_R relative changes which are quasi–similar to those of R . This suggests continuous increase of the film transmittance associated with H absorption with no effect on the film magnetic anisotropy. This surprising behavior may be due to the specific structure of the electrodeposited alloy. Indeed, the deposition procedure (**Fig. 5.14**) yields Pd/PdCo/Pd stack with a relatively low Pd content in the alloy since at the Co deposition potential, the Pd deposition slows down significantly. Therefore, after transforming the upper Pd layer into Pd–H, H diffusion is slowed down by Co, since the diffusion coefficient of H into Co is rather small. The time constant for the formation of Pd–H phase in the lower Pd layer is very much increased. The absence of any influence of H absorption in the lower layer on the film magnetic anisotropy remains however intriguing.

5.6. Conclusion

In this Chapter, the preparation of Pd/Co bilayers and PdCo alloys by electrodeposition and sputter deposition are shown. From former studies, we know that the electrodeposited layers on Au(111) present a bi-dimensional atomically flat morphology. For sputtered bilayers on Pt(3nm)/Ta(4nm)/SiO_x(50nm)/Si, AFM images demonstrate a granular structure with a typical size range of 10-30 nm.

The influence of H adsorption/absorption on the magnetic properties of Pd/Co bilayers and PdCo alloys was described. In the case of Pd/Co bilayers, no significant variations of the magnetic properties were observed upon H adsorption. However, H absorption induces noticeable variations of M_R and H_c . The drop of M_R as a function of potential is very well correlated with the decrease of R . The origin is due to H_{abs}-induced modification of optical properties when Pd is changed into a β Pd-H phase. The changes of H_c with H absorption indicate variations of the magnetic anisotropy. It may be explained by the variation of the magnetoelastic anisotropy upon H absorption. In the case of PdCo alloys, similar effects of H absorption on M_R and R were observed compared to bilayers. The variation of H_c implies a PMA drop for both types of alloys. H absorption may even induce a quasi-total SRT for PdCo sputtered alloy (~30% Co). H_c time response of H_{abs}-induced changes for Pd/Co bilayers and PdCo alloys is typically less than 1s for all samples.

5.7. References

- [1] A. Weidinger, D. Nagengast, C. Rehm, F. Klose, B. Pietzak, Metallic multilayers and hydrogen, *Thin Solid Films*, 275 (1996) 48-53.
- [2] K. Munbodh, F.A. Perez, C. Keenan, D. Lederman, M. Zhernenkov, M.R. Fitzsimmons, Effects of hydrogen/deuterium absorption on the magnetic properties of Co/Pd multilayers, *Physical Review B*, 83, 094432 (2011).
- [3] T.P.L. Pedersen, C. Liesch, C. Salinga, T. Eleftheriadis, H. Weis, M. Wuttig, Hydrogen-induced changes of mechanical stress and optical transmission in thin Pd films, *Thin Solid Films*, 458 (2004) 299-303.
- [4] L.L. Jewell, B.H. Davis, Review of absorption and adsorption in the hydrogen-palladium system, *Appl. Catal. A-Gen.*, 310 (2006) 1-15.
- [5] K. Kalli, A. Othonos, C. Christofides, Characterization of reflectivity inversion, alpha- and

beta-phase transitions and nanostructure formation in hydrogen activated thin Pd films on silicon based substrates, *Journal of Applied Physics*, 91 (2002) 3829-3840.

[6] H. Duncan, A. Lasia, Mechanism of hydrogen adsorption/absorption at thin Pd layers on Au(111), *Electrochimica Acta*, 52 (2007) 6195-6205.

[7] A.J. Maeland, T.R.P. Gibb, X-ray diffraction observations of Pd-H₂ system through critical region, *Journal of Physical Chemistry*, 65 (1961) 1270-1272.

[8] E.A. Owen, E.S.J. Williams, X-ray study of the hysteresis effect observed in the palladium-hydrogen system, *Proceedings of the Physical Society*, 56 (1944) 52.

[9] G.R. Stafford, U. Bertocci, In Situ Stress and Nanogravimetric Measurements During Hydrogen Adsorption/Absorption on Pd Overlayers Deposited onto (111)-Textured Au, *J. Phys. Chem. C*, 113 (2009) 13249-13256.

[10] D.E. Azofeifa, N. Clark, W.E. Vargas, H. Solis, G.K. Palsson, B. Hjorvarsson, Hydrogen induced changes in the optical properties of Pd capped V thin films, *J. Alloy. Compd.*, 580 (2013) S114-S118.

[11] W.C. Lin, C.J. Tsai, X.M. Liu, A.O. Adeyeye, Critical hydrogenation effect on magnetic coercivity of perpendicularly magnetized Co/Pd multilayer nanostructures, *Journal of Applied Physics*, 116, 073904 (2014).

[12] W.C. Lin, C.J. Tsai, B.Y. Wang, C.H. Kao, W.F. Pong, Hydrogenation induced reversible modulation of perpendicular magnetic coercivity in Pd/Co/Pd films, *Applied Physics Letters*, 102, 252404 (2013).

[13] B. Hjorvarsson, C. Chacon, H. Zabel, V. Leiner, Adjustable magnetic interactions: the use of hydrogen as a tuning agent, *J. Alloy. Compd.*, 356 (2003) 160-168.

[14] S. Emori, Magnetic Domain Walls Driven by Interfacial Phenomena, in: Department of Materials Science and Engineering, Massachusetts Institute of Technology, 2013.

[15] Y.H. Liu, D. Gokcen, U. Bertocci, T.P. Moffat, Self-Terminating Growth of Platinum Films by Electrochemical Deposition, *Science*, 338 (2012) 1327-1330.

[16] R.M. Bozorth, D.D. Davis, P.A. Wolff, J.H. Wernick, V.B. Compton, Ferromagnetism in Dilute Solutions of Cobalt in Palladium, *Physical Review*, 122 (1961) 1157-1160.

[17] H. Naohara, S. Ye, K. Uosaki, Electrochemical deposition of palladium on an Au(111) electrode: effects of adsorbed hydrogen for a growth mode, *Colloid Surf. A-Physicochem. Eng. Asp.*, 154 (1999) 201-208.

[18] Nicol, M. J. and H. I. Philip (1976). "Underpotential deposition and its relation to anomalous deposition of metals in alloys." *Journal of Electroanalytical Chemistry* 70(2): 233-

237.

- [19] Cadre, F. L. (2013). Etude STM in situ de la microstructure et de la croissance de films ultraminces d'alliages sur Au(111) synthétisés par co-dépôt. Département Physique, Ecole Polytechnique. Doctorat.
- [20] K. Munbodh, F.A. Perez, D. Lederman, Changes in magnetic properties of Co/Pd multilayers induced by hydrogen absorption, *Journal of Applied Physics*, 111, 123919 (2012).
- [21] von Rottkay, K., et al. (1999). "Refractive index changes of Pd-coated magnesium lanthanide switchable mirrors upon hydrogen insertion." *Journal of Applied Physics* 85(1): 408-413.
- [22] Okamoto, S., et al. (2002). "Enhancement of magnetic anisotropy of hydrogenated Pd/Co/Pd trilayers." *Journal of Magnetism and Magnetic Materials* 239(1-3): 313-315.
- [23] Gutjahr-Loser, T., et al. (2000). "Magnetoelastic coupling in Co thin films on W(001)." *Journal of Magnetism and Magnetic Materials* 220(1): L1-L7.
- [24] Sakamaki, M., et al. (2009). "Correlation of magnetism and structure for ultra thin Au/Co/Au films: evidence for magnetoelastic effects." 14th International Conference on X-Ray Absorption Fine Structure (Xafs14), Proceedings 190: 6.
- [25] Sander, D. (1999). "The correlation between mechanical stress and magnetic anisotropy in ultrathin films." *Reports on Progress in Physics* 62(5): 809-858.
- [26] Fujiwara, H., et al. (1983). "Magnetocrystalline anisotropy and magnetostriction of Pd-Co alloys." *Journal of Magnetism and Magnetic Materials* 31-34, Part 2(0): 809-810.
- [27] Engel, B. N., et al. (1991). "Interface magnetic anisotropy in epitaxial superlattices." *Physical Review Letters* 67(14): 1910-1913.
- [28] Nesbet, R. K. (1960). "Magnetic Hyperfine Structure of the Ground State of Lithium." *Physical Review* 118(3): 681-683.
- [29] Bohmhold, G and E. Wicke (1967). "Diffusion of hydrogen and deuterium in palladium and Pd alloys. I. Gas volumetric measurement." *Zeitschrift Fur Physikalische Chemie-Frankfurt* 56 (3-4): 133-155.

Chapter 6 Conclusions

In this work, we investigated the influence of surface chemistry and the electric field on the magnetic anisotropy of ultrathin layers of Co and Pd-Co bilayers/alloys. To study the magnetic anisotropy of the layers in different chemical and electrostatic conditions, we used an all electrochemical approach to deposit bi-dimensional atomically flat Co(0001) layers with controlled thickness on Au (111)/Si (111) substrate which was prepared by electrochemical etching, to easily modify the electrode surface chemistry, and to apply strong electrical fields at the surface of the electrode while avoiding short circuit problems often encountered in solid devices.

We showed that by exchanging the electrolyte of different pH (from pH ~ 4 to pH ~12) and controlling the applied potentials, the surface chemistry can be easily altered from H-terminated Co to Co covered with oxide layers of different oxidation states and structures. Cyclic voltammograms of as deposited Co layers in pH ~ 12 electrolyte presented three different oxide layers as a function of potential, of which the first two was extensively studied in our work. DFT calculations demonstrated that the most stable structure of the reduced surface is covered by a (1×1) H layer for $U < -1.3\text{V}$, whereas that of the oxidized Co surface presents an expanded atomic plane, with the structure (6×6)-CoOH, that is fully covered by OH for $-1.25\text{V} < U < -1.15\text{V}$; and by (5×5)-Co(OH)₂ for $U > -1.15\text{V}$. Integrated anodic and cathodic charge and real time in-situ reflectivity proved that the formation of (6×6)-CoOH adlayer is reversible, whereas during one potential sweep between -1.65V and -0.45V, ~ 4-ML (5×5)-Co(OH)₂ was developed and ~2-ML Co was dissolved. Real time in situ magnetic characterization demonstrated that a surface oxidation with (6×6)-CoOH adlayer enhances the surface magnetic anisotropy energy of Co/Au (111) ultrathin films with a global $K_s = 0.55 \text{ erg/cm}^2$ compared to 0.1 erg/cm^2 for the H covered surface. However, the influence of oxidation with (5×5)-Co (OH)₂ on MAE is more complicated to interpret. It increases firstly the MAE, and then reduces greatly the MAE with further oxidation. Nevertheless, our magnetic measurements showed an increase of the surface magnetic anisotropy energy up to

0.72erg/cm² with respect to that of the H-covered Co surface induced by the intermediate oxidation state during the (5×5)-Co (OH)₂ formation,.

The modification of the surface chemistry was achieved also by adsorption of other molecules. We found that the variations of the MAE induced by different molecular layers are due to the changes of the surface anisotropy K_S . K_S value is essentially related to the linkage Co-X, with X = H, OH, C and S. It increases with the linkage in the following order: H<OH<S ~ C. A correlation between K_S and the Co vertical strain induced by the molecular layers seems to exist. We also presented the MEC effects of H-, OH-, CO- and S- covered Co layers in both of acidic and alkaline electrolytes. Two mechanisms have been identified: a pure electrical effect corresponding to a linear and reversible variation of K_S with U for H-, OH- and S- covered Co over the whole investigated potential range, and CO- covered surface when no HER takes place; and modification of the surface chemistry induced by the electric field for CO-terminated surface in pH ~ 3.5-4 electrolyte when the CO-Co interface was changed to that covered with co-adsorption of CO and H_{ads}. The sign and value of $\Delta K_S/\Delta U$ depends also strongly on the linkage, and its absolute value increases in the following order: S<H<CO<OH.

Prior to study the Pd-Co thin films, Pd on Au (111)/Si (111) were investigated. We observed also changes of optical properties upon absorbing H into Pd layers, the effect of which has been presented already by previous studies. We established a correlation between H_{abs}-induced $\Delta R/R$ and the anodic charge Q_{an} corresponding to oxidation of H_{ads/abs}. This correlation allows determining the deposited Pd thickness, by using simple matrix formalism adapted for stratified media upon changing Pd into β Pd-H phase. We found that the Pd electrochemical deposition rate at -0.7V is ~ 0.1ML/s whereas at -1.1V, 1-2ML of Pd is grown with no dependence on the deposition time. Then Pd/Co bilayers and PdCo alloys were achieved either by electrodeposition on electrochemically etched Au(111)/Si(111), or by sputter deposition on the sputtered Pt(3nm)/Ta(4nm)/SiO_x (50nm)/Si substrate. We then presented the influence of hydrogen on the MAE of the Pd-Co thin films. In the case of Pd/Co bilayers, H adsorption shows no significant modification of the magnetic properties. On the contrary, H absorption reduces M_R , which correlated very well with the drop of R as a

function of potential. It implies that the M_R decrease is due to the H_{abs} -induced changes of optical properties. The variations of H_c upon H absorption ($\Delta H_c/H_c \sim 26\%$ and $\sim -10 \text{ -- } -6\%$ for electrodeposited and sputtered bilayers respectively) may be explained by the changes of the magnetoelastic anisotropy energy. In the case of PdCo alloys, similar effects of H_{abs} on M_R and R were observed. H_c decreases for both of the electrodeposited and sputtered alloys, indicating a drop of MAE upon H absorption. It can even induce a SRT for sputtered PdCo alloy with $\sim 30\%$ Co. H_c time response for all of the Pd-Co thin films is within 1s.

The experimental results demonstrated promising effects of modification of MAE changes of Co thin films by modifying the surface chemistry and by applying an electric field through an all electrochemical approach. Possible mechanisms have been proposed in this work. However, to better understand the correlation between K_S and the surface chemistry, the E -induced changes of the surface anisotropy of Co covered with different molecular layers $\Delta K_s^{\text{Co-MOL}}/\Delta U$, more refined theoretical works are required (e.g. DFT calculations).

Regarding the H-induced variations of the magnetic anisotropy of Pd-Co thin films, further studies about the structures, chemical compositions, surface morphology, etc. will shed lights on the origins of changes. It is also interesting to perform the *in situ* MOKE microscopy experiments to observe the domain walls' motions upon H absorption in the different Pd-Co systems.

Appendix: Study of Pd deposition on Au(111)/Si(111) and H adsorption/absorption in the Pd/Au system

A.1. Introduction

Palladium electrodeposition on Au(111) has been largely studied previously by several techniques as cyclic voltammetry (CV), potentiostatic current transient measurements, in situ scanning tunneling microscopy (STM), electrochemical quartz crystal microbalance (EQCM), etc. [1, 2]. Baldauf and Kolb reported an electrochemical layer-by-layer growth of the palladium on a gold single crystal electrode [3 - 5]. Damien *et al.* has also reported on a procedure to decorate Au(111) steps with flat Pd islands [6]. **Fig. A.1** presents a cyclic voltammogram adapted from [2]. Naohara *et al.* claim that the two cathodic peaks C_1 and C_2 at $U \sim +0.14V_{MSE}$ and $U \sim +0.05V_{MSE}$ respectively are due to the Pd deposition; and the anodic peak A at $U \sim +0.28V_{MSE}$ reflects the dissolution of Pd. Another cathodic peak C_H and the corresponding anodic peak A_H at $U \sim -0.52V$ indicates the hydrogen adsorption and desorption on Pd.

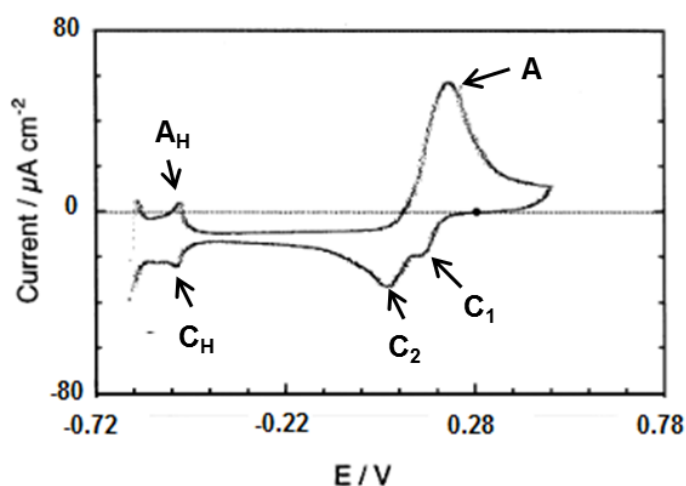


Fig. A.1: Current as a function of applied potential of an Au(111) electrode in 50mM H_2SO_4 containing $0.5mM PdCl_4^{2-}$, adapted from [2].

Previous studies about Pd deposition on Au through reduction of K_2PdCl_4 has proved that the adsorption of anions $[\text{PdCl}_4]^{2-}$ plays a crucial role [1 - 6]. A layer of PdCl_4^{2-} is present on the Au surface before the Pd deposition onset. It was also shown that Pd deposition proceeded two dimensionally in a large potential range down to $\sim -0.43\text{V}$, where hydrogen adsorption on Pd took place. EQCM measurement also showed the surface mass was steadily increased because of Pd deposition even in the potential region where hydrogen adsorption took place ($\sim -0.6\text{V}$) [2].

As stated in **Chapter 5**, due to the stability range of Co layers, we will be interested in Pd deposition at potentials $< -0.7\text{V}$. However, Pd deposition in these conditions has been rarely reported in literature. Recently, in the case of Pt deposition, Liu *et al.* [7] claimed a rapid self-terminating monolayer-by-monolayer electrodeposition process from a $\text{K}_2\text{PtCl}_4 - \text{NaCl}$ electrolyte. Despite the large negative potential, Pt deposition was inhibited at potentials just negative of proton reduction and the surface was reactivated for further Pt deposition by stepping the potential to more positive values, where the hydrogen is oxidized and fresh sites for the adsorption of PtCl_4^{2-} become available. They claim that PtCl_4^{2-} adsorption plays an important role in the deposition process. Their STM images illustrates that the morphology of monoatomic deposited Pt on Au(111) resulted from the coalescence of 2D Pt islands, with linear defects due to lifting of the reconstructed Au surface.

In our work, we are going to investigate the electrochemical deposition of Pd on Au (111) in a large potential window extending into the hydrogen evolution region ($U \sim -1.1\text{V}$). In addition, we will study the influence of H adsorption on Pd and H absorption into Pd on the optical properties of the Pd layers. As given in **Chapter 5**, it has been since long known that there are two phases in the Pd- H_2 system [8]: the α -phase which has lattice constants close to Pd metal with a ratio of H: Pd ~ 0.03 at room temperature; and the β -phase as more hydrogen dissolves in the metal and the lattice constant increases with a ratio of H: Pd ~ 0.6 [9, 10]. Both the α - and the β -phase have the same metal lattice structure and consist of octahedrally coordinated hydrogen atoms.

A.2. Experimental methods

Electrodeposited ultraflat epitaxial Au(111)/Si(111) is used as substrates. The preparation is described in **Chapter 2**. The sample is mounted in the P-MOKE flow cell under potential control. To deposit Pd thin films, 0.1mM K_2PdCl_4 + 0.1M K_2SO_4 + 1mM KCl + 1mM H_2SO_4 pH ~ 3.5-4 electrolyte was used. After Pd deposition, a 0.1M K_2SO_4 + 1mM KCl + 1mM H_2SO_4 pH ~ 3.5-4 electrolyte (acidic blank electrolyte) is introduced into the cell in order to remove all the remaining Pd(II) ions. After ~ 10min of circulation, potential scans are carried out to explore the H adsorption/absorption region. The optical properties were monitored by measuring in-situ the sample reflectivity at 633nm.

A.3. Results and discussion

Figure A.2 presents the electrochemical current density and the relative change of the sample reflectivity with respect to that at 0V for Pd deposition at -0.7V and -1.1V. The determination of Pd thickness using the cathodic charge during deposition is not so reliable because of side reactions (H_2 evolution, O_2 reduction, etc.). When Pd is deposited at -0.7V, the relative reflectivity increases with Pd deposition time. $\Delta R/R$ is around 1.1% at the end of 100-second growth. We calculated the expected reflectivity increase upon Pd deposition using the matrix formalism well-suited for a stratified medium. We find a quasi-linear increase of $\Delta R/R$ with Pd thickness with a slope of 8% nm^{-1} . The measured increase $\Delta R/R$ yields a thickness of ~ 0.1nm which correspond to ~ 0.5ML of Pd. This value is very low knowing that previous studies have shown significant Pd growth at ~ -0.6V [2]. This discrepancy will be explained below.

When Pd is deposited at -1.1V on top of the first Pd layer prepared at -0.7V, $\Delta R/R$ goes down immediately by ~ 4.3%. It continues to drop during the first 250-s deposition of Pd at -1.1V, with $\Delta R/R$ ~ -7.4%, where the reflectivity reaches a plateau. As we will see below, this behavior is induced by H absorption in the deposited Pd layers, which will be given in detail later.

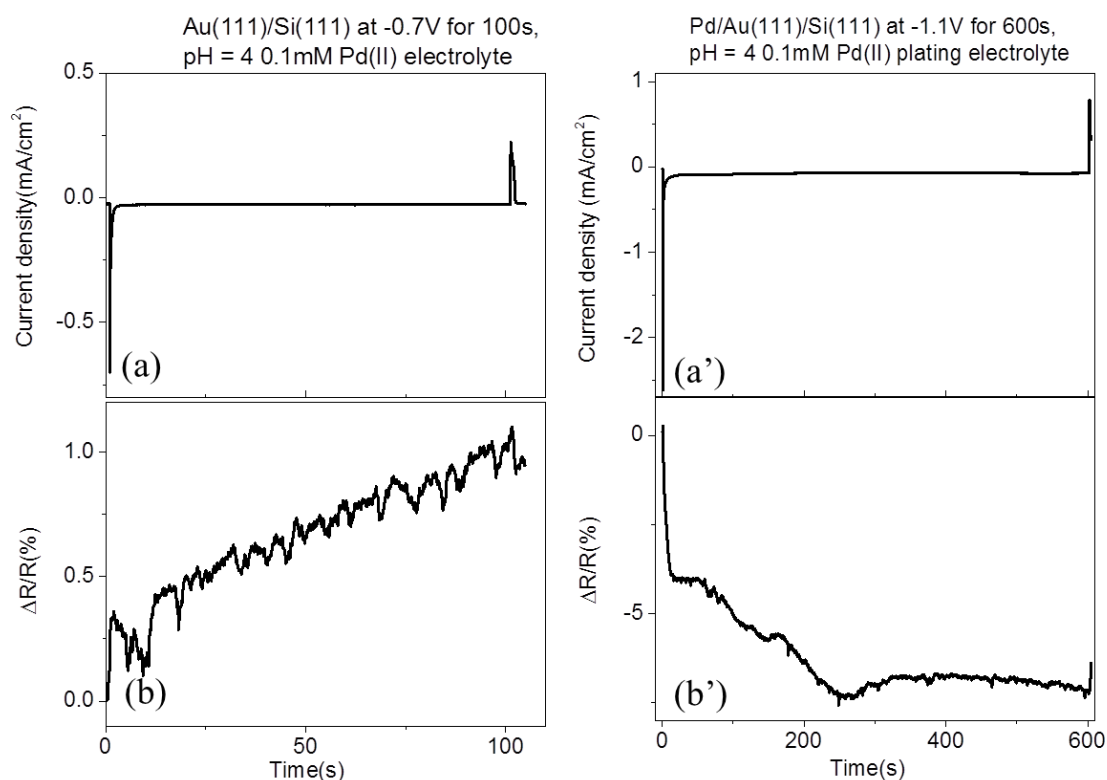


Fig. A.2: (a) electrochemical current density and (b) variations of the relative reflectivity of Au(111)/Si(111) in pH ~ 4 0.1mM K_2PdCl_4 plating electrolyte. The applied potential is switched from 0V to -0.7V, then held at -0.7V for 100s; and finally changed back to 0V. (a') and (b') same as (a) and (b) for Pd deposition at -1.1V on top of the Pd layer prepared in (a) and (b). Pd deposition time is 600s.

Figure A.3 displays the cyclic voltammogram and $\Delta R/R$ in a pH ~ 3.5 – 4 0.1M blank electrolyte of different deposited Pd layers. For the Pd/Au(111) layers deposited at -0.7V for 100s (**Fig. A.3.(a)-(b)**), the cathodic current flow of (a) starts to increase from -0.58V and reaches a maximum at ~ -0.64V (**Fig. A.3.(a)**). This peak symbolized as C_1 corresponds to the adsorption of H_{ads} on Pd. On the positive sweep, an anodic peak A_1 indicates the oxidation of H_{ads} . **Fig. A.3.(b)** shows the changes of $\Delta R/R$ with respect to that at -0.3V during the potential scan. $\Delta R/R$ presents a slight reversible increase around 0.1 – 0.15% with the cathodic peak and goes back to zero after the anodic peak.

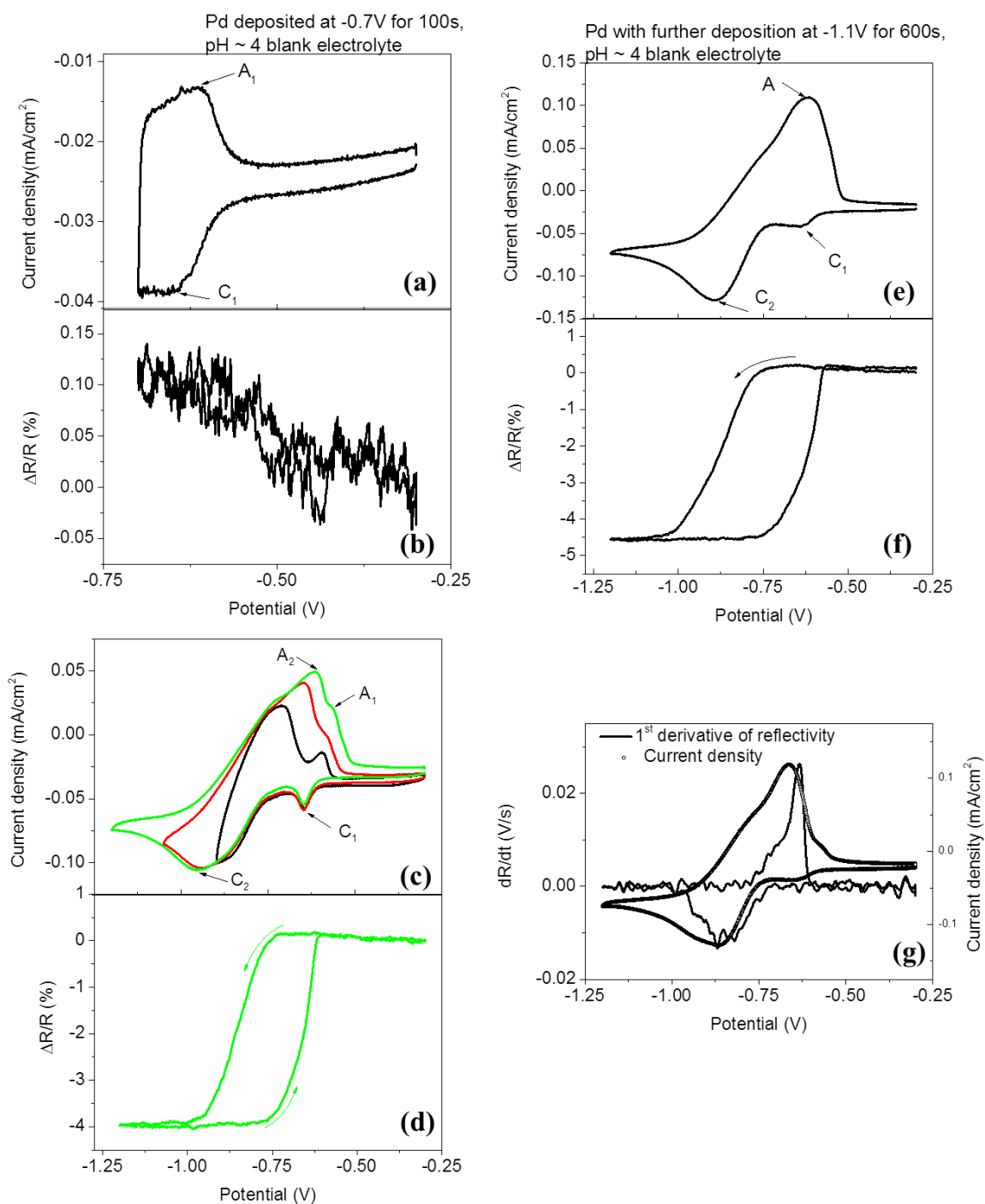


Fig. A.3: (a) electrochemical current density and (b) $\Delta R/R$ versus potential in an acidic blank electrolyte between -0.3V and -0.7V of the Pd firstly deposited at -0.7V for 100s; (c) and (d) same as (a) and (b) in an extended potential range and different Pd deposition conditions (see text for details); (e) and (f) same as (c) and (d) for a Pd deposition of 290s at -0.7V followed by 600s at -1.1V; (g) the 1st order derivative of $\Delta R/R$ versus time (left y-axis, line) and electrochemical current density (right y-axis, open circle) as a function of potential under the same experimental conditions as (e). The rate of all the potential scans is 10mV/s.

Figure A.3.(c) presents three successive potential scans from -0.3V to more and more negative potentials (-0.9V, -1.1V and -1.2V) for Pd layers deposited by repeated sweeps between -0.8V and -0.5V (15 sweeps at 100mV/s) separated by potential steps at -0.8V (450s in total). We observe two additional peaks: cathodic peak C_2 , where H^+ is transformed to H_2 gas and involves as well the absorption of H_{abs} into Pd; anodic peak A_2 corresponding to H_2 (dissolved in the electrolyte) oxidation and H_{abs} transformation into H^+ . Since these two processes take place in the same potential range, it is different to attribute the electrochemical charge to one of them. **Fig. A.3.(d)** shows $\Delta R/R$ during the potential scan. $\Delta R/R$ decreases with the cathodic peak C_2 and goes back with the anodic peaks A_2 and A_1 . The absolute value of $\Delta R/R$ reaches 4%. A hysteresis of $\sim 0.2V$ is present between the negative and the positive sweeps. It is not clearly correlated with the positions of peaks C_2 and A_2 . For a Pd layer prepared by 290s at -0.7V followed by 600s at -1.1V, we observed a similar behavior (**Fig. A.3.(e)-(f)**). The observed reflectivity drop in the HER potential range is consistent with previous studies which demonstrated that Pd becomes more transparent when it is loaded with H [11]. This is a clear indication that we have H absorption in the deposited Pd layers. From this drop, one may estimate the Pd thickness using a stratified medium model and considering that $n_{Pd} = 1.9 + 4.2i$, and $n_{Pd-H} = 1.8 + 3.2i$ (Pd-H β phase). Our calculations yield $\sim 1.6nm$ of Pd ($\sim 7ML$). We will see in the following that this value is consistent with other measurements.

In order to clarify the correlation between the reflectivity and the electrochemical current, the 1st order derivative of reflectivity versus time dR/dt during the same potential scan presented in **Fig. A.3.(f)** is shown (**Fig. A.3.(g)**). It is interesting to notice that on the negative sweep, dR/dt and the beginning of the HER peak overlap; on the positive sweep, dR/dt coincides with the end of the anodic peak A_2 .

To further clarify the mechanism of the H-induced reflectivity change, a series of potential steps experiments are carried out in a pH $\sim 3.5-4$ blank electrolyte, on Pd/Au layers firstly deposited at -0.7V for 100s (see **Fig. A.4**). The potential is stepped from -0.3V to -0.7V, -1.1V and -1.2V and then kept at these potentials for different durations. Except for -0.7V,

where the reflectivity remains almost unchanged, we observe a reflectivity decrease for all the potentials. **Fig. A.4.(b)** demonstrates that the variation of the relative reflectivity $\Delta R/R$ reaches a plateau after ~ 6 s. $\Delta R/R$ does not depend neither on the potential nor on the time as long as it's in the HER region provided it's longer than 6s.

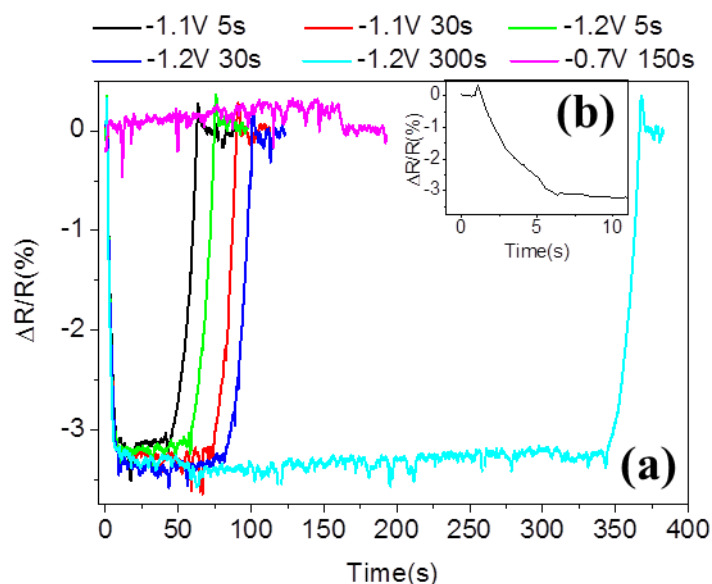


Fig. A.4: (a) $\Delta R/R$ versus time with respect to that at $-0.3V$ of the Pd layer deposited at $-0.7V$ for 100s during a series of the potential steps experiments in a pH $\sim 3.5-4$ blank electrolyte. The potential is switched from $-0.3V$ to $-0.7V$ for 150s (magenta line); to $-1.1V$ for 5s (black line) and 30s (red line); to $-1.2V$ for 5s (green line), 30s (blue line) and 300s (cyan line). Then the potential is swept back to $-0.3V$ at $10mV/s$. The inset (b) presents $\Delta R/R$ during the first 10s.

In order to gain insight into the deposition of Pd in the potential region of HER, we performed similar experiments after growing Pd at $-1.1V$ for 600s on the already existed Pd/Au (deposited at $-0.7V$ during 290s). We also grow two other Pd layers on top at $-1.1V$ during 1200s and 250s. After each Pd deposition, a specific potential step experiment is carried out. To estimate electrochemically the amount of H_{abs} , one has to minimize the contribution of the oxidation of dissolved H_2 in the electrolyte to the peak A_2 . For this purpose, after the negative potential step, the potential is stepped back to $-0.9V$ for 60s (where H_2 evolution current and H_{abs} oxidation current are low) to remove dissolved H_2 in the electrolyte in the vicinity of the electrode. Afterwards, a potential ramp is performed to $-0.3V$ to oxidize H_{abs} . The results are presented in **Fig.A.5**.

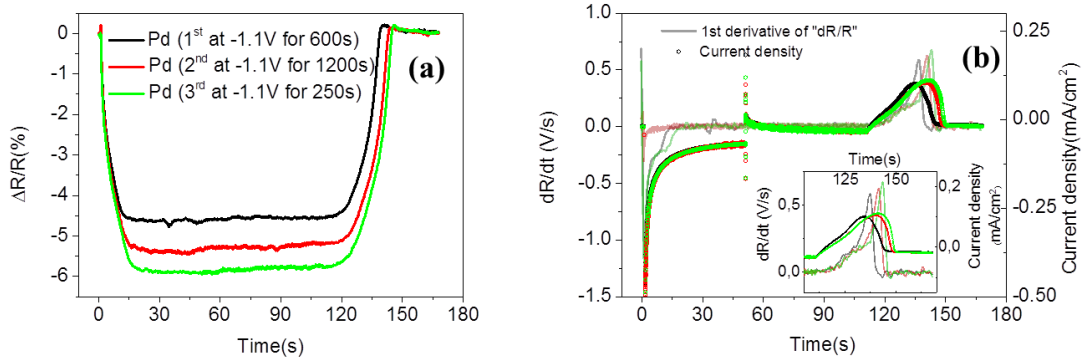


Fig. A.5: (a) the variation of the relative reflectivity with respect to that at -0.3V; (b) the 1st order derivative of reflectivity versus time dR/dt (left y-axis, line); and the electrochemical current density (right y-axis, open circle) during potential-step experiments: the potential is applied at -0.3V, and then held at -1.2V during 50s; prior to oxidize the adsorbed and absorbed H with a potential ramp until -0.3V at 10mV/s, the potential is maintained at -0.9V for 60s. Three Pd/Au electrodes are investigated: the 1st deposition at -1.1V for 600s on the already existing Pd; the 2nd one with further deposition at -1.1V for 1200s; and the 3rd one with still another deposition at -1.1V for 250s. The inset of the image (b) is the zoom between 105s and 170s.

The absolute value of $\Delta R/R$ increases typically by $\sim 0.7\%$ after each Pd deposition (**Fig. A.5.(a)**). **Fig. A.5.(b)** presents the 1st order of derivative of reflectivity versus time dR/dt , as well as anodic electrochemical current density during the potential ramps from -0.9V to -0.3V. Anodic peak A_2 and the positive peak of dR/dt are clearly different. This difference does not originate from the current contribution of the oxidation of dissolved H_2 since this is minimized by the potential step at -0.9V. This difference may be due to the fact that R is a local measurement while the current is due to the total area of the sample. The integrated anodic charge $Q(HOR)$ is 1.6, 1.85 and 2.07mC/cm² respectively. This increase of $\sim 0.2\text{mC/cm}^2$ shows that increase of the Pd thickness does not depend on the deposition time at -1.1V.

We performed similar potential step experiment (at -0.7V) on Pd layers with different thickness. **Fig. A.6** presents the correlation between $\Delta R/R$ (% , absolute value) and $Q_{an}(HOR)$. A linear relation is established and the best fitting gives:

$$Q_{an}(HOR)(\text{mC}/\text{cm}^2) = 0.39|\Delta R/R| (\%) + 0.46 \quad (\text{A.1})$$

The constant term is a surface term. It is partly due to the charge necessary to oxidize

the adsorbed H ($0.24\text{mC}/\text{cm}^2$). The origin of the remaining charge ($0.22\text{mC}/\text{cm}^2$) is not clear. It may be due to the presence of multilayer islands at small Pd thickness yielding significant $Q(HOR)$ but negligible $\Delta R/R$. In the following, we will only consider the term with $\Delta R/R$.

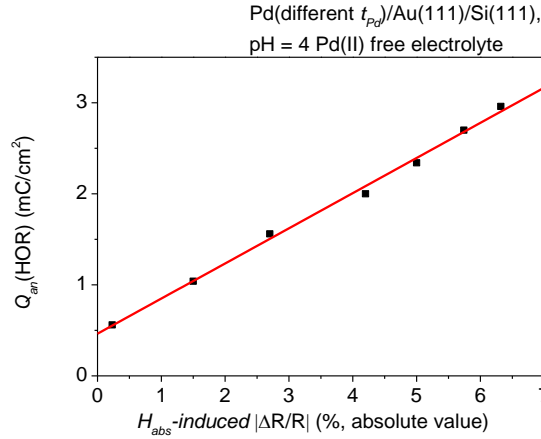


Fig. A.6: anodic charges corresponding to remove the saturated H_{ads} and H_{abs} from Pd of different thickness as a function of the absolute value of H_{abs} -induced variation of the relative reflectivity $\Delta R/R$ (%). Pd of different thickness is achieved through successive depositions at -0.7V for certain durations in a $\text{pH} \sim 3.5-4$ 0.1mM K_2PdCl_4 plating electrolyte. After each deposition, the same $\text{pH} \sim 3.5-4$ acidic blank electrolyte is exchanged into the EC cell to perform a potential-step experiments in order to saturate H_2 loading in Pd of different thickness and record the induced $\Delta R/R$ in real time; and then remove the incorporated H_2 from the corresponding Pd/Au(111)/Si(111) system through the hydrogen oxidation reaction. The quantity of the saturated H_{ads} and H_{abs} is thus estimated from the anodic charge Q corresponding to the hydrogen oxidation reaction.

It would be interesting to correlate $\Delta R/R$ with the Pd thickness, one way to do that is using $Q(HOR)$ assuming that it is entirely due to the oxidation of H_{abs} . Considering that $\sim 0.49\text{mC}/\text{cm}^2$ is required for depositing 1ML Pd, the nominal Pd thickness can be extrapolated using $Q(HOR)$:

If H_{abs} form a Pd-H α -phase, i.e., the ratio of H: Pd is ~ 0.03 [9], then $t_{Pd}^{nominal}$ can be expressed as:

$$t_{Pd}^{nominal} = \frac{2 \times Q(HOR)}{0.03} / (0.49) = 136 \times Q(HOR) \quad (\text{A.2})$$

If H_{abs} form a Pd-H β -phase, i.e., the ratio of H: Pd is ~ 0.63 [9], then t_{Pd}^{nominal} can be written as:

$$t_{Pd}^{\text{nominal}} = \frac{2 \times Q(\text{HOR})}{0.63} / (0.49) = 6.5 \times Q(\text{HOR}) \quad (\text{A.3})$$

where t_{Pd}^{nominal} is in ML. Since we don't expect any H absorption if the Pd local thickness is 1ML (2ML or more are necessary), to recover the actual Pd thickness, one needs to add 1ML.

Combining equation (A.1), (A.2) and (A.3), we obtain:

$$t_{Pd} = 53 \times \left(\frac{\Delta R}{R}\right) (\%) + 1 \quad (\alpha \text{ phase}) \quad (\text{A.4})$$

$$t_{Pd} = 2.5 \times \left(\frac{\Delta R}{R}\right) (\%) + 1 \quad (\beta \text{ phase}) \quad (\text{A.5})$$

In the case of Pd layer deposited at -0.7V for 100s, equations (A.4) and (A.5) yield $\sim 186\text{ML}$ and $\sim 10\text{ML}$ respectively. The first value is unreasonably large, suggesting that the Pd-H phase is the β phase. This Pd thickness of 10ML is consistent with an optical calculation which yielded $\sim 7\text{ML}$. The increase of $|\Delta R/R| \sim 0.7\%$ after each Pd deposition at -1.1V yields 1.7ML. We may thus conclude that at -1.1V, Pd deposition allows depositing between 1 and 2ML of Pd enough to cover the Co layer (see **Chapter 5**), whereas at -0.7V, Pd thickness increases with time at a typical rate of $\sim 0.1\text{ML/s}$.

A.4. Conclusions

We studied the growth of Pd on Au/Si(111) using the oxidation charge of absorbed H and the sample reflectivity. We devised a method to minimize the contribution of dissolved H_2 in the solution to the measured charge. We established a linear correlation between the measured anodic charge and the variation of the relative reflectivity which allowed us to write an equation yielding the Pd layer thickness as a function of relative reflectivity. We could demonstrate that the Pd growth rate at -0.7V is $\sim 0.1\text{ML/s}$ whereas at -1.1V, 1-2 ML of Pd is deposited with no dependence on the deposition time.

A.5. References

- [1] M.E. Quayum, S. Ye, K. Uosaki, Mechanism for nucleation and growth of electrochemical palladium deposition on an Au(111) electrode, *Journal of Electroanalytical Chemistry*, 520 (2002) 126-132.
- [2] H. Naohara, S. Ye, K. Uosaki, Electrochemical deposition of palladium on an Au(111) electrode: effects of adsorbed hydrogen for a growth mode, *Colloid Surf. A-Physicochem. Eng. Asp.*, 154 (1999) 201-208.
- [3] M. Baldauf, D.M. Kolb, A hydrogen adsorption and absorption study with ultrathin Pd overlayers on Au(111) and Au(100), *Electrochimica Acta*, 38 (1993) 2145-2153.
- [4] L.A. Kibler, M. Kleinert, R. Randler, D.M. Kolb, Initial stages of Pd deposition on Au(hkl) - Part I: Pd on Au(111), *Surface Science*, 443 (1999) 19-30.
- [5] L.A. Kibler, M. Kleinert, D.M. Kolb, Initial stages of Pd deposition on Au(hkl) part II: Pd on Au(100), *Surface Science*, 461 (2000) 155-167.
- [6] A. Damien, In Situ STM Study of the growth and dissolution processes on bimetallic Pd/Au(111) substrates and of ultrathin alloy layers on Au(111), in: *Physic*, Ecole Polytechnique, 2009.
- [7] Y.H. Liu, D. Gokcen, U. Bertocci, T.P. Moffat, Self-terminating growth of platinum films by electrochemical deposition, *Science*, 338 (2012) 1327-1330.
- [8] L.L. Jewell, B.H. Davis, Review of absorption and adsorption in the hydrogen-palladium system, *Appl. Catal. A-Gen.*, 310 (2006) 1-15.
- [9] G.R. Stafford, U. Bertocci, In situ stress and nanogravimetric measurements during hydrogen adsorption/absorption on Pd overlayers deposited onto (111)-textured Au, *J. Phys. Chem. C*, 113 (2009) 13249-13256.
- [10] D.E. Azofeifa, N. Clark, W.E. Vargas, H. Solis, G.K. Palsson, B. Hjorvarsson, Hydrogen induced changes in the optical properties of Pd capped V thin films, *J. Alloy. Compd.*, 580 (2013) S114-S118.
- [11] T.P.L. Pedersen, C. Liesch, C. Salinga, T. Eleftheriadis, H. Weis, M. Wuttig, Hydrogen-induced changes of mechanical stress and optical transmission in thin Pd films, *Thin Solid Films*, 458 (2004) 299-303.